8-1-1978

The effect of dopants SiO2, GeO2, and SnO2, on the microstructure and magnetic properties of Mn-Zn ferrites

Santosh Kumari

THE EFFECT OF DOPANTS SiO_2, GeO_2 AND SnO_2 ON THE MICROSTRUCTURE AND MAGNETIC PROPERTIES OF Mn-Zn FERRITES

BY

SANTOSH KUMARI (MISS)

A THESIS SUBMITTED TO THE
UNIVERSITY OF DELHI, DELHI
FOR THE AWARD OF THE DEGREE OF
DOCTOR OF PHILOSOPHY
IN PHYSICS

NATIONAL PHYSICAL LABORATORY
NEW DELHI-110012 (INDIA)

AUGUST, 1978

DECLARATION

This is to certify that the work presented in this thesis has been carried out exclusively by the candidate herself using the normal laboratory facilities and services.

To the best of the candidate's knowledge this work has not formed the basis for the award of any other degree.

(Santosh Kumari)
CANDIDATE

SUPERVISOR

Acknowledgements

The authoress records her deep sense of gratitude and indebtedness to her guide and mentor, Prof. G.C. Jain, Head, Division of Materials, National Physical Laboratory, New Delhi, for his keen interest and constant encouragement throughout the course of this work.

An equally important contributory factor to this work has been, her close association with Dr. B.K. Das, Scientist Incharge, Ferrite Section, NPL. His scientific insight in the subject added immensely to the quality of the presented study.

The SEM work was primarily successful due to the patient efforts of Dr. Allen Hepworth, Indian Institute of Technology, New Delhi.

Thanks are due to the administrative and scientific staff of DMRL, Hyderabad, for generously making available their EPMA facilities.

A timely quantum of help came from an old colleague Mr.Charanjit S. Bhatia, University of Minnesota, USA and Mr. Clair T. Hovland, Physical Electronics Ind., USA who provided with the Auger electron spectroscopy data.

Due thanks are accorded to the NCERT for providing the financial assistance during the course of study.

The authoress is grateful to Prof. A.R. Verma, Director, NPL for extending all laboratory facilities.

And finally, the authoress would like to acknowledge the help and cooperation of all her colleagues in the Ferrite Section and friends at the NPL.

(Santosh Kumari)

Preface

Ferrite have found a variety of uses in electronic and communication engineering. Mn-Zn ferrites ($Mn_{1-x}Zn_xFe_2O_4$) are widely used as filter core materials over a range of frequencies varying from several hundred Hz to several MHz. There are many other applications such as in television receivers as deflection yokes and E.H.T. cores etc.

The development of a ferrite suitable for a particular application is an interesting scientific problem and technological challenge. The properties of ferrites are determined by a number of intrinsic properties and their interaction with the ceramic microstructure.

Impurities, present in or added to the raw materials used for processing ferrites, play an important role in determining the properties of the ferrites. The cost of ferrites is very much related to the purity level of the raw materials used. It is, therefore, both scientifically and economically important that the behaviour of ferrites is studied with additions of controlled amounts of impurities commonly present in the raw materials cheaply available.

Silica (SiO_2) is commonly found in the raw materials and is also, to some extent, contributed by atmospheric dust. In order to determine the tolerance of SiO_2 as an impurity in

the raw materials and during processing, a systematic study has been carried out to investigate the effect of SiO_2 addition in the raw materials. The effect of controlled additions of oxides of germanium and tin to the raw materials has also been studied since Si, Ge and Sn are all elements of the IV group in the periodic table.

The studies have been presented in five chapters.

Chapter I gives the background essential for the present study. This chapter deals with the important properties of ferrites. The properties of ferrites can be classified in two categories. Firstly intrinsic properties i.e. those properties which are decided by the basic composition of the ferrite. Secondly extrinsic properties i.e. those properties which depend upon the microstructure and processing parameters. The literature presently available with special reference to impurities and their effect on the magnetic properties has also been discussed.

The effect of impurities on the magnetic properties of ferrites depends upon whether they go in solid solution with the ferrite or stay insoluble. The nature of the three impurities - SiO_2, GeO_2 and SnO_2 in the ferrite has been studied in chapter II by employing scanning electron microscopy, X-ray and Auger microprobe and X-ray diffraction (lattice parameter measurement) techniques. Both SiO_2 and GeO_2 have been found to have a limited solubility in the ferrite and tend to segregate at the grain boundaries. SiO_2 has been found to form a compound at the grain boundaries. Si-rich inclusions have also been detected in the grains at larger concentrations of SiO_2 (1.28 mol%). Ge-enrichment

at the grain boundaries has been observed with the help of Auger electron spectroscopy.

No detectable segregation of SnO_2, was observed with the help of XMA even for as high a concentration as 5.70 mol%. This may be due to a high solid solubility of SnO_2 in the ferrite. Ferrite lattice has been found to expand on additions of SnO_2 up to a level of 5.70 mol%, the highest concentration studied.

The third chapter deals with the effect of these impurities - SiO_2, GeO_2 and SnO_2 doped in various amounts on the microstructure of the Mn-Zn ferrite. It has been discussed that the impurities present could affect the microstructure in a number of ways. Impurities present in solid solution could give rise to an impurity drag effect which impedes boundary motion. The insoluble impurities would disturb the course of normal grain growth during sintering more drastically. It has been discussed that small concentrations of the insoluble impurity such that the impurity remains as a dispersed phase result in abnormal or discontinuous grain growth. At higher concentrations, the impurity phase would exist as plates or films on the grain boundaries altering the kinetics for growth.

Microstructure studies of SiO_2 and GeO_2 doped Mn-Zn ferrites show that these impurities lower the sintering temperature thereby enhancing the rate of grain growth. Both of these impurities give rise to discontinuous grain growth. Giant grains with almost entire porosity being intragranular are formed at a SiO_2 content of 0.08 mol% and at a GeO_2 content of 1.28 mol%. From these observations,

it is inferred that up to these levels they exist as dispersed phase therefore giving rise to discontinuous grain growth. At a level higher than 0.64 mol% SiO_2 and 3.82 mol% GeO_2 somewhat regular grain structure reappears though with much higher intragranular porosity as compared to undoped ferrite. It is discussed that at these levels, the impurities are present as second phase film around the grains suppressing the abnormal grain growth.

SnO_2 additions are not found to affect the microstructure even up to a level of 5.70 mol%. These results are in agreement with the findings in the first chapter that SnO_2 goes in solid solution with the ferrite.

In chapter IV, the effect of these impurities on the magnetic property - initial permeability, μ_i, and resistivity ρ of the Mn-Zn ferrite has been studied. It is known that an increase in density increases the saturation magnetization, M_s, and hence the initial permeability. It has also been discussed that in samples containing intragranular porosity, an increase in pore to pore distance, D_p, increases the span of domain walls and hence the μ_i.

In the case of SiO_2 as dopant, it has been observed that μ_i increases up to a SiO_2 concentration of 0.04 mol%. This is in confirmity with the increase in the product $M_s.D_p$, in this range. At a SiO_2 concentration of 0.08 mol%, even though M_s increases, μ_i decreases on account of a decrease in D_p because here the microstructure shows large intragranular porosity. Beyond a silica concentration of 0.32 mol%, although the product $M_s.D_p$ does not decrease, the μ_i is found to decrease because of the formation of a nonmag-

netic layer at the grain boundaries and precipitation inside the grains.

In the case of GeO_2, similar effects are observed though the peak in μ_i occurs at a content of 0.64 mol%.

SnO_2 additions are not found to affect μ_i appreciably.

A study of the temperature variation of μ_i shows that in the case of SnO_2, there is a shift in the secondary maximum peak (SMP) indicating a solubility of SnO_2 in the ferrite. Such an observation is not appreciable in SiO_2 and GeO_2. The μ_i-T curves further show a flatness at higher impurity concentrations in all the three cases presumably due to wall discontinuities at the grain boundaries.

A study of disaccommodation with various concentrations of these impurities shows that the disaccommodation decreases with impurity concentrations, the maximum change being in SnO_2. The results have been discussed in terms of the solubility of Sn^{4+} ions and their tendency to localize Fe^{2+} ions.

Variations in the resistivity with temperature for the three impurities indicate that the predominant conduction mechanism is the electron hopping from Fe^{3+} to Fe^{2+} and that Sn^{4+} - Fe^{2+} pairs dissociate at higher temperatures.

Chapter V deals with the effect of these impurities on the core losses of the Mn-Zn ferrite. The core losses have been studied at a flux density of 0.2 wb/m^2 (2000 gauss) and up to a frequency of 15.75 KHz.

At 15.75 KHz, the core losses decrease up to a silica content of 0.04 mol% corresponding to an increase in μ_i. At higher silica contents the core losses are always higher going through a peak at 0.08 mol%. The peak becomes more predominant

as frequency increases.

Similar effects have been observed in the case of GeO_2 additions though the peak in the core losses occurs at 1.28 mol%. This peak is also found to be more predominant at higher frequencies.

SnO_2 additions are not found to affect the core losses appreciably.

The hysteresis loops under similar conditions have also been studied. The measurements of loop areas suggest that the core losses measured are essentially the hysteresis losses. Core losses/frequency therefore represent the loop area.

At low impurity concentrations (up to 0.04 mol% SiO_2 and 0.64 mol% GeO_2), core losses decrease mainly due to a decrease in H_c which has been found to follow the relationship $H_c \propto D_p^{-0.5}$. At a SiO_2 concentration of 0.08 mol% and a GeO_2 concentration of 1.28 mol%, an increase in loop area with frequency is observed. These very samples also exhibit giant grains with large trapped porosity. These effects have been attributed to the relaxation of amplitude permeability at high field strengths. At higher field strengths, closure domains are formed at intragranular pores enabling the domain walls to become detached from the pores. This process is a comparatively slow process and therefore the amplitude permeability is subjected to a strong relaxation even at frequencies of 10 to 50 KHz.

At further higher SiO_2 and GeO_2 contents the core losses/frequency are always high but are independent of frequency. The coercive force, H_c is found to be much higher than that given by the relationship $H_c \propto D_p^{-0.5}$. It is discussed

that this increase in H_c has been brought in by the presence of inclusions inside the grains. The presence of the grain boundary phase around the grains is also responsible for increasing the losses since it gives rise to wall discontinuities resulting in the demagnetizing effects. This phase also puts the grains under stress while cooling further deteriorating the core losses.

Finally, the major conclusions drawn from the entire study are listed under the 'CONCLUSIONS'.

Contents

CHAPTER - I

BACKGROUND

1.1. FERRITES AND SPINEL STRUCTURE

The term ferrite denotes a group of compounds containing iron oxides which have the general formula $MeO.Fe_2O_3$, where Me is a divalent metal ion such as Mn^{2+}, Fe^{2+}, Ni^{2+}, Zn^{2+} etc. A typical ferrite is magnetite, Fe_3O_4 (or FeO, Fe_2O_3). *By replacing the divalent iron in* Fe_3O_4 by another divalent ion, various ferrites can be formulated. By mixing two or more kinds of Me^{2+} ion, one can obtain mixed ferrites.

Ferrites have the so-called spinel structure. The unit cell of a spinel lattice consists of 8 formula units of $Me^{2+}Fe_2^{3+}O_4$. Figure 1.1(a) shows one-eights of the unit cell of a spinel. In it, the oxygen anions form a closed packed f.c.c. lattice with the cations in the interstitial sites of two types - A-sites and B-sites as shown in the figure. Tetrahedral A-sites are situated half way between the corner and the centre of the cube surrounded by four oxygen ions Octahedral B-sites are situated at the centre of a cube and a cube edge surrounded by six oxygen ions.

Thus in the unit cell, in total, there are 32 oxygen sites of which all are occupied but of the 64 A-sites only 8 are occupied which have their nearest B-sites empty. Out of the 32 B-sites only 16 are occupied; these B-sites form rows lying parallel to the face diagonals with alternate rows occupied. The body centered B-sites are only occupied in alternate f.c.c. cubes, i.e. in those with vacant A-sites.

The cation distribution on A and B sites, in general

is represented by

$$\underbrace{Me^{2+}_{\delta}\ Fe^{3+}_{1-\delta}}_{A}\qquad \underbrace{Me^{2+}_{1-\delta}\ Fe^{3+}_{1+\delta}}_{B}\ O_4$$

The limiting case of $\delta = 1$ is called a normal spinel and $\delta = 0$ is called an inverse spinel. Most of the ferrimagnetic spinels (except a few such as $Zn^{2+}\left[Fe^{3+}_2\right]O_4$ which is a normal spinel) are more or less inverse.

The various factors that can influence the distribution of cations on A and B sites[1-5] are - the ionic radius, the electronic configuration[6,7] and the electrostatic energy.[8,9]

1.2. SATURATION MAGNETIZATION

M_{S_o}, the saturation magnetization at 0^oK, is the resultant dipole moment for unit volume when the dipole moments associated with all the molecules are aligned in the direction of the applied magnetic field. M_{S_o}, is therefore given by

$$M_{S_o} = N\mu_m \qquad (1.1)$$

where N is the number of molecules per unit volume and μ_m is the net magnetic moment of one molecule.

From a comparison of different exchange interactions it follows that in a spinel the A-B interaction is by far the greatest, therefore the ions at the A-sites are coupled with spins antiparallel to those on the B-sites. The exchange coupling between the metallic ions act through the oxygen ions. The resultant moment per molecule in a spinel is

$$\mu_m = 2\mu_B - \mu_A \qquad (1.2)$$

where μ_B and μ_A are the magnetic moments associated with ions on B-site and A-site respectively.

In a mixed zinc ferrite, the cation distribution is

given by

$$\underbrace{Zn_{\delta}^{2+}\ Fe_{1-\delta}^{3+}}_{A}\quad\underbrace{Me_{1-\delta}^{2+}\ Fe_{1+\delta}^{3+}}_{B}\ O_4$$

since the Zn^{2+} ions always occupy the tetrahedral sites.

The net dipole moment per molecule μ_m for such a mixture is then given by the equation

$$\mu_m = 10\delta + m(1-\delta)\ \mu_B \qquad (1.3)$$

where m is the magnetic moment of Me^{2+} ion in Bohr magneton.

It is evident from Eqn. 1.3 that addition of zinc to these ferrites will boost up their saturation magnetization.[10-14] This is shown in Fig. 1.2. It is seen from Fig.1.2 that the magnetic moment decreases for values of δ larger than 0.6. This is due to the fact that for larger amount of Zn the A-sublattice gets so much diluted that the A-B interaction weakens.

Perfect alignment of dipole moments of all molecules is only possible at $0^{o}K$. At any finite temperature, the saturation magnetization M_S is related to that at $0^{o}K$ (M_{S_o}) by

$$M_S/M_{S_o} = L(\alpha) \qquad (1.4)$$

where $L(\alpha)$ is the Langevin function, $\coth\alpha - \frac{1}{\alpha}$ and

$$\alpha = \frac{\mu_o \mu_m H_e}{kT}$$

H_e is the effective field at a dipole.

If the dipoles are restricted to finite set of orientations relative to the applied field, $L(\alpha)$ is replaced by $B_J(x)$ where $B_J(x)$ is the Brillouin function.

Equation 1.4 is valid for temperature T less than T_c, the Curie temperature. At $T - T_c$ the value of M_S/M_{S_o} dis-

FIG. 1·2

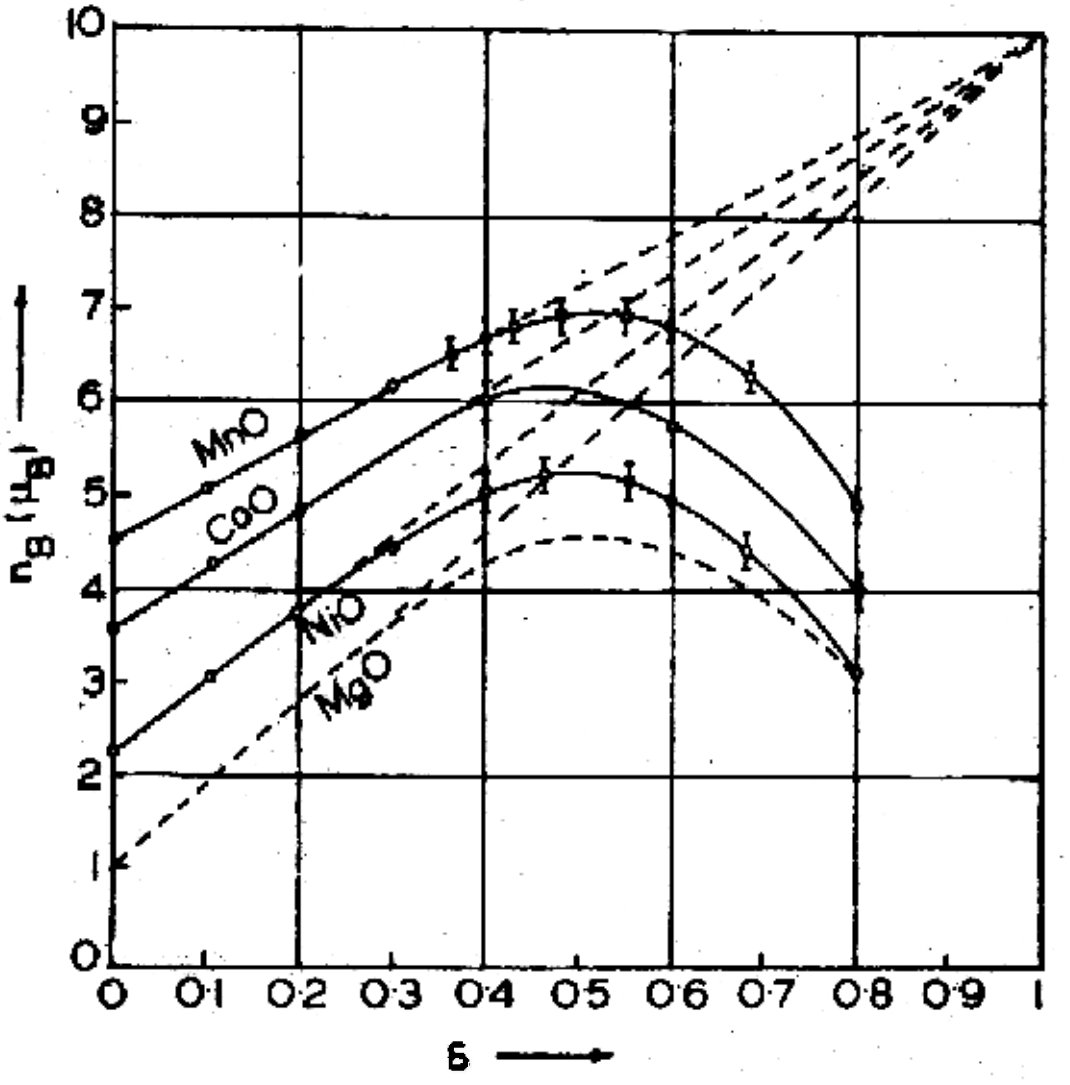

Saturation magnetization of mixed ferrites $M_{1-\delta}Zn_\delta Fe_2O_4$ in Bohr magnetons per unit formula (Guillaud, 1951)

appears and the material looses its ferrimagnetic behaviour at $T \geq T_c$.

Figure 1.3 gives the M_s versus T curves for various Mn-Zn ferrites.[15,16]

1.3 THE CURIE TEMPERATURE

The Curie temperature T_c is the temperature at which the ferro or ferrimagnetic material changes to a paramagnetic one. In a spinel ferrite let E_A be the energy needed to invert the spin of an ion at site A. The average thermal energy needed to create absolutely non-interacting ions is kT_c.

Hence

$$kT_c \simeq \frac{A}{A+B} E_A + \frac{B}{A+B} E_B$$

where A and B are the number of magnetic ions at sites A and B respectively.

In a normal ferrite A = 1, B = 2 and hence

$$kT_c = E_A/3 + 2E_B/3$$

If Zn is added to the ferrite and we consider a ferrite of composition

$$Zn_{\delta}^{2+} Fe_{1-\delta}^{3+} [Mn_{1-\delta}^{2+} Fe_{1+\delta}^{3+}] O_4$$

$$kT_{c_\delta} = \frac{1-\delta}{3+\delta} E_A + \frac{2}{3-\delta} E'_B$$

since δ sites at A occupied by zinc have zero magnetic moment. Zn being a non-magnetic ion and does not take part in exchange interaction. E'_B is the energy needed to invert spins an ions at B-sites in the Zn-mixed ferrite and is related to E_B by

$$E'_B = (1-\delta) E_B$$

So

$$kT_{c_\delta} = \frac{1-\delta}{3-\delta} E_A + \frac{2(1-\delta)}{3-\delta} E_B = \frac{1-\delta}{1-\delta/3} kT_c \qquad (1.5)$$

Fig 1.3

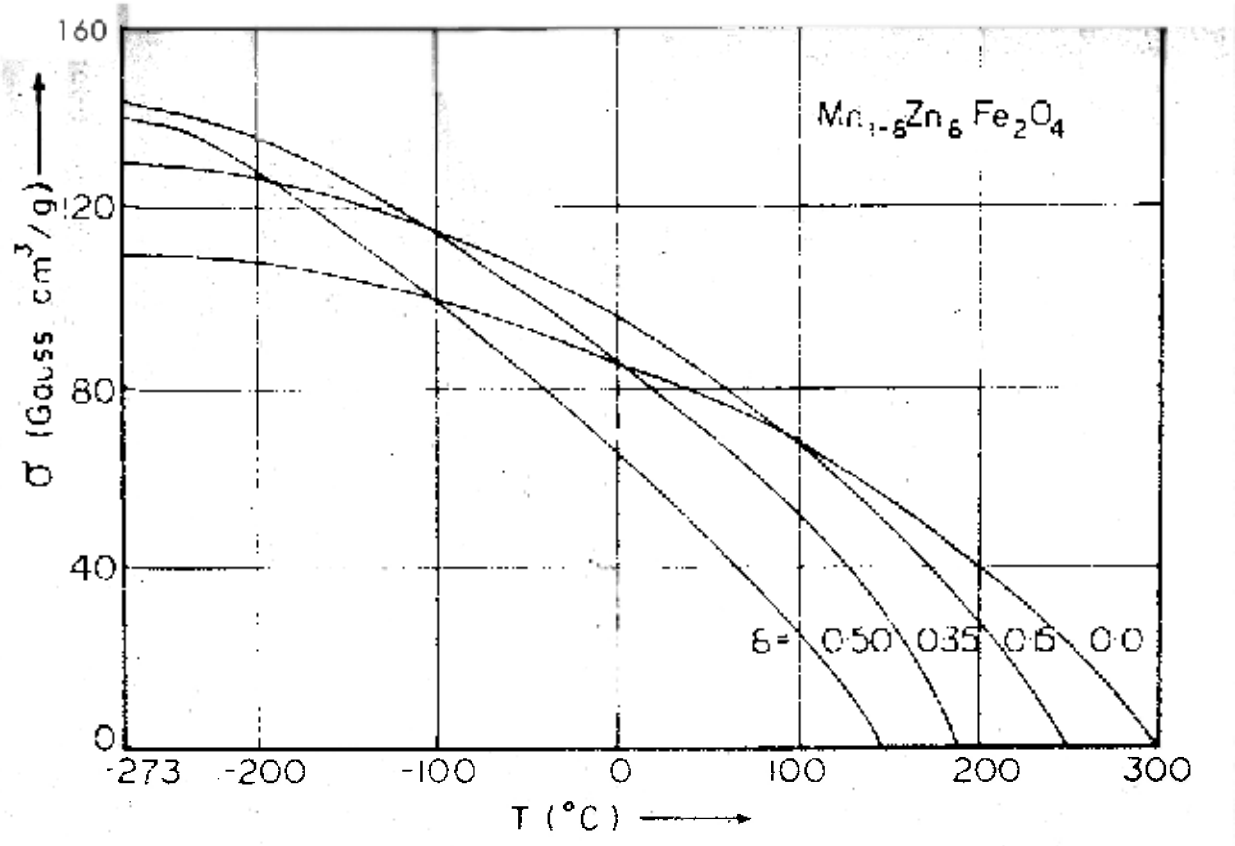

Saturation magnetization per gram, σ, as a function of temperature for some ferrites of the $Mn_{1-\delta}Zn_{\delta}Fe_2O_4$ series.

Hence the Curie temperature decreases by addition of ions with non-magnetic moment like Zn.[17]

1.4. MAGNETOCRYSTALLINE ANISOTROPY AND MAGNETOSTRICTION

1.4.1. Magnetocrystalline Anisotropy

The preference of a magnetization vector to lie along certain crystallographic directions in the crystal can be expressed by a magnetocrystalline anisotropy energy. In a cubic crystal (as in spinel ferrites) the expression for the anisotropy energy has, by reasons by symmetry, the following form

$$E_1 = K_0 - K_1 (\alpha_1^2\alpha_2^2 + \alpha_2^2\alpha_3^2 + \alpha_3^2\alpha_1^2) + K_2(\alpha_1^2\alpha_2^2\alpha_3^2) + \ldots . \qquad (1.a)$$

where α_1, α_2 and α_3 are the direction cosines of the magnetization with respect to the cubic axes and K_0, K_1 and K_2 are the anisotropy constants. In the absence of any external field, the magnetization vector lies in the direction in which E_1 is minimum called the easy direction. When $K_1 > 0$, the cubic axes are the easy directions and if $K_1 < 0$, the easy directions correspond to the body diagonals. The application of an external magnetic field along a direction different from an easy direction causes a deviation of the magnetization to another direction so that the torque due to the external field is balanced by the torque originating in the anisotropy energy.

The origin of the anisotropy of an ion on a certain lattice site is found in the spin-orbit interaction.[18,19] In spinel ferrites the anisotropy energy originates from the contributions of individual magnetic ions. It has been found that the contribution to K_1 of different ions is different

and depends on the type of site it is occupying and its neighbouring ion configuration. For example, Fe^{3+} ion has a positive contribution to anisotropy on A-sites but has a negative contribution when on B-site.[20-23] Fe^{2+} ion has a positive contribution on B-site.[24-26] The contribution of Mn^{2+} to anisotropy has been found to be very small.[27] The temperature variation of the anisotropy contributions of various ions are also different.[28-30]

1.4.2. Magnetostriction

Magnetostriction is that phenomenon wherein the shape of a ferro or ferrimagnetic specimen changes during the process of magnetization. Magnetostriction originates in the interaction between the atomic magnetic moments, as in magnetic anisotropy. Therefore an extra contribution to the magnetic anisotropy is given by the magnetostriction. For a cubic crystal it can be expressed as[16]

(1.7)

where λ_s is the saturation magnetostriction coefficient and λ_{100} and λ_{111} are the magnetostriction constants for (100) and (111) directions. For a polycrystalline substance the average λ_s will be

$$\lambda_s = 2/5 \ \lambda_{100} + 3/5 \ \lambda_{111} \qquad (1.8)$$

1.4.3. Concept of Total Anisotropy

The anisotropy value that can be deduced for polycrystalline material from the resonance frequency measurement by using the Snoek formula is larger than the magnetocrystalline anisotropy value.[31] It has been found that the additional components to K_1 seem to be related to the polycrystalline nature of the material. This is thought to be

related to the stresses generated inside a polycrystalline material when it is cooled from above its Curie temperature to form domains (see section 1.5). This leads to the idea of total anisotropy for poly-ferrimagnets. Globus[32,33] has given the following expression for the total anisotropy K

$$K = K_1 + \lambda_s \sigma_n - A_d \qquad (1.9)$$

where

K_1 = magnetocrystalline anisotropy constant

$\lambda_s \sigma_n$ = magnetoelastic energy of the polycrystalline sample

λ_s = saturation magnetostriction

σ_n = internal stresses

A_d = dipolar energy (demagnetization energy)

The contribution of A_d was later shown to be negligible for ferrites as the large value of A_d could not explain the compensation of anisotropies.

Hence

$$K \simeq K_1 + \lambda_s \sigma_n \qquad (1.10)$$

1.5. MAGNETIC DOMAINS AND HYSTERESIS

The presence of ferromagnetic domains was first predicted by P. Weiss[34] in 1907 in his famous hypothesis of the molecular field. Inside such a domain, all the spins are lined up parallel to one another. The domain structure is a natural consequence of the various contributions to the energy - exchange, anisotropy and magnetic of a ferromagnetic body. The transition layer which separates adjacent domains magnetized in different directions is termed as 'domain wall' or 'Bloch wall' named after F. Bloch (1932).[35] The actual thickness and energy of the transition layer is the result of

a minimumisation of the exchange and anisotropy energies.[36] Figure 1.4 gives some examples of Weiss domain structure with so-called 90° and 180° walls in which there is a flux closure (a), domain structure around inclusions (b) and domain in a polycrystal (c).[37]

In a ferro (or ferri) magnetic material, an external field produces a magnetization parallel to the field. This is known as 'technical magnetization'. In a homogenous ferro (ferri) magnetic material the magnetic moment increases under the action of an applied magnetic field in three stages as shown in Fig.1.5(a). In an inhomogenous material i.e. which contains voids, inclusions, precipitates, internal stresses or crystal boundaries etc., the displacement of domain walls requires fairly large field and thus the wall displacement and rotation can take place simultaneously.

Another feature of inhomogenous magnetic materials is that the stable domain structure is not a unique function of the applied field. The domain structure which is attained by increasing the field to H is different from that attained by decreasing the field from a high value to H, so that the intensity of magnetization is different for both cases. The familiar hysteresis loop is obtained due to this. Figure 1.5(b) shows a typical hysteresis loop defining the related parameters - saturation magnetization, remanence and coercive force.

1.5.1. Remanence

In all ferro (ferri) magnetic materials, if the magnetic field is reduced to zero, the material retains certain flux density known as remanence, B_r, which is equal to $\mu_o M_r$. After the magnetic field is reduced to zero, the demagnetizing

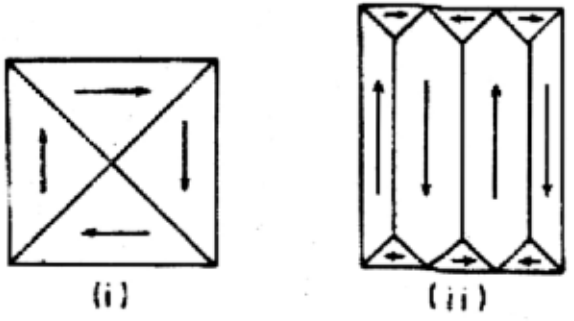

(a) Examples of Weiss domain configurations in which flux closure occurs.

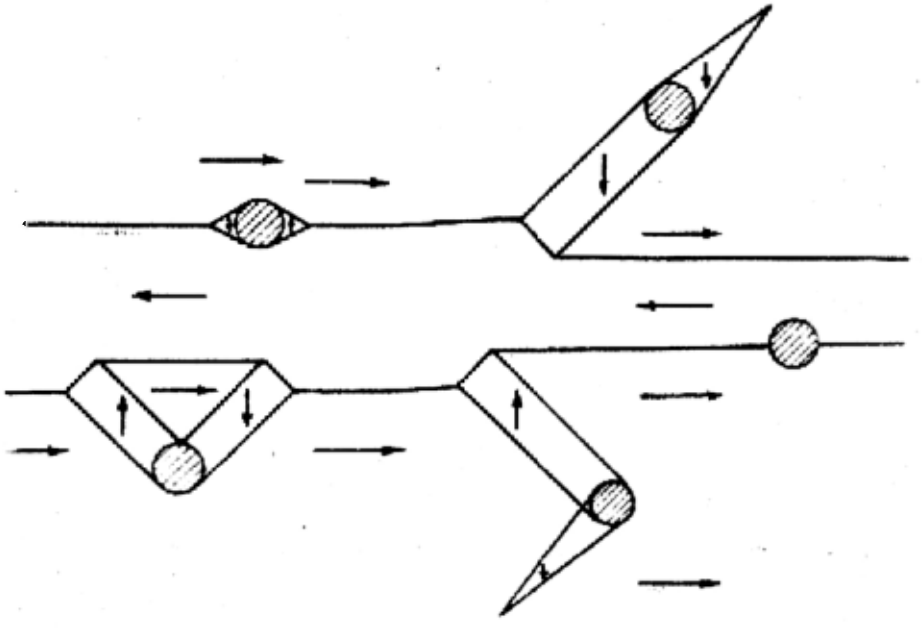

(b) Domain structure around inclusions.

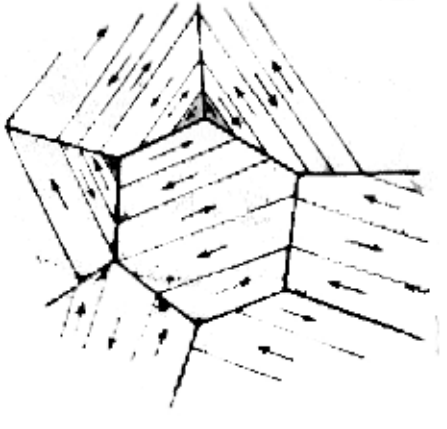

(C) Domain structure of a polycrystal

where p represents the porosity of the material.

Dijkstra and Wert[40] have considered spike formation around non-magnetic inclusions and have concluded that

$$H_c = \frac{3 \gamma_{180^0} I K^*}{M_s d} \qquad (1.12)$$

where

γ_{180^0} = energy of 180^0 domain wall

d = diameter of inclusion

K^* = length of spike/d

I = volume fraction of inclusions

It has been shown that H_c varies with d in a manner giving maximum H_c when d = wall thickness δ.

From the above considerations it is evident that for low H_c, the ferrite should have no intragranular pores and very few non-magnetic inclusions.

1.5.3. Theoretical Model for Magnetization Mechanism

By using carefully prepared samples and accurate measurements, Globus discovered the existence of two fundamental parameters for the magnetization mechanisms in ceramic ferrimagnets the total anisotropy and the grain size. Also, the initial susceptibility was found to be proportional to the grain size. To explain these features, Globus[32,33,41-45] put forward a theoretical model relating the grain diameter with the motion mechanisms of the domain wall. The first principles of the model are givenbbelow

(i) A 180^0 domain wall in a spherical grain, is in a diametral position in the spontaneous magnetization state.

(ii) The wall perimeter remains pinned to the grain boundary for any position of the wall inside the grain.

(iii) When submitted to a magnetic field, the pinned wall

field tries to orient the magnetic moments randomly but the various anisotropies prevent the complete randomisation of the moments and hence a residual magnetization is left.

On cooling a strain free polycrystalline material from above T_c, domains form and the direction of magnetization in each domain is determined by the crystalline anisotropy. So when the material is magnetized to saturation and the magnetic field is brought down to zero, thereafter, a large number of individual magnetization vectors are turned from the original easy directions into another. In general this will be accompanied by a shape change. Such strains will cause M_r to decrease unless magnetostriction at saturation λ_s is zero. Hence a low value of λ_s and a high value of K_1 leads to a higher value of M_r/M_s. The higher the Curie temperature the higher will be absolute magnitude of M_r since M_s increases with decreasing ration T/T_c.

1.5.2. Coercive Force

Coercive force, H_c, is defined as the magnetic field strength necessary to bring down the remanent flux density to zero. If the domains walls are easy to move the material has low coercive force. On the other hand if the boundary is difficult to move the material would have high coercive force.

Impurities and other defects which due to their binding energy with domain walls try to impede the movement of the walls. The nature of such interactions between domain wall and imperfections has been under considerable investigations.[38-40] According to Neel,[38] for ferrites with negative K_1 and $|K_1| >> \mu_o M_s^2$

$$H_c = \qquad (1.11)$$

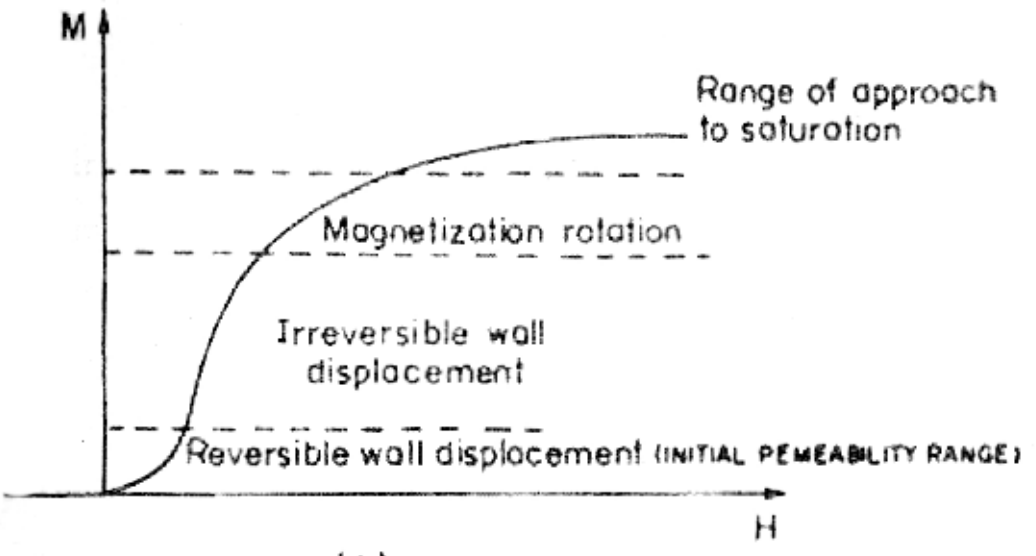
M
Range of approach to saturation
Magnetization rotation
Irreversible wall displacement
Reversible wall displacement (INITIAL PEMEABILITY RANGE)
H

(a)

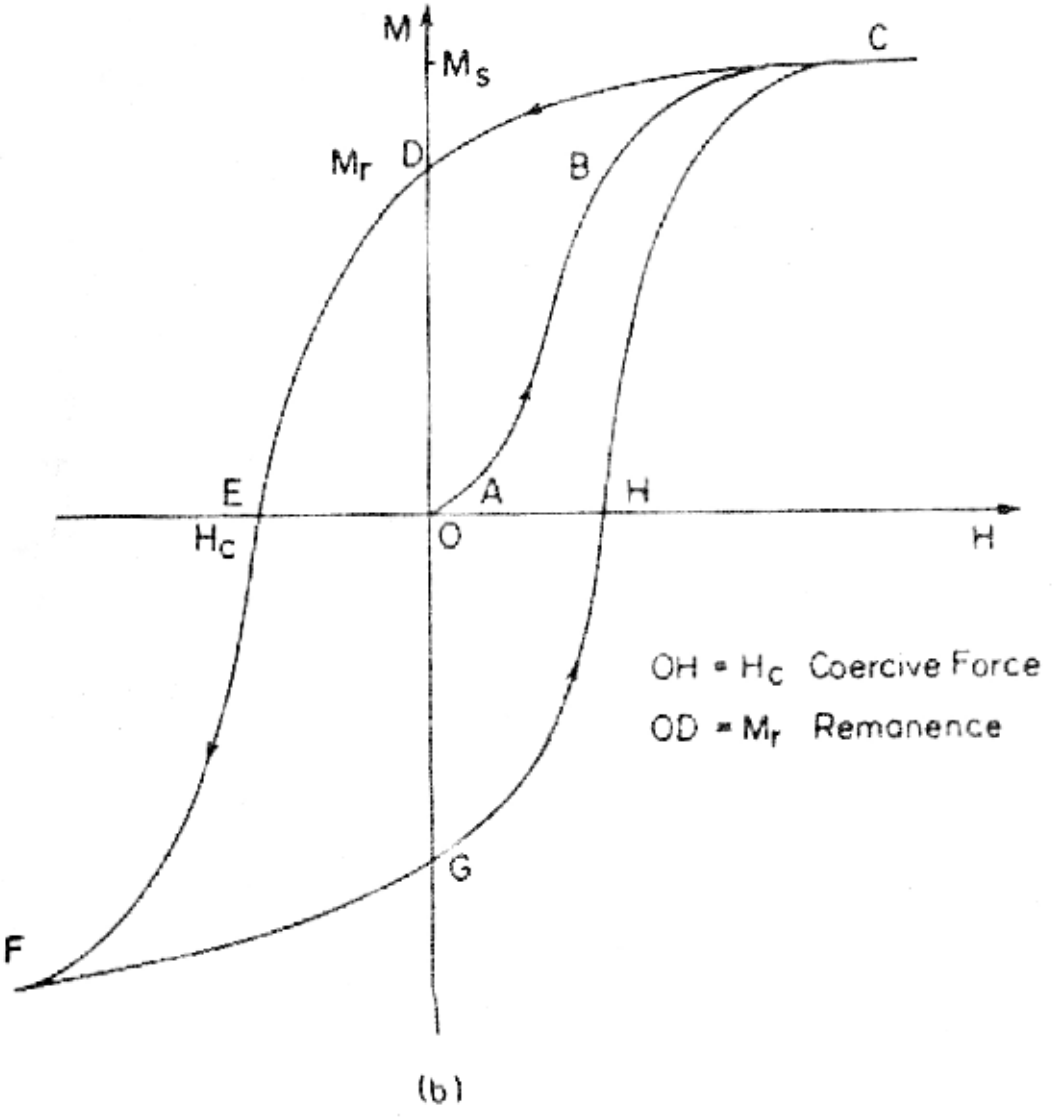
M
Ms
C
Mr
D
B
E
A
H
Hc
O
H
OH = Hc Coercive Force
OD = Mr Remanence
G
F

(b)

Fig : 5

bulges; if it unpins itself, it moves to be pinned again in another position.

(iv) The parameters which control the unpinning are related to the nature of the wall and not to the nature of the grain boundary; the unpinning would result from a rupture mechanism of the wall along its edge.

(v) The existence of several magnetization axes in each grain of a soft cubic material, allows the walls to choose the best directions to follow the toroid symmetry (Fig.1.6(a)).

(vi) The cooperation between the walls of neighbouring grains ensures the flux continuity while they move.

(vii) Simplifications are used to facilitate the analysis as compared with the actual conditions, it will be then considered -

- in case of the reversible mechanisms, a spherical bulging of the wall inside a spherical grain.

- in case of the non-reversible mechanisms, a displacement of a flat wall in a spherical grain, the wall surface variation being considered as the parameter which controls by itself only the displacement.

This model successfully explains the various reversible and irreversible processes occuring in poly-ferrimagnets. For the point of view of present work, the static initial susceptibility, initial magnetization curve and the hysteresis loop have been explained in terms of this model.

(a) Static Initial Susceptibility

When submitted to a weak magnetic field, the wall bulges remaining fixed to the grain boundary in its diametral position.

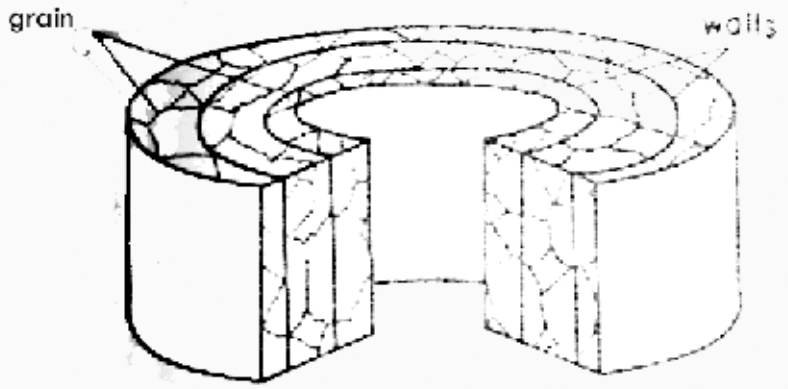

(a)

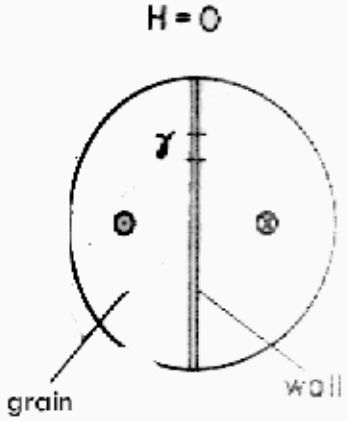

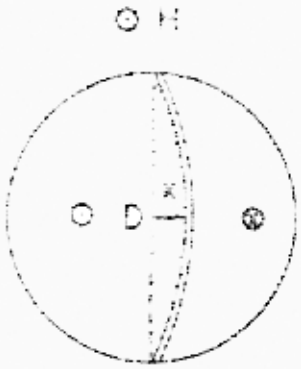

(c)

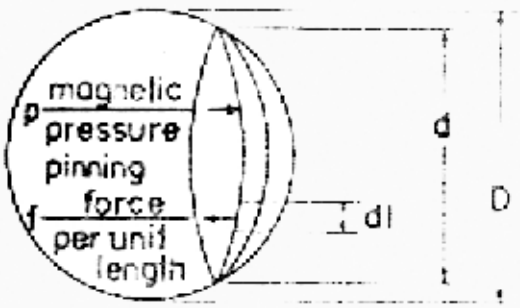

thrust $P = pS = 2M_S H \frac{\pi d^2}{4}$

pinning $F = fL = f \pi d$

(d)

Fig. 16

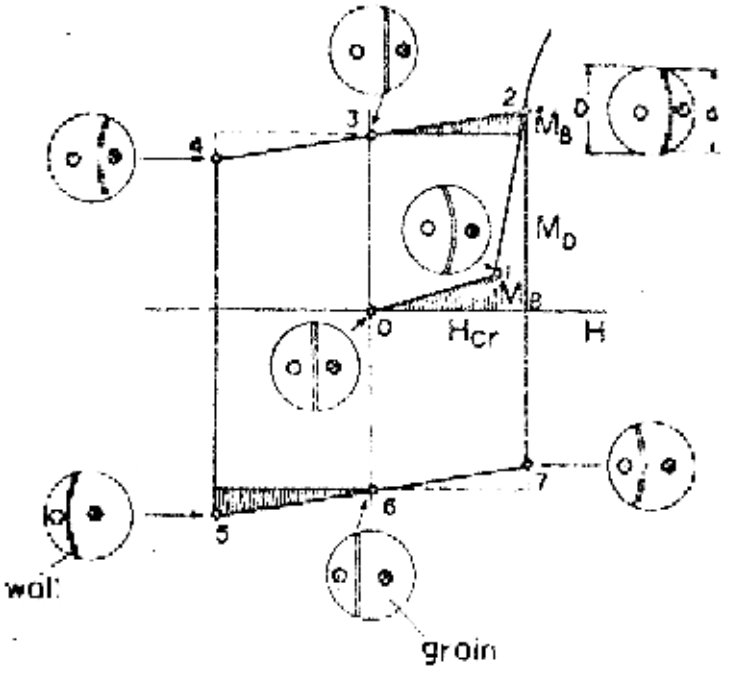

M_B Bulging magnetization

M_D Displacement magnetization

(e)

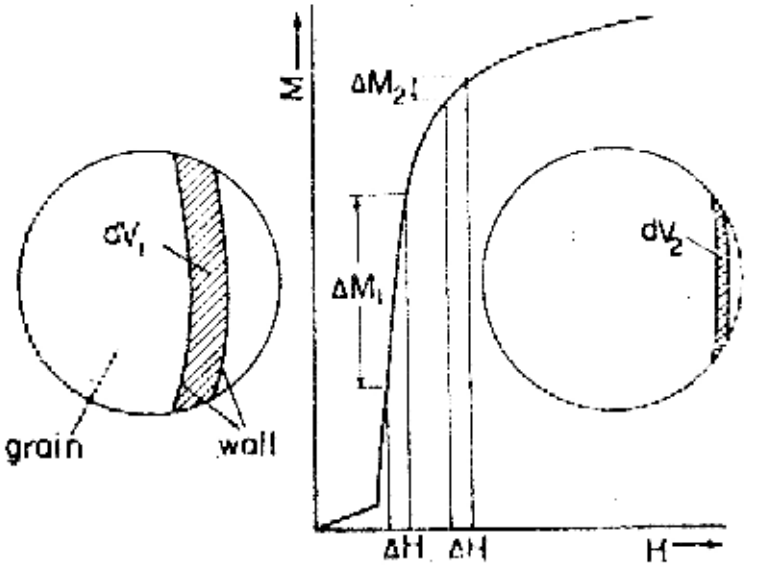

(f)

Fig 1·6

the energy needed to release an electron from the ion for a jump to the neighbouring ion, so giving rise to electrical conductivity. It has been pointed out by Jonker[68] that in these non-impurity (intrinsic) semiconductors the influence of temperature on the concentration of the conduction carriers is relatively small. This means that the temperature influence on the conductivity is only a result of the change of the mobility of the electrons or holes with temperature. E_i is determined according to the relation

$$E_i = 0.198.10^{-3} \frac{d}{d(1/T)} (\log \rho) \qquad (1.29)$$

For ferrites, the value of E_i lie between 0.1 and 0.5 eV.

1.8. CORE LOSSES IN FERRITES

If a loss free winding having N turns is placed round a closed magnetic core of cross sectional area A and magnetic length l and an alternating voltage E is applied, a power loss (volume) density, $P_m = E^2 G/Al$, will be observed, where G is the conductance appearing across the winding due to the magnetic losses in the core. These are termed as the core losses and are dissipated as heat in the core. The major losses contributing to the core losses are the hysteresis losses, eddy current losses and the residual losses.[66,69]

(i) Hysteresis Losses

The energy lost during each cycle in a unit volume of the material due to hysteresis is equal to the loop area. It is called the hysteresis energy loss (volume) density and is denoted by W_h

$$W_h = \frac{1}{\mu_i} \oint B dH \qquad \text{ergs cm}^{-3} \text{ cycle}^{-1} \qquad (1.30)$$

The hysteresis power dissipated in a core of volume v

In first approximation it is assumed that the specific properties (energy per unit surface γ and thickness δ) of a bulged wall are the same as those of the flat wall.

For such a bulged wall (Fig.1.6(b,c)) the equilibrium condition between the increase of the wall energy (surface) and the field energy (volume swept by the wall can be written as follows

$$\Delta E = -2M_s H \frac{\pi}{6} x \left(\frac{3D^2}{4} + x^2\right) + \gamma \left[\pi\left(\frac{D^2}{4} + x^2\right) - \frac{\pi D^2}{4}\right] \qquad (1.13)$$

After derivation, by neglecting the terms with x^2, one obtains

$$x = \frac{M_s H}{8\gamma} D^2$$

The magnetization due to the volume swept is

$$M = \frac{2dV}{V} M_s = aHD$$

where

$$a = \frac{3}{16} \frac{M_s^2}{\gamma}$$

Then the initial susceptibility value χ is

$$\chi = aD = \frac{3}{16} \frac{M_s^2}{\gamma} \cdot D$$

This explains the proportionality between the χ and the grain diameter D.

(b) Hysteresis Loop

A diametral wall pinned along its perimeter in a spherical grain bulges under the action of a weak field, resulting in a magnetization proportional to H and D. The wall unpinning occurs when the thrust due to the magnetic field ($F = 2M_s H \frac{\pi D^2}{4}$) becomes larger than the pinning force on a boundary ($F = f \pi D$, where f is the pinning force per unit length, (Fig.1.6(d))). Increasing the field leads to an

increase in the wall bulging, up to a value such as P = F, which permits a critical unpinning field H_{cr} to be determined

$$H_{cr} = \frac{2f}{M_s . D} \qquad (1.15)$$

When $H > H_{cr}$, one obtains $P > F$, what makes the wall break off from this diametral position and move inside the grain.

While moving in the spherical grain, each field value corresponds to an equilibrium between the new values of the thrust and the pinning force so that the magnetic field makes the wall bulge just at the limit of the next break off.

On the initial magnetization curve plotted on Fig.1.6(e), point 2 corresponds to the magnetization value due to the joint effects of the displacement and the bulging. When decreasing the applied fields, the wall becomes flat, and at point 3 the magnetization M is only due to the displacement(remanence). Since H changes its sign, the wall bulges in the inverse direction. When the field (-H) reaches the value of the critical field corresponding to a wall diameter d, the wall detaches itself, cross over the grain and becomes pinned in the other position of diameter d, (since the pinning fields of all the intermediate positions are smaller than the applied field). So the representative point jumps from 4 to 5, the magnetization at 5 being again due to the joint effect of the displacement and the bulging.

(c) Initial Magnetization Curve

If the field is increased from zero, an initial magnetization curve is described each point being, as it is well known the tip of a hysteresis loop.

When the wall is just a little displaced from its diametral position (Fig.1.6(f)), a small increase of the field produces a small wall surface variation but a very large

variation of the volume swept, which results in a very fast increase of the magnetization.

On the contrary, when the wall is displaced far away from its diametral position, a large increase of the field is needed to produce an appreciable decrease of the wall surface; however that gives only a small increase of the volume swept, thus a small increase of the magnetization.

1.6 THE INITIAL PERMEABILITY

The initial permeability, μ_i defined as

$$\mu_i = \frac{1}{\mu_o} \lim_{H \to 0} \frac{dB}{dH} \qquad (1.16)$$

comes into play due to a reversible process. In the reversible part of the B-H loop the magnetization can be due to both rotation of the spins and reversible movement of domain wall. Various workers have shown that the rotation of magnetization contributes only a small part of the actual initial permeability.

Kersten[46] and Neel[38] later derived μ_i due to the reversible domain wall displacement giving a fair agreement between the calculated and the observed value of μ_i for iron. Kersten postulated that a domain wall tends to be trapped by inclusions or voids because the wall can save its area at such inclusions or voids, thus reducing the total wall energy, the displacement of the area, causing a restoring force on the wall. Neel suggested to take into account of the free poles formation. Kersten[39] later modified the assumption by assuming the flexibility of domain walls and derived

$$\mu_i \sim \frac{M_s}{\sqrt{K_1}} \qquad (1.17)$$

This could also explain the observed temperature dependence of μ_i for iron, nickel and cobalt (Kersten[39]).

Perhaps the best model to explain the dependence of μ_i

on the motion of domain wall in a polycrystalline material is given by Globus.[47] In such a model, the equation of motion of the wall can be written as

$$m \frac{\partial^2 z}{\partial t^2} + \beta \frac{\partial z}{\partial t} - \gamma \nabla^2 z + 2 M_s H \exp(i\omega t) \qquad (1.18)$$

where

z = displacement of the wall

m = effective mass of the wall

β = damping constant

and γ = wall energy.

This gives the static initial permeability (i.e. when $\omega \ll \omega_r$) as

$$\mu_i' - 1 = \frac{M_s^2 D}{\gamma}$$

and

$$\mu_i'' = \frac{M_s^2 \beta \omega D^3}{\gamma^2} \qquad (1.19)$$

where

D = grain diameter.

Experimentally also the μ_i has been found to increase linearly with the grain size for a number of ferrites and garnets with pore free grains. Globus further claims that experimental results in Ni-ferrite and YIG show

$$\mu_i - 1 \propto \frac{M_s^2 D}{K_1}$$

which implies if Eqn.1.19 is true

$$\gamma \propto K_1$$

which is contradictory to Landau and Lifschitz equation, $\gamma = 2\sqrt{AK_1}$, where A is the exchange constant, since A is not proportional to K_1. Globus also calculated γ from hysteresis loss measurement[48,49] and found the values obtained

to be in excellent agreement with the Landau and Lifschitz equation. The role of γ occuring in Eqn.1.19 given by $\gamma \sim M_s^2 D/(\mu_i - 1)$ is yet to be fully understood.

In a very recent paper, Hoekstra and others[50] have made an attempt to interpret the initial permeability of polycrystalline Mn-Zn ferrites in terms of intrinsic magnetic properties. They measured M_s and K_1 on the single crystals and compared the temperature dependence of μ_i measured on polycrystalline toroids of the same composition with the theoretically calculated values according to (i) $\mu_i \sim \frac{M_s}{\sqrt{K_1}}$ and (ii) $\mu_i \sim \frac{M_s^2}{K_1}$. Though they could obtain similar temperature dependence of μ_i in both the cases, the absolute value of μ_i measured was found to be an order of magnitude smaller than the theoretically calculated value given by (i) and an order of magnitude greater than the value given by (ii). They have discussed their results saying that a description of the bulging process should include the demagnetizing energy that pins the wall at the grain boundaries.

As has been said earlier, the magnetostriction accompanies the magnetization and therefore the domain walls will not be free to expand on formation in the solid materials giving rise to internal stresses in the system. Movement of domain wall under such stresses contribute μ_i according to[51]

$$\mu_i \sim \frac{M_s^2}{\lambda_s^2 E} \qquad (1.20)$$

where

$\lambda_s E$ = internal stresses

E = Young's modulus of elasticity.

The above formulation suggest that the initial permeability would increase with decrease in λ_s.

Globus, however, in Ni-ferrites and YIG has shown that the reversible processes (i.e. μ_i) are determined by K_1 and the irreversible processes (i.e. B-H loop) are determined by $K (= K_1 + \lambda_s \sigma_n)$. He postulates that stresses are present inside the domains where magnetization is high and inside the wall the magnetization is vanishingly low, the domain wall does not 'see' these stresses when it bulges.

It has been conclusively proved by Globus that intergranular porosity does not affect μ_i whereas intragranular pores can pin the domain walls decreasing the effective span and affect μ_i. In such a case, μ_i has been found to be proportional to pore to pore distance D_p.[52]

It is obvious from the above discussions and has been shown experimentally also that in order to have high μ_i, the material must have high M_s, low λ_s and K_1, large pore free grains and good chemical homogeneity.[53]

1.6.1. Temperature Dependence of Initial Permeability

Both the quantities M_s and K_1 vary with temperature so that μ_i can be a complicated function of temperature and as a rule should increase with temperature showing a maximum just below the Curie point (Hopkinson effect). Using the actual temperature dependence of M_s and K_1, Kersten[54] explained the observed temperature dependence of μ_i for iron, cobalt and nickel.

In ferrites, μ_i-temperature curve is sometimes found to be passing through a secondary peak at a lower temperature for certain compositions as shown by Guillaud.[53] Enz[55] and Ohta[56] demonstrated that the variation of anisotropy has predominant effect on the temperature variation of μ_i. Enz

inferred, that the low temperature peak of μ_i corresponded to the change of sign of K_1 i.e. to its passage through zero.

In Mn-Zn-Fe^{2+} ferrites, Fe^{2+} ions on B-sites give a positive anisotropy contribution which has a smaller temperature dependence than the negative anisotropy contribution of the Fe^{3+} ions (Fig.1.7). By increasing the Fe^{2+} ions the compensation temperature T_o can be shifted to a lower value. In μ_i-T curve this leads to a secondary maximum at T_o.

To obtain useful materials small chemical inhomogeneities are introduced, especially with respect to the distribution of the ferrous ions.[57,58] The material then consists in effect of a mixture of ferrites with different contents of ferrous ions, and therefore different temperature T_o. The resulting μ_i-T curve of the material is shown in Fig.1.8 as the solid curve, which is a weighted average of the dashed curves for the different compositions. By this technique a temperature insensitive permeability is obtained in a relatively large temperature range T_2 to T_1.

Globus and Duplex[59] have reported that ferrimagnetic materials which are identified in their fundamental properties (composition, M_s, T_c, λ_s) as well as in their granular structure (porosity, size and shape of grains) can present very different μ_i-T curves. The proposed interpretation is based on the existence of different degrees of wall continuity across the grain boundaries. It is suggested that the degree of wall continuity is associated with the relative crystallographic axes orientation of the grains. According to them comparatively flatter μ_i-T curves are obtained in materials where the wall continuity is affected.

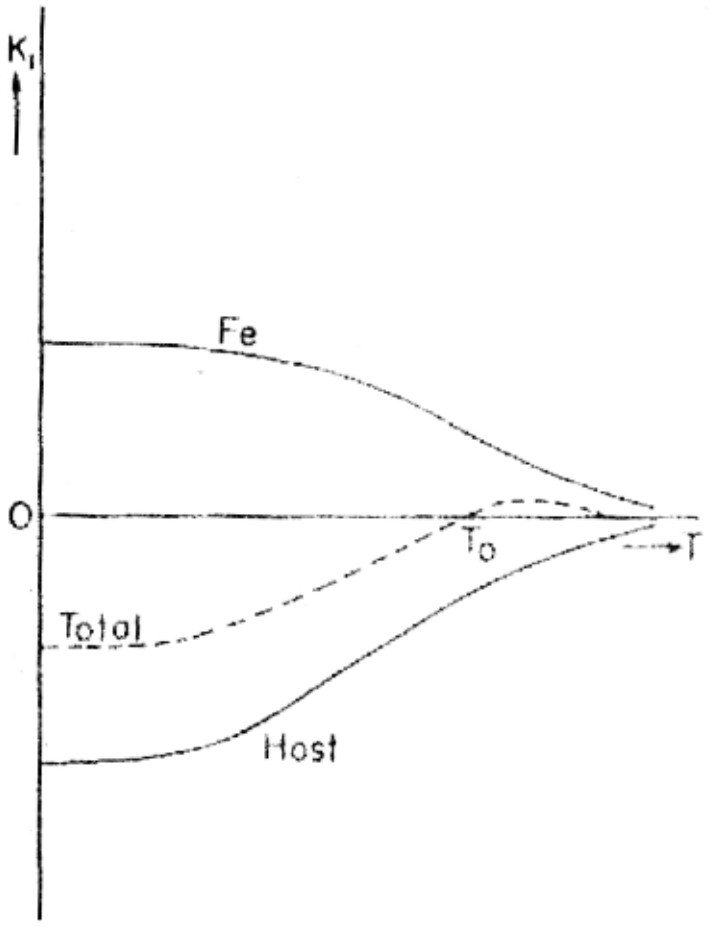

Fig. 1-7 Anisotropy constant K_1 as a function of temperature in case of a positive contribution compensating the negative one at temperature T_o.

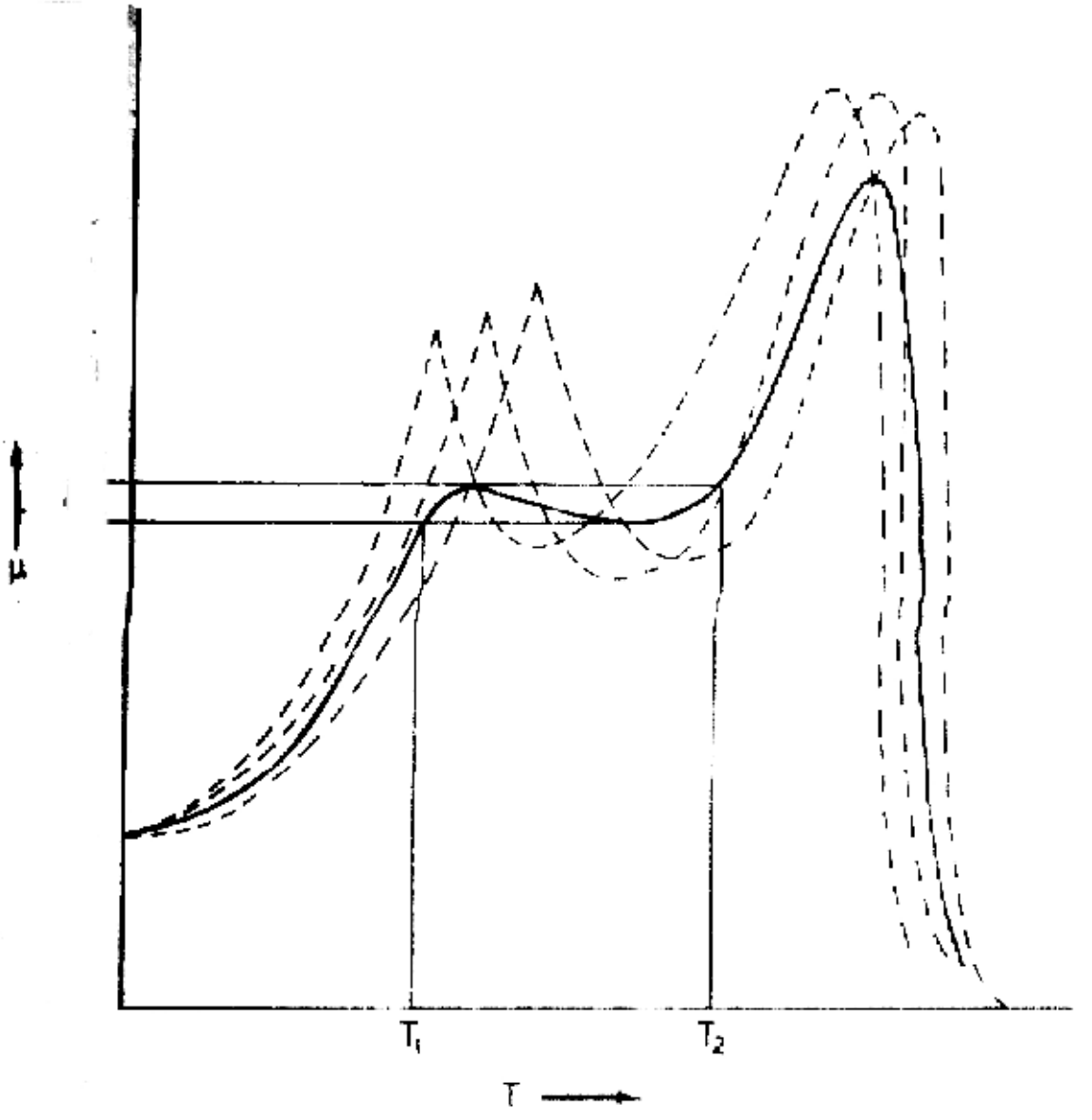

Fig. 1·8 Permeability as a function of temperature for an inhomogeneous MnZn Fe^{II} ferrite.

It is important to study the variation of μ_i with temperature since this gives how the inductance of a coil would vary with temperature. One of the ways of defining the temperature factor (T.F) of μ_i is

$$T.F = \frac{\mu_1 - \mu_2}{\mu_1^2 (T_1 - T_2)} \times 10^6 \qquad (1.21)$$

where μ_1 and μ_2 are μ_is at temperatures T_1 and T_2 respectively.

1.6.2. Time Decrease of Initial Permeability : Disaccommodation

If a magnetic material is given a disturbance, which may be magnetic, thermal or mechanical, the permeability observed immediately after the cessation of the disturbance is normally found to be raised to an unstable value from which it returns, as a function of time, to its undisturbed or stable value. This phenomena has been called time-change of permeability but is usually referred to as disaccommodation. The process is repeatable indefinitely.

There are a number of possible mechanisms of disaccommodation in ferrites and they all depend on migratory processes within the lattice. These processes often involve the anisotropic or preferred distribution of ferrous ions and/or cation vacancies over the four octahedral sublattices of the spinel structure. The preference for a particular sublattice depends on the direction of the domain magnetization and, therefore, on the position of the domain walls. The distribution tends to fix, and be fixed by, the location of the domain walls, giving rise to a more stable or lower permeability state. After the disturbance the vacancies and domain walls are no longer in a mutually low energy state (therefore the initial

permeability is higher) but the lower energy state is progressively approached as the ferrous ions and/or cation vacancies migrate to the new preferred sites conditioned by the new domain wall positions. In other words the disturbed domain wall, having taken up a new position, sinks slowly into an energy trough at that position, loosing mobility and reducing domain wall contribution to the permeability as it does so. The rate at which the vacancies are redistributed or diffuse depends very much on the temperature, shorter time constants being observed at the higher temperature.

Permeability changes with time are expected to be logarithmic

$$\mu_i(t) \propto \log t/\tau \qquad (1.22)$$

where τ is the relaxation time and is given by[60]

$$\tau = \frac{1}{9.6 \times f_0 \times n} \exp(-Q/kT) \qquad (1.23)$$

where

f_0 = frequency factor = Lattice vibrational frequency

n = cation vacancy concentration

and Q = activation energy of cation/vacancy diffusion[61]

In Mn-Zn ferrites $Q \simeq 0.7$ eV. Reviews of the whole field of disaccommodation have been given by Braginski[62] and Krupicka and Zaveta.[63]

One of the ways of defining the disaccommodation factor showing the time dependence of μ_i is

$$D.F = \frac{\mu_1 - \mu_2}{\mu_1^2 \log t_2/t_1} \qquad (1.24)$$

where μ_1 and μ_2 are the μ_i's at time t_1 and t_2 respectively after demagnetization.

1.6.3. Frequency Dependence of Initial Permeability

The real part of μ_i is essentially frequency independent till one reaches the resonance. Figure 1.9(a) shows the real and imaginary parts of the initial permeability spectrum for a high permeability Mn-Zn ferrite. The frequency of resonance, f_{rd} is given by[64]

$$f_{rd} \propto \frac{1}{D^2} \quad \text{for } D > D_c$$
$$\propto \frac{1}{D} \quad \text{for } D < D_c \qquad (1.25)$$

where D_c is the critical diameter.

Under the action of a weak field the wall pinned to the grain boundary bulges and the form of this bulging would be determined with respect to the need of keeping the cooperativity of the domain walls through the whole torcidal sample, in order to avoid the appearance of demagnetizing fields.

It has been observed that the homogenous granular structured materials show relaxation and inhomogeneous granular structured (big and small grains) materials show resonance (Fig.1.9(b,c)). According to Globus[65] the resonance in inhomogeneous materials is obtained due to the disturbance of the cooperativity of the domain walls in a chain of grains.

The intergranular porosity does not disturb the relaxation character because the domain wall may choose the best way from one grain to another, by keeping off the pores, in order to maintain its continuity through the material. The inclusions and pores inside the grain also may present relaxation character. It is logical to think that the defects in the grains, if they follow a regular distribution, may not break the cooperative action of the domain wall as far as the fre-

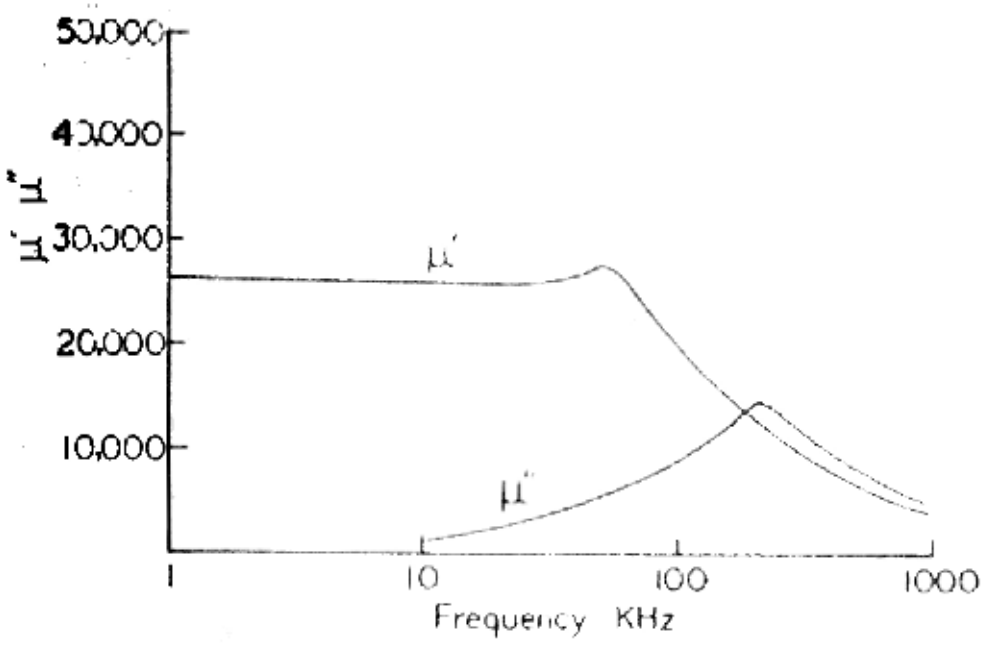

(a)

Dispersion of the complex initial permeability for a high permeability Mn Zn ferrite (After Roess, 1970)

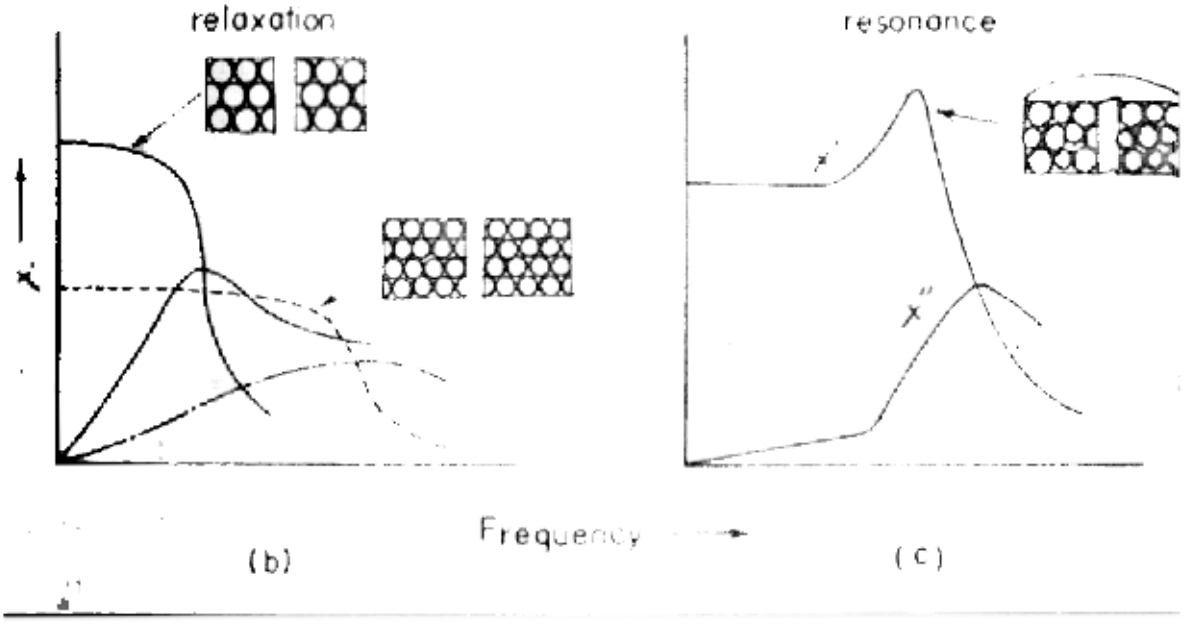

Fig 1.9 Relation between the frequency spectrum \ character and the h9omogeneity of the granular structure : b) homogeneous structure - relaxation character, c) inhomogeneous structure-resonance character

quency response is concerned.[65]

1.6.4. Field Dependence of Initial Permeability

For use as an air inductor, it is ideal if for the ferrite, B is proportional to H. But, due to the hysteresis present in all magnetic materials,

$$B(H) = \mu_0 H - a_1 H^3 + a_2 H^5 + \ldots\ldots \quad (1.26)$$

This makes the initial permeability dependent on the applied field which introduces third harmonic distortion, D into the signal. It can be shown that[66]

$$D = \frac{V_3}{V_1} = 0.6 \tan \delta_h \quad (1.27)$$

where $\tan \delta_h$ = hysteresis loss tangent.

It can be understood using simple Globus model that to minimise third harmonies, the ferrite should have pore free grains of uniform size and good homogeneity.

1.7. D.C. RESISTIVITY

The electrical conduction in ferrites is mainly due to hopping of electrons between ions with multiple valencies. The main contribution is due to electron hopping between Fe^{3+} and Fe^{2+} ions. Therefore the low resistance of Mn-Zn ferrite is mainly associated with the relatively large concentration of ferrous ions without which the lowest crystal anisotropies can not be obtained

Ferrites are semiconductors, with thermally activated nature of the conductivity mechanism, corresponding to a relation of the type

$$\rho = \rho_0 \exp (E_a/kT) \quad (1.28)$$

where $\rho_0 = \rho$ (resistivity at $T \to \infty$, and E_a represents an activation energy which, according to Verwey and De Boer[67] is

which is subjected to an alternating field of amplitude H and frequency f is

$$P_h = W_h \cdot f \qquad \text{ergs sec}^{-1} \qquad (1.31)$$

(ii) Eddy Current Losses

Ferrites are semiconductors and commercial grades have resistivities ranging from 10 Ωcm to >10^8 Ωcm at room temperatures. Mn-Zn ferrites are low resistivity ferrites.

An alternating magnetic flux in a conductive medium will induce eddy currents in that medium and these will result in an energy loss called eddy current loss. The magnitude of this loss depends, among other things, on the conductivity, size and shape of the medium and, as it is well known, may be reduced by subdivision of the medium into electrically insulated regions, e.g. laminations or grains.

At low frequencies, the eddy current power loss (volume) density is given by

$$P_e \sim \frac{(\pi \hat{B} f d)^2}{\rho \beta} 10^{-16} \qquad \text{watts cm}^{-3} \qquad (1.32)$$

where $\hat{B}$ is the peak value of the flux density, d is the average grain size, ρ is then the bulk resistivity and β is a dimensional constant ~ 20 for spherical grains.

(iii) Residual Losses

Residual loss is defined as the loss which remains after the subtraction of hysteresis and eddy current losses from the total losses.[69] There are probably several loss processes that contribute to residual loss and different processes may apply at different parts of the frequency spectrum. Generally speaking, the wall relaxations contribute to these losses. These wall relaxations usually have loss maxima at frequencies

above 1 MHz. However, a tail of these losses may extend to lower frequencies. As this tail may also vary to some extent with frequency, it may be difficult to distinguish between eddy-current losses and residual losses.

(iv) Power Loss in the Winding

A conductor placed in an alternating magnetic field will have e.m.f. induced in it and these will give rise to eddy currents and associated power losses.[70] The magnetic fields may be due to currents flowing in other conductors or due to current flowing in the conductor in question. The losses may be represented as an increase in resistance of the current carrying conductors above the value measured with direct current; this increase of resistance becomes larger as the frequency increases.

1.9. MICROSTRUCTURE

In a number of applications the use of ferrite single crystals is either necessary or desired. However, it is very difficult to prepare sufficiently large, homogenous single crystals, especially when the chemical composition, needed to obtain a desired electrical or magnetic property, is a sharply defined one. Moreover, the shaping of single crystals is difficult.

The ceramic process makes it possible to prepare complex chemical compositions and shapes much more economically. In addition there are a number of cases where the use of a polycrystalline material is required e.g. for obtaining high coercive force,[71] for reducing eddy current losses, which can be suppressed by internal laminations along the grain boundaries.[85,86] Thus, for most applications polycrystalline

materials, prepared by a ceramic method, are used.

In a ceramic process the starting material is a powder which is made into a dense solid by first compacting it into the desired shape and then sintering this compact at a high temperature to remove porosity. The final microstructure develops during the sintering process. During sintering densification and grain growth all occur at the same time and give rise to a great variety of microstructures.

1.9.1. Sintering and Grain Growth

Sintering in crystalline solids has been dealt with in detail by Coble and Burke.[72] Sintering essentially occurs in three stages. These three stages of sintering may be explained by diffusion models in which the main assumptions made are that the pores are vacancy sources, the grain boundaries are vacancy sinks, and the controlling mechanism of material transport is bulk diffusion.

(i) Initial Stage

Initially, the 'neck-growth' takes place between the adjacent particles while the grain growth is totally inhibited. Atomic diffusion can be quantitatively accounted for the initial rate of neck growth.[73]

(ii) Intermediate Stage

When the density is at approximately 60% of its theoretical value, grain growth sets in.[74] The structure still has a completely continuous pore phase coincident with three grain edges throughout the matrix. The grains in an ideal case then have the term of a regular tetrakaidecatredron (a 14-sided polyhedron having six square faces and eight hexagonal faces). The lattice vacancies from the pores can be transported to the

grain boundaries where they get annihilated. As a result the pores fill up and the density increases with the logarithm of time in general. The densification of the powder compacts in this stage has been quantitatively modelled by Coble[75] based on atom transport by diffusion.

The densification rate decreases somewhat due to an increase in the grain size. At about 95% of theoretical density the pore phase becomes discontinuous, terminating the intermediate stage.

(iii) Final Stage

If discontinuous grain growth occurs, a large number of closed pores, trapped inside the grains and isolated from the grain boundaries cannot shrink any more. Then sintering is practically stopped. If discontinuous grain growth can be avoided, the last few percent of porosity are eliminated by discharging vacancies at grain boundaries. The compact then sinters to a high density, and in some cases theoretical X-ray density has been achieved.

A schematic representation of typical structures observed during sintering is given in Fig.1.10. All the geometric aspects of grain growth may be deduced from three general principles.[76]

(1) Grain boundaries which are essentially the areas of mismatch (discontinuities) in the microstructure, represent locations with higher energies. Therefore, a 'driving force' exists which tends to reduce the grain boundary areas. As a result, they form a three-dimensional array that is geometrically similar to a soap froth.

(2) All the grain boundaries have about the same surface

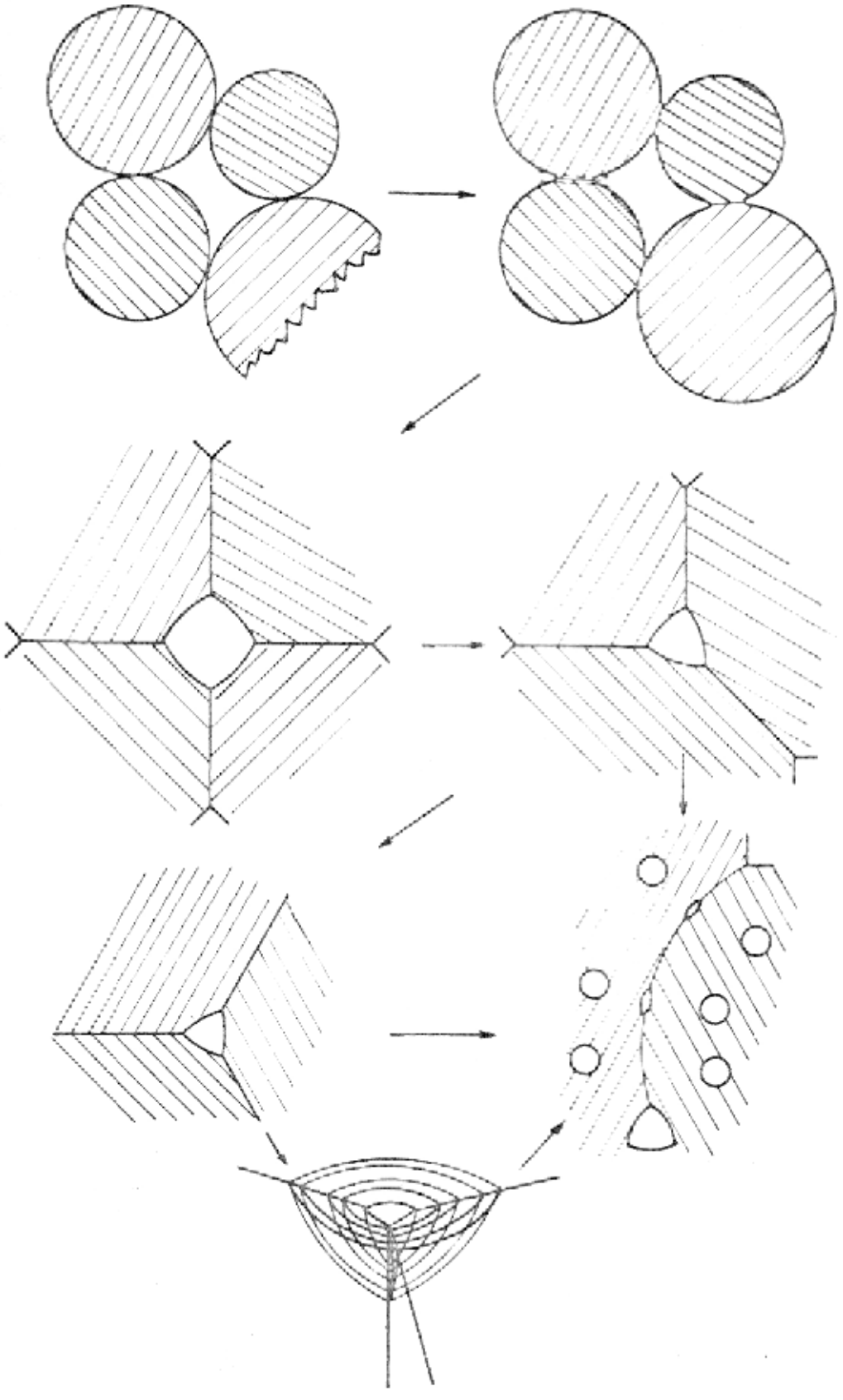

Fig. 1-10 Schematic representation of typical structures observed during sintering. All views are two-dimensional except bottom center, which is a perspective view of a closed pore at a corner where four grains meet. After Coble and Bruke.

tension; they radiate at angles of 120° from a point at which three of them meet. Topology requires that the boundaries extend from one three-boundary contact to another, and this requirement generally introduces a curvature into the grain boundary. The surface tension then causes the boundaries to migrate toward their centers of curvature. Six sided grains have flat sides; all other grains have curved sides - convex if number of sides is less than six and concave if number of sides is more than six. Thus the grains with more than six sides grow at the cost of those with less than six sides (Fig.1.11). As the grain diameter increases, the curvature of the grain boundary decreases. Therefore the velocity of grain boundary decreases.

(3) Second phase inclusions on the grain boundaries will impede grain boundary movement. Pores in the initial stage of the sintering process may also act as a second phase inclusion.

From these principles it follows, with a few simplifying assumptions, that the grain boundary velocity, v, is given by

$$v \propto \frac{dD}{dt} = A.M.\sigma.\frac{1}{D} \qquad (1.33)$$

where

D = average grain diameter

A = geometrical constant

σ = interfacial energy of the grain boundary

M = mobility of the grain boundary.

On integrating, one gets,

$$D^2 - D_0^2 = A M \sigma t \qquad (1.34)$$

or

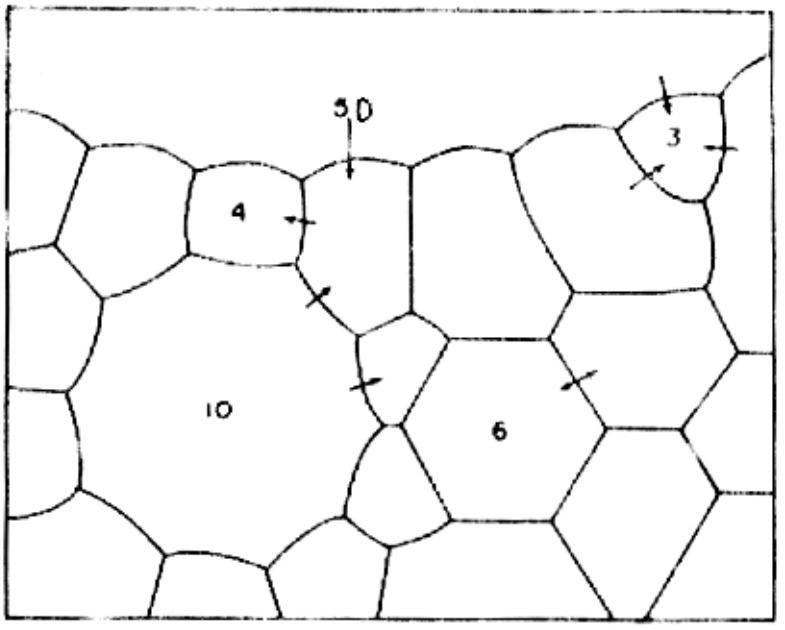

Fig. 1-11

Topology of grains. A grain with six sides can have straight sides; fewer than six-sided grains curve outward and more than six-sided grains curve inward. The more sides a grain has, the more strongly curved are its boundaries. The arrows indicate that the boundaries migrate towards their centre of curvature.

$$D^2 - D_0^2 = Kt \qquad (1.35)$$

where AMO⁻ = K is a temperature dependent rate constant, D_0 is grain size at time t = 0. Increasing the temperature causes the rate K to increase according to the Arrhenius relationship

$$K = K_0 \exp(-Q/RT) \qquad (1.36)$$

where Q is the activation energy for grain growth.

In general, however, the commonly observed grain growth data is roughly described by Beck's empirical relationship[77]

$$D - D_0 = Kt^n \qquad (1.37)$$

Equation 1.35 predicts that the exponent $n = \frac{1}{2}$. In fact a value of $n < \frac{1}{2}$ is usually found. This discrepancy in 'n' is attributed to a rather incorrect assumption that the shape of the grain size distribution curve does not change with time.

1.9.2. Pores and Inclusions

If the grain growth be unimpeded, the grains will keep on growing according to Eqn.1.37 until the sample becomes a single crystal. But this is rarely observed as in the presence of pores or inclusions or both, a limiting grain size will reach according to Eqn.1.38 as given by Zener.[78]

$$D_{crit} = \beta \cdot \frac{d_i}{f} \qquad (1.38)$$

where D_{crit} is the limiting grain size, when a uniform dispersion of pores or inclusions of diameter d_i and volume fraction f prevents grain growth, β is some constant.

When a grain boundary intersects an inclusion or a pore, a portion of the boundary equal to the cross-sectional area of the inclusion or pore is eliminated (Fig.1.12(a)). As a result, there is a binding force of the inclusion or pore to the grain

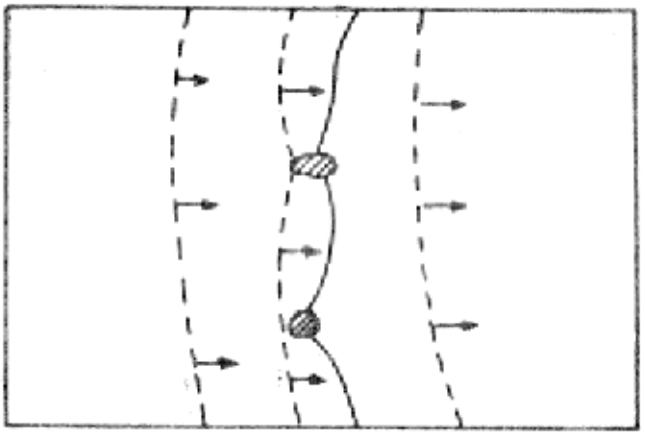

(a) Growth inhibition Pores or second phase inclusions generally retard boundary movements because they introduce reversals in boundary curvature.

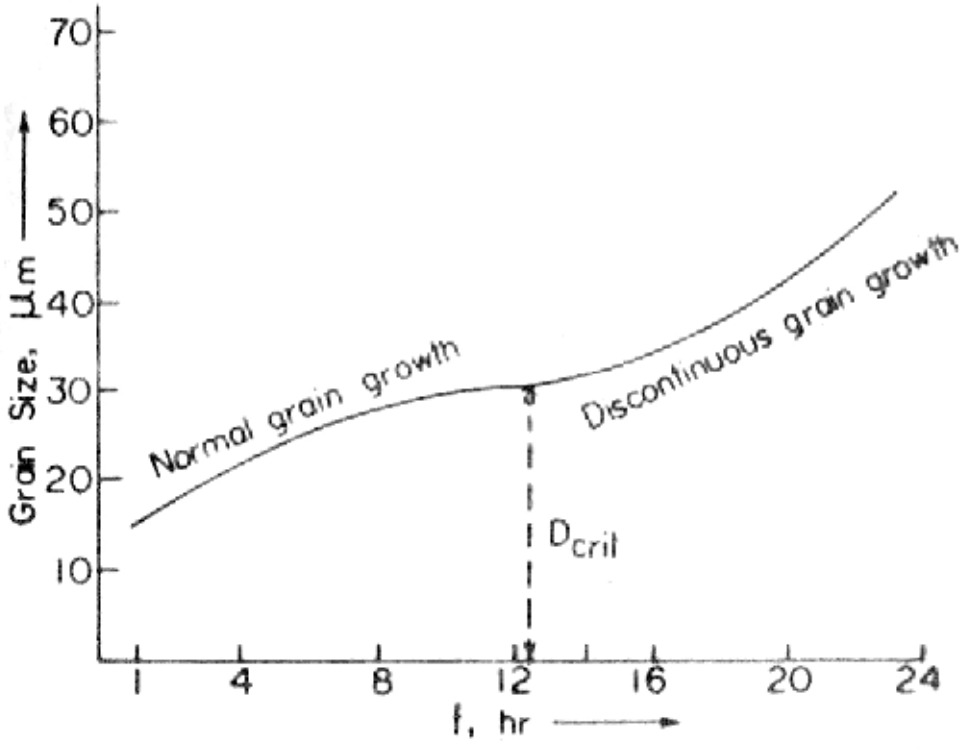

(b) An illustration of the limiting grain size in a Mn-Zn ferrite sintered at 1340°C (Ref. 79)

Fig. 1·12

(a) The grain boundaries being disordered, have higher resistivity than the bulk of the grain therefore the increase in the concentration of such barriers like grain boundaries makes the system more resistant to electrical breakdown.[85]

(b) The formation of a high resistive layer of some compound at the grain boundaries by the addition of certain impurities or by the oxidation of the grain boundaries also results in the increase in the resistivity and decrease in the high frequency eddy current losses.[86]

(ii) Initial Permeability, Coercive Force and Hysteresis Losses

The importance of grain size and porosity can be interpreted in terms of the existence of domain walls and the effect of interaction with grain boundaries and pores on the case of wall migration.

The pores or non magnetic inclusions make no contribution to the magnetization and in addition, when an alternating magnetic field is applied, it causes cone or spike shaped demagnetizing fields.[87] For the same total porosity, a large number of small pores produces a larger area with demagnetizing fields than does a small number of big pores. For intergranular pores, the adverse effects are much smaller. Globus and others,[42,88] have studied the effects of microstructural features on various properties in details. They have concluded that the Globus model can be extended to the case where the domain walls are pinned at intragranular pores and D (grain size originally) can be interpreted as the average distance between the intragranular pores, D_p, i.e. the span of the

domain wall.

This explains why the increase in intragranular porosity causes the permeability to fall even if the average grain size increases.

The effect of intragranular porosity on H_c has also been considered by Goodenough,[89] Kersten[90] and Dijkstra and Wert.[91] Kersten considered only surface tension effects of pores, derived the coercive force, H_c as

$$H_c \sim \frac{K_1}{M_s} S\, p^{2/3} \qquad (1.39)$$

where p is the intragranular porosity and S a factor depending on the ratio of domain wall width, δ, to a pore diameter, d. The value of S is maximum when $d \simeq \delta$. Dijkstra and Wert[91] considered spike formation at the pores and have arrived at similar conclusions although the functional dependence of H_c on p and d according to them is different, as given below

H_c =

where γ_{180^o} is the wall energy of 180° domain wall of width δ_{180^o} and L is the length of the spike.

Jain and others[88] have experimentally found H_c proportional to $D_p^{-0.5}$ in Mn-Zn ferrites, where D_p is the average pore to pore distance. According to them the μ_i is given by a small displacement from the pinned position whereas for H_c, the domain wall has to bow out considerably before breaking away from the pores.

Since H_c is very much a function of porosity, therefore so is the area of the hysteresis loop i.e. the hysteresis losses. Therefore high hysteresis losses are encountered in

ferrites having inclusions or discontinuous grain structure.

1.10. EFFECT OF IMPURITIES ON THE PROPERTIES OF Mn-Zn FERRITES - A BRIEF REVIEW

Snoek[92] found that Mn-Zn ferrites could be useful in practice because of their high initial permeability and low loss compared to other ferrite systems over a frequency range of several hundred KHz. Since then a great deal of work both of fundamental as well as of technological nature has been done to improve the magnetic properties of Mn-Zn ferrites. Guillaud,[53] Shichijo,[93] Ohta,[56] Roess,[94] Perduijn and Broschek[95] to mention a few have extensively studied the whole field of Mn-Zn ferrites. They found, in general, that the composition as well as the manufacturing conditions have tremendous role in determining the magnetic properties. They also concluded that the extremely high purity of the raw materials used was very essential for producing high permeability ferrites. Guillaud[53] found that in most cases, impurities proved to be poisonous for obtaining good magnetic properties.

Later, the effects of various impurities on the performance of Mn-Zn ferrites were studied by several workers[96-106] and some beneficial effects were brought into focus. Akashi[97,98] had shown that the resistivity and the magnetic quality factor could be increased by using the correct combination of CaO and SiO_2 additions. Hirota[99] arrived at similar results for CaO and GeO_2 additions. CaO and SiO_2 also proved to be useful for lowering the disaccommodation.[100] Substitutions of titanium or tin in Mn-Zn ferrites resulted in better performance from stability point of view i.e. time variation of permeability.[101-104] Tsubara and others[105] showed that the addition of higher

valence elements such as Sn influence the disaccommodation spectrum of Mn-Zn ferrites in such a way as if the Fe_2O_3 content were increased, while lower valence elements such as Li act as if the MnO content increases. Stijutjes and others[106] showed that the solubility of small ions to Mn-Zn ferrites is limited on the side of small ionic radii and this property could be utilized in obtaining increased resistivity and reduced magnetic losses.

Effects of additives on the microstructures were also studied by a number of authors.[107-109] Attempts were made to locate the distribution of impurities in the microstructure.[106] Silica was found to have strong effect on the microstructure promoting coarse crystallization[110] because of its ability to form a grain boundary phase said to be liquid at firing temperatures.[111-112]

However, in spite of the rich literature available in this field, a systematic study correlating the microstructures with important electrical and magnetic properties for various levels of doping a particular additive was found missing. Also most of the work done has been confined in the direction of developing ferrites for low field applications. Little has been done on the effects of impurities on the high field performance of Mn-Zn ferrites. Recently Giles and Westendorp[109] have studied the microstructure and power losses of a Mn-Zn ferrite as a function of silica additions. The results obtained by them were found to be very interesting and from the authoress's point of view the work needed further investigation.

To fill this gap in literature, the effect of doping a

Mn-Zn ferrite separately with three impurities - SiO_2, GeO_2 and SnO_2 on the microstructure and various magnetic properties has been studied.

REFERENCES

1. E.W. Gorter, Philips Res. Repts. 9, 295-320, 321-365 403-443 (1954).
2. G. Blasse, Philips Res. Repts. Suppl. 3, 1 (1964).
3. E.J.W. Verwey et al. J. Chem. Phys. 16, 1091 (1948).
4. F. de Boer et al., J. Chem. Phys., 18, 1032 (1950).
5. J. Smit, Solid State Com. 6, 745 (1968).
6. S. Roberts and A. Von Hippel, J. Appl. Phys. 17, 610-616 (1946).
7. S.D. Dunitz and L.E. Orgel, J. Phys. Chem. Solids, 3, 318-323 (1957).
8. E.J.W. Verwey and E.L. Heilmann, Jr. Chem. Phys. 15, 174-180 (1947).
9. F. de Boer et al, Jr. Chem. Phys. 18, 1032-1034 (1950).
10. Ch. Guillaud and H. Creveaux, Compt. R. Acad. Sci. Paris, 230, 1256 (1950).
11. Ch. Guillaud and H. Creveaux, Compt. R. Acad. Sci. Paris, 230, 1458 (1950).
12. Ch. Guillaud, J. Phys. Rad., 12, 239 (1951).
13. Ch. Guillaud and M. Sage, Compt. R. Acad. Sci. Paris, 232, 944 (1951).
14. E.W. Gorter, Proc. IRE, 43, 1945 (1955).
15. A. Broese van Groenou et al. Mater. Sci. Eng., 3 (1968-69), 317-392.
16. J. Smit and H.P.S. Wijn, Ferrites, Philips Tech. Library (1959).
17. H. Forestier, Annales Chimie Xe Serie tome IX, 316 (1928).

18. J.H. Van Vleck, Phys. Rev., 52, 1178 (1937).

19. J. Kanamori, in Magnetism, I, p.127, Ed. G.T. Rado and H. Suhl, Academic Press, New York (1963).

20. V.J. Folen, J. Appl. Phys., 32, 166 S (1960).

21. V.J. Folen and G.T. Rado, J. Appl. Phys., 29, 438 S (1958).

22. K. Yoshida and M. Tachiki, Prog. Theor. Phys. (Kyoto), 17, 331 (1957).

23. A. Broese Van Groenou et al, J. Appl. Phys., 38, 1133 (1967).

24. R.F. Pearson, Proc. Phys. Soc. (London), 74, 505 (1959).

25. R.F. Pearson, J. Appl. Phys., 31, 137 S (1960).

26. J. Smit et al, J. Phys. Soc. Japan, 17 (Suppl. B-1) 268 (1962).

27. J.S. van Weiringen, Lanolt - Bornstein Tables, p.2942 (1962).

28. W.P. Wolf, Phys. Rev., 108, 1152 (1957).

29. J.H. Van Vleck and C. Kittel, Phys. Rev., 118, 1231 (1960).

30. Y. Syono, Japan J. Geophys., 4(1), 71 (1965).

31. J.B. Geodenough, Phys. Rev. 95, 917 (1954).

32. A. Globus, C.R. Acad. Sci. 255 (1962) 1709.

33. A. Globus, Thesis, Paris (1963).

34. P. Weiss, J. Phys., 6, 661 (1907).

35. F. Bloch, Zeitz. F. Physik 74, 295-335 (1932).

36. C. Kittel, Reviews of Modern Physics, Vol.21, pp.541-583, Oct. 1949.

37. S. Chikazumi,'Physics of Magnetism', John Wiley & Sons, Inc.

38. L. Neel, Cashiers Phys., 25, 19 (1944).

39. M. Kernsten, Z. Agnew Phy., 7, 397 (1947).

40. L.J. Dijkstra and C. Wert, Phys. Rev., 79, 979 (1950).

41. A. Globus, Proc. S.M.M. 2, Cardiff (1975), to be published

42. A. Globus, Supplement au J. de Physique 1977, Int. Conf. of Ferrites ICF 2.

43. A. Globus and P. Duplex, C.R. Acad. Sci. Paris, 262-, 238-, 1188 (1966).

44. A. Globus and P. Duplex, IEEE Trans. Magn., Mag-2, 441 (1966).

45. A. Globus and P. Duplex, J. Appl. Phys., 39, 727 (1968).

46. M. Kersten, Phys. Z., 44, 63 (1943).

47. A. Globus, "Magnetization Mechanism and Specific Polycrystalline Properties in Soft Magnetic Materials", Invited talk, Soft Magnetic Materials, 2, Cardiff Conf., 1975.

48. M. Guyot, These, Universite de Paris-SUD, Orsay 1975.

49. M. Guyot and A. Globus, Phys. Stat. Sol.(b), 447 (1973).

50. B. Hoekstra et al, Intermag-78, May, 1978.

51. R. Backer, Zeit. F. Phys., 33, 905 (1932).

52. G.C. Jain et al., J. Mater. Sci, 11, 1335 (1976).

53. Ch. Guillaud, Proc. IEEE, 104 Suppl. B, 165 (1957).

54. M. Kersten, Zeit. F. Phys., 8, 313-322, (1956).

55. U. Enz, Physica 24, 609 (1958).

56. K. Ohta, J. Phys. Soc. Japan 18, 684 (1963).

57. H.P. Peloschek and A.J. de Rosy, Proc. Intern. Powder Metallurgy Magnetic Core Conf., New York, June 14-17, 1965, p.61-71.

58. H.P. Peloschek and D.J. Perduyn, IEEE Trans. Magnetics, 4, 453-455 (1968).

59. A. Globus and P. Duplex, Phys. Stat. Sol. 31, 765 (1969).

60. S. Iida, J. Phys. Soc., Japan, 17, 123 (1962).

61. J.L. Snoek, New Developments in Ferromagnetic Materials, Elsvier Publications, New York (1947), 54.

62. A. Braginski, Phys. Stat. Sol. 11, 603-616 (1965).

63. S.Krupicka and K. Zaveta, J. Apl. Phys. 39, 930-938 (1968).

64. B.K. Das and P. Chaudhary, J. Mater. Sci, 13, 84 (1978).

65. A. Globus, C.R. Hebd. Séon. Acad. Sci 255 (1962), 1193.

66. E.C. Snelling, Soft Ferrites : Properties and Applications, London ILIFFE Books Ltd. 1969, Chap.II.

67. E.J.W. Verwey and J.H. de Boer, Rec. trav. chim. Pays Bas, 55, 531-590

68. G.H. Jonker, J. Phys. and Chem. of Solids

69. Jan Smit, Magnetic Properties of Materials, McGraw Hill Book Company, 1971, p.95.

70. V.G. Welsby, The Theory and Design of Inductance Coils, Macdonald and Co. Ltd., London, 2nd Edition, (1960).

71. C. Kooy and U. Eng., Philips Res. Repts., 15 (1960),7.

72. R.L. Coble and J.E. Burke, Sintering in Crystalline Solids, Fourth Intern. Symp. Reactivity Solids, Amsterdam, 1960, pp.38-51, Elsevier. Amsterdam, 1961.

73. G.C. Kuczyanski, J. Appl. 21, 632 (1950).

74. R.L. Coble, J. Appl. Phys., 32, 787 (1961).

75. R.L. Coble, J. Appl. Phys., 32, 793 (1961).

76. J.E. Burke, Grain Growth in Ceramics, in "Kinetics of High-temperature Processes", W.D. Kinger (ed), pp.109-120, Wiley, New York, 1959.

77. P.A. Beck et al.. Trans. AIME. 175. 372 (1948).

78. C. Zener, Personal Communication to C.S. Smith, reported in Trans. AIME, 175, 15, (1948).

79. G.C. Jain et al, Indian J. Pure & Appl. Phys.14, 87(1976).

80. H.C. Graham et al, J. Am. Ceram. Soc. 54, 548 (1971).

81. G.H.Jonker and Stuijts, Philips Tech. Rev. 32, 79 (1971).

82. Broese van Groeneu et al., Mater. Sci. Eng. 3, 317 (1968-69).

83. B. Jofle et al., "Piezoelectric Ceramics", Academic Press, New York.

84. K.J. Stanley, "Oxide Magnetic Materials", Oxford Univ. Press, London and New York,

85. N. Hirose and H. Sasaki, J. Am. Ceram. Soc. 54, 320 (1971).

86. H. Kono,Ferrites: Proc. Int. Conf. July, 1970, Japan, p.137.

87. E. Roess, Z.F. Angew Phys., 31, 124 (1970).

88. G.C. Jain et al, J. Mater. Sci., 11, 1335 (1976).

89. J.B. Goodenough, Phys. Rev. 95, 917 (1954).

90. M. Kersten, Phys. Z. 44, 63, (1943).

91. L.J. Dijkstra and C.A. Wert, Phys. Rev. 79 (1950), 979.

92. J.L. Snoek, New Developments in Ferromagnetic Materials, Elsevier Publications, Inc., New York (1947).

93. Y. Shichijo, Trans. Jap. Inst. Metals, 2 (4), 204 (1961).

94. E. Roess, Proc. Int. Conf. Ferrites : Japan, 1970, p.203, (1971).

95. D.J. Perduijn and H.P. Peloschek, Proc. Brit. Ceram. Soc., 10, 263 (1968).

96. Ch. Guillaud and M. Paulus, Proc. Int. Conf. Magnetism and Crystallography, Kyoto, 1961, J. Phys. Soc. Japan 17, Suppl. B-I, 632 (1961).

97. T. Akashi, Trans. Japan Inst. Metals, 2, 171 (1961).

98. T. Akashi, N.E.C. Rsearch & Developm. 8, 89 (1966).

99. E. Hirota, Japan. J. Appl. Phys. 5, 1125 (1966).

100. T. Hiraga, Proc. Int. Conf. Ferrites : Japan 1970, p.203.

101. J.E. Knowles and P. Raukin, Colloque C1, Supplement au n° 2-3, Tome 32, Fe'vrier-Mars 1971, page C1-845, Journal de Physique.

102. J.E. Knowles, Philips Res. Repts, 29, 1974, p.93.

103. A.D. Giles and F.F. Westendorp, Colloque C1, Supple'ment au n° 4, Tome 38, Avril 1977, Page C1-47, Journal de Physique.

104. A.D. Giles and F.F. Westendorp, J. Phys. D: Appl. Phys., Vol.9, 1976, p.2117.

105. T. Matsubara et al, Proc. Int. Conf. Ferrites: July 1970, Japan, p.214.

106. T.G.W. Stijntjes et al, Proc. Int. Conf. Ferrites : July 1970, Japan, p.194.

107. T. Iimura, Journal of the Japan Society of Powder and Powder Metallurgy, 16 (1969), p.217.

108. G. Rossi and J.E. Burke, J. Am. Ceram. 56,(12), p.654,1973.

109 A.D. Giles and F.F. Westendorp, Colloque C1 Supple'ment au n° 4, Tome 38, Avril 1977, p. C1-317, ICF-2, Journal de Physique.

110. Y. Bando et al, Proc. 1970 Int. Perm. Magnet. Conf. NY4, p.339 (1971).

111. C. Kooy, Sci. Ceram, 1, 21 (1961).

112. F.M.A. Carpay et al., Sci. Ceram. 8, p.23, 1975.

CHAPTER - II

NATURE AND DISTRIBUTION OF SiO_2, GeO_2 AND SnO_2 IN THE Mn-Zn FERRITE

2.1. INTRODUCTION

The effect of impurities on the magnetic properties of ferrites depends upon whether the impurities go in solid solution with the ferrite or stay insoluble. If the impurity has a solid solubility, the impurity ions could occupy either interstitial or substitutional sites in the ferrite lattice. This would result in lattice expansion or contraction depending upon the size and type of the impurity ion. Lattice parameter measurement, therefore is a convenient method to find whether the impurity is soluble or not.

The insoluble impurity, on the other hand, would not affect the lattice parameter and would stay as a second phase (solid or liquid like). The distribution of this impurity phase in the microstructure is very important in determining the ultimate properties of ferrites[1] as would be discussed in the forthcoming chapters.

The scanning electron microscope (SEM) with an X-ray microanalyser (XMA) is an instrument that allows analysis of microvolumes of a solid, in situ.[2] The region of analysis could be pin-pointed with an optical microscope and analysis of neighbouring microvolumes combined could show the distribution of a chemical element within the solid. The XMA is fundamentally an instrument for analysing regions of a solid down to 1 µm across.

Auger electron spectroscopy (AES) or scanning Auger microprobe (SAM) is a convenient and sensitive method for

chemical analysis of a surface layer of a few nm thickness.[3]

These tools have been used to study the nature and distribution of these impurities SiO_2, GeO_2 and SnO_2 in the Mn-Zn ferrite.

2.2. EXPERIMENTAL METHODS

2.2.1. Processing of the Mn-Zn Ferrites

Mn-Zn ferrites $(MnO)_{28.2}\ (ZnO)_{18.8}\ (Fe_2O_3)_{53.0}\ (MeO_2)_x$, where Me stands for Si, Ge and Sn, were prepared using the usual ceramic techniques. The flow diagram of the various steps involved in the ferrite processing is shown in Fig.2.2.1. The basic composition (i.e. when x = 0) can be written as $Mn_{.564}\ Zn_{.375}\ Fe_{2.06}\ O_4$. This particular composition is found to be suitable as a core material with Curie temperature around $160^{o}C$.[4]

(i) Wet-mixing of the Raw Materials

The constituent raw materials of desired grade and purity (Table 2.2.1) were weighed to give the proportions required for the selected compositions. Batches of 500 gms were made for each additive level and weighing was carried out to an accuracy of 10 mg. Tables 2.2.2 - 2.2.4 give the details of the batches prepared.

In compositions where small amounts of impurities were doped, following procedure was adopted to obtain homogeneous mixing of the additive with the other main oxides

(a) First a binary of the required additive oxide with Fe_2O_3 was prepared by wet mixing (1% for SiO_2, 5% for GeO_2 and SnO_2).

(b) Appropriate amount of this binary was added in the chosen composition taking proper account of its Fe_2O_3 content.

A TYPICAL FLOW-DIAGRAM SHOWING VARIOUS PROCESSES INVOLVED IN THE PROCESSING OF FERRITES FOR THE PRESENT STUDY.

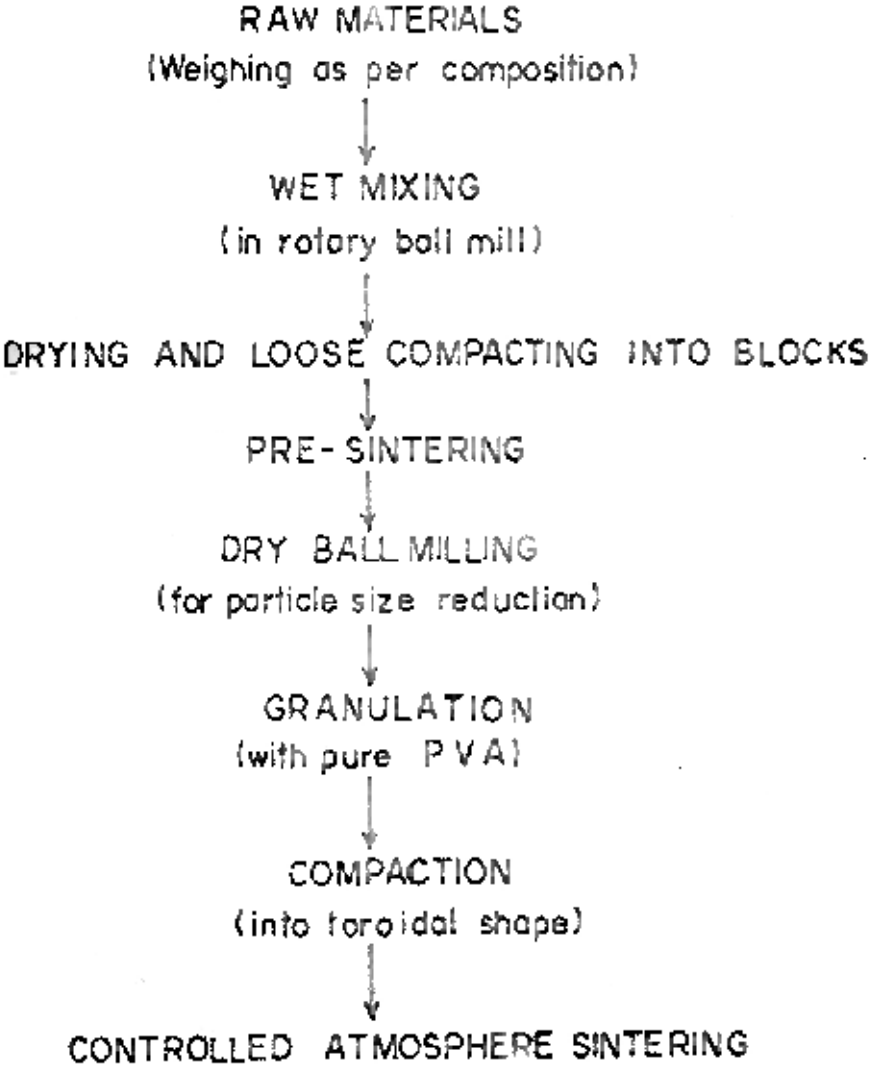

Fig. 2·2·1

Table 2·2·1

RAW MATERIALS

Constituent	Make	Purity	Major impurities
Iron Oxide (Fe_2O_3)	Bayer's (German)	99·7 %	·01 wt % SiO_2, 50 ppm other metallic impurities
Manganese Oxide	S. Merck	MnO content ≈89·2 %	·005 wt.% SiO_2, 50ppm other metallic impurities
Zinc Oxide (ZnO)	S. Merck	≥ 100 %	Metallic impurities in traces.
Silicon dioxide (SiO_2)	Prepared in the Laboratory.	99·99 %	Less than 100ppm metallic impurities.
Germanium dioxide (GeO_2)	Specpure JMC 515 (U.K.)	99·999 %	5ppm metallic impurities.
Stannic Oxide (SnO_2)	Specpure JMC 540 (U.K)	99·999 %	20 ppm metallic impurities.

The raw materials containing known amount of the additive impurity were then wet ball milled for final mixing in stainless steel jar (15cm x 15cm) with cylindrical stainless steel balls (1cm x 1cm) and using demineralised water as medium. (Ordinary tap water should not be used as it could contribute varying amounts of CaO and SiO_2, up to 0.05 and 0.01 percent by weight, respectively). A powder to balls to demineralised water ratio of 1:3:2 (by weight) and mixing to 65,000 revolutions (speed : 3000 rev/hour) gave sufficient mixing of the raw materials.

(ii) Pre-sintering

After wet mixing, the product was dried and then loosely compacted into discs of 4 cm diameter at a pressure of 1.6×10^6 Kg/m^2 using a hydraulic press. The pre-sintering was done at a temperature of $900^{\circ}C$ for one hour in air in a batch furnace. The heating and cooling rates during the pre-firing were kept at $100^{\circ}C$/hour.

(iii) Particle Size Reduction : Dry Ball Milling

The pre-sintered ferrite was dry ball milled for 80,000 revolutions (Speed : 3000 rev/hour) with the help of the same stainless steel jars and balls with powder to balls ratio of 1:2 by weight.

The average particle size distribution of the powder obtained was measured on a 'JOYCE LOEBL' particle size analyser. The particles were also viewed in a transmission electron microscope (TEM : Philips EM 200). Figure 2.2.2. shows the particle size distribution of the dry ball milled powder. In this distribution the peak of the distribution was obtained at 0.6 μm.

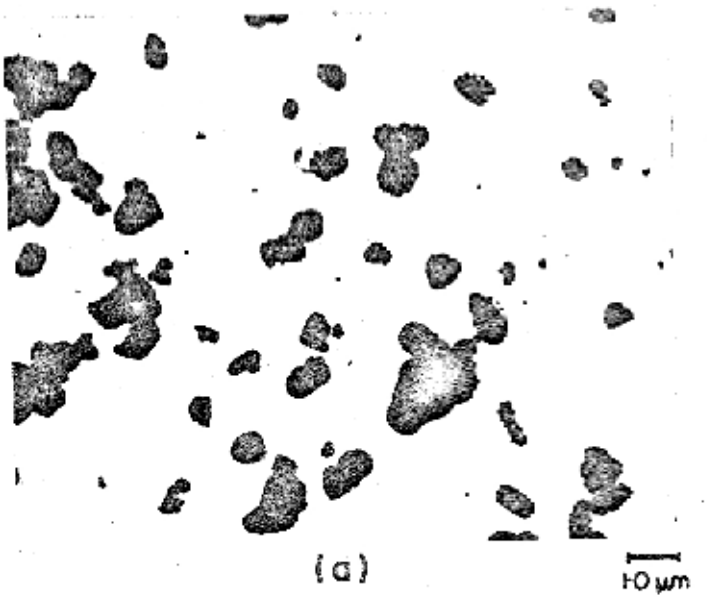

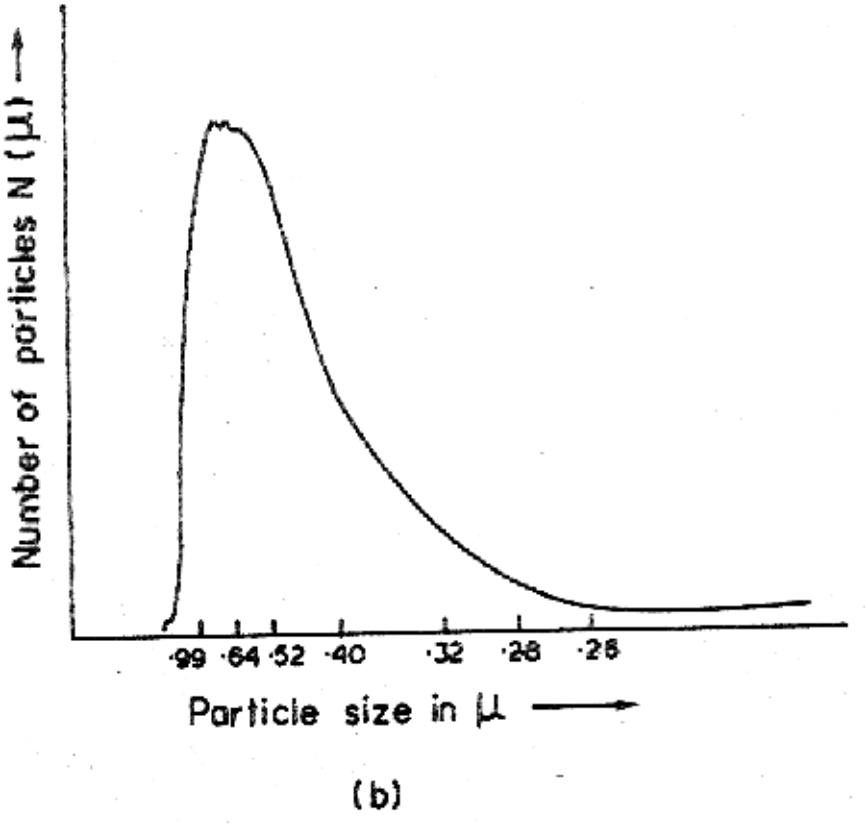

(b)

Fig. 2·2·2 Particle size distribution of dry ball-milled powder

Up to this step, an iron pick up from the jars and balls was estimated to be 0.25 mol% and this was adjusted for while loading the initial composition.

(iv) Pressing into Toroidal Shapes

To ensure a good flow of the powder and a reproducible filling of the die, the powder was granulated into larger agglomerates using 13% polyvinyl alcohol solution.[5] The granules were then pressed into toroidal shapes (OD = 16mm, ID = 10mm, thickness = 2mm) at a pressure of 12.0×10^6 Kg/m^2.

(v) Sintering

Sintering was carried out using a gas tight muffle furnace heated with silicon carbide heating rods capable of going up to 1400°C. The sinterings were carried out at various temperatures and times in either pure nitrogen or in oxygen. Ultra high purity nitrogen (containing $\leq$ 5 ppm O_2 by volume) and commercial grade oxygen were used for this purpose. Cooling was always done in pure nitrogen to avoid the oxidation of excess ferrous ions to ferric ions. A flow rate of 500 ml/min in general was maintained with the help of flow meters. The heating and cooling rates of the furnace were maintained at 100°C/hour with the help of a temperature controller-cum-programmer capable of controlling the temperature to an accuracy of $\pm$ 5°C.

2.2.2. Scanning Electron Microscopy (SEM) and X-ray Microprobe Analysis (XMA)

Scanning electron microscopy and X-ray microprobe analysers have proved to be very useful techniques to study metal and ceramic surfaces.[2,6,7] The basic principle is the same for the SEM and for the X-ray microanalyser.[7] In both instruments, the specimen is irradiated by a finely focused electron

beam. This releases secondary electrons, backscattered electrons, Auger electrons, characteristic X-rays, and several other types of radiation from a small part of the specimen (Fig.2.2.3).

Generally, in the surface SEM, secondary electrons are collected to form the image. In the microanalyser characteristic X-rays are collected. This can be related to the specimen composition. The basic features of an SEM/XMA are

(i) Beam Diameter

Normally in the SEM, a current of typically 10^{-11} amp is focused into a spot of diameter 100 Å on the specimen. The smallest beam diameter that has been achieved with a surface SEM is 25 Å. In the microanalyser a much higher beam current (up to 10^{-6} amp) is employed to generate detectable X-ray signals at the expense of a significant loss in spatial resolution of approximately 0.1 to 1 μm.

(ii) Magnification

This is controlled by varying the size of the area that is scanned on the specimen. Magnifications can be varied over a wide range, typically from 15 to 100,000 times or more. Low magnification micrographs are useful for identifying areas, but they cannot be photographically enlarged to any extent because of the limited number of resolvable lines on the cathode-ray tube.

(iii) Low and High-resolution Surface SEM

A low resolution image (such as the X-ray image, the luminescent image, or the induced-signal image) is one in which the resolution is limited to first order by the electron penetration into the solid specimen. A high-resolution

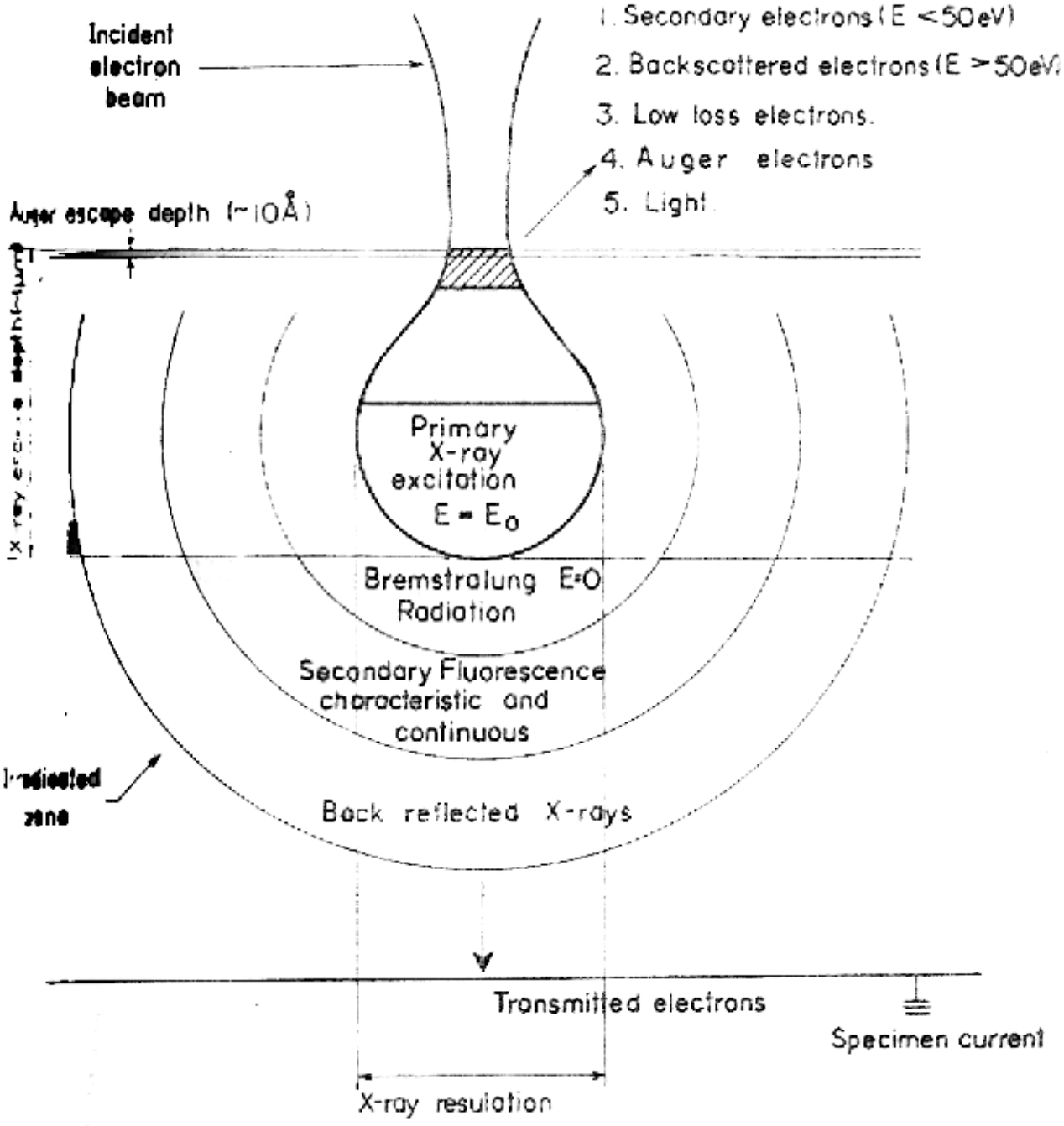

Fig. 2.2.3 Electron - specimen interactions.

method is one in which the signal is obtained at the point at which the primary electron enters the specimen. The secondary electron image and the low loss image are both high resolution according to this definition.

(iv) Types of Image

Images in the SEM and the micro-analyser are obtained by "looking at" the specimen along the incident beam and with the apparent illumination coming from the signal detector. Thus, if the collector is changed, then the field of view will stay the same, although in general the appearance of the image will be quite different. Variety of images would be obtained in the SEM depending upon the signal chosen to display the image e.g.

(a) Secondary Electron Image

This is the most generally useful type of image for studying surface topography. It can also be made sensitive to crystal orientations, voltages, and magnetic fields. The detector in this case is sensitive to electrons that emerge from the specimen with less than 50 eV energy.

(b) Backscattered Electron Image

This is obtained by collecting electrons that leave the specimen with more than 50 eV energy. The appearance of the backscattered electron image will depend on the angle of incidence and on the position and the energy sensitivity of the backscattered electron detector. This image is greatly influenced by the topography and the atomic number of the site being viewed.[8]

(c) Specimen Current Image

In some cases, a useful image can be obtained by coll-

ecting the current which flows between the specimen and ground. This requires a larger beam current than is usual in the SEM, and so this type of image is only useful if a larger beam current must be used for some other reason - such as, for example, in the microanalyser where the higher current might be needed to give an acceptable X-ray count rate.

(d) X-ray Image

This is obtained by collecting the characteristic X-rays and is used to display the distribution of chemical elements in the microanalyser. The X-ray detection is carried out with the help of crystal spectrometer using any of the two systems - wavelength dispersive system or energy dispersive system. In a wavelength dispersive system, an X-ray spectrometer analyses the X-rays according to wavelength and they are detected by a proportional or scintillation counter, which records the arrival of individual X-ray quanta (photons). By traversing the specimen with the electron beam the analysis can be extended to show the distribution of its constituents. The distribution of any element along a chosen line in the surface is given graphically called the line scan. The instrument can also provide a pictorial representation of the distribution of any element within an area, with regions of high and low concentration indicated by light and shade on a photograph.

In an energy dispersive system, the electron beam is focussed on a predetermined point and the intensities of characteristic X-rays emitted are analysed. For this purpose the spectrometer is moter driven through the complete range of angles and the output is applied to a pen recorder, to give a spectrum with peaks indicating the constituents. To a fixed

approximation the X-ray intensity is proportional to the concentration of the element, but deviations from linearity occur owing to the influence of the other constituents on both the penetration of electrons and the absorption of X-rays.

A Cambridge Stereoscan S4-10 SEM equipped with wavelength dispersive X-ray microanalyser was used for the work reported. Some X-ray microprobe analysis were done on the CAMECA, M.S.46 (French make) electron microprobe analyser.

Polished pieces of sintered toroids were mounted on the specimen stage with the help of air-drying silver paint. The specimen were not given a conducting coating in view of their semiconducting nature. Normally an accelerating voltage of 30 kV was used in order to have better collection efficiency of X-rays.

2.2.3. Auger Electron Spectroscopy (AES)

In terms of the physical processes involved, the Auger electron spectroscopy technique is similar to the electron microprobe technique. Both are based on electron beam excitation of the specimen and by focusing the beam, both can achieve good spatial resolution. The difference between them is that in the X-ray microprobe emitted X-rays are detected and in AES emitted electrons are detected.[9] In both cases, the energy of the detected particle is characteristic of the parent atom and identifies the atomic species present. The surface-specific nature of the Auger spectroscopy technique results from the very short (approximately 10 Å) escape depth of the Auger electrons. The relatively longer escape depth of the X-rays detected in the XMA results in an analysis depth of approximately 1 µm for this technique.

The difference in escapte depth (mean free path) between the X-rays and Auger electrons also influences the lateral spatial resolution that can be achieved by the two techniques. The long mean free path of X-rays in a material limits the lateral spatial resolution of XMA to approximately 1 /um even though the electron beam used for excitation can be made considerably smaller. The very short escape depth of the Auger electrons, on the other hand, means that the area analysed in AES is essentially the size of the cross section of the electron beam (Fig.2.2.3). Therefore, the AES technique should be capable of considerably higher lateral spatial resolution than the XMA.

Surface elemental composition is determined from Auger spectra, Auger line scans and Auger images. An Auger line scan is a display of the amplitude of a selected Auger signal as the electron beam scans a single line across the analysis region; an Auger image is a micrograph obtained using a selected Auger signal to intensity-modulate a cathode ray display as the electron beam is scaned over the specimen. The Auger spectrum reveals all elements present at the point of analysis.[10]

The depth distribution of the various elements of interest can be determined using the thin film analysis capability of the instrument. This operating mode provides an automatic readout of the changes in Auger signal amplitudes as the surface is sputter-etched, providing a plot of composition versus depth.

Specimen cut from the ferrite samples were attached to a fracture apparatus, ultrasonically cleaned and mounted in

the ultra-high vacuum part of the AES. The fine-grained samples fracture mainly along the grain boundaries. It is therefore indeed possible by this method, to analyse the composition of the grain boundaries.[11,12]

The samples were analysed for AES at Physical Electronics Industries, Inc., USA on request. An electron gun with spot size of 2000 Å (0.2 μm) was used. The Auger spectra were obtained by using a primary electron energy of 10 KeV with a beam current of 1-2 μA.

2.2.4. Lattice Parameter Measurements

A sintered toroid of each batch was ground under clean conditions using a pestle and a mortar. The ground powder after sieving through 325 mesh sieve was mounted in the Debye-Scherrer X-ray camera (114.6mm dia) and its X-ray diffraction pattern was taken using an iron source and an exposure time of about 20 hours. Lattice parameter was calculated using the standard extrapolation method.[13]

2.3. EXPERIMENTAL RESULTS

2.3.1. Distribution of Si in the Microstructure

(a) Detection of Si

At low silica levels, the etch pits or the particles revealed by etching and any grain boundary phases present were too small (1 $(\mu m)^3$) to identify by microprobe analysis. At the two highest silica concentrations, a distinct grey-coloured second phase along the grain boundaries could be seen even at ordinary magnifications in an optical microscope (ref. Fig. 3.3.1 in chapter III). This second phase was then analysed under an X-ray microprobe. Figure 2.3.1. shows X-ray micro analysis displays for Si and other constituents for the specimen

with a silica concentration of 1.28 mol% (or 0.64 wt%). It is clearly indicated from this figure that the phase seen along the grain boundaries is a Si-rich phase and Si is mainly distributed along the grain boundaries.

Attempts were made to take X-ray line scans for Si across a grain and a grain boundary in order to see Si-rich inclusions. Figure 2.3.2 shows two sets of X-ray line scans for Si and other constituent elements across a grain, inclusion and a grain boundary. Si-peaks are observed at the inclusions and at the grain boundaries. Fe-line scans show dips, where Si-peaks are observed.

(b) Topography of Si-rich Phase

For this purpose various modes of operation of an SEM i.e. the secondary electron (SE) emission mode, the back-scattered electron (BSE) mode and the absorbed specimen current (ASC) mode were used. Figure 2.3.3 gives the micrographs of a lump of the second phase present at a three grain boundary intersection taken at different modes and at different accelerating voltages. The important features observed are[14]

(i) The SE images show that it is a typical case of charging phenomenon at this second phase, which therefore appears to be a non-conducting phase. The bright regions are the highly charged regions and shadows around may be due to inability of the primary beam reaching there. This is because of the strong negative charge in the neighbour hood. The charging effects are reduced to a great extent at 30 KV as the penetration depth is more here to reach the ferrite present just below this phase. This also indicates the topography of this phase which is thick in the middle and shallow at the corners.

100 μ × 100 μ

(a)

(b) Si

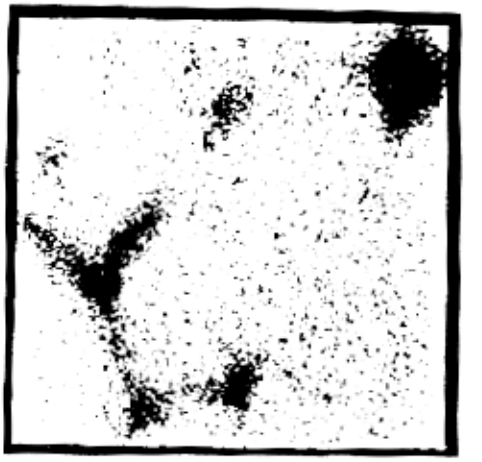

(c) Fe

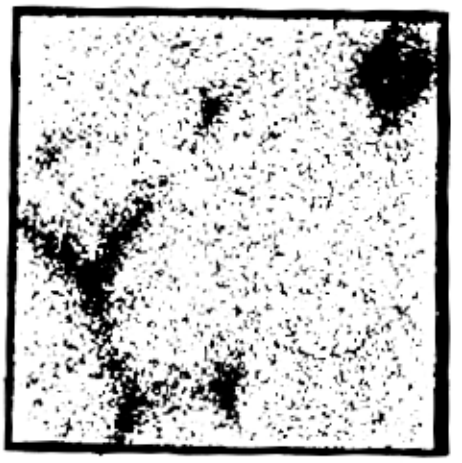

(d) Mn

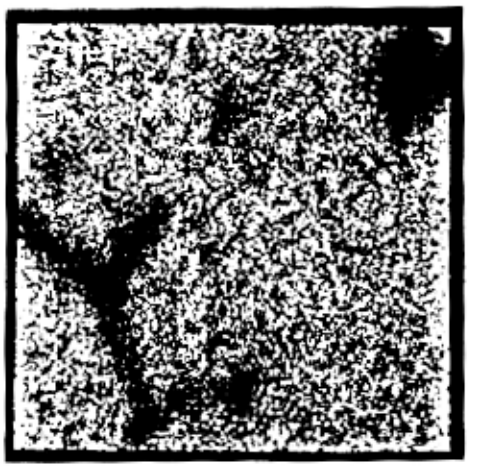

(e) Zn

Fig. (a): Specimen current picture of selected area of the Mn–Zn Ferrite containing 0·64 wt.% silica. (b)–(e): X-ray micro-analysis displays of constituent elements of area shown in (a).

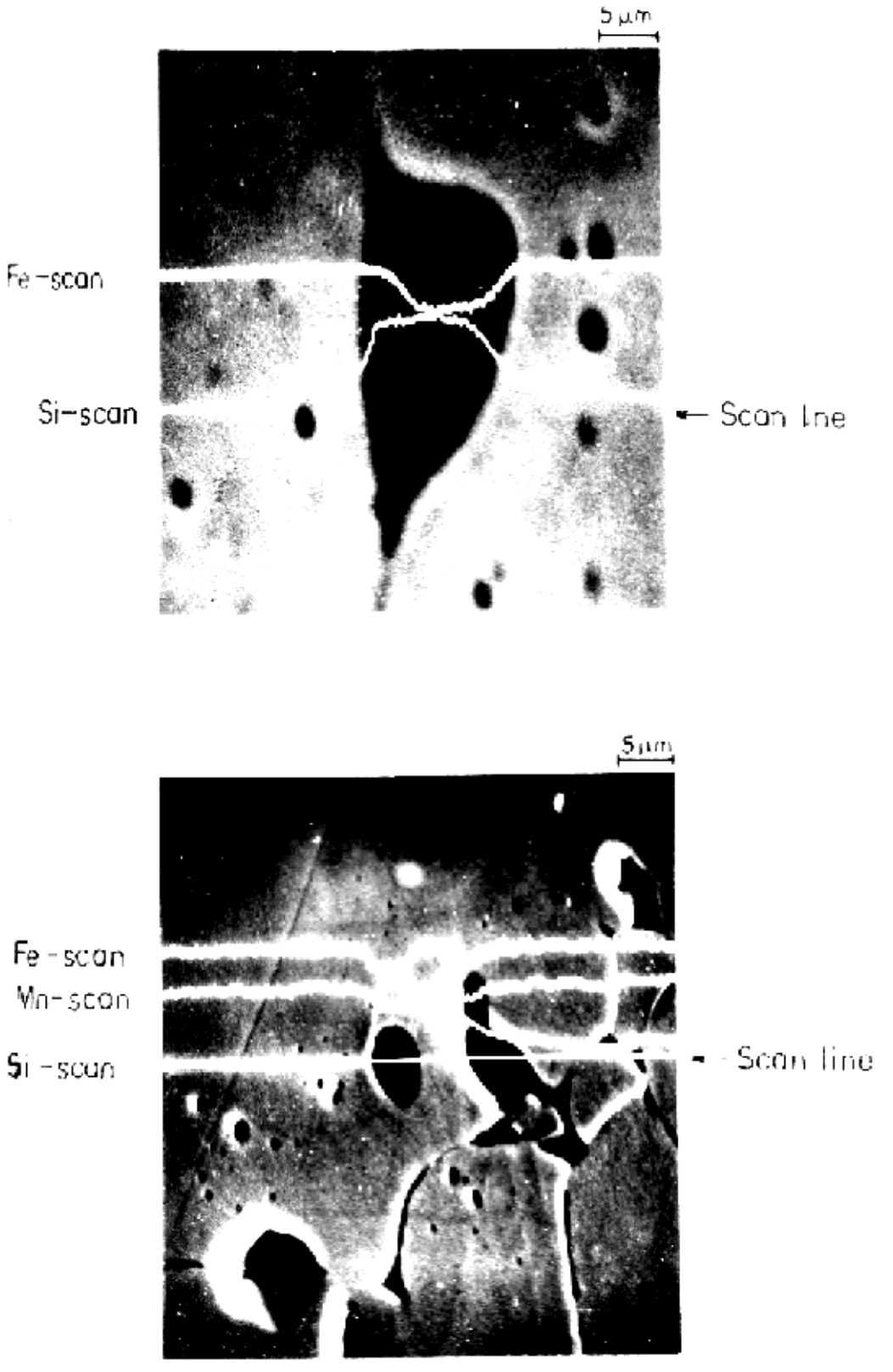

Fig. 2·3·2 XMA line scans across a grain and a grain boundary in a Mn-Zn ferrite doped with 1·28 mol % SiO_2.

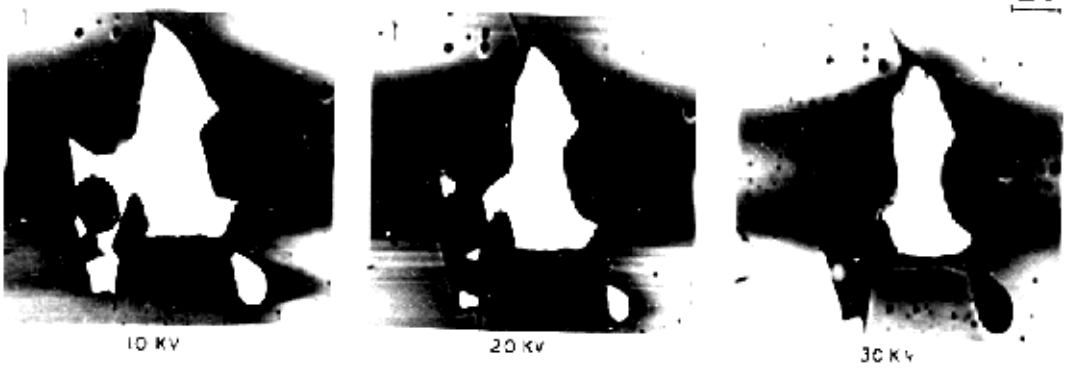

10 KV 20 KV 30 KV

SECONDARY ELECTRON EMISSION IMAGE

10 KV 20 KV 30 KV

BACK SCATTERED ELECTRON IMAGE

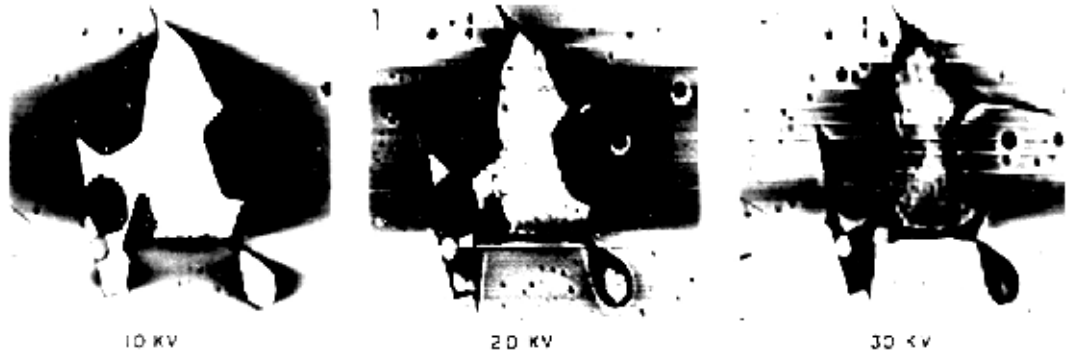

10 KV 20 KV 30 KV

ABSORBED SPECIMEN CURRENT IMAGE (Inverted)

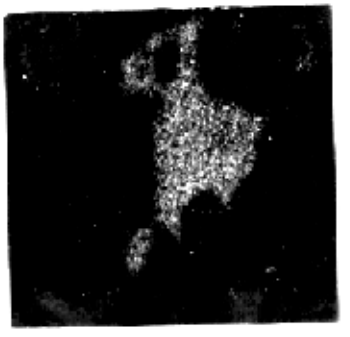

30 KV

X-RAY IMAGE (Si K_α)

(ii) The BSE images show a contrast reversal as one goes from 10 KV to 30 KV. This is understandable as the BSE image essentially gives topographic contrast superimposed with elemental contrast; and on top of this are the possible charging effects. The bright area at 10 KV is bright on account of its topography and charging. At 30 KV, where the charging is minimum, the contrast is in agreement with the composition as Si has lower backscattering coefficient being lighter (Z = 14) than the background elements.[15]

(iii) The ASC images give an information about the absorption power of the phase which is much less as compared to that of the matrix, however, this effect directly corresponds to the charging effects.

(iv) The SEM on its XMA mode shows this phase to be rich in silicon

In the sample with 1.28 mol% SiO_2 (or 0.64 wt% SiO_2), the area fraction (=volume fraction) of the silica-rich second phase was measured using 'IMANCO Quantimet 720' and was computed to be 2.94%.

2.3.2. Distribution of Ge in the Microstructure

(a) Detection of Ge

Up to a GeO_2 addition of 3.82 mol%, no second phase was observed in the microstructure with the help of an optical microscope.

X-ray microanalysis (XMA) were carried out on the sample containing 3.82 mol% GeO_2. The results did not show any preferred segregation of Ge. Since the XMA resolution is limited to about a micron, this sample was analysed under an Auger microprobe.

Figure 2.3.4 shows - (a) a specimen current picture of a freshly fractured sample of the Mn-Zn ferrite containing 3.82 mol% GeO_2; and (b) an Auger image for Ge of the same area. It is evident from these pictures that there exists Ge-enrichment at the grain boundaries. For a semi quantitative information, points were chosen on the grain boundaries and also inside the grains on the fractured surface. Auger spectra were taken on each of the points. Figure 2.3.5 shows differential Auger spectra ($\frac{d\,N(E)}{dE}$) obtained at point nos.1,2 and 4 on the grain boundaries and point nos.3 and 5 in the grains. Differentiating the spectrum removes the effects of the constantly varying background encountered in AES. It is therefore very useful for speedy element identification and simplifies the detection of trace constituents.

Each spectrum is showing a set of peaks, corresponding to each of the constituents. First peak on the left corresponds to carbon contaimination which might have been caused while polishing the specimen. The Ge peak is obtained at an electron energy of 1149 eV.

From these spectra, the ratios of the peak to peak heights of Ge and Zn were computed and are given in Table 2.3.1. These ratios were taken to eliminate the sensitivity factor for each element which drops out when one is working with ratios. These analyses reveal that the grain boundary of the GeO_2 doped (3.82 mol% GeO_2) ferrite is enriched with Ge by a factor of 5.

(b) Grain Boundary Phase

A batch with higher concentration of GeO_2 (6 mol% GeO_2) was made in order to 'see' a second phase at the boun-

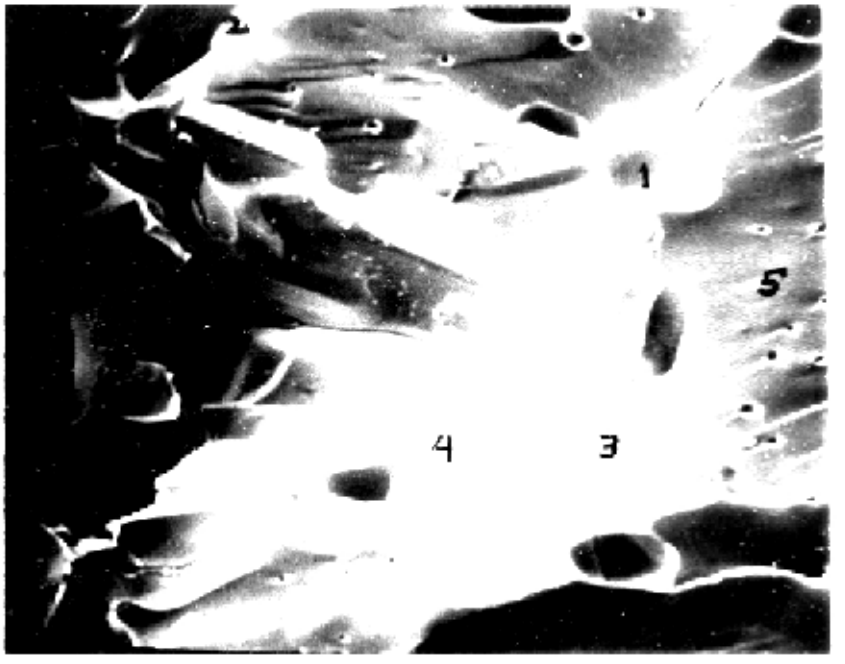

FRACTURED SURFACE

SPECIMEN CURRENT PICTURE (1000 x)

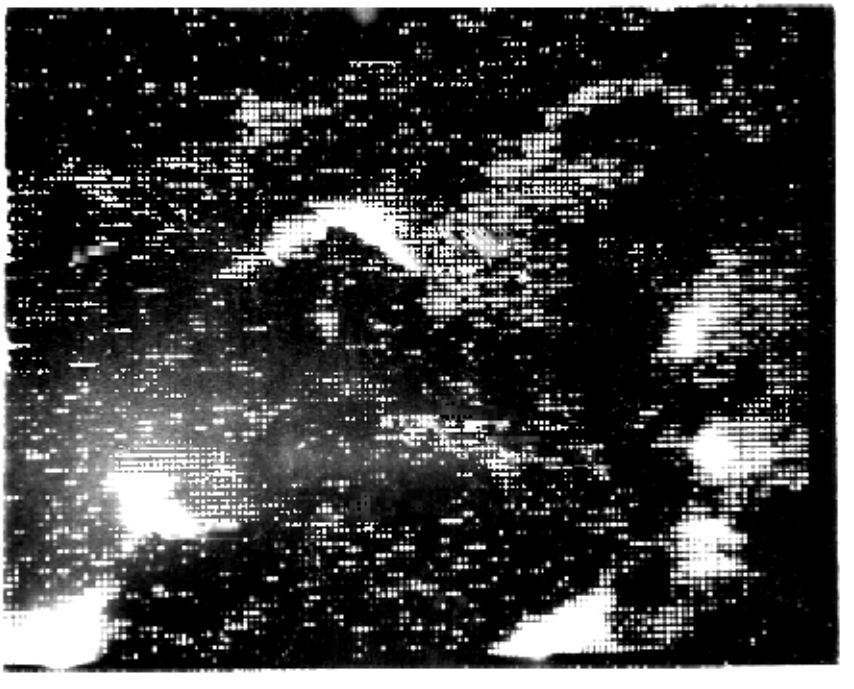

Ge AUGER PICTURE OF ABOVE AREA (1000 x)

Fig. 2·3·4

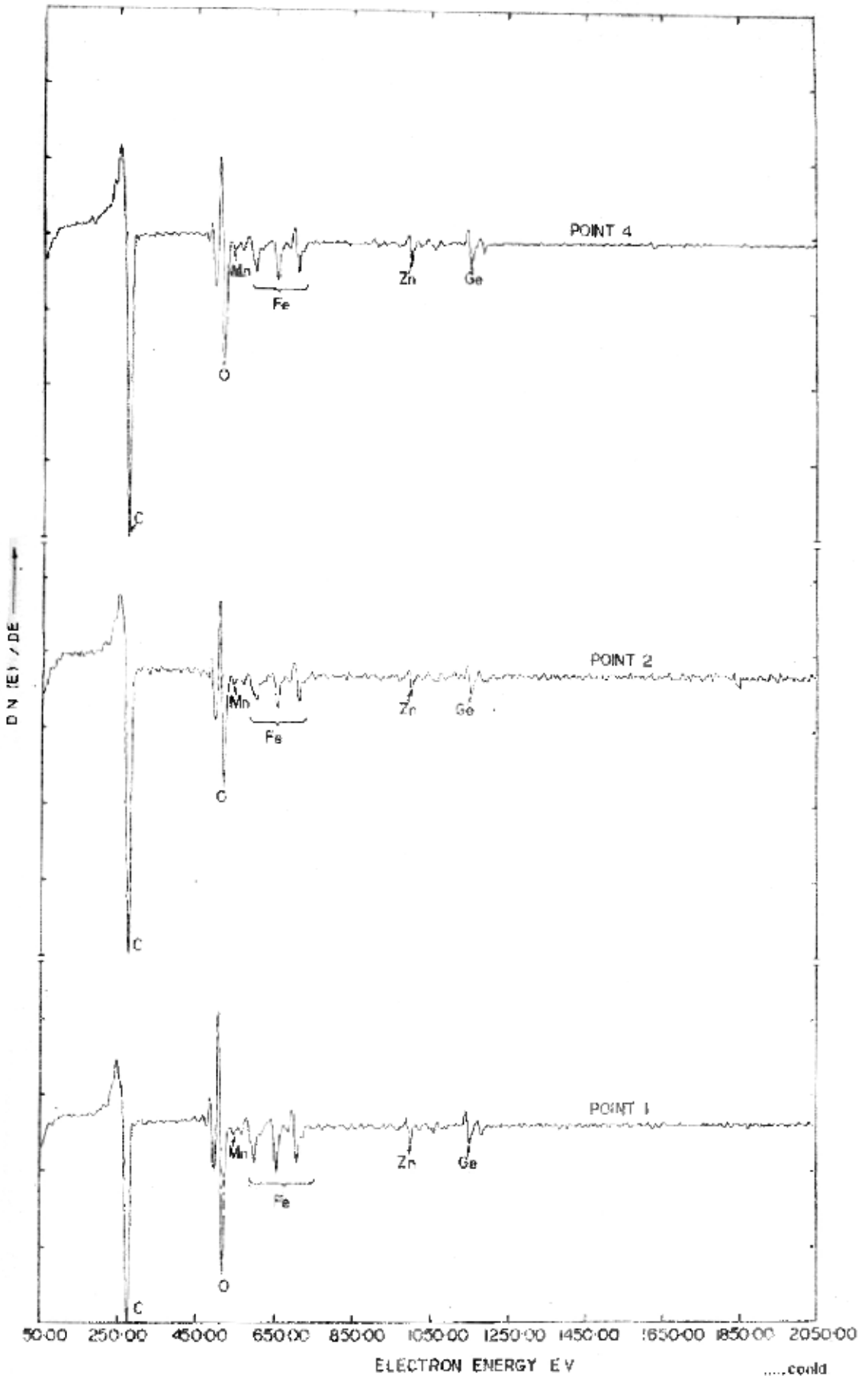

.....contd

Fig 2·3·5 Auger Spectra of a freshly fractured surface of the Mn-Zn ferrite doped with 3·82 mol % GeO_2

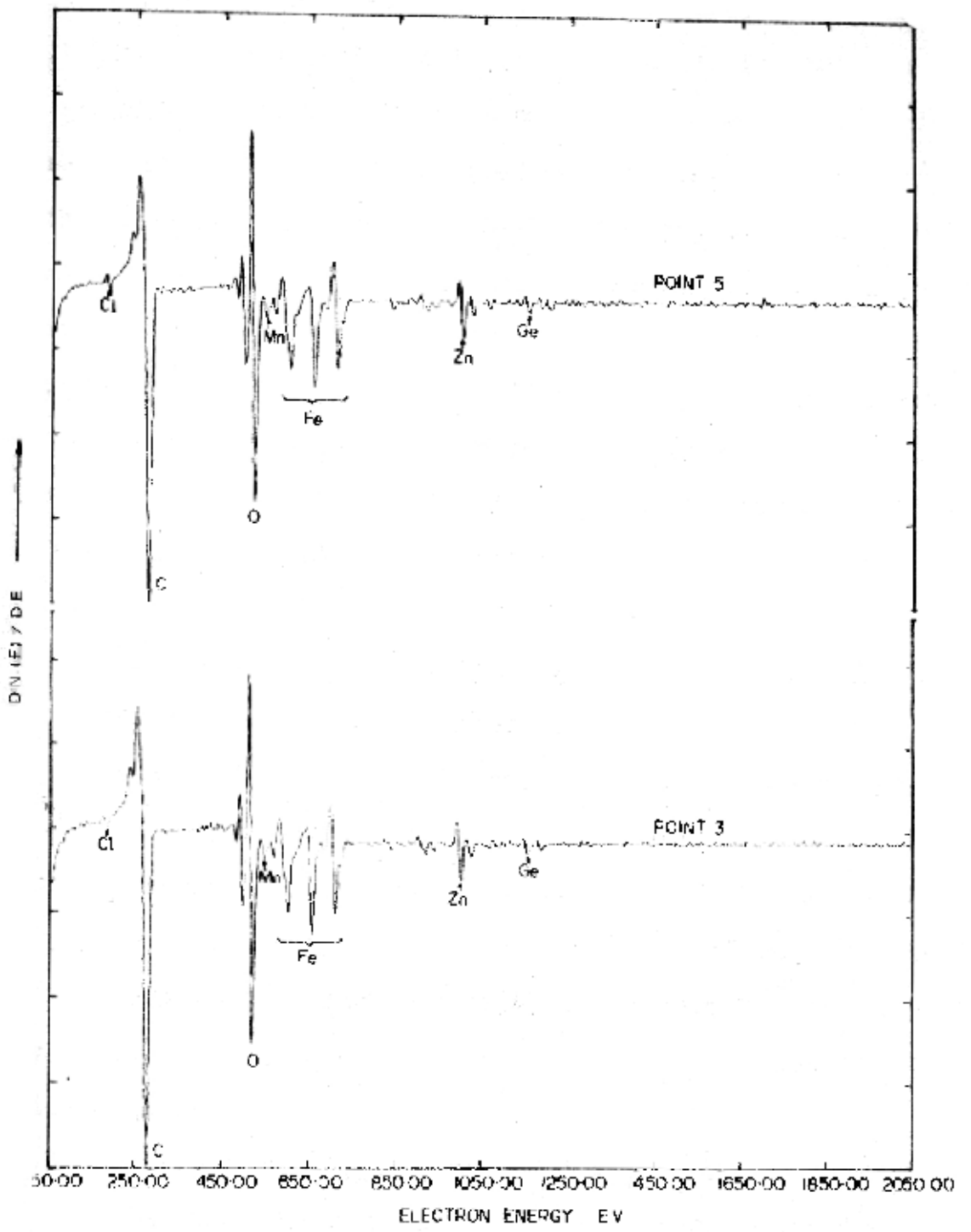

Table 2·3·1

(Peak to peak height of Ge)/ (Peak to peak height of Zn)	On the grain boundary			In the grain	
	Point 1	Point 2	Point 4	Point 3	Point 5
	1·22	1·66	1·22	0·26	0·30

daries similar to the one seen in the case of SiO_2. An optical micrograph of the polished surface of this specimen is shown in Fig.2.3.6. A grey coloured liquid like phase is observed at the grain boundaries which is submicron in size. X-ray microprobe point analysis were carried out on various points lying on this second phase and also inside the grains. Figure 2.3.6 shows XMA point analysis at a point A inside a grain and at a point B on this grain boundary phase. It is observed that three Ge peaks corresponding to X-ray energies of 1.24, 9.88 and 10.96 KeV are obtained at point B as against a very feeble 9.88 Ge peak at point A. To identify these Ge peaks, such analysis were also carried out on spec-pure GeO_2 shown in Fig. 2.3.6(a).

These results indicate the formation of a Ge-rich phase at the grain boundaries at larger concentration of GeO_2.

Attempt was made to observe the phase contrast between the ferrites and this second phase under the backscattered and absorbed specimen current mode of the SEM. Since Ge (Z=32) has atomic number very close to those for Fe (Z=26), Zn (Z=30) and Mn (z=25), their backscattering coefficients[15] are also very close, therefore no contrast for the two different phases could be observed.

2.3.3. Distribution of Sn in the Microstructure

X-ray microanalysis carried out on SnO_2 doped ferrites even up to a dopant level of 5.70 mol%, gave no evidence for Sn segregation. Figure 2.3.7 shows the X-ray microanalysis display for Sn for the specimen with 5.70 mol% SnO_2. A uniform distribution of Sn in the microstructure is observed.

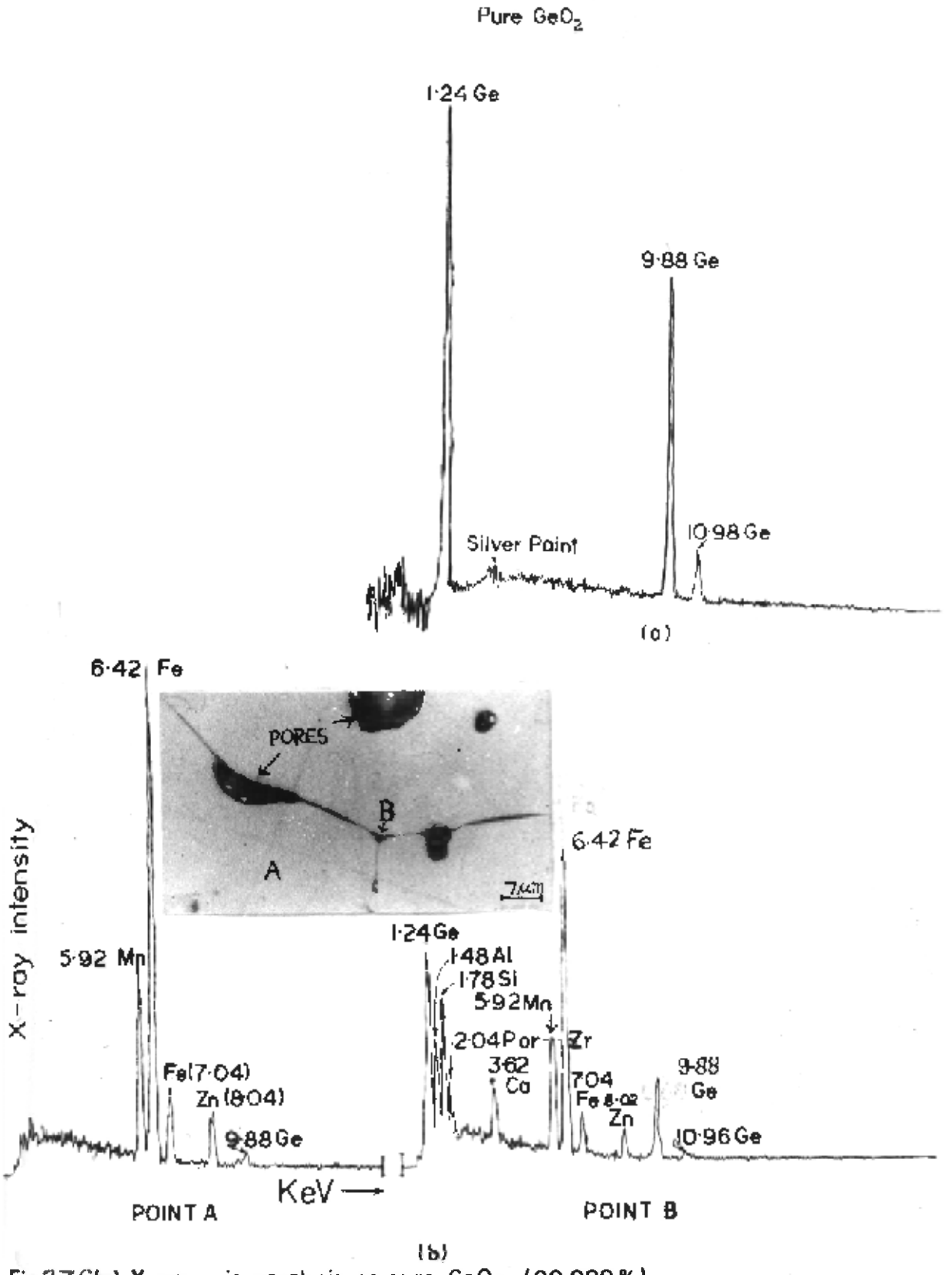

Fig. 2.3.6 (a) X-ray microanalysis on pure GeO_2 (99·999 %)

(b) X-ray microanalysis at a point A in a grain and at a point B on a grain boundary.

100 μ x 100 μ

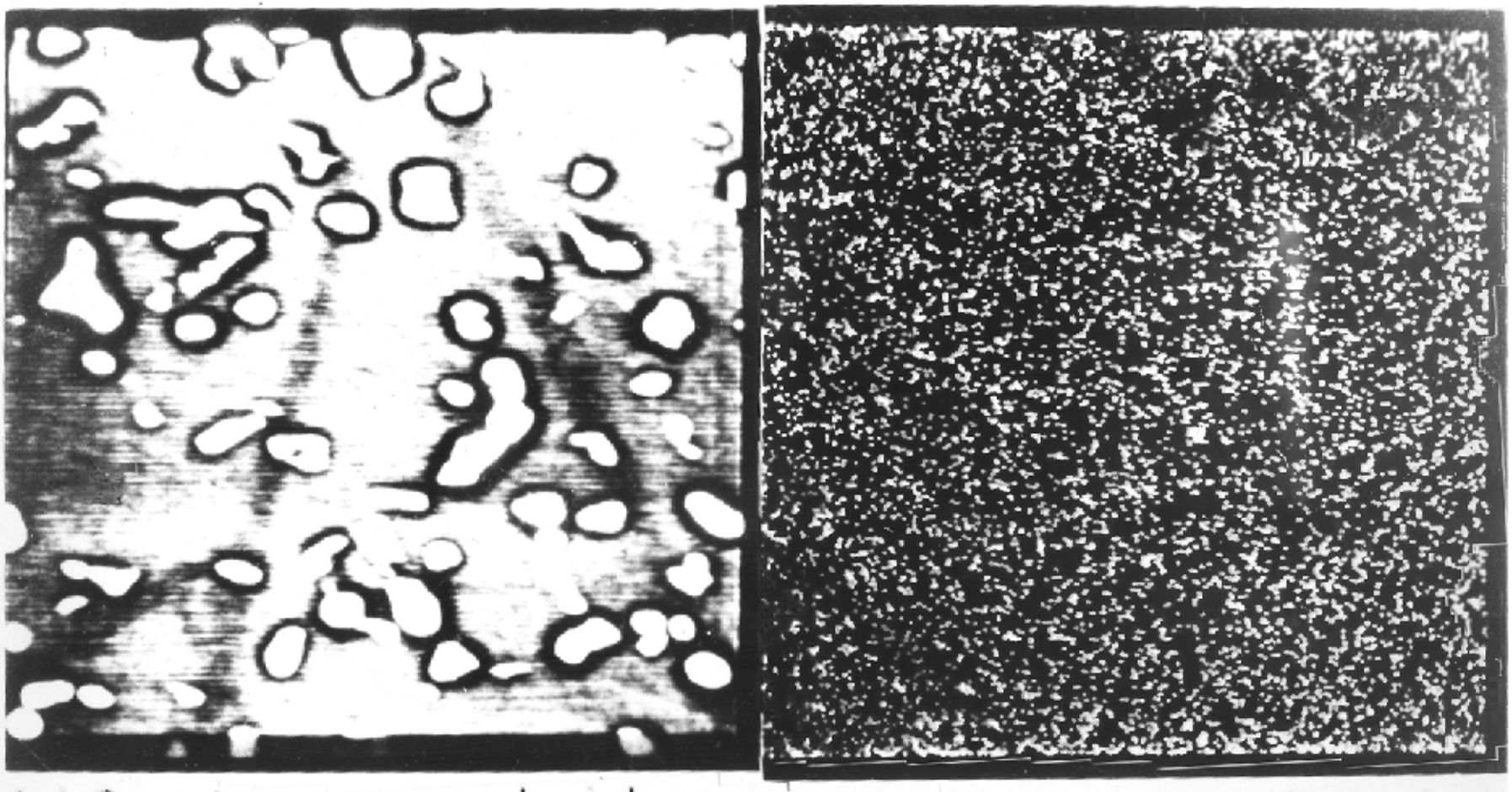

(a) Specimen current picture

(b) X-ray microanalysis display of Sn (L_{α})

2.3.4. Lattice Parameters

Lattice parameters for the Mn-Zn ferrites doped with various amounts of all the three impurities - SiO_2, GeO_2 and SnO_2 are shown in Fig.2.3.8. Practically no change in lattice parameter is obtained in the case of SiO_2 up to a level of 1.28 mol%. In the case of GeO_2 additions, slight decrease in the lattice parameter is observed.

SnO_2 additions, on the other hand, show a significant increase in the lattice parameter. At a level of 5.70 mol%, a change of 9.4% in the lattice parameter is observed.

2.4 DISCUSSIONS

2.4.1. Nature of SiO_2 in the Ferrite

As reported in the results, a well defined Si-rich phase was detected in the Mn-Zn ferrite. At a silica content of 1.28 mol% SiO_2, the volume fraction of this phase was found to be 2.94%. This increase in the effective volume fraction clearly indicates the presence of a possible compound that silica might be making with the host oxides. SEM studies showed that this phase was a liquid like phase, non conducting in nature.

Silica has been found to exist as a liquid like grain boundary phase in ferrites by several workers.[1,16-18] Evidence for this boundary phase has also been obtained using electron microprobe techniques and Auger spectroscopy.[11] Giles and Westendorp[19] used a combination of etching, scanning microscopy (SEM) and electron microprobe analysis to study the silica phase in Mn-Zn ferrite. By etching away the ferrite grains using concentrated hydrochloric acid, they could observe white 'skeleton' formed by the grain boundary phase which was

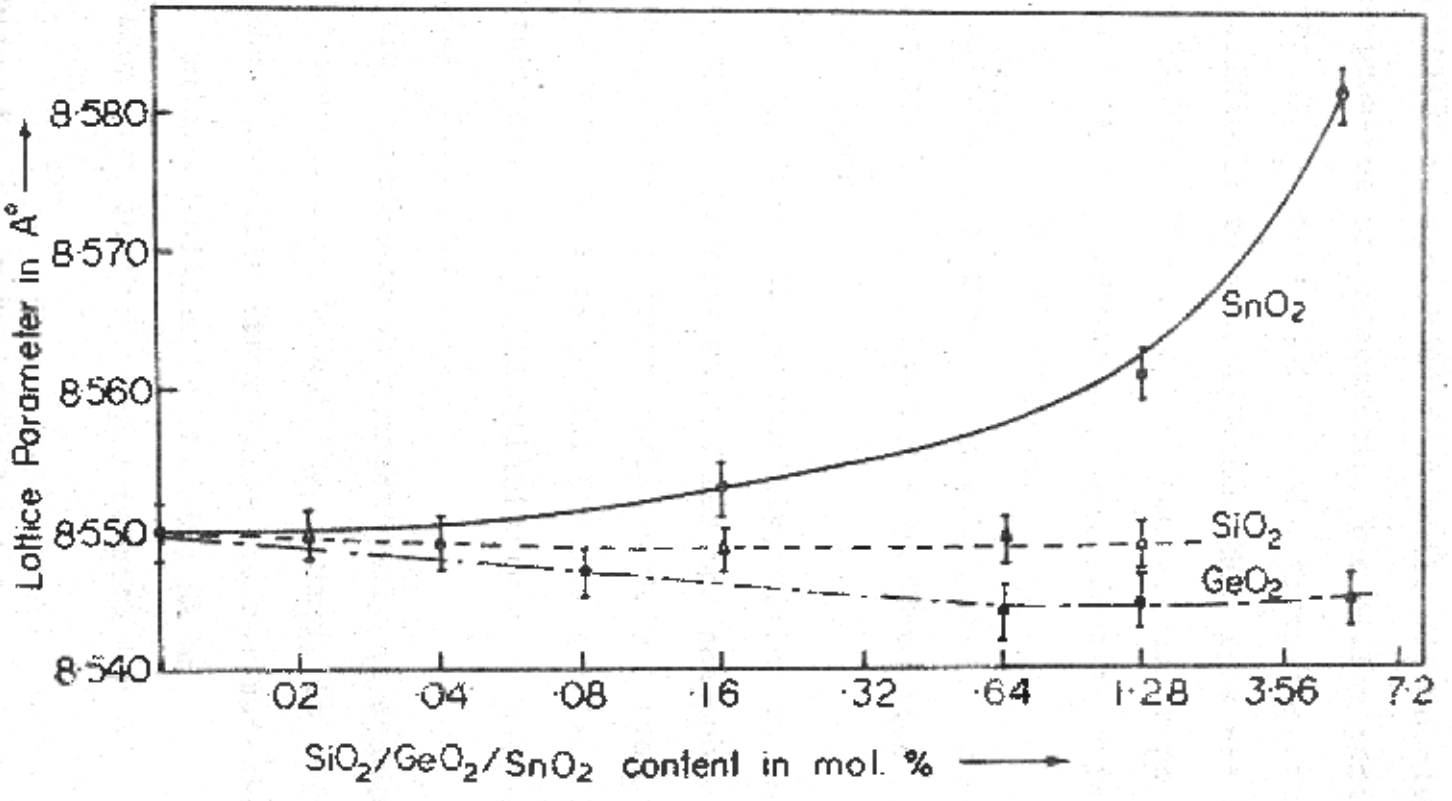

Lattice parameters for various impurity dopings.

Fig. 2·3·8

identified as pure silica or an eutectic containing silica using microprobe and chemical analysis. Quenching experiments showed that the phase starts appearing at about 1250°C and contained silica in amorphous from while slow cooled ones showed the presence of an eutectic, the silica part of which was observed as α-crystobalite. The formation of α-crystobalite is difficult to explain since this does not usually form below 1470°C,[20] however, the conditions of pressure and the influence of the surrounding cubic ferrite crystals on the silica as it cools are unknown.

It was also concluded[17] that the acidic oxides or slags are the most suitable additives for the formation of a homogenous liquid layer.

Regarding the solid solubility, silica is not expected to dissolve in the ferrite matrix for the reasons of the size of Si^{4+} ion. It has an ionic radius $\sim$0.39 Å (see table 2.4.1). much smaller than the ions in the ferrite matrix. The various factors determining the solid solubility have been discussed in section 3.4.1 of chapter III.

Lattice parameters show practically no change on SiO_2 additions. Even if some solubility existed, it is not possible to locate the solubility limit since the raw materials used themselves contained silica ($\sim$.01 wt%) as an impurity. A Si-segregation even in the undoped ferrite was observed (ref. Fig.2.3.6).

2.4.2. Nature of GeO_2 in the Ferrite

Lattice parameter measurements show that Ge^{4+} has a limited solubility in the ferrite but comparing with the corresponding SiO_2 results, it can be said that Ge^{4+} is more

Table 2·4·1

Various Ionic Radii and Calculated Site Radii For a Mn-Zn Ferrite :

Ions/Site	Radii (Å)
Tetrahedral Site	0·52
Octahedral Site	0·80
O^{2-}	1·32
Fe^{3+}	0·67
Fe^{2+}	0·83
Mn^{2+}	0·91
Zn^{2+}	0·83
Si^{4+}	0·39
Ge^{4+}	0·44
Sn^{4+}	0·69

soluble than Si^{4+} in the ferrite.

A limited solubility in case of Ge^{4+} is in fact expected on account of its small size (ionic radius $\sim$ 0.44Å) as compared to the constituent ions in the ferrite (see table 2.4.1).

Hirota[21] doped appropriate mixtures of $CaO-GeO_2$ in Mn-Zn ferrites and found that it helped in achieving low losses and high quality factor. He interpreted his results arguing that CaO and GeO_2 form $CaGe_2O_4$ - a slag like compound along the grain boundaries. According to him, the Ge^{4+} ions would go into solution with the ferrite but the moment they encountered CaO, they would form calcium germinate and flow towards the boundaries. However, in the present case where GeO_2 has been added alone, no significant solubility of GeO_2 is indicated. It is thought that some amount GeO_2 might be forming a compound with calcium which is present as a raw material impurity ((about 5 ppm).

It is worthwhile to notice that in case of 1.28 mol% silica, about 3% volume fraction of the Si-rich phase was obtained whereas even with 6 mol% GeO_2 much smaller traces of the Ge-rich phase could be seen (volume fraction could not be measured here because of large porosity). Possibly it could be due to the fact that unlike SiO_2, GeO_2 may not be forming compounds with the host oxides and most of it might be staying as pure GeO_2.

2.4.3. Nature of SnO_2 in the Ferrite

Lattice parameter and microprobe analysis results suggest that unlike SiO_2 and GeO_2, SnO_2 is not a second phase additive and therefore must be going into solution with the ferrite. The solubility of Sn^{4+} in the ferrite is in fact

expected considering its size (ionic radius $\sim$.69 Å). From valency and size considerations, the Sn^{4+} ion should prefer octahedral B-sites. However, if one assumes a purely statistical distribution, then one third of the tin would lie on A-sites and two third on B-sites. Such a situation is anticipated at high temperatures because there the distribution of the ions on A and B sites is presumably random. But as the ferrite is cooled down, the tetravalent ions tend to migrate to the preferred B-sites. This process is greatly facilitated by the presence of cation vacancies; a similar behaviour has been found in magnesium ferrite.[22] It is also probable that it proceeds more slowly for the relatively large tin ion. Thus if the vacancy concentration is very small, it is likely that on cooling at a normal rate, the high temperature distribution of the tin ions becomes "frozen in". Knowles[23] has studied the distribution of tin ions in stoichiometric and nearly stoichiometric Mn-Zn ferrites and has experimentally shown the presence of some tin ions on A-sites.

A tin ion, when goes to an A-site will either displace a Mn^{2+} or an Fe^{3+} ion to a B-site. Knowles[23] has also shown that with the substitution of an increasing amount of tin, the results are generally consistent with the displacement to B-sites of some Fe^{3+} and an increasingly large fraction of Mn^{2+}, for, as the Sn^{4+} content is increased the lattice constant increases also, and Mn^{2+} is a considerably larger ion than Fe^{3+}.

REFERENCES

1. F.M.A. Carpay and A.L. Stuyts, Science of Ceramics, 8, (1975), 23.
2. S.N. Ruddlesden and A.C. Airey, Res. Paper No.602, The Brit. Ceram. Res. Association, 1967.
3. A. Joshi et al, ed. A.W. Czandevna, Elsevier Scientific Publishing Company, Amsterdam (1975).
4. R.S. Tebble and D.S. Craik, "Magnetic Materials", Chap.7, Wiley Inter Science.
5. E.C. Snelling, Soft Ferrites, Ilifee Books Limited, London (1969).
6. L.N. Johnson, J. Dent. Res., May-June 1972, Vol.51, No.3, p.789.
7. O.C. Wells, Scanning Electron Microscopy, McGraw Hill Book, Inc., New York, 1974.
8. L.N.Johnson and W. Kammrath, Proc. V. Ann. SEM Symp. Illinois, USA, April 1972, p.90.
9. P.W. Palmberg, G.E. Riach, R.E. Weber and N.C. MacDonald, Hand book of Auger Electron Spectroscopy, Physical Electronics Industry, Edina, 1976.
10. N.C. MacDonald, G.E. Riach and R.L. Gerlach, Application of Scanning Auger Microanalysis, Res/Developm., Aug.1976, Vol.27, No.8, p.42-46, 48-50.
11. P.E.C. Franken et al., Ceramurgia International, 3 (1977), 122.
12. P.E.C. Franken and Harry V. Doveren, 'Determination of the grain boundary composition of soft ferrites by Auger electron spectroscopy', (to be published).

13. N.F.M. Henry, H. Lipson and W.A. Wooster, 'The interpretation of X-ray diffraction photographs', Macmillan & Co. Ltd., London, 1960.

14. G.C. Jain, B.K. Das, Santosh Kumari and A. Hepworth, Xth Ann. Conf. of EMSI, Bombay, Dec., 1977.

15. L.L. Hench and R.W. Gould, 'Characterization of Ceramics', Dekker, New York, 1971.

16. C. Kooy, Sci. Ceram. 1, 21, 1961.

17. H. Kono, Ferrites : Proc. Internat. Conf. July 1970, Japan, p.137.

18. T.G.W. Stijntjes et al, Ferrites : Proc. Internat. Conf. July, 1970, Japan, p.194.

19. A.D. Giles and F.F. Westerndorp, Journal de Physique, ICF-2, Colloque C-1, 1977, p.C1-317.

20. E.M. Levin et al, 'Phase diagrams for ceramists', (Am. Ceram. Soc., 1956).

21. E. Hirota, Jap. J. Appl. Phys. Vol.5, No.12, p.1125, 1966.

22. E. Luca, GH Maxima and M.L. Crans, Phys. Stat. Sol (a), 14, K153-K155, 1972.

23. J.E. Knowles, Philips Res. Repts. 29, 1974, p.93.

CHAPTER - III

EFFECT OF SiO_2, GeO_2 AND SnO_2 ADDITIONS ON THE MICROSTRUCTURE OF THE Mn-Zn FERRITE

3.1. INTRODUCTION

A knowledge of the microstructure of a polycrystalline body is essential in any attempt to study and control its properties. This is particularly important in the field of ceramics, where the overwhelmingly important form is the polycrystalline body. The control of microstructure becomes essential in ferrites because most of the important properties are microstructure-sensitive as has been described in chapter I. The various factors that influence the microstructure of ferrite may be listed as - the impurities present, the sintering parameters and the powder parameters i.e. particle size and distribution of the various constituents.[1-4] The effect of various added concentrations of the three impurities - SiO_2, GeO_2 and SnO_2 on the microstructure has been studied and discussed in this chapter.

3.2. EXPERIMENTAL METHODS

3.2.1. Metallographic Analysis

(i) Lapping and Polishing

The sintered toroids were carefully lapped on 240-, 400- and 600 grit silicon-carbide wet papers successively. After a proper cleaning, these were polished on a micro-cloth wheel using 6 μm, 1 μm and 1/4 μm diamond pastes in succession.

(ii) Etching

The lapped and polished specimen were ultrasonically cleaned in trichloroethylene and were then etched chemically

to reveal the microstructural details. Normally the etching was done in 3:1 solution of hydrochloric acid with ethyl alcohol with ultrasonic agitation for a few minutes.

(iii) Grain-size Measurement

The average grain size of the etched samples was estimated using a relationship derived by Fulman.[5] For this purpose, regularly spaced, parallel straight lines were drawn on the photomicrographs taken on a Carl Zeiss Light Incident 'Epityp-II' universal metallurgical microscope. The number of grains intersecting a line of known length drawn on the photomicrograph were counted and the average length, $\bar{l}$ of the intercepts of individual grain on this line was determined for a number of such lines. The average grain diameter $\bar{d}$ was obtained from the following relation

$$\bar{d} = 1.5\ \bar{l} \qquad (3.1)$$

This method is valid only when the grain size distribution is fairly uniform. In case where the grain size distribution is non-uniform, the average grain diameter, $\bar{d}$, was obtained from the following relation

$$\bar{d} = \frac{\pi}{2\ \bar{m}} \qquad (3.2)$$

where $\bar{m}$ is the average of the reciprocals of the diameters of individual grains.

The average pore to pore distance was determined by dividing the grain size with the square root of the average number of pores inside the grain.

3.3. EXPERIMENTAL RESULTS

3.3.1. Microstructure

(i) SiO_2 additions

Figure 3.3.1 gives the microstructure for various additions

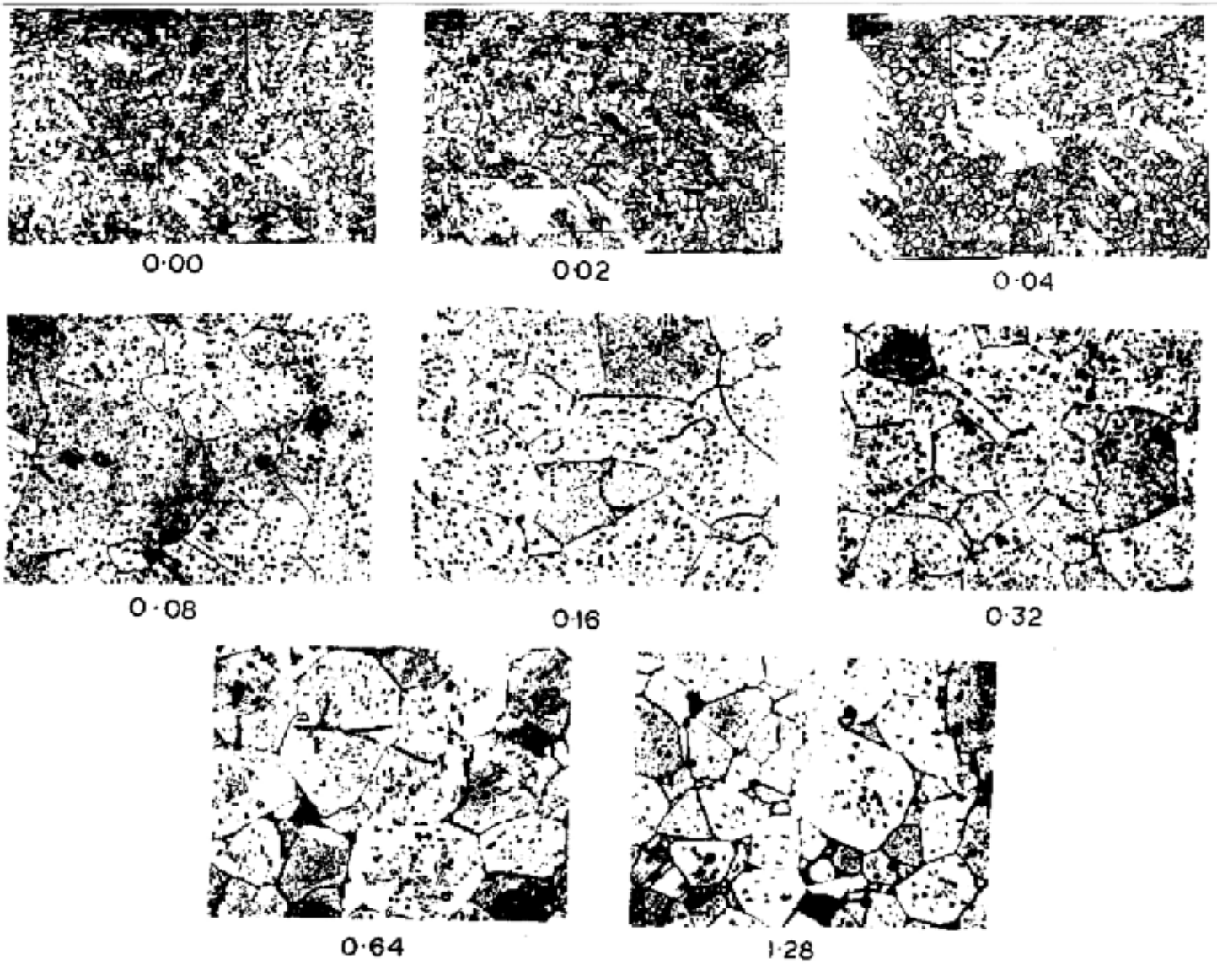

Fig. 3·3·1 MICROSTRUCTURES CORRESPONDING TO DIFFERENT SiO_2 CONTENTS (INDICATED IN MOL % AGAINST EACH MICROGRAPH).

of silica for the 'standard firing schedule' (1275°C/45 min in N_2). The microstructures observed agree well with the work of Giles and Westendorp.[6] Specimen with .04 mol% SiO_2 shows the presence of duplex structure - the onset of discontinuous grain growth. Intermediate levels of SiO_2 (.08 to .32 mol%) exhibit coarse crystallization with very large intragranular porosity which is found to be at its maximum for .08 mol% SiO_2 where almost all the porosity is intragranular. The structure goes to somewhat fine grained one with thicker grain boundaries and comparatively lesser intragranular porosity at the two highest silica levels. It may be noticed that here the average size of pores or pits is higher as compared to that observed at lower SiO_2 levels.

Average grain sizes are plotted in Fig.3.3.2. The region of high discontinuous (or cannibal) grain growth extends from .08 mol% SiO_2 to 0.32 mol% SiO_2.

At higher sintering products, this range of high discontinuous grain growth extends on both sides of low as well as high silica contents (Fig.3.3.3).

In Fig.3.3.4, average grain sizes obtained at different sintering temperatures for different silica levels are shown. It may be noticed that the grain growth sets up earliest in the specimen with highest silica content. The grain growth goes discontinuous earlier in the intermediate silica level (.08 mol% SiO_2). In other words, it can be said that silica lowers the sintering temperature.

(ii) <u>GeO_2 Additions</u>

Almost similar changes in the microstructure with various GeO_2 contents are observed (Fig.3.3.5), but the corresponding

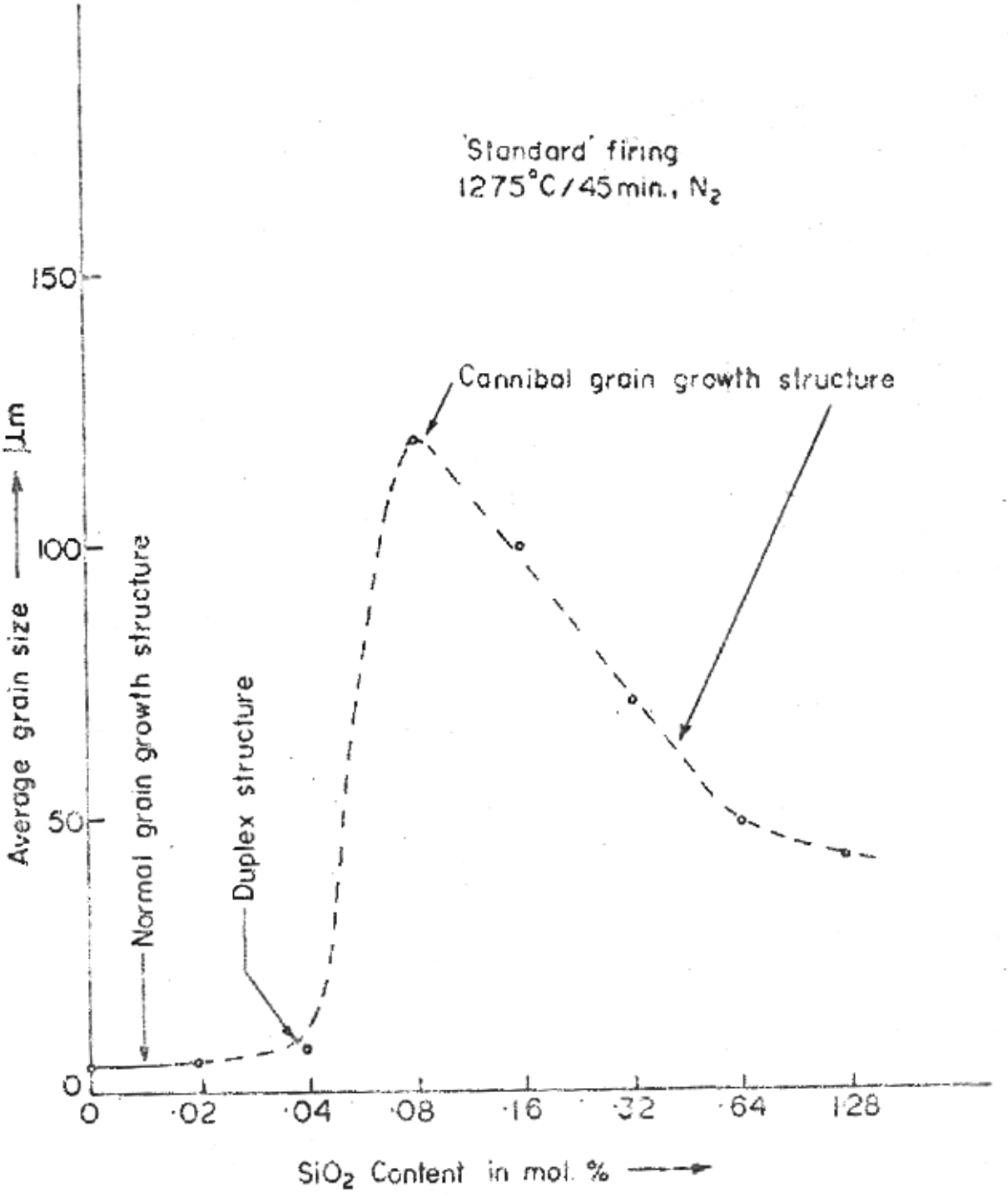

Average grain size vs. SiO_2 content.

Fig. 3·3·2

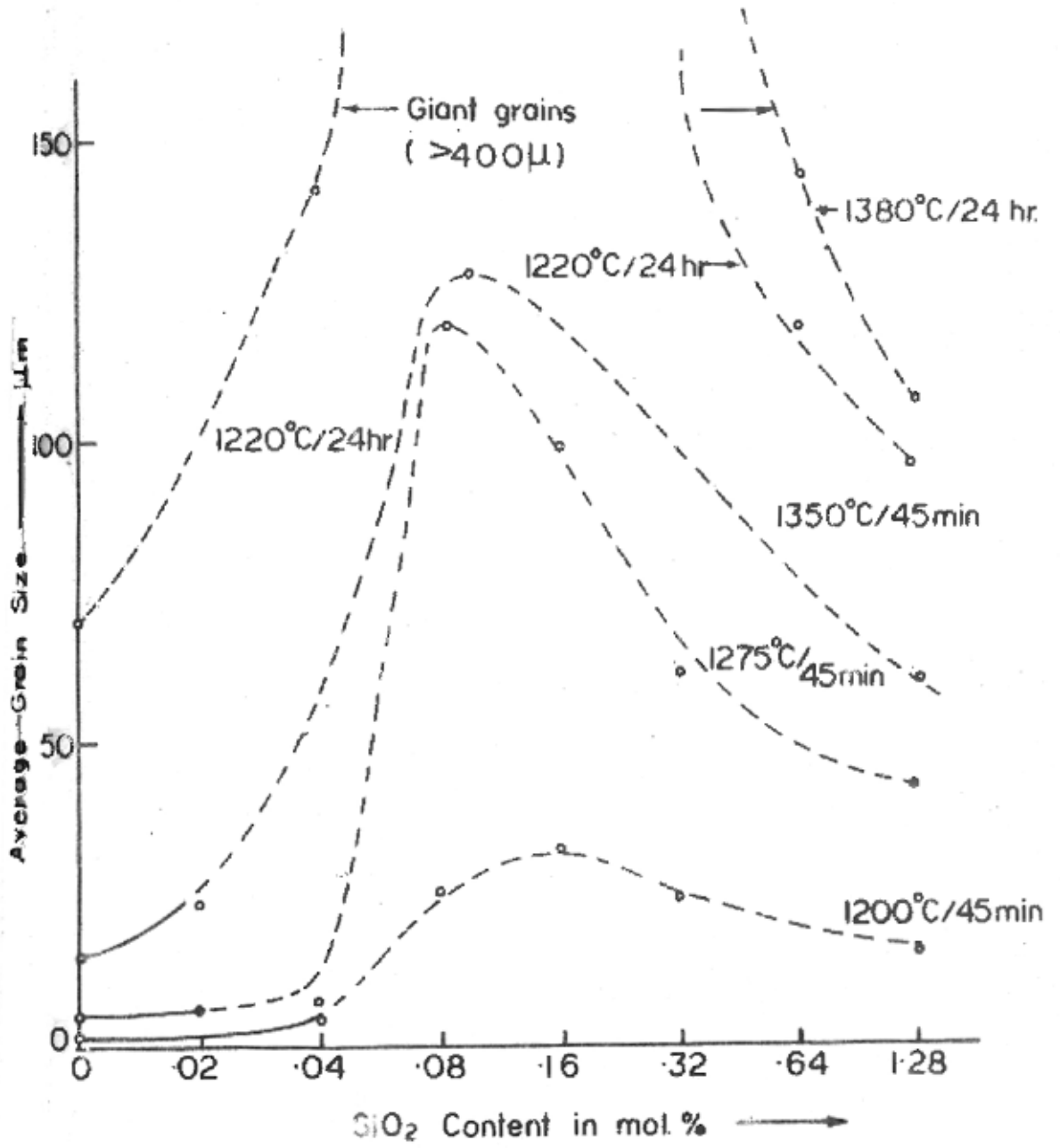

Average grain size vs. SiO_2 content for different sintering products.

Fig. 3·3·3

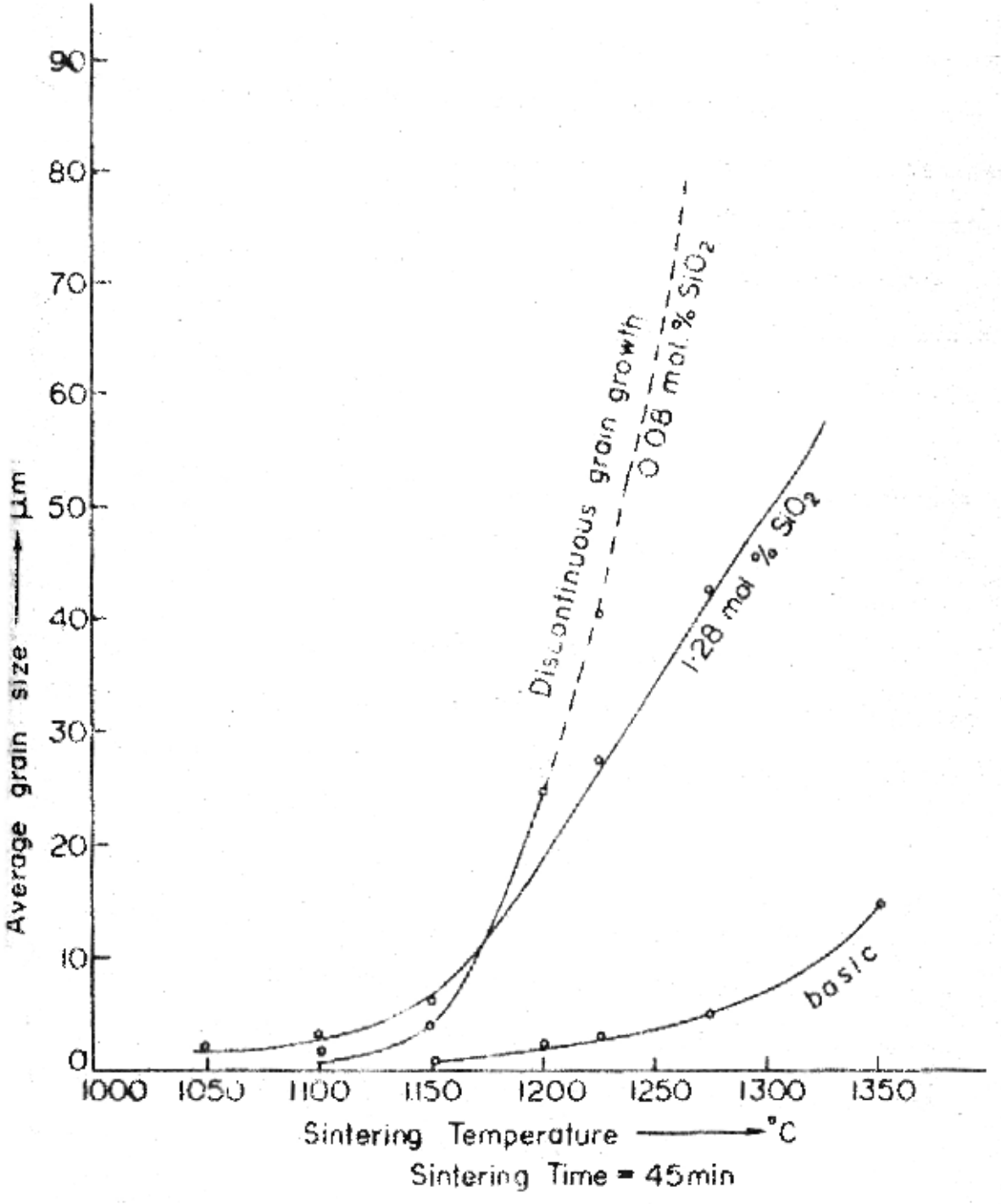

Fig.3.3.4

Average grain size vs sintering temperature for various SiO_2 contents

doping levels are higher in this case. The discontinuous grain growth sets in rather slowly, at much higher contents as compared to that observed on SiO_2 additions. Initially, there is some increase in grain size along with occurance of some trapped pores (.08 mol% GeO_2 onwards). The structure goes sufficiently coarse at a GeO_2 content of 1.28 mol%, almost similar to what is obtained at a silica content of .08 mol%. At further higher GeO_2 content, the structure tends to be somewhat regular with reduced intragranular porosity and at 3.82 mol% GeO_2, the microstructure looks fairly regular. Figure 3.3.6 gives the average grain sizes for various GeO_2 levels.

At higher sintering products, the region of discontinuous grain growth extends almost in a similar way as observed in case of silica additions (Fig.3.3.7). Like SiO_2, GeO_2 also lowers the sintering temperature. Figure 3.3.8 shows that the grain growth sets up at a much lower temperature in GeO_2 - rich samples and goes discontinuous earliest in samples doped with intermediate levels of GeO_2 (1.28 mol% GeO_2).

(iii) SnO_2 Additions

Unlike the above two impurities, SnO_2 additions are not found to affect the microstructure of the Mn-Zn ferrite as shown in Fig.3.3.9. However, at high sintering products, it is observed that the discontinuous grain growth tends to set in, in the ferrites with higher SnO_2 contents (Fig.3.3.10).

3.4. DISCUSSIONS

As reported under the results, the addition of both SiO_2 and GeO_2 has strong effect on the microstructure of the Mn-Zn ferrite whereas the addition of SnO_2 leaves the microstructure unaltered. To explain these results some general considerations

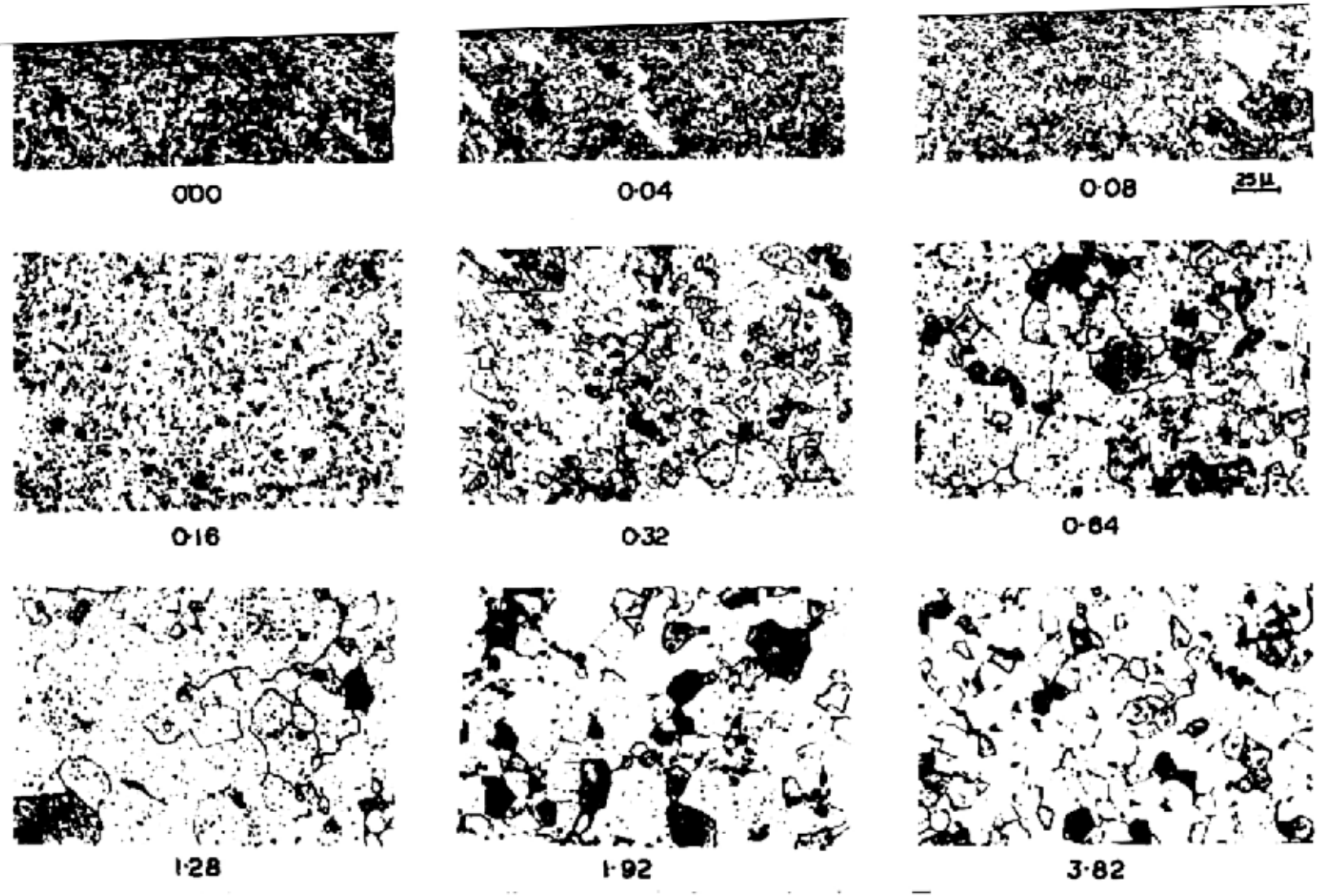

Microstructures corresponding to different GeO_2 contents (indicated in mol. % against each micrograph).

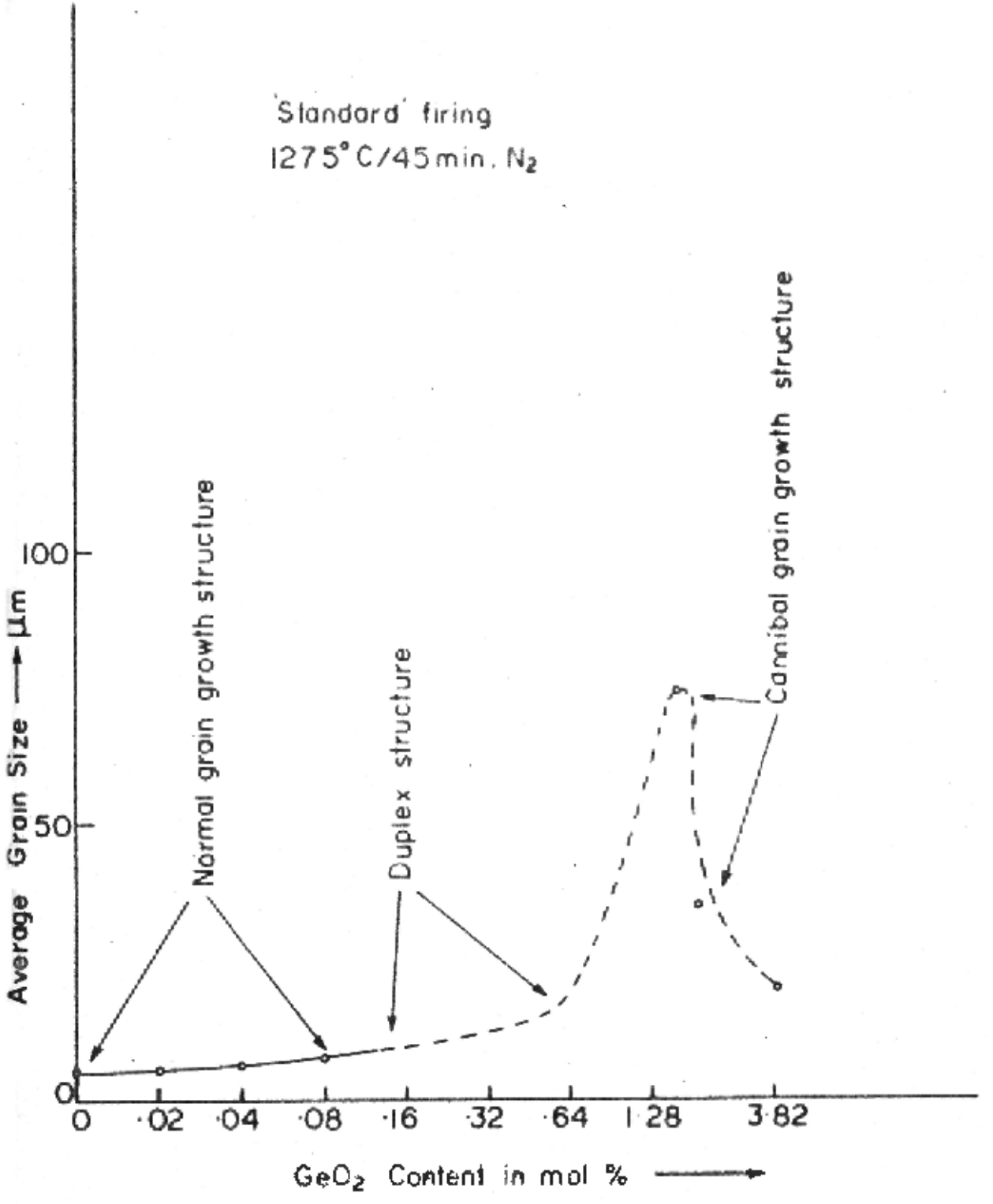

Fig. 3·3·6

Average grain size vs. GeO_2 content.

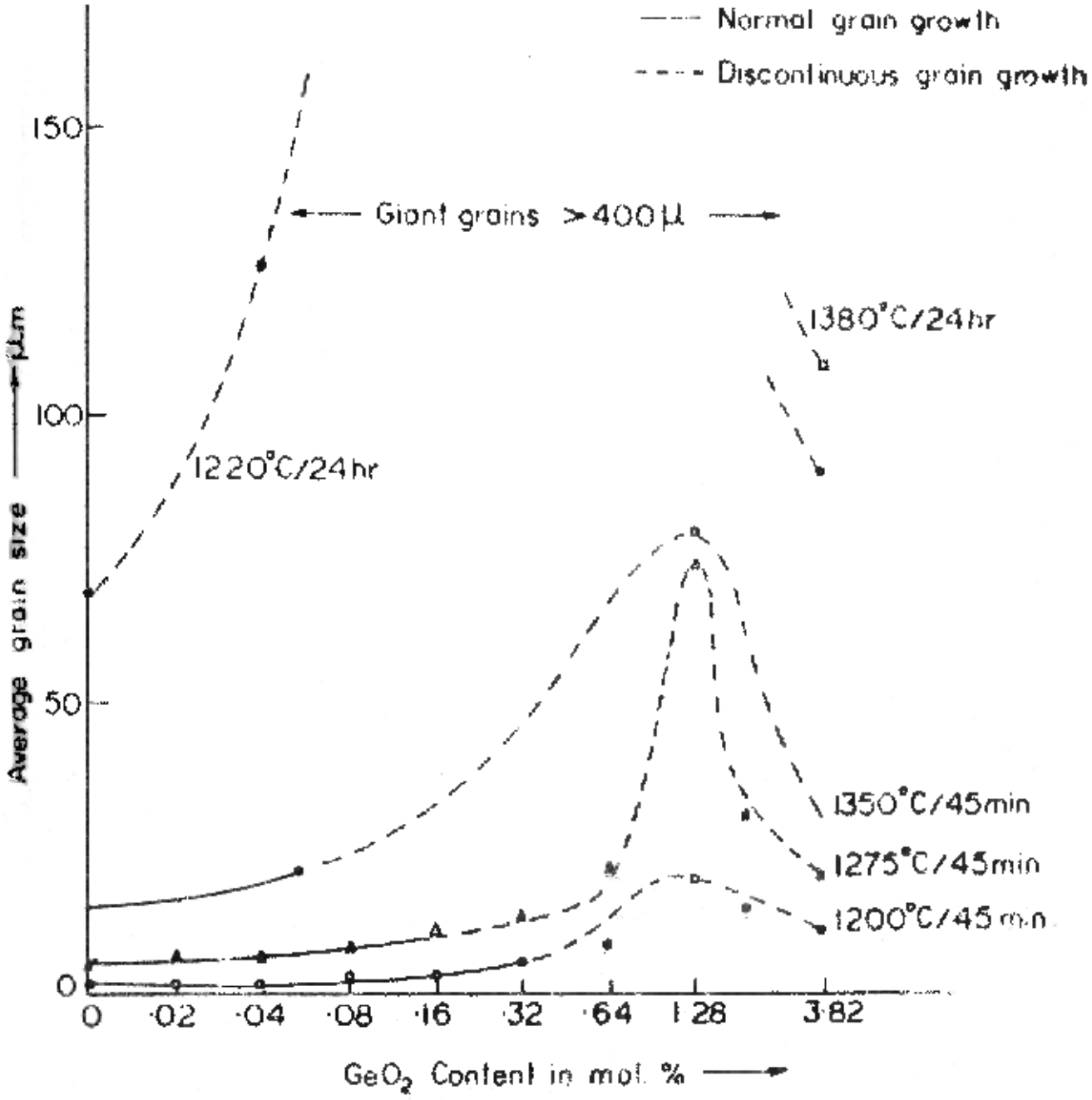

Average grain size vs GeO_2 content for different sintering products

Fig·3·3·7

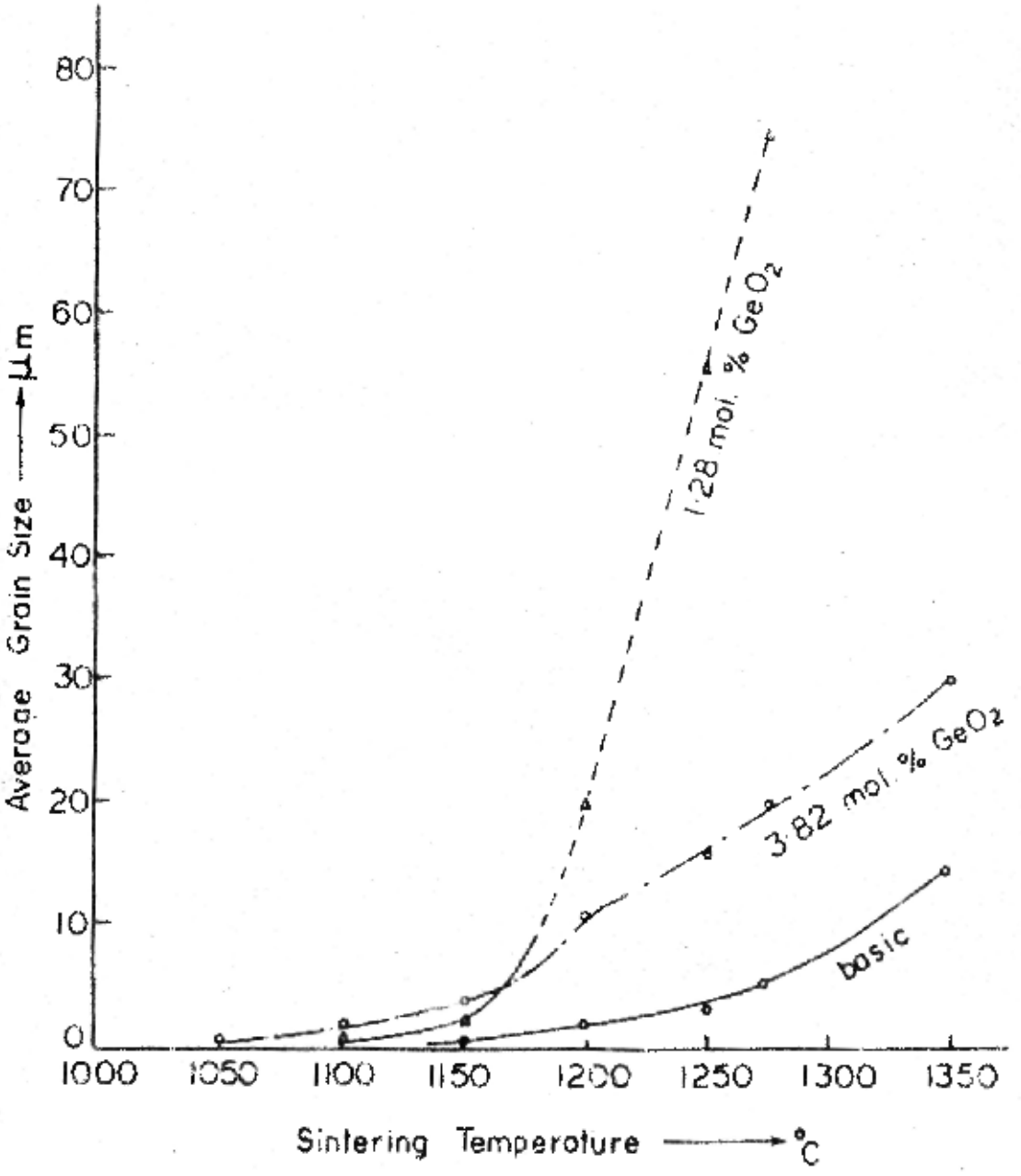

Average grain size vs sintering temperature for various GeO_2 levels

Fig. 3·3·8

$Mn_{.564}Zn_{.375}Fe_{2.06}O_4$ /1275°C / 45 Min , N_2

SnO_2 mol %

10 μ

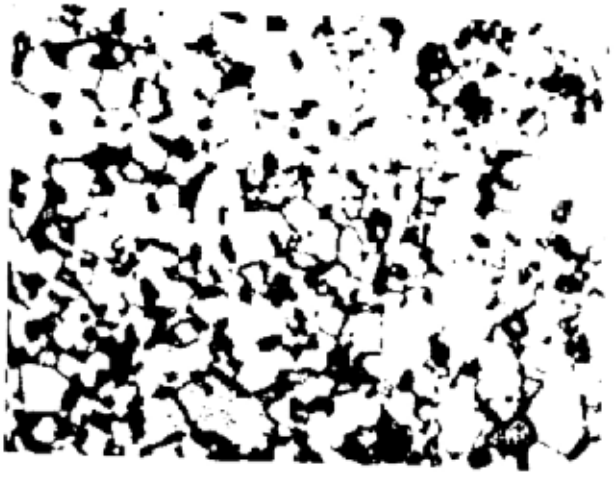

0·00

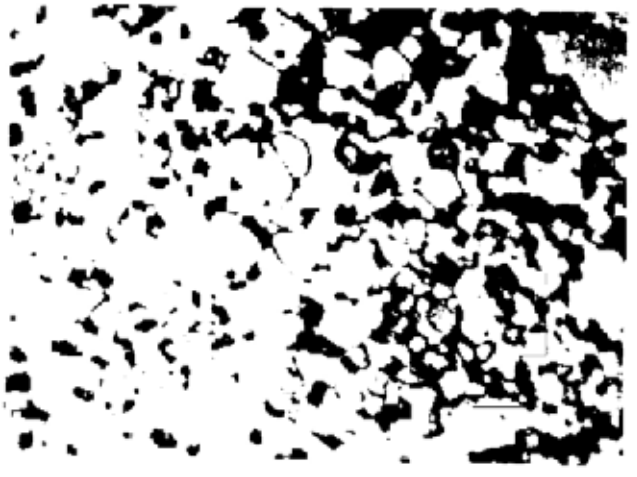

0·04

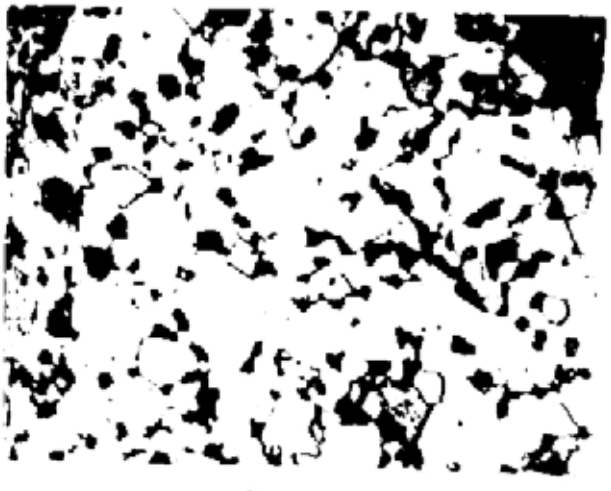

1·28

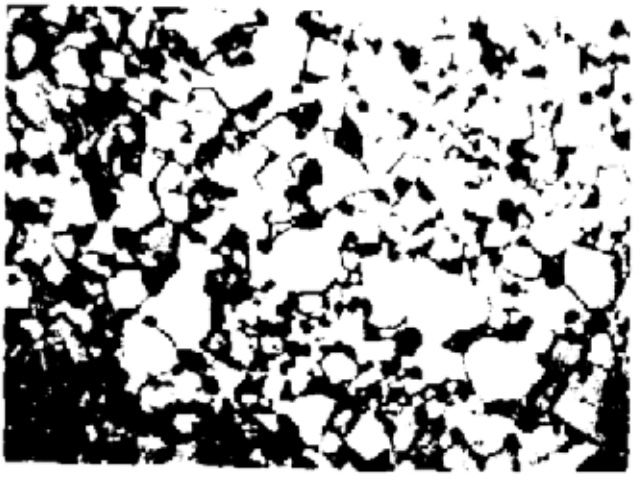

5 70

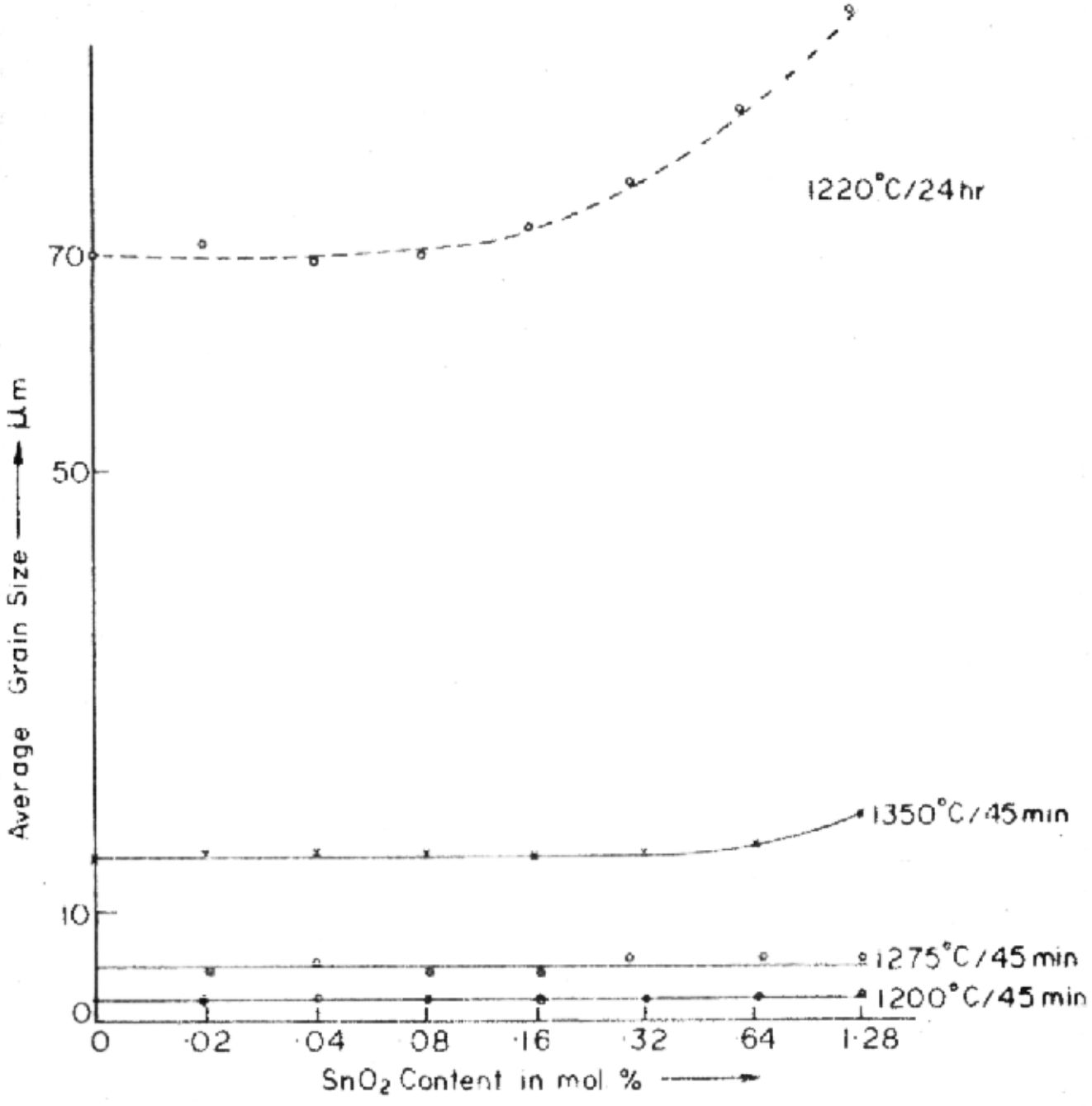

Average grain size vs SnO_2 content for various firings

Fig. 3·3·10

will be taken up first.

3.4.1. General Considerations

(i) Role of the Impurity Additive

The impurity additive can either go into solid solution, segregate at the grain boundaries or form a second phase at a certain stage of sintering changing thereby the course of grain growth. These possibilities depend on the ionic radii, the ionic state and the chemical affinity of the impurity ions with its surroundings.

(a) Solid Solubility and Segregation

The solid solubility is known to be restricted if the difference between the ionic radii of the solute impurity ion and the radii of the available sites in the solvent matrix is more than 15%.[7] Also from the principle of 'relative valency effect'[8] the solid solubility is known to be restricted if the valency of the solute ions is very much different from the ions in the solvent matrix. Besides, the solid solubility is also dependent on the temperature. At high temperatures even large size solute atoms (larger than the sites available in the solvent matrix) can go into solid solution. Such atoms introduce a distortion energy in the grain interior which can be estimated from the elastic theory using the following relation given by McLean.[9]

$$Q = \frac{24 \quad K \; G \; r^3 \; (r_1 - r_o/r_1)^2 \; N}{3 \; K + 4 \; G} \qquad (3.3)$$

where K is the bulk modulus of the added ion, r_o is the radius of the unoccupied site, r_1 is the radius of the isolated ion, r is the r adius of the ion in its original position, G is the shear modulus of the matrix, and N is the Avogadro's number.

Also, it is known from the elastic theory that at the grain boundaries the lattice is distorted and the atoms have more room around them than in the bulk. Therefore, large size solute atoms tend to segregate at the grain boundary and small size solute atoms tend to segregate away from the grain boundaries. The concentration of the solute segregation at the grain boundaries (C_{gb}) depends on the temperature and is given by

$$C_{gb} = C_o \exp(-E/RT) \qquad (3.4)$$

where C_o is the solute concentration inside the grains and E is the difference in energy between a solute atom located at a grain boundary and the one in the interior of a grain. Solute segregation at the grain boundary may reduce at high temperatures but during slow-cooling this segregation occurs back at the grain boundaries.

Impurities present in solid solution can give rise to an impurity drag effect which impedes boundary motion.[10] The effect arises from any preferred segregation of the impurity either at or away from the grain boundary area. If, for example, because of size or charge differences, the impurity can occupy energetically favourable sites at the grain boundary, boundary motion implies either that the impurities must diffuse along with the boundary or that their energy is raised as they are left behind.[11]

(b) Second Phase Additives

Another possibility is that the impurity additive may exist as second phase in the grain boundary and thereby may affect grain growth in a number of ways. Some of the situations that can arise are briefly noted below

1) The second phase may exist as a solid or as a liquid at the processing temperature and its effect on boundary migration will depend strongly on its distribution in the boundary, which in turn will depend on the various interfacial energies or more precisely on the ratio of the clean boundary energy and the interfacial energy between the two phases.[12] Where this ratio is small, the second phase will, at small concentrations, form isolated spheres in the host matrix. In this configuration, the behaviour will be similar to that for porosity as treated in chapter I. Although the energies of interaction between the grain boundaries and pores or inclusions are similar, the effect of pores and inclusions on the grain growth may however be different. The pores that are empty or contain soluble gases may be reduced in size or eliminated. Secondly, the pores can migrate with the boundary by diffusion of matrix around the pore surface, while the inclusions of similar size are less mobile.[13] The inclusions, therefore, impede the grain growth much more severely than the pores do. The Zener's approach to a limiting grain size assumes that the inclusions which inhibit grain growth are homogeneously distributed. On the other hand, if the dispersion of inclusions is not homogeneous, a local region without inclusions can grow to a sufficient size to become a discontinuous grain growth nucleus. To do this it only needs to acquire a sufficient number of sides (more than six) so that the boundaries it forms are concave. In such a case discontinuous grain growth occurs. Thus, small amounts of additions which remain as dispersed phase (in a solid or liquid form) will result in discontinuous grain growth if their distribution is not homogeneous.

2) Where the energy ratio is high, the second phase will exist as plates or films on the grain boundaries. In addition to the effect on the driving force for growth arising from change in the boundary energy, the film will alter the kinetics for growth since migration now requires diffusion of atoms from the shrinking grain through the boundary phase to the growing grain. This reduction in mobility of the boundary then has a similar effect to the solid solution situation in suppressing abnormal growth and slowing normal growth.[14]

(ii) Grain Growth in the Presence of Liquid Phase

In contrast to the solid state sintering, the sintering in the presence of a liquid phase has not been studied in details. Kingery's original work,[15] however, can be mentioned who has studied the sintering in the presence of a liquid phase and has divided the process into three stages namely - (i) the rearrangement process, (ii) the solution reprecipitation process, and (iii) the coalescence and grain growth process.

The course of grain growth process is strongly influenced by the presence of a liquid phase. The effect may arise from a number of causes, and it may be either an increase or a decrease in the grain growth rate.

If the liquid phase remains as a dispersed phase in the form of small droplets, the rate of normal grain growth will be inhibited. On the other hand, if the liquid wets the grain boundaries reasonably well and separates all the grains by a liquid film, the rate of grain growth either decreases or increases depending upon the amount and geometrical distribution of the phase and upon the freezing point of the liquid. In general, the presence of a liquid phase has been found to

increase the rate of grain growth only when the liquid has a very low freezing point compared to that of the solid grains.[16] If the system is such that a liquid phase is present at the grain boundaries at a lower temperature, appreciable grain growth can occur by solution and reprecipitation mechanism.

3.4.2. Effect of SiO_2, GeO_2 and SnO_2 on the Microstructure

Having discussed the nature of SiO_2, GeO_2 and SnO_2 in ferrite in chapter II and with the general considerations given above it becomes simple to explain the changes in the microstructure with the addition of these additives.

SiO_2

The various features observed can be explained as below

(i) At low SiO_2 contents, the second phase would be discretely distributed in the ferrite in the form of isolated spheres. At .02 mol%, the concentration of this phase would be too low. Such a situation does not cause abnormal grain growth. However, it enhances the normal grain growth increasing the grain size.

(ii) At a content of .04 mol%, somewhere giant grains with trapped porosity are seen. Here, the second phase may be present heterogeneously such that the Zener's condition gets satisfied for certain regions and some grains acquire more sides than six and start growing at the expense of neighbouring small grains, where grain boundary movement is impeded.

(iii) At a further higher SiO_2 content (.08 mol%), the volume fraction of inclusions would increase so that D_{crit} goes down sufficiently and the Zener's condition is satisfied at a much earlier stage of sintering. This results in a complete discontinuous grain growth or the cannibal grain growth with almost all the porosity being intragranular reaching the end-point

density. This is clearly shown in Fig.3.4.1 which shows the fractured surface of this specimen. The pore shape (intragranular) suggests that the discontinuous grains have grown without sufficient filling up of the corners (ref. Fig.1.10) leaving almost all the porosity in the grains.

(iv) At a silica content of .16 mol% and above, the second phase present would be sufficient to cover all round the grain boundaries in the initial stage of sintering. This film around the grains would suppress abnormal growth as described under the general considerations. Therefore comparatively smaller grain sizes are observed at .64 and 1.28 mol% contents of silica.

It has also been observed that the presence of silica lowers the sintering temperature of the Mn-Zn ferrite. The grain growth and densification set up at considerably lower temperatures in SiO_2 doped ferrites. Giles and Westendorp[6] observed that samples with 0.16 wt% SiO_2 sintered to a normal density of 4.6 gm cm^{-3} at 1140°C; this is the typical of the density normally achieved with undoped materials fired at 1275°C.

This effect could be attributed to the ability of SiO_2 to form a liquid like phase at sintering temperatures.[17,18] It was concluded by Kono[19] that the acidic oxides or slags like SiO_2 are the more suitable additives for the formation of a homogeneous liquid layer with nearly constant thickness at the grain boundaries during sintering.

This liquid phase may be wetting the grain boundaries reasonably well.[20] Therefore appreciable grain growth can take place at comparatively lower temperatures in SiO_2 doped ferrites than in pure ferrites by a solution and reprecipitation mechanism as discussed under the general considerations.

(a)

(b)

Fig 3·4 Secondary electron Picture of a fractured surface of the Mn-Zn Ferrite with discontinuous grain structure; (a) doped with 0·08 mol. % SiO_2 (b) doped with 1·28 mol % GeO_2. It is a typical intrangular fracture showing clearly the morphology of the intrangular pores.

GeO_2

It has been discussed in chapter II that GeO_2 has a limited solubility in the ferrite. Ge-enrichment at the grain boundaries has also been observed at high GeO_2 contents. From the microstructure results presented in this chapter, it can be seen that the effect of adding GeO_2 to a Mn-Zn ferrite on its microstructure is similar to that of adding SiO_2 to it. However, the corresponding contents are higher in case of GeO_2. These facts lead to the conclusion that GeO_2 is also a second phase additive like SiO_2.

It has also been discussed in chapter II, that GeO_2 might be staying as pure GeO_2 unlike SiO_2 which forms compounds with the neighbouring oxides. GeO_2 has a melting point $\sim 1100^{\circ}C$ and therefore should exist as liquid at sintering temperature. This explains the observation that like SiO_2, GeO_2 also lowers the sintering temperature since appreciable grain growth can take place at much lower temperatures by a solution and reprecipitation mechanism.

For reasons similar to those given for SiO_2, the discontinuous grain growth in GeO_2 doped ferrites suggests the presence of a dispersed phase up to a content of 1.28 mol%. At this content of GeO_2 the coarse grain growth is at its maximum similar to the one seen at a SiO_2 content of .08 mol% (see also Fig.3.4.1).

At a higher content of 3.82 mol%, the reappearance of a regular-grained structure indicates the presence of a second phase layer all around the grains (which has been observed) which suppresses the abnormal growth.

SnO_2

No change in the microstructure has been observed on the additions of SnO_2 in the Mn-Zn ferrite. These results also indicate the solid solubility of SnO_2 in the ferrite as has been shown by the change in the lattice parameter with the addition of this additive.

An impurity in a complete solid solution with the ferrite is not expected to affect the kinetics of grain growth significantly since during sintering the rate of all atom transport processes is controlled by the rate of movement of the slowest moving spices. In ferrites, the diffusion of interstitial cations is known to be much rapid than that of the oxygen ions.[21] The diffusion of large sized oxygen ions in its close packed sublattice should therefore be the rate determining factor during the sintering of ferrites. However, the impurities present in solid solution can give rise to an impurity drag effect[10,11] which arises from any preferred segregation of the impurity.

Discontinuous grain growth has been reported in Ti-substituted slow cooled ferrite (containing 0.05 wt% CaO and .01 wt% SiO_2) and the observed effects have been attributed to the segregation of a $CaO-SiO_2-MnO-TiO_2$ kind of phase at the grain boundaries above 1200°C.[22] These effects in case of SnO_2 additions can only be known if the nature of SnO_2 segregation at the boundaries and complete grain growth kinetics are studied.

REFERENCES

1. G. Chol et al, IEEE Trans. Magnetics, Mag 5, (1969) p.281.
2. C. O'Hora et al., Proc. Brit. Ceram. Soc. 10 (1968) p.245.
3. Max Paulus, IEEE Trans. Magnetics, Mag 11, (1975) p. 1312.
4. G.C. Jain et al., Indian J. of Pure & Appl. Phys. Vol. 14, Feb. 1976, p.87.
5. R.L. Fullman, Trans. AIME, 197, 447, p.1267 (1953).
6. A.D. Giles and F.F. Westendorp, Journal de Physique, ICF-2, Colloque C-1, 1977, p.C1-317.
7. J.W. Christian, The Theory of Transformation in Metals and alloys, Pergamon Press (1965).
8. R.W. Cahn, Physical Metallurgy, North Holland Publishing Co., New York (1970).
9. D.McLean, Grain Boundaries in Metals, Clavendan Press Oxford (1957).
10. R.W. Cahn, Acta Met. 10, 789 (1962).
11. R.J. Brook, Treatise on Material Science & Technology, Vol.9, p.331 (1976).
12. C.S. Smith, Trans, AIME, 175, 15 (1948).
13. J.R. Mac Ewan et al, Proc. Brit. Ceram. Soc., No.7, 245 (1967).
14. D.W. Budworth, Mineral Mag. 37, 833 (1970).
15. W.D. Kingery, J. Appl. Phys. 30, 301 (1959).
16. J.E. Burke, in Kinetics of High Temperature Processes, Ed.W.D. Kingery, John Wiley & Sons, New York, p.109(1959).
17. C. Kosy, Sci. Ceram. 1, 21, 1961.
18. F.M.A. Carpay and A.L. Stuijts, Sci. Ceram. 8, p.23, 1975.

19. H. Kono, Ferrites : Proc. Intermat. Conf. July 1970, Japan, p.137.

20. T.G.W. Stijntjes et al, Ferrites : Proc.Internat. Conf. July 1970, Japan, p.194.

21. A.L. Stjijts, in Ceramic Microstructures, Chap. 19, John Wiley, New York, p.443 (1968).

22. P.E.C. Franken, Intermag Conf., Italy, 1978.

CHAPTER - IV

EFFECT OF SiO_2, GeO_2 AND SnO_2 ADDITIONS ON THE INITIAL PERMEABILITY AND RESISTIVITY OF THE Mn-Zn FERRITE

4.1. INTRODUCTION

The initial permeability, μ_i, is probably the most important parameter to characterize ferrites for technical applications. The effect of the three additives SiO_2, GeO_2 and SnO_2 on the initial permeability (at 1 KHz) has been studied and discussed in this chapter. As explained in chapter I, the μ_i is strongly dependent on the microstructure. The results of chapter III, where the microstructures are discussed would be used to interpret the data presented in this chapter.

Apart from the magnitude of μ_i, it is its variation with temperature and time which is also very important from the stability point of view. These effects have also been studied.

The D.C. bulk resistivity is another important parameter of ferrites because it determines the eddy current losses. Useful information may be obtained by studying the resistivity variation with the amounts of impurities doped.

4.2. EXPERIMENTAL METHODS

4.2.1. Saturation Magnetization and Density

The initial magnetization curves were plotted using the D.C. ballistic galvanometer method.[1] The B-H curve was converted into the M-H curve and an estimate of M_s was made from the graph within an accuracy of $\pm$ 10%.

The density of the sintered toroids of various batches,

after lapping, cleaning and drying them was measured by water immersion method.[2]

4.2.2. The Initial Permeability

30 turns of 30 SWG enameled copper wire were wound on the sintered toroid of average dimensions : OD=14mm, ID=9mm, h=2mm and their inductance (L) was measured on a Marconi 0.1% LCR bridge at a flux density of less than 5×10^{-4} Wb/m^2 and at a frequency of 1 KHz. The initial permeability was computed as

$$\mu_i = L/L_o \qquad (4.1)$$

where

$L_o = 4.6 \times N^2 \times \log \frac{OD}{ID} \times h \times 10^{-9}$ henry, is the air core inductance.

N = number of turns

OD, ID, h = outer diameter, inner diameter, thickness of the toroid respectively.

μ_i-T Curves

The entire μ_i-T curves from $-30^{\circ}C$ to the Curie temperature were plotted for various samples. The inductance of the sample was measured at intervals of $2\text{-}5^{\circ}C$. In the neighbourhood of the secondary maximum peak, observations were taken very carefully at very close intervals of temperature.

Disaccommodation

The disaccommodation was measured using the A.C. demagnetization procedure.[3] The A.C. field method consists of subjecting the material to a saturating alternating field for a few periods and then the amplitude is reduced progressively from just above the knee of the B-H loop to zero. Care was taken not to apply excessive voltage to avoid heating of

the specimen.

Percentage disaccommodation (DA) was calculated as

$$DA = \frac{\mu i_{90} - \mu i_{300}}{\mu i_{90}} \times 100\ \% \qquad (4.2)$$

where

μi_{90} = μ_i at 90 secs after demagnetization and

μi_{300} = μ_i at 300 secs after demagnetization.

Number of observations were taken on one sample in order to check the reproducibility. The normalized disaccommodation or the disaccommodation factor (D.F) is expressed as

$$D.F = \frac{DA}{\mu_i} = \frac{\mu i_{90} - \mu i_{300}}{\mu i_{90}^2} \times 10^6 \qquad (4.3)$$

The temperature throughout the disaccommodation measurements was kept at 25 ± 1°C. The μ_i's were measured on Siemens Universal Bridge.

4.2.3. D.C. Bulk Resistivity

The toroids were coated on their two faces with thin film of Indium amalgam which gave the ohmic contacts.[4] The D.C. resistance R was measured with the help of a bridge at an applied voltage of 0.1 volts and the resistivity ρ was calculated as

$$\rho = \frac{R\ (OD^2 - ID^2)}{4 \times \text{thickness}} \qquad (4.4)$$

The resistivity was measured in the temperature range of 0°C to 150°C.

4.3 EXPERIMENTAL RESULTS

4.3.1. Saturation Magnetization and Density

The saturation magnetization and density for various additions of SiO_2, GeO_2 and SnO_2 are shown in Fig.4.3.1(a,b,c)

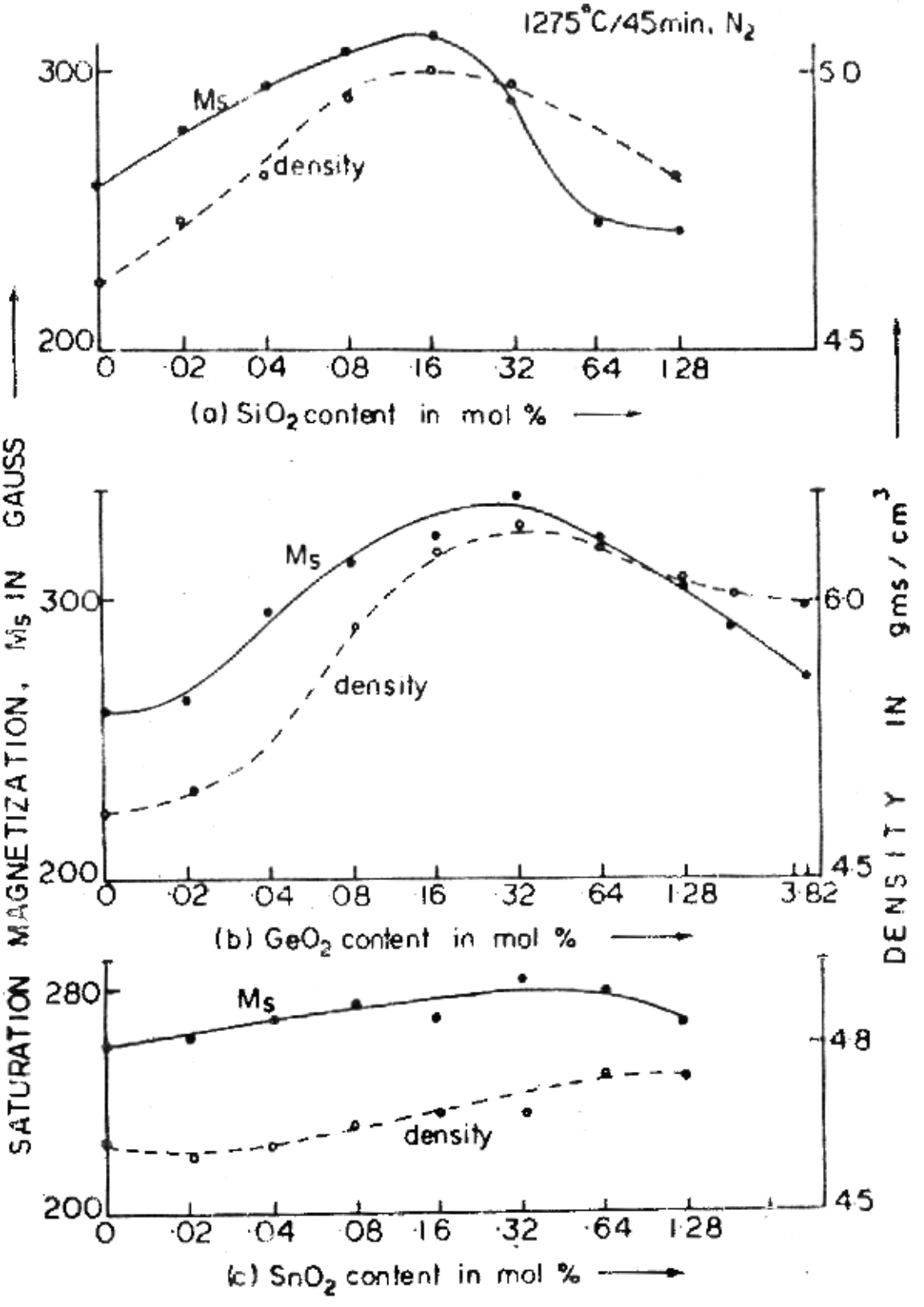
1275°C/45min, N2
300
200
Ms
density
5·0
4·5
0 ·02 ·04 ·08 ·16 ·32 ·64 1·28
(a) SiO2 content in mol %
Ms
density
300
200
6·0
4·5
0 ·02 ·04 ·08 ·16 ·32 ·64 1·28 3·82
(b) GeO2 content in mol %
280
200
Ms
density
4·8
4·5
0 ·02 ·04 ·08 ·16 ·32 ·64 1·28
(c) SnO2 content in mol %
SATURATION MAGNETIZATION, Ms IN GAUSS
DENSITY IN gms/cm3

Fig 4·3·1

for the sintering schedule of 1275°C for 45 min in nitrogen and cooling in nitrogen. In all cases M_s varies with impurity content in a fashion similar to the density variations.

SiO_2

M_s and density increase with SiO_2 content up to a level of 0.16 mol% SiO_2 after which they show a fall. Density for SiO_2 doped samples is always found to be higher than that for the undoped sample in the range of silica content studied. M_s for .64 and 1.28 mol% SiO_2 falls even below the basic value for undoped ferrite.

GeO_2

Similar variation of M_s and density with various GeO_2 contents is obtained but here the peak is obtained at around .32 mol% GeO_2. GeO_2 additions also yield higher values of density as against that for undoped samples.

SnO_2

Unlike the above two cases, the SnO_2 additions have not been found to affect M_s and density appreciably.

4.3.2. The Initial Permeability

For the 'standard' firing

For the sake of comparision, the μ_i for all the three impurities against the mol% of the impurity doped have been plotted on the same graph (Fig.4.3.2).

The variations in μ_i with various additions of SiO_2 and GeO_2 are found to be similar and can be divided into three regions as shown in the figure. Initially the μ_i increases up to a content of .04 mol% in case of SiO_2 and .64 mol% in case of GeO_2 (region I). After the peak there is a sudden drop beyond which the μ_i remains almost constant up to .32

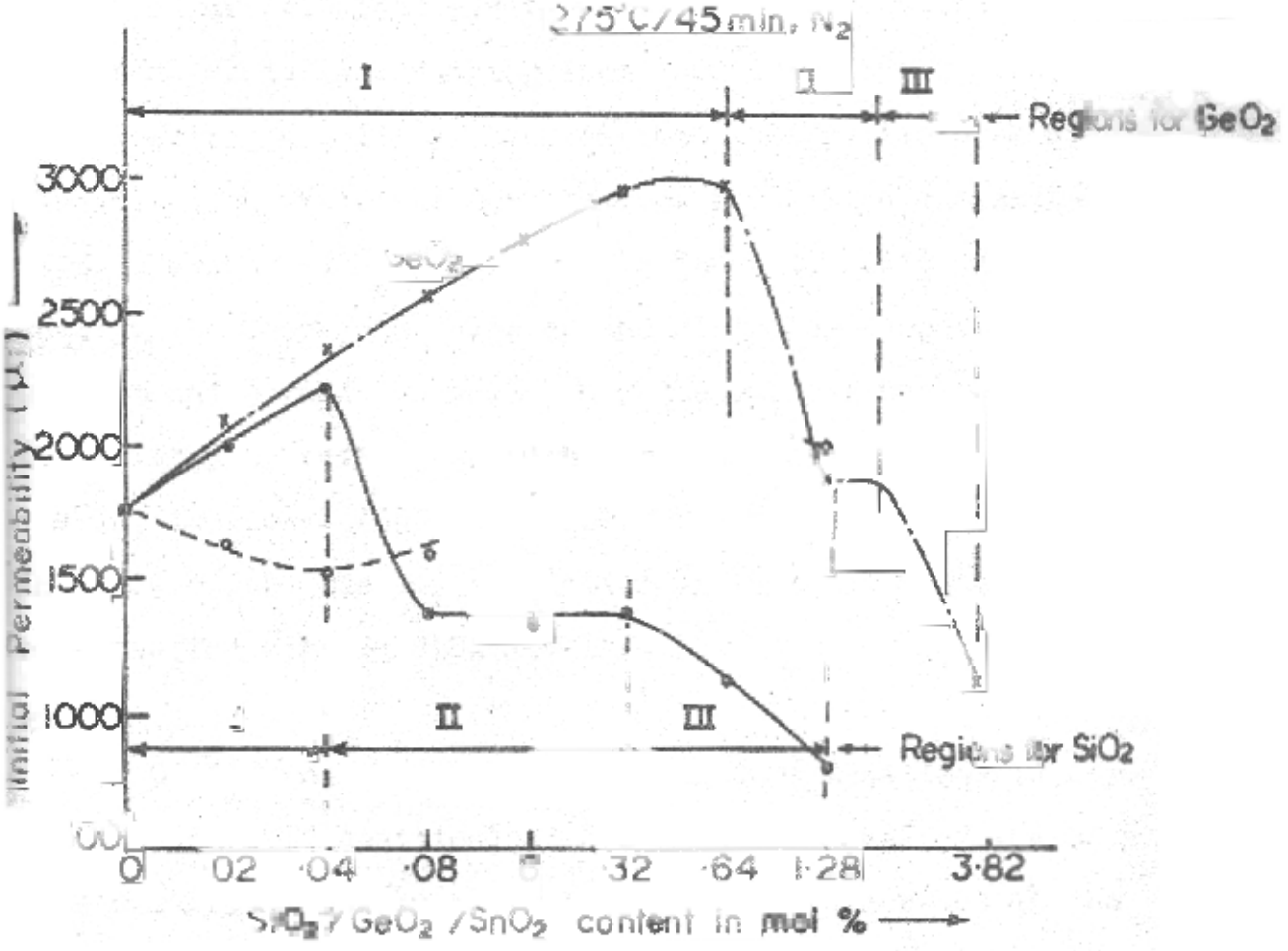
275°C/45 min, N2
I
II
III
Regions for GeO2
Regions for SiO2
3000
2500
2000
1500
1000
Initial Permeability (μi)
0
02
·04
·08
32
·64
1·28
3·82
SiO2 / GeO2 / SnO2 content in mol %

Fig. 4.3.2

mol% in case of SiO_2 and 1.92 mol% in case of GeO_2 (region II). Further additions of both SiO_2 and GeO_2 give much lower values of permeability (region III). On the whole, the GeO_2 additions give higher μ_i.

SnO_2 additions, on the contrary do not show any significant change in the μ_i (variations are within $\pm$ 10%).

For various firings

SiO_2

Figure 4.3.3(a) gives μ_i against SiO_2 contents for different sinterings ranging from 1200°C to 1350°C each for 45 min in nitrogen. It is observed that the μ_i improves significantly with sintering temperatures for silica contents $\leq$ 0.08 mol%. However, the peak in μ_i is found to shift more and more towards the lower SiO_2 side as the sintering temperature goes up. At and beyond .08 mol% SiO_2, the μ_i can not be enhanced appreciably by raising the sintering temperature. At 1350°C the μ_i is always found to be decreasing with SiO_2 contents. In Fig.4.3.3(b) the μ_i is plotted against the sintering temperatures for various SiO_2 levels.

GeO_2

Similar curves are plotted for GeO_2 additions in Fig. 4.3.4(a and b). Additions of GeO_2 up to a level of .64 mol% give remarkable improvement in the μ_i with increase in the sintering temperatures. It is noticed that the behaviour shown in these graphs is similar to the one observed in case of SiO_2 although here at 1350°C the μ_i still increases with impurity content. GeO_2 contents of 1.28 mol% and above seem to freeze the value of μ_i irrespective of the sintering temperature.

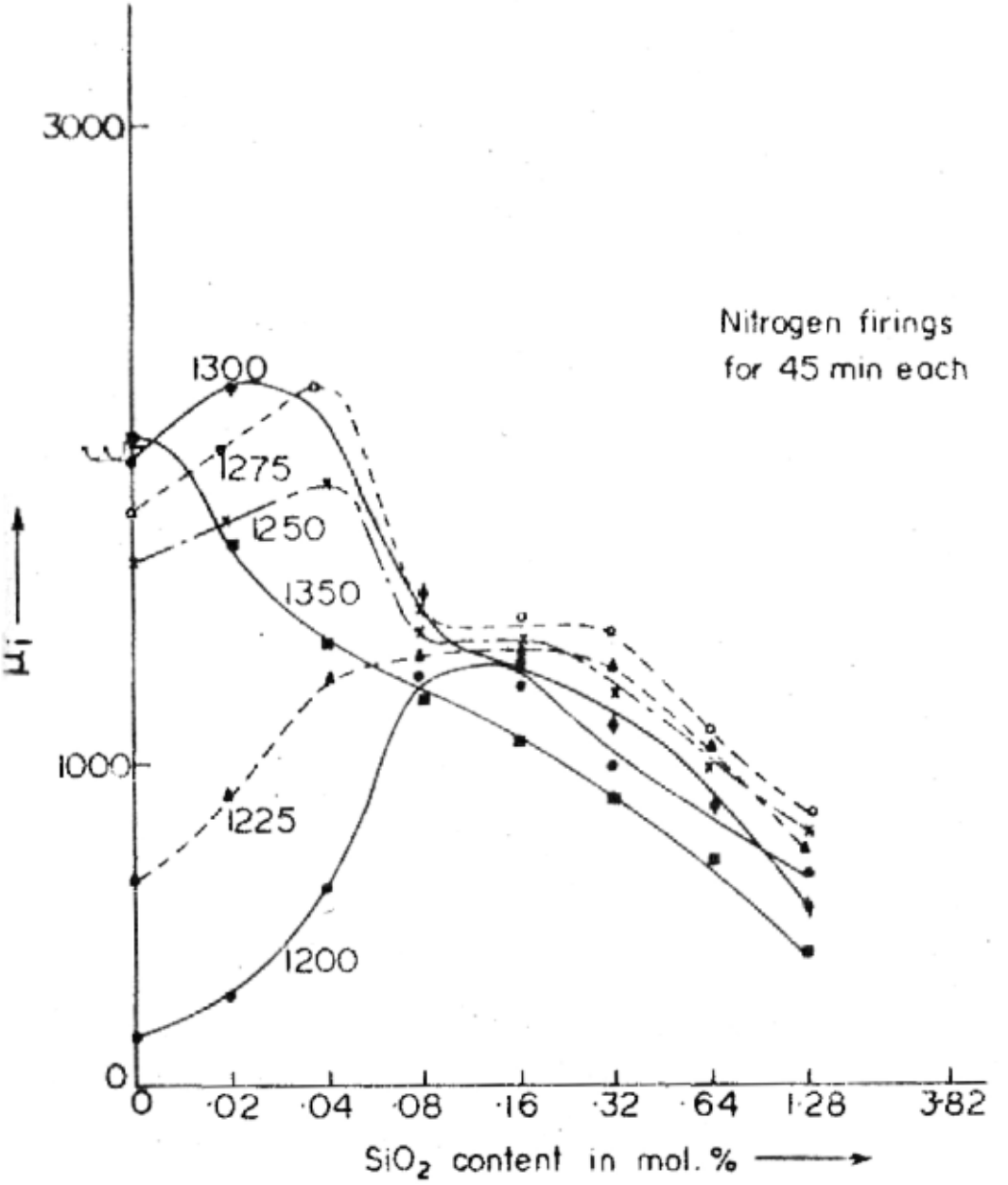
3000
1000
0
μi
Nitrogen firings
for 45 min each
1300
1275
1250
1350
1225
1200
0
·02
·04
·08
·16
·32
·64
1·28
3·82
SiO2 content in mol. %

Fig. 4·3·3(a)

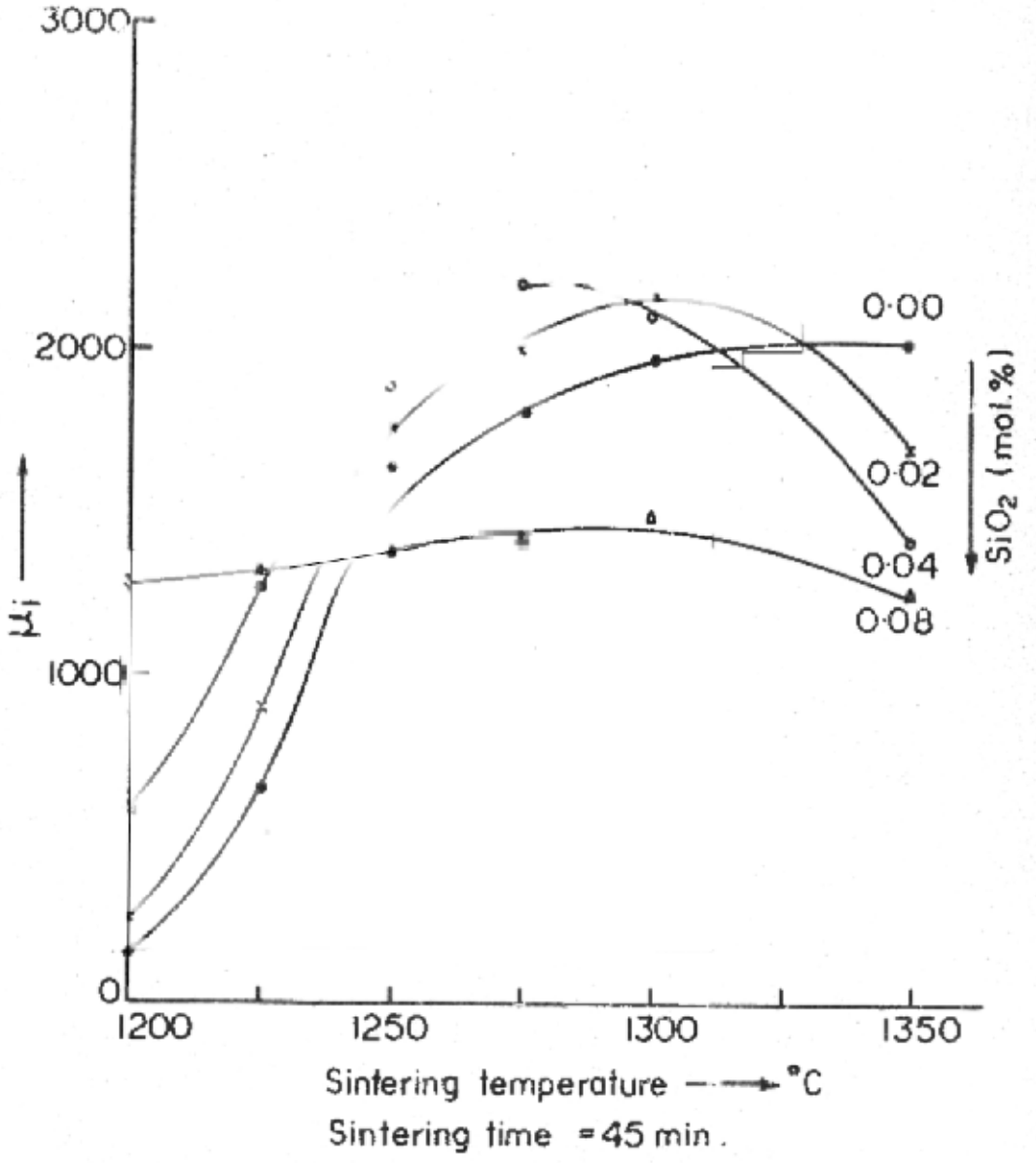
3000
2000
1000
0
μi
0·00
0·02
0·04
0·08
SiO2 (mol.%)
1200
1250
1300
1350
Sintering temperature → °C
Sintering time = 45 min.

Fig. 4·3·3 (b)

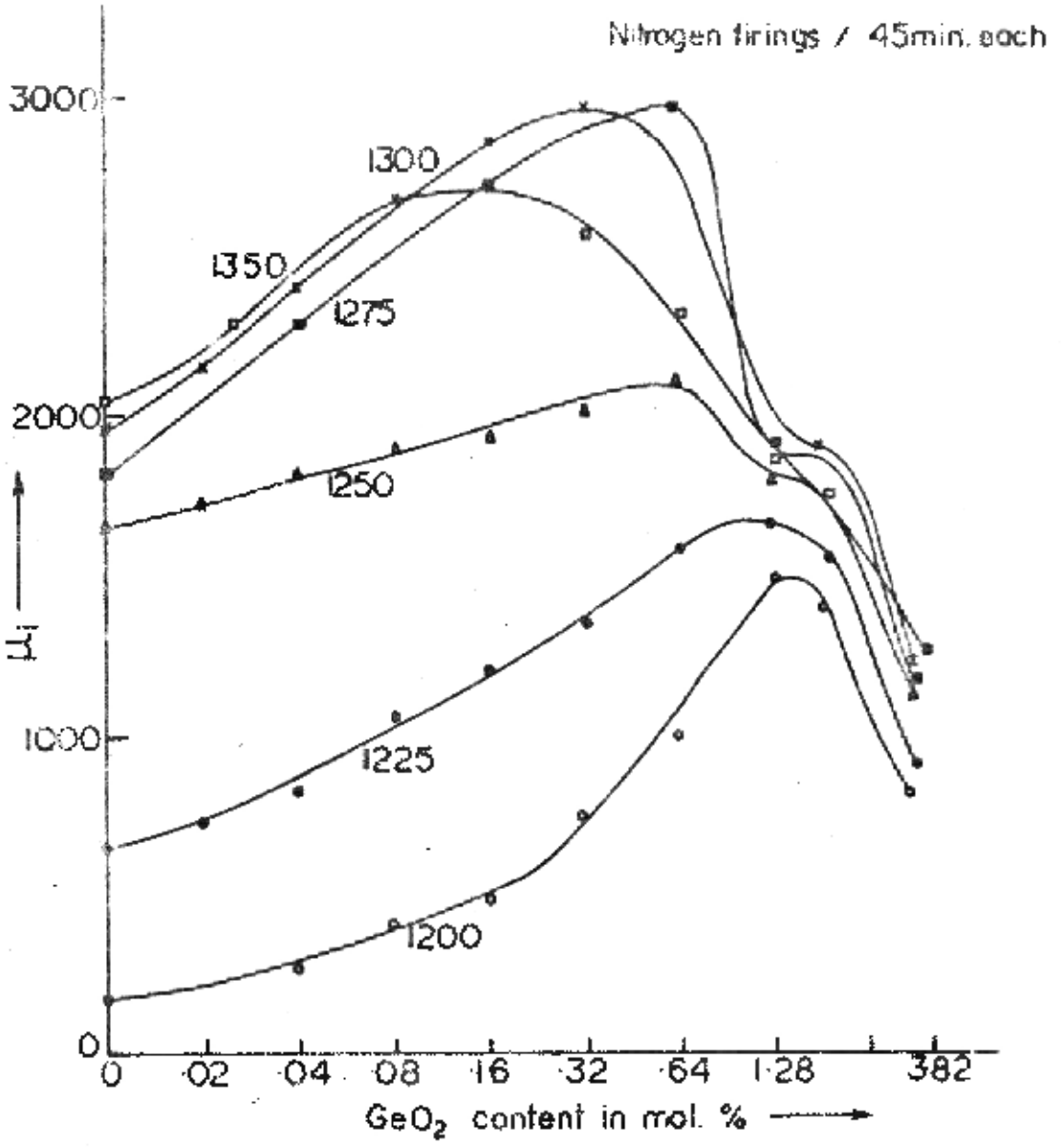
Nitrogen firings / 45min. each
3000
2000
1000
0
μ_i
1300
1350
1275
1250
1225
1200
0
·02
·04
·08
·16
·32
·64
1·28
3·82
GeO_2 content in mol. %

Fig. 4·3·4 (a)

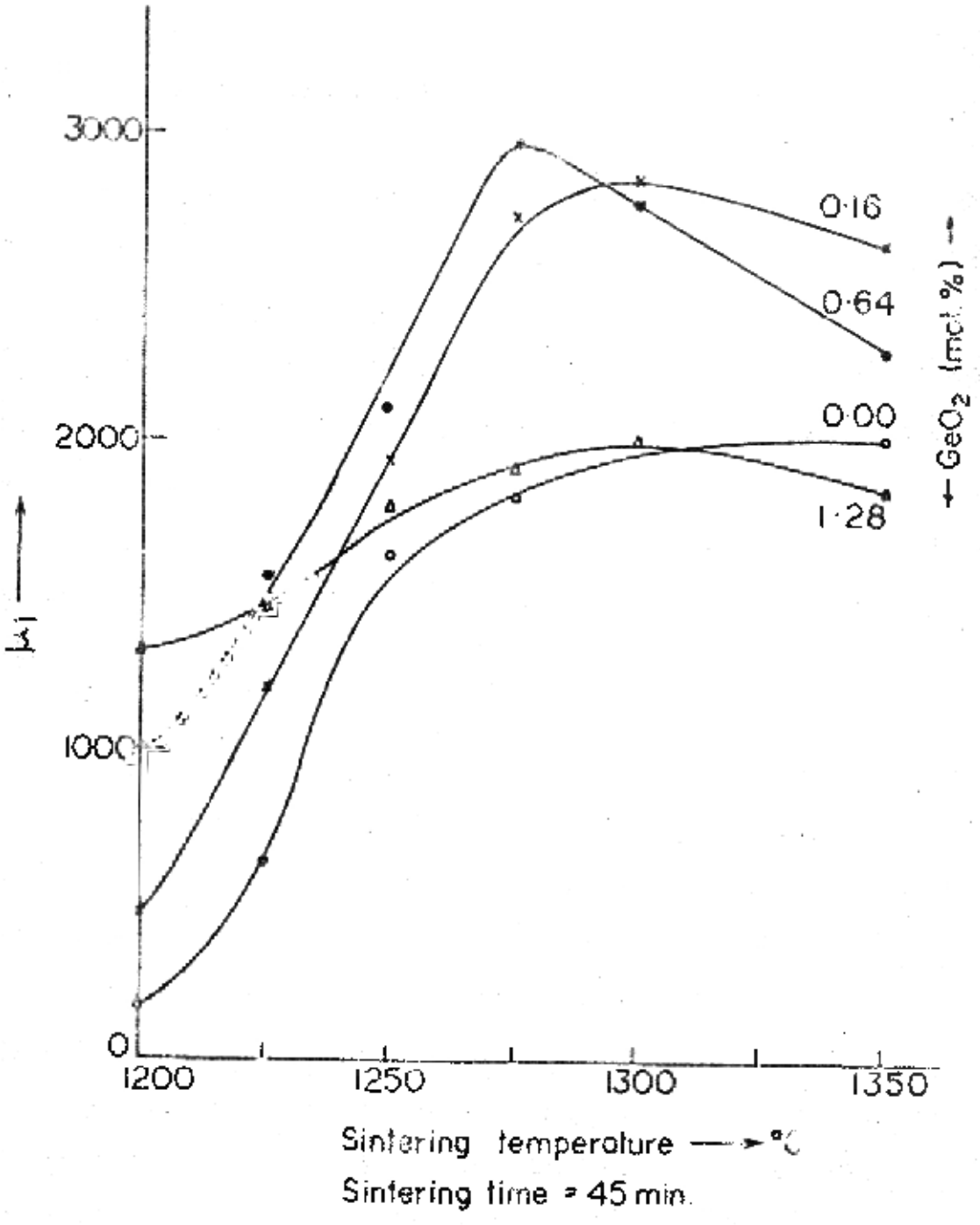
3000
2000
1000
0
μi
0·16
0·64
0·00
1·28
+ GeO2 (mol %) +
1200
1250
1300
1350
Sintering temperature → °C
Sintering time = 45 min.

Fig. 4·3·4(b)

Figure 4.3.5 gives μ_i for all the three additives for an oxygen firing of 1320°C for one hour in oxygen, then 3 hours of equiliberisation at 1320°C in nitrogen containing 1% oxygen and then cooling in pure nitrogen. Samples fired under this sintering schedule were analysed for μ_i-T, disaccommodation and resistivity.

4.3.3. μ_i-Temperature Curves

SiO_2 (Fig.4.3.6)

The basic composition shows the secondary maximum peak (SMP) occuring at 50°C and the Curie temperature close to 165°C. No change in the position of SMP is observed with the doping of SiO_2. The SMP is found to be more pronounced for a silica content of .08 mol%, the content which gives lot of discontinuous grain growth.

At higher SiO_2 contents (0.64 and 1.28 mol%) the curves obtained are quite flat with a gradual fall to zero μ_i at the Curie point.

GeO_2 (Fig.4.3.7)

Slight shift in the SMP towards the lower temperature side is observed as the GeO_2 content goes up. SMP becomes more pronounced for 1.28 mol% GeO_2 - the sample which shows extreme discontinuous grain growth. At 3.82 mol% GeO_2, quite flat μ_i-T curve is obtained with a broader primary peak.

SnO_2 (Fig.4.3.8)

The SMP is found to be shifting more and more towards the lower temperature side as the SnO_2 content increases. 1.28 mol% SnO_2 shows a shift of as much as 30°C in the SMP from the basic ferrite. The primary peak is found to be broadening with SnO_2 additions.

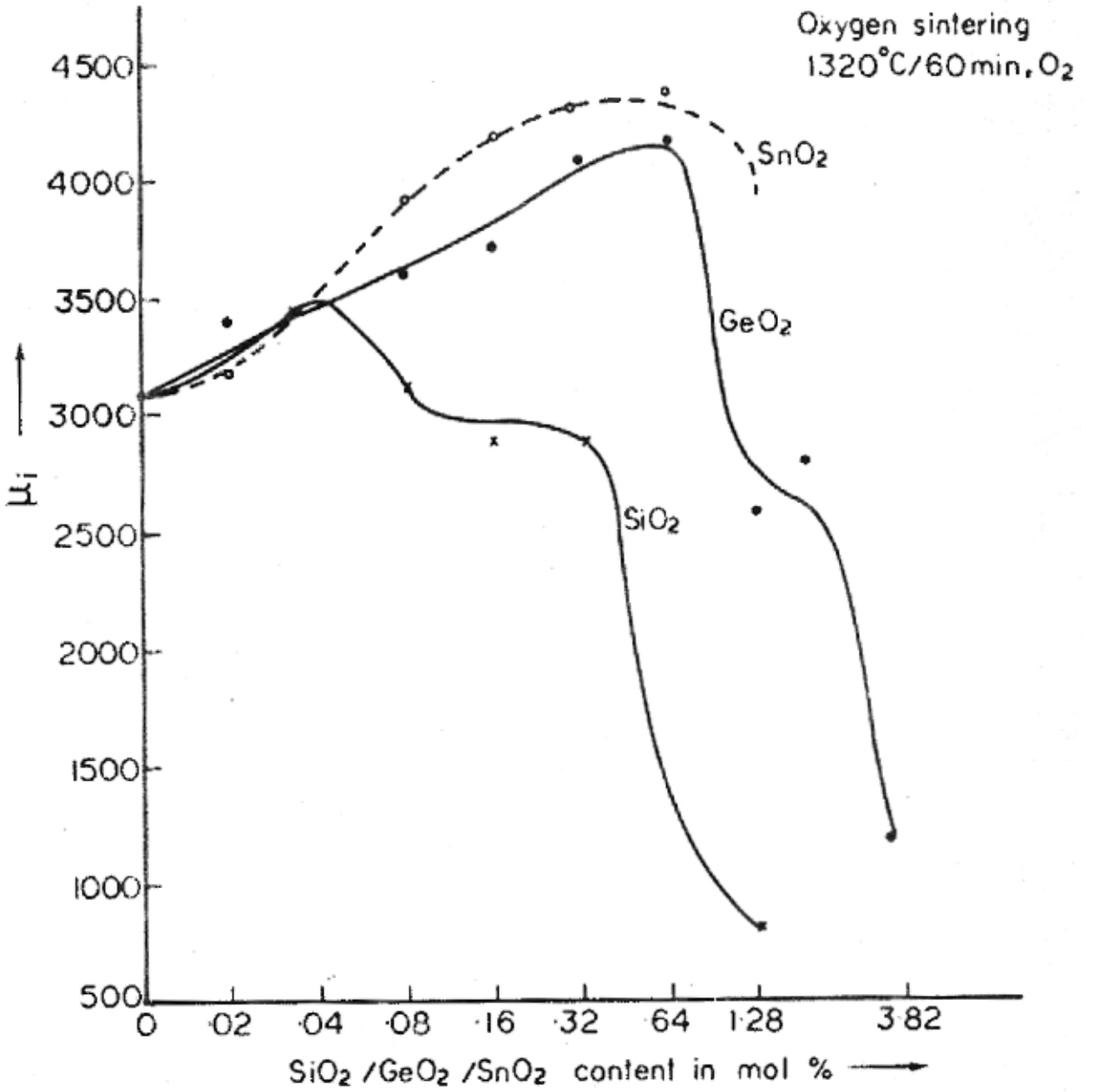
Oxygen sintering
1320°C/60min, O2
SnO2
GeO2
SiO2
μi
4500
4000
3500
3000
2500
2000
1500
1000
500
0
·02
·04
·08
·16
·32
·64
1·28
3·82
SiO2 /GeO2 /SnO2 content in mol %

Fig. 4·3·5

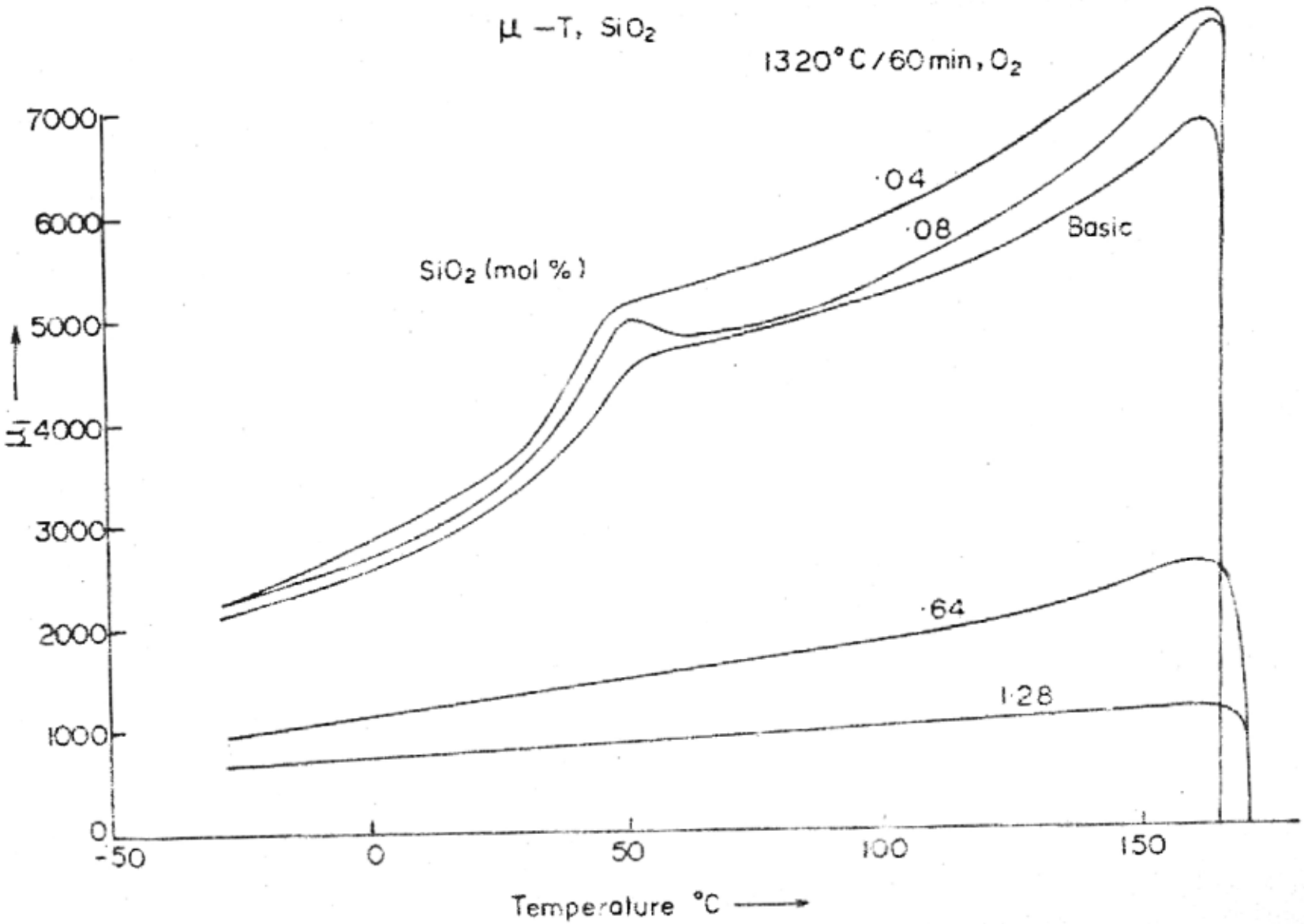
μ –T, SiO2
1320°C/60min, O2
7000
6000
5000
4000
3000
2000
1000
0
μ
SiO2 (mol %)
·04
·08
Basic
·64
1·28
-50
0
50
100
150
Temperature °C

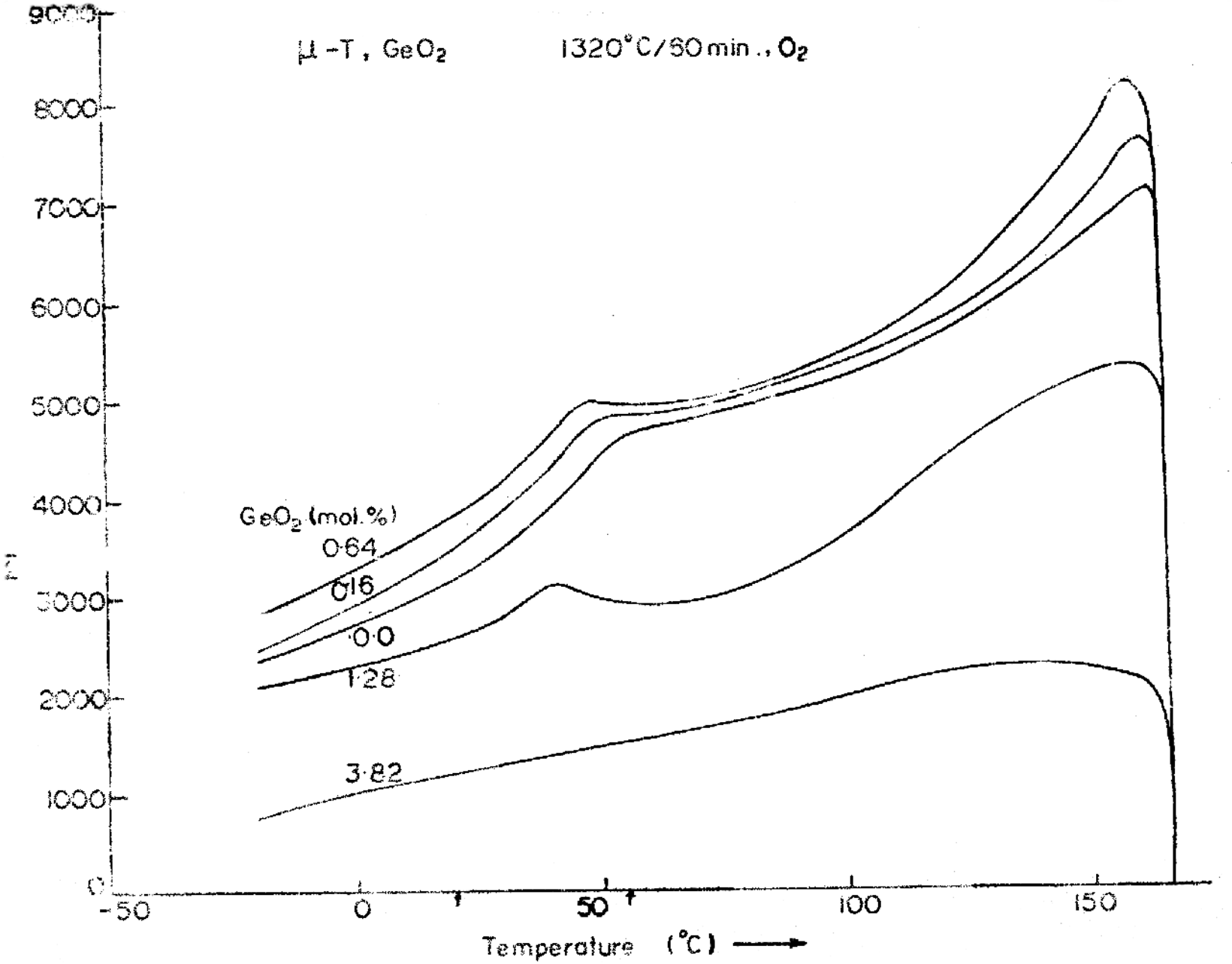
μ -T , GeO2
1320°C/60 min., O2
9000
8000
7000
6000
5000
4000
3000
2000
1000
0
μ
GeO2 (mol.%)
0·64
0·16
0·0
1·28
3·82
-50
0
50
100
150
Temperature (°C) ⟶

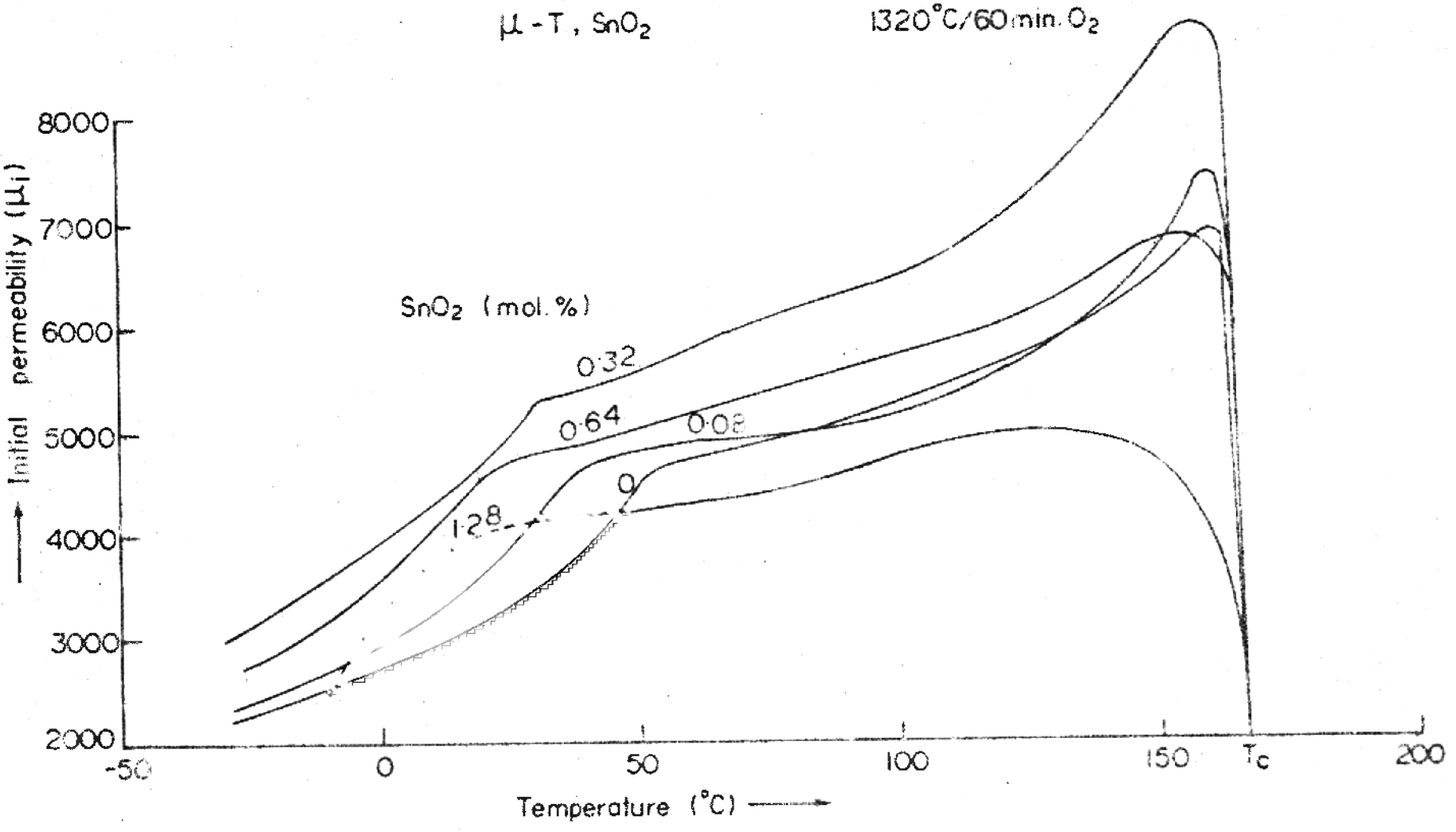
μ - T, SnO2
1320°C/60 min. O2
Initial permeability (μi)
8000
7000
6000
5000
4000
3000
2000
SnO2 (mol. %)
0·32
0·64
0·08
0
1·28
-50
0
50
100
150
Tc
200
Temperature (°C)

Fig. 4.3.8

Temperature Factor (T.F)

The temperature factors defined as $\frac{\mu_{i55} - \mu_{i20}}{\mu_{i20}^2 \Delta T} \times 10^6$ were computed from these curves for all samples. Figure 4.3.9(a) shows the variation in T.F for various additions of different additives. For SiO_2, it remains essentially constant up to 0.32 mol% SiO_2 and then rises sharply. Similarly, for GeO_2, it shows a dip at 1.28 mol% GeO_2 and then a sudden increase. With the addition of SnO_2, the T.F has always been found to decrease up to a doping level of 1.28 mol% SnO_2.

These temperature factors have been computed over a large temperature range (35°C). For a better idea of μ_i fluctuations with temperature, the T.F computed over close intervals of temperature (10°C) have been shown in Fig.4.3.9(b). It is observed that at the normal operating temperatures (10-50°C), maximum benefit in T.F is obtained with SnO_2 additions.

4.3.4. Disaccommodation

All the three additives are found to decrease the percentage disaccommodation in the initial permeability (Fig.4.3.10(a)). For SiO_2, it decreases slightly up to a content of .08 mol% and then remains almost constant. For GeO_2 it decreases to a further lower value and then tends to become constant. Increasing additions of SnO_2 keep on lowering the disaccommodation. An addition of 1.28 mol% SnO_2 lowers the DA to about one fourth of the basic value.

To characterise a magnetic material for its stability, it is the parameter called the disaccommodation factor D.F ($=DA/\mu_i$) which is important and is plotted in Fig.4.3.10(b). The large increase in D.F at highest SiO_2 and GeO_2 contents is due to low values of μ_i there. For SnO_2 D.F is found to be always decreasing.

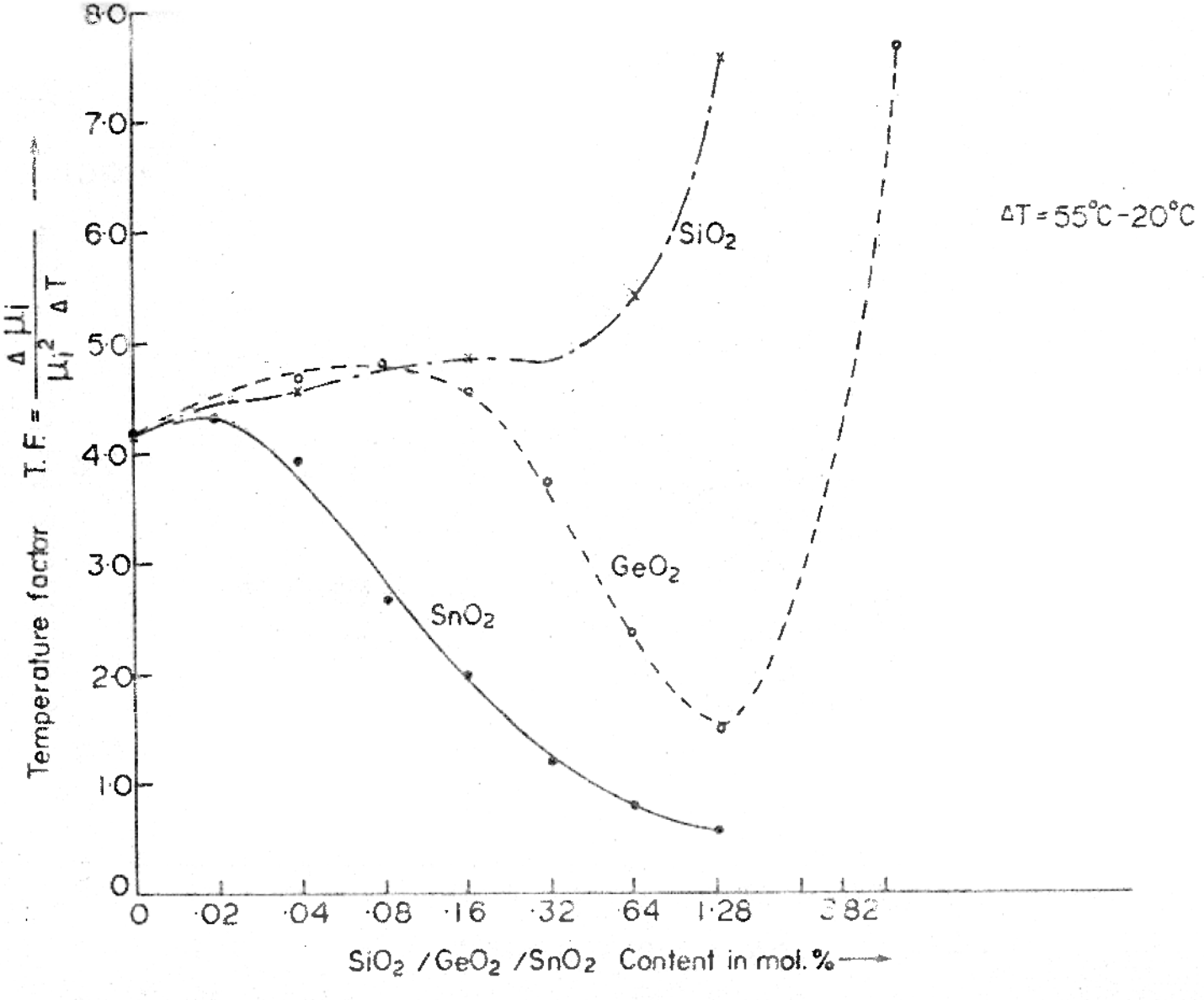
8·0
7·0
6·0
5·0
4·0
3·0
2·0
1·0
0
Temperature factor T. F. = $\frac{\Delta \mu_i}{\mu_i^2 \Delta T}$
SiO2
GeO2
SnO2
ΔT = 55°C - 20°C
0
·02
·04
·08
·16
·32
·64
1·28
3·82
SiO2 / GeO2 / SnO2 Content in mol. %

Fig. 4·3·9 (a)

T. F. vs. temperature interval for various impurity dopings.

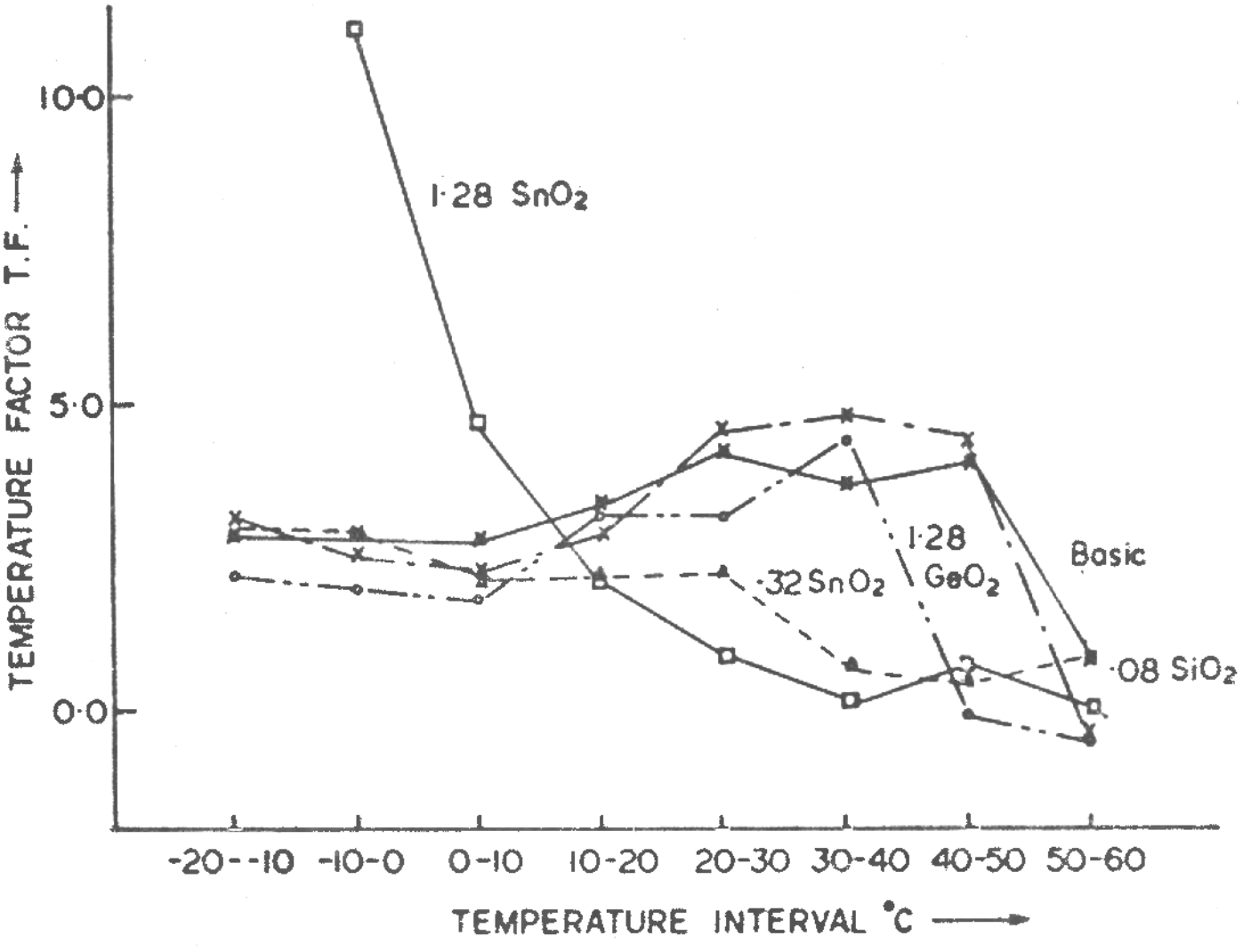

Fig. 4·3·9 (b)

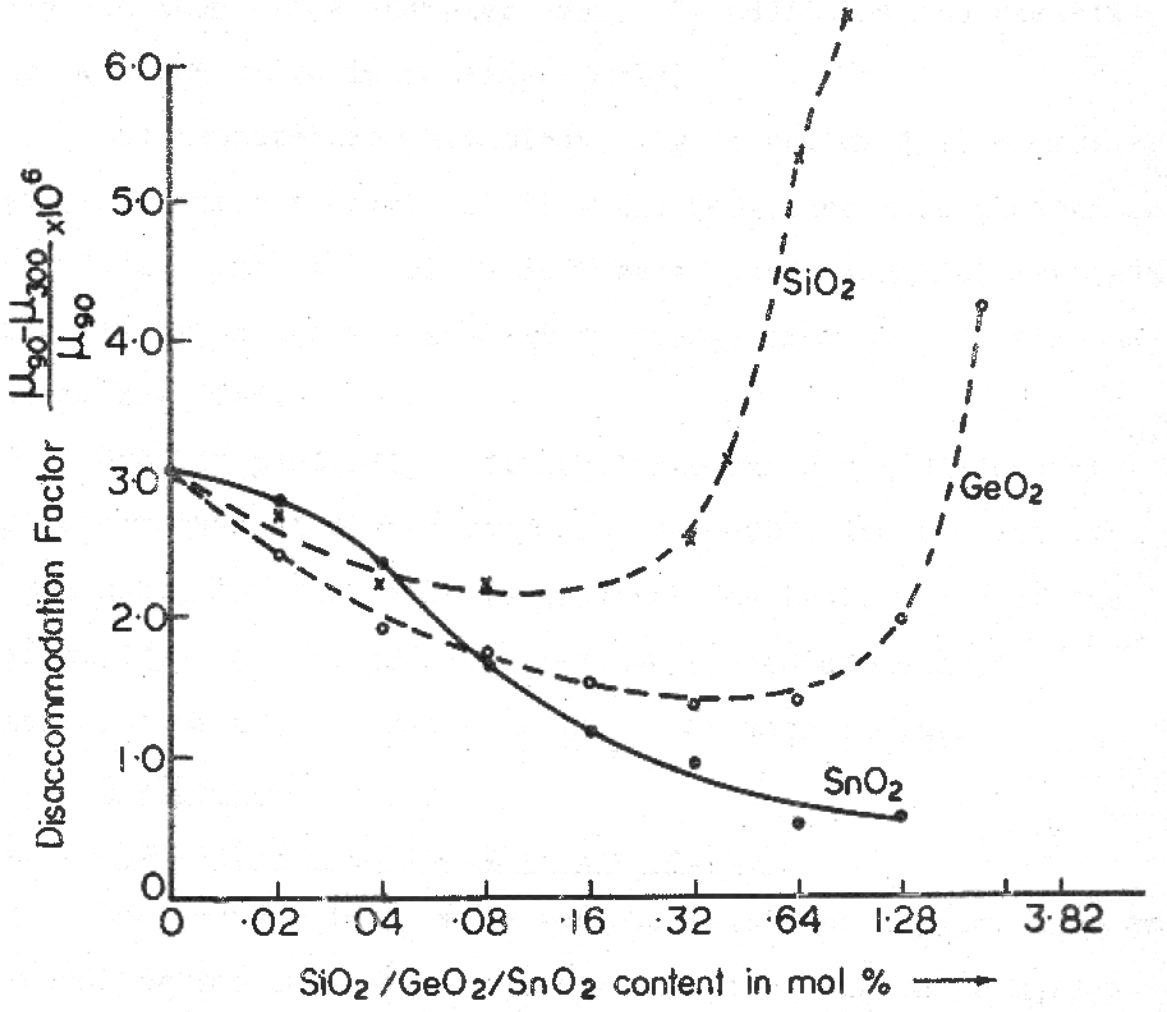
Disaccommodation Factor $\frac{\mu_{90}-\mu_{300}}{\mu_{90}} \times 10^6$
6·0
5·0
4·0
3·0
2·0
1·0
0
SiO2
GeO2
SnO2
0
·02
04
·08
·16
·32
·64
1·28
3·82
SiO2 /GeO2/SnO2 content in mol % ⟶

Fig. 4·3·10 (b)

4.3.5. D.C. Bulk Resistivity and its Temperature Variation

Figure 4.3.11(a and b) show the resistivity for various impurity levels for the 'standard' and 'oxygen' firing respectively. For both SiO_2 and GeO_2, the resistivity decreases first going to a minimum at .08 mol% SiO_2 and 1.28 mol% GeO_2 respectively and then rises sharply. For SnO_2 additions the resistivity is found to be increasing slowly.

The temperature variations (log ρ versus 1/T) of resistivity for various levels of SiO_2 and GeO_2 have been plotted in Fig.4.3.12. Arrhenius plots of ρ gave almost parallel straight lines giving an average activation energy of $\simeq$ 0.10 eV for the process involved.

Similar plot (Fig.4.3.12(b)) for various additions of SnO_2 shows that at higher temperatures $\sim 100^{\circ}C$ the resistivity of the doped ferrite tends to approach the basic value of the resistivity. At low temperatures the curves are almost parallel with the same average value of the activation energy.

4.4. DISCUSSIONS

4.4.1. Saturation Magnetisation and Density

The changes in M_s with various levels of doping, more or less follow the changes in density such that the ratio M_s/density remains essentially constant. The quantity $\sigma = M_s$/density (gauss cm^3/g) called the saturation magnetization per gram is a compositional dependent material property. σ is an intrinsic quantity of the material which is not the case with measured M_s in porous substances.[5]

The increase in measured M_s is therefore due to the increase in density. Up to a content of 0.16 mol% SiO_2, density increases. It has been shown in chapter II that the presence of

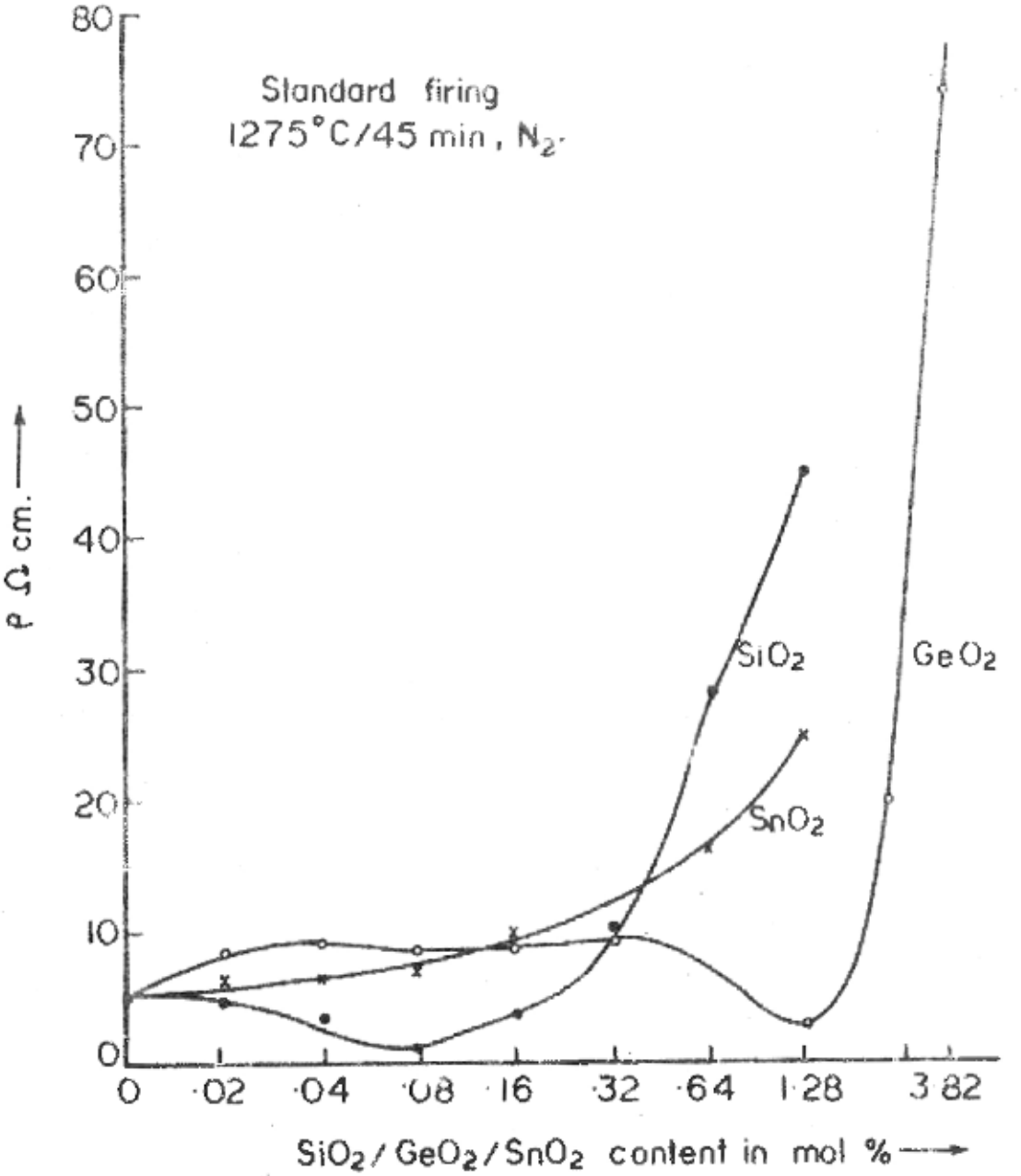
Standard firing
1275°C/45 min, N2
ρ Ω cm.
80
70
60
50
40
30
20
10
0
SiO2
GeO2
SnO2
0
·02
·04
·08
·16
·32
·64
1·28
3·82
SiO2 / GeO2 / SnO2 content in mol %

Fig. 4·3·11 (a)

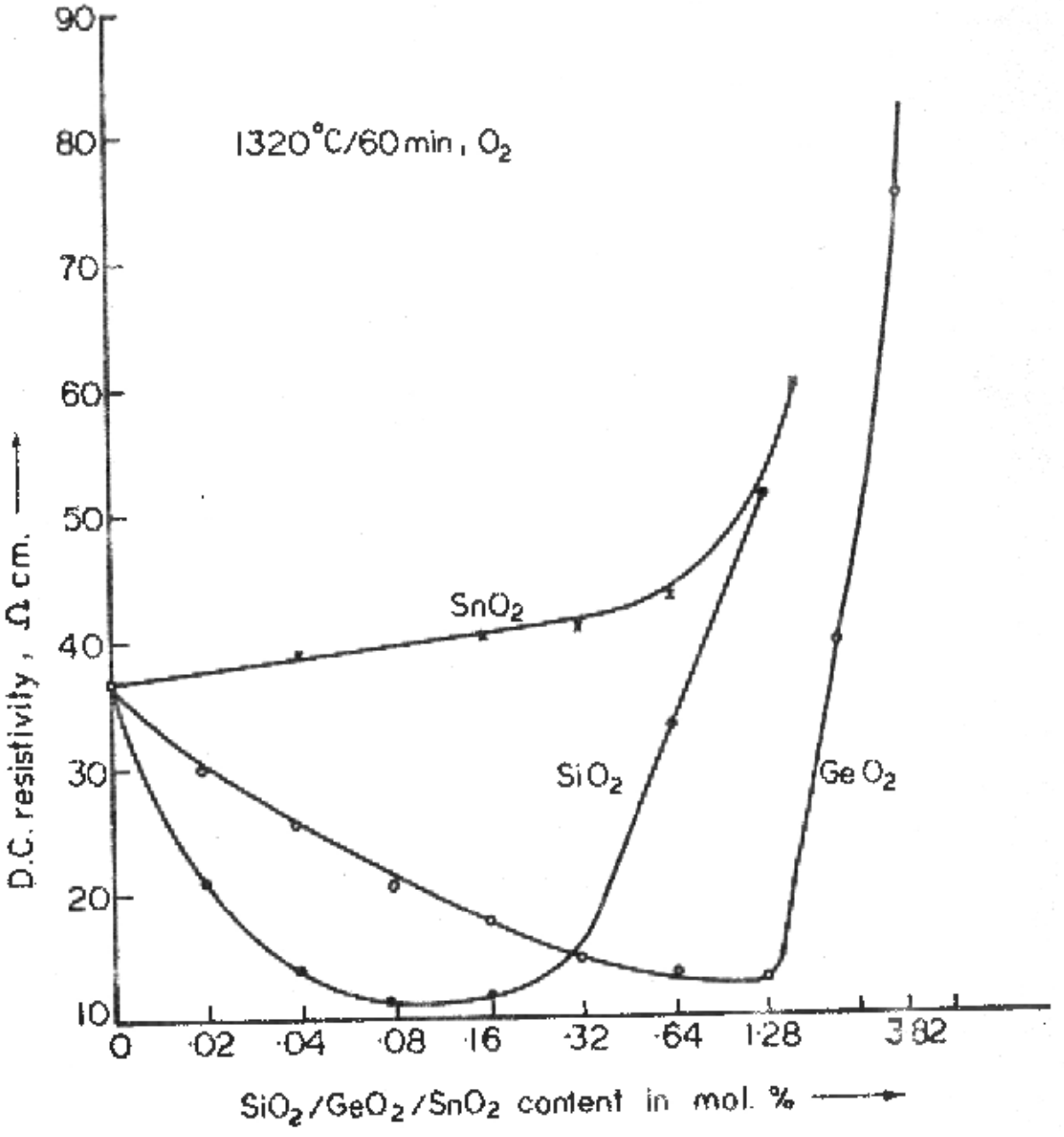
1320°C/60 min, O2
SnO2
SiO2
GeO2
D.C. resistivity, Ω cm.
SiO2/GeO2/SnO2 content in mol. %
90
80
70
60
50
40
30
20
10
0
·02
·04
·08
·16
·32
·64
1·28
3·82

Fig. 4·3·11 (b)

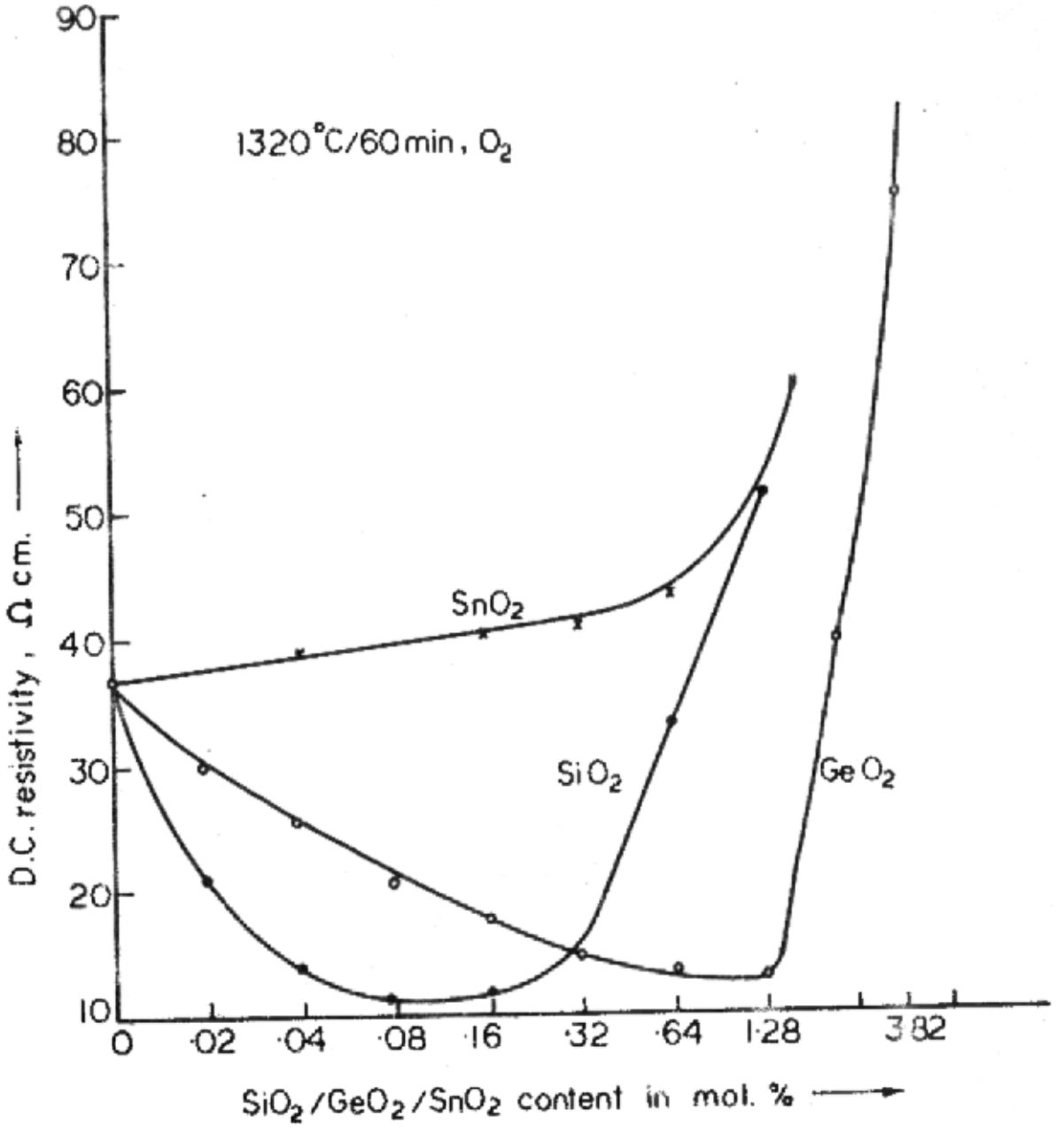
1320°C/60 min, O2
SnO2
SiO2
GeO2
D.C. resistivity, Ω cm.
90
80
70
60
50
40
30
20
10
0
·02
·04
·08
·16
·32
·64
1·28
3·82
SiO2/GeO2/SnO2 content in mol. %

Fig. 4·3·11 (b)

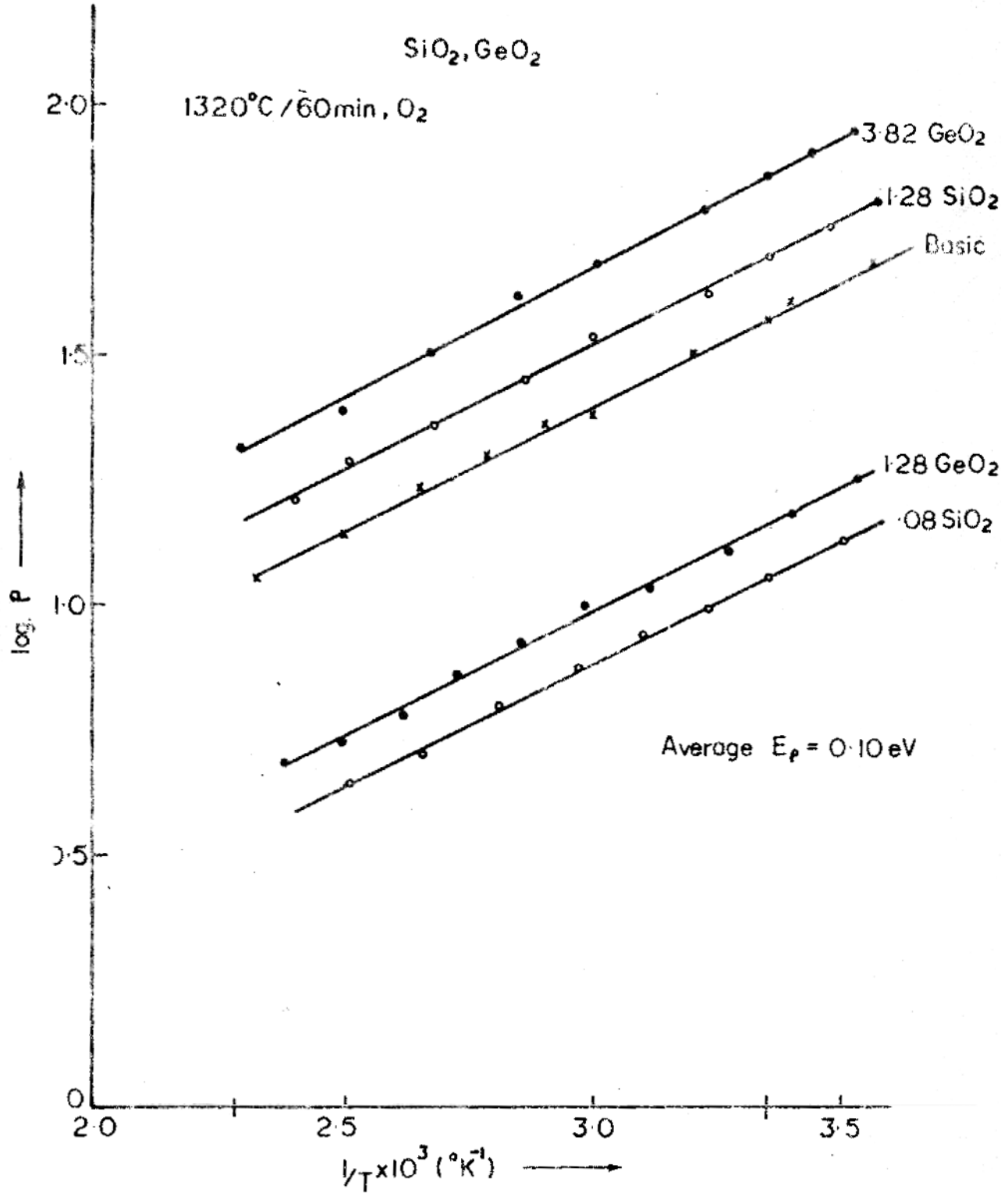
SiO_2, GeO_2
1320°C / 60min, O_2
3·82 GeO_2
1·28 SiO_2
Basic
1·28 GeO_2
·08 SiO_2
Average E_ρ = 0·10 eV
log. ρ
2·0
1·5
1·0
0·5
0
2·0
2·5
3·0
3·5
$1/T \times 10^3$ (°K^{-1})

Fig. 4·3·12 (a)

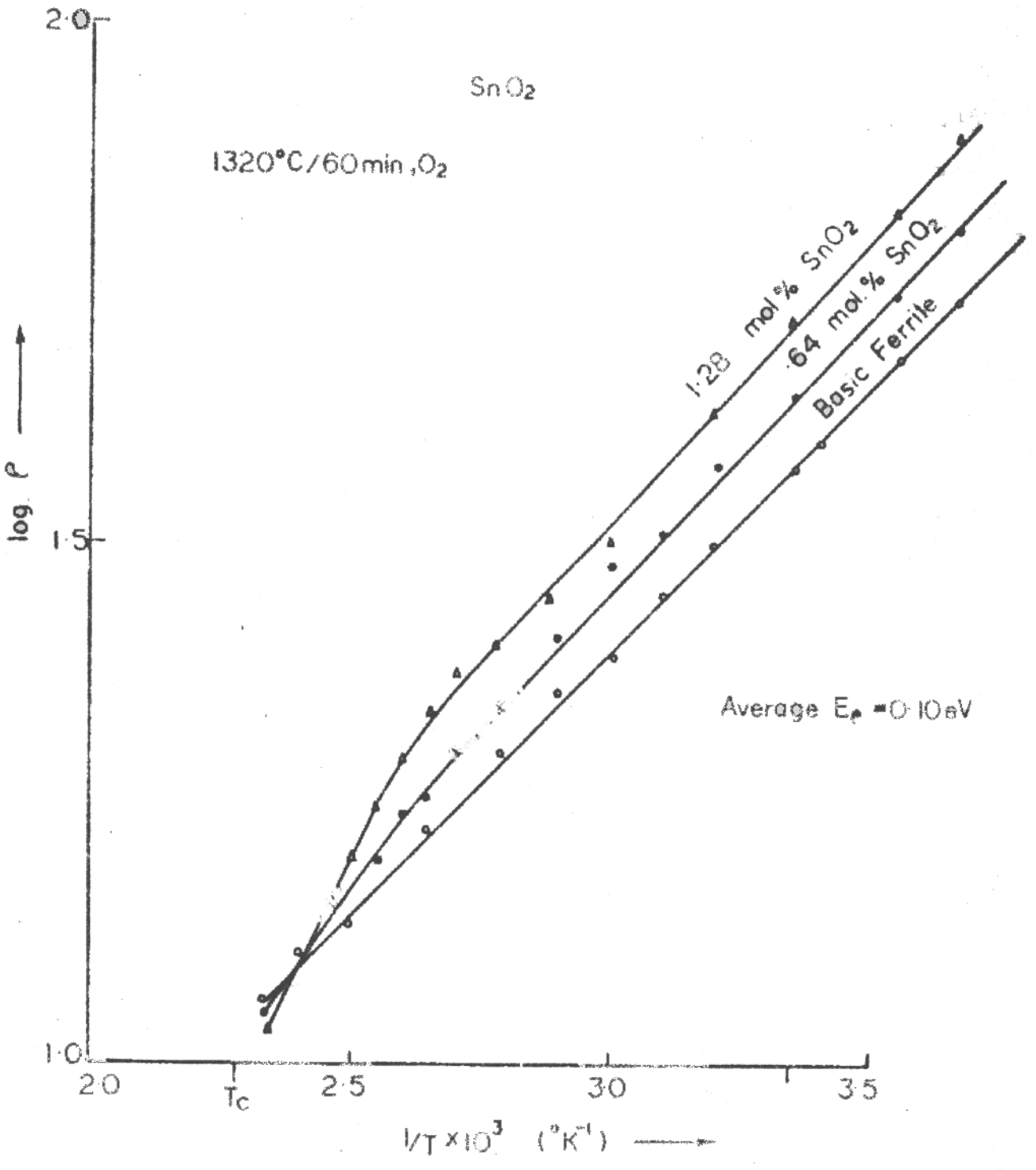
2·0
1·5
1·0
log. ρ
SnO2
1320°C/60min, O2
1·28 mol% SnO2
·64 mol.% SnO2
Basic Ferrite
Average Ea = 0·10eV
2·0
Tc
2·5
3·0
3·5
1/T ×10³ (°K⁻¹)

Fig.4·3·12 (b)

silica impurity lowers the sintering temperature i.e. the ferrite with higher content of silica sinters faster than the pure ferrite. This has also been observed by Giles and Westendorp.[6] They have shown that for the same sintering product higher densities are achieved in silica doped ferrites as against in the undoped one.

Density is found to be decreasing beyond a content of 0.16 mol% SiO_2. This corresponds to the region where the grain structure tends to get back to somewhat normal. The grain growth in this region is restricted as compared to that in intermediate levels. This accounts for lower densities obtained in this region.

It may be noticed that at SiO_2 contents of 0.64 and 1.28 mol%, even though the density values are higher than that of the basic, the M_s falls below the basic value. This may be because the non-magnetic second phase around the grains and inclusions etc. do not contribute to magnetisation.

Similar explanation should hold for GeO_2 additions. The change in M_s at higher concentration of SiO_2 is more than the change in M_s for higher concentration of GeO_2. This may be due to a smaller non-magnetic second phase in the case of GeO_2.

4.4.2. The Initial Permeability

SiO_2 and GeO_2

Referring to Fig.4.3.2, the increase in μ_i up to an addition of .04 mol% SiO_2 and .64 mol% GeO_2 (region I) is mainly achieved through the increase in M_s (Fig.4.3.1). The sudden drop at .08 mol% SiO_2 and at 1.28 mol% GeO_2 is due to occurance of discontinuous grain growth, giving giant grains with large number of intragranular pores.

The product $M_s.D_p$ is plotted against various additions of SiO_2 and GeO_2 in Fig.4.4.1. It is self-explanatory that up to 0.32 mol% SiO_2 and 1.92 mol% GeO_2 levels, the μ_i is determined by the product $(M_s.D_p)$. This is in agreement with earlier established results that in case of ferrites with intragranular porosity, the μ_i is determined by the pore to pore distance, D_p.[7] Beyond these points, the μ_i deteriorates even though the product $M_s.D_p$ does not. At these points (0.64, 1.28 mol% SiO_2, 3.82 mol% GeO_2), the corresponding microstructures suggest the presence of a layer of second phase around the grains and also some precipitates inside the grains (as seen in case of 1.28 mol% SiO_2). This non-magnetic layer around the grains is bound to introduce wall discontinuities across the grain boundaries, resulting in a loss of certain amount permeability.[8] The non-magnetic inclusions inside the grains would hinder the reversible movement of domain walls lowering the μ_i.[9] Since it was not possible to 'see' the inclusions and their size and distribution inside the grains, no quantitative description can be given to their effect.

SnO_2

Additions of SnO_2, on the other hand, have not been found to affect M_s and density significantly and since no change in the microstructure is observed, the μ_i is mainly determined by the anisotropy and its variation with temperature. This could be clearly seen from the μ_i-T curves.

Effect of Sintering Temperatures

Referring to Fig.4.3.3(a), at a sintering temperature of 1200°C, peak in the μ_i is obtained at .08 mol% SiO_2 (and at 1.28 mol% GeO_2). Further increase in the sintering temperature does not improve the μ_i appreciably beyond .08 mol% SiO_2 (and

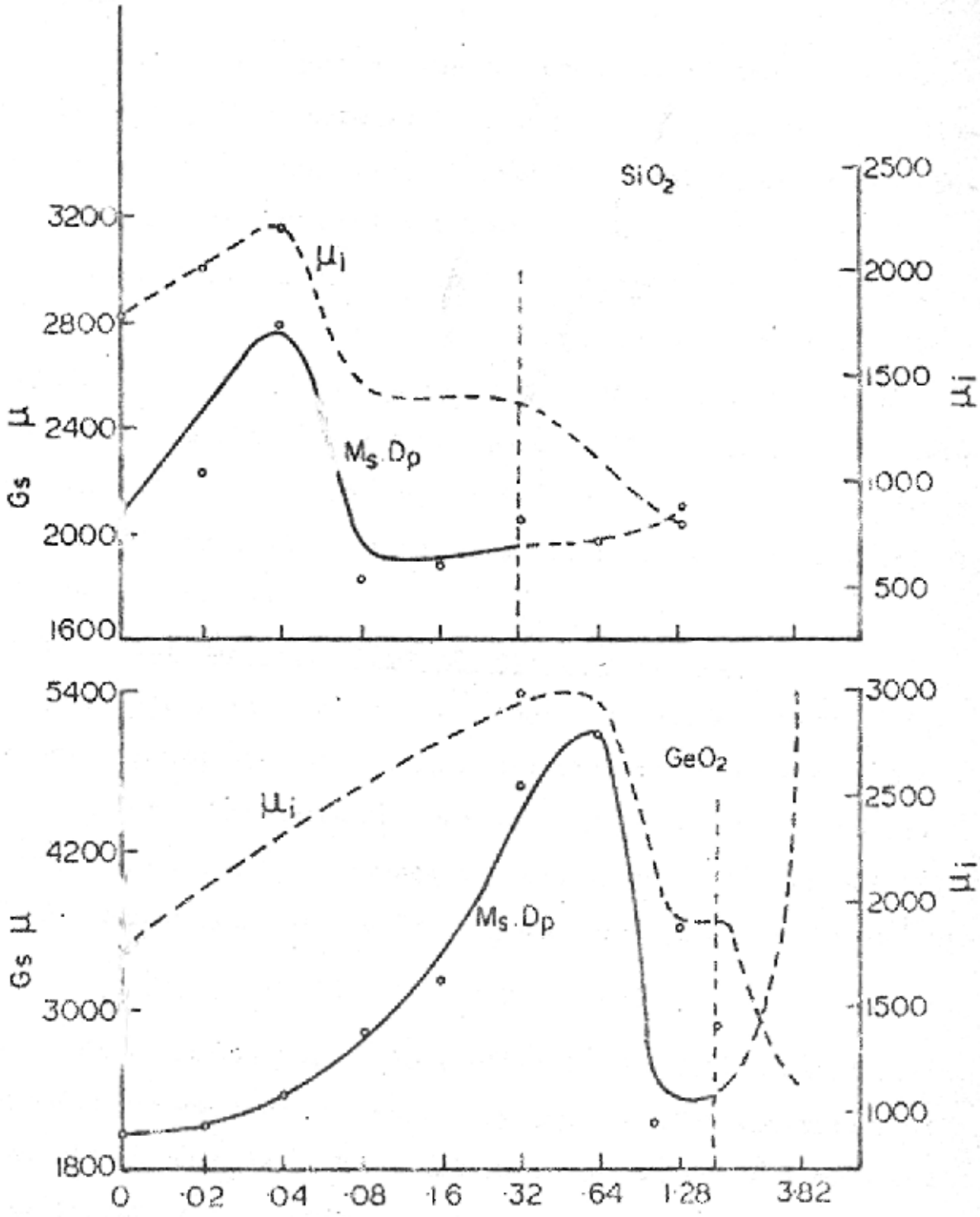
SiO2
μi
Ms. Dp
Gs μ
μi
3200
2800
2400
2000
1600
2500
2000
1500
1000
500
GeO2
μi
Ms. Dp
Gs μ
μi
5400
4200
3000
1800
3000
2500
2000
1500
1000
0
·02
·04
·08
·16
·32
·64
1·28
3·82

Fig. 4·4·1

1.28 mol% GeO_2). This is because at these levels of SiO_2 and GeO_2, cannibal grain growth takes place even at 1200°C leaving almost all the porosity in the grains stopping further densification.

Below these levels, the improvements in the μ_i occur mainly through the increase in the grain size and till the discontinuous grain growth sets in and the final value of the density that can be achieved has been reached.

Some fall in the μ_i at higher temperatures is expected due to the excessive zinc evaporation from the surface of the sample, specifically when sintering is done under nitrogen. This and the higher mobility of pore facilitating their coalescence are the reasons why oxygen sintered samples have a higher permeability than nitrogen sintered samples (see Figs.4.3.3.(b), 4.3.4(b) and 4.3.5)).

4.4.3. Temperature Variation of Initial Permeability

Previous investigations[10] show that the position of the secondary permeability maximum (SMP) depends primarily on the Fe^{2+} content. For manganese contents of $z = 0.52$ to 0.55, an empirical relationship between the calculated Fe^{2+} content (Y) and the temperature of the SMP, T_o has been given by Konig[11] as

$$T_o/T_c \simeq 0.88 - 2.9\ Y \quad \text{for } 0 < Y < 0.2 \qquad (4.5)$$

This relationship also applies if the Fe^{2+} content of the basic composition is changed by intralattice substitutions of different cations. The addition of monovalent and divalent metal oxides to the basic mixture before sintering causes a decrease in the Fe^{2+} content; the addition of trivalent and quadrivalent metal oxides causes an increase of the Fe^{2+} con-

tent.[12] This effect has been used to shift the SMP of iron-rich samples from low temperatures to a predetermined temperature. The idea was to change the anisotropy by means of relatively small amounts of substitutions, without much change in the Curie temperature and saturation magnetization.

$\underline{SiO_2}$

The secondary maximum peak (SMP) is not found to be shifting with silica additions. The SMP becomes more pronounced for .08 mol% SiO_2 where extreme discontinuous grain growth is observed. As has been said earlier, in case of grains having intragranular porosity the domain walls attach themselves to the pores within the crystallities as long as the pore diameter is equal to or larger than the thickness of the domain wall (as the blocking of domain walls at pores is determined by the ratio of pore size to wall thickness.[13]) In the temperature ranges of large anisotropy, the spacing of these pores determines the value of the initial permeability in the same way as the crystallite diameter does in the homogeneous (regular-grained) ferrites. In the range of K_1 zero crossing, the domain walls become very thick, the spacing of the pores with diameters equal to or larger than the domain wall thickness increases and the μ_i increases sharply.[14]

At higher levels of SiO_2 (0.64 and 1.28 mol%) the μ_i-T curves become quite flat and the SMP can not be located. Also the primary peaks are not sharp. Recently Franken[15] observed similar effects for TiO_2 additions in Mn-Zn ferrite. He has attributed the flattening of the μ_i-T curves to the heterogeneities caused by the Ti-concentration gradient across the grain boundaries which he observed using Auger analysis. In the present case also, the Si-rich second phase along the grain

boundaries would be giving rise to concentration (or compositional) gradients across the grain boundaries which has been varified in the present case.

The non-magnetic phase at the grain boundaries would also give rise to wall discontinuities. Globus and Duplex[8] have demonstrated that the degree of wall continuity strongly modifies the thermal spectra of initial permeability for a given composition in Ni-Zn ferrites. Their observations show that the two materials with same values of saturation magnetization, Curie temperature, saturation magnetostriction, porosity, and grain size but one sintered directly from constituent oxides and the other from the milled ferrite powder exhibited remarkably different temperature variation of initial permeability. The former one gave sharper temperature variation of μ_i with a much bigger primary peak whereas the later one gave a slow varying μ_i-T curve with a much shorter primary peak. They have attributed this effect to the fact that the wall continuity is more perfect in the former material than that in the later.

GeO_2

As concluded earlier inchapter II, the solubility of Ge^{4+} ions is more in Mn-Zn ferrite as compared to that of Si^{4+}. The effect of introducing quadrivalent Ge^{4+} ions would result in the increase in ferrous ion content. This would account for the slight shift in the SMP towards the lower temperature side.

At 1.28 mol% GeO_2, a well defined SMP is observed. Similar reasons could be attributed to this effect as those given for 0.08 mol% SiO_2, for, the grain structure is also very discontinuous here. At 3.82 mol% GeO_2, the occurance of flat μ_i-T curve could be interpreted in terms of the existence of Ge-

concentration gradients across the grain boundaries which would also affect the degree of wall continuity.

SnO_2

The substitution of Sn^{4+} ions in the intralattice positions would result in the increase in the Fe^{2+} ion content. This in turn should shift the SMP towards the lower temperature side which is exactly observed in the present case. Apart from this, the shape of the curve is also found to be changing, becoming more and more flat as the SnO_2 content increases. Similar effects have been observed in case of TiO_2 additions.[15]

In the presence of Fe^{2+} ions, Sn^{4+} is known to influence the anisotropy[16] in a similar way as Ti^{4+} does.[14] In fact, the behaviour of Sn^{4+} ions in affecting the properties of Mn-Zn ferrites is quite similar to that of Ti^{4+} ions with some difference which has been attributed to their ionic size difference[16] (Ti^{4+} = .60 Å, Sn^{4+} = .69 Å).

4.4.4. Disaccommodation

As mentioned in chapter I the after effect processes causing disaccommodation in Mn-Zn ferrites involve cation vacancies and ferrous ions. At room temperature, the disaccommodation is mainly caused by the migration of cations. The existence of Fe^{2+} facilitates the diffusionof cations. Cation migration causes an elevation of local potential. The cancellation of this local potential by electron charge displacement from Fe^{2+} to Fe^{3+} is one possible way Fe^{2+} facilitates diffusion. But the interaction between ionic distortion surrounding Fe^{2+} and that surrounding a cation vacancy should be considered as another mechanism. When electron hopping occurs, the change of the ionic distortion of Fe^{2+} would cause a change of the distortion

of a cation vacancy, thus facilitating the diffusion.[17]

It has been shown by a number of workers that the amplitude of this process is proportional to the product of the (small) concentration of ferrous ions and cation vacancies, which suggests that the effect is associated with Fe^{2+} - vacancy pairs.

According to Braginski,[18] there is another process causing disaccommodation, customarily referred to as 'process II' which is associated with the ordering of ferrous ion pairs through the agency of the diffusion of vacancies, which do not themselves contribute to the induced anisotropy. Thus, if the ferrous ion content per formula unit is Y, the amplitude of II is for small Y, proportional to Y^2.

The actual content of Fe^{2+} per formula unit of a typical Mn-Zn ferrite may be 'a', and if a substitution of bM^{4+} (M^{4+} : quadrivalent ion) is made, then since each M^{4+} ion localizes an Fe^{2+} ion, only (a-b) Fe^{2+} are free to participate in process II. The amplitude of II is then reduced by a factor of $(a/b)^2$.

Reported results indicate that all the three impurities SiO_2, GeO_2 and SnO_2 lower the $(DA)_{RT}$ (at room temperature) with reduction in DA being proportional to their respective solubility. Similar results have been reported in case of SiO_2 additions.[19] It has been observed that SiO_2 additions lower the DA at all temperatures in the range $-20^{\circ}C$ to $100^{\circ}C$.[20] The behaviour of GeO_2 as an additive on the disaccommodation of ferrites is expected to be more or less similar to that of SiO_2 as is observed in the present case. In case of SnO_2, however, the results seem to differ with those obtained by Matsubara and others[20] shown in Fig.4.4.2. It is observed from the figure that the DA at room

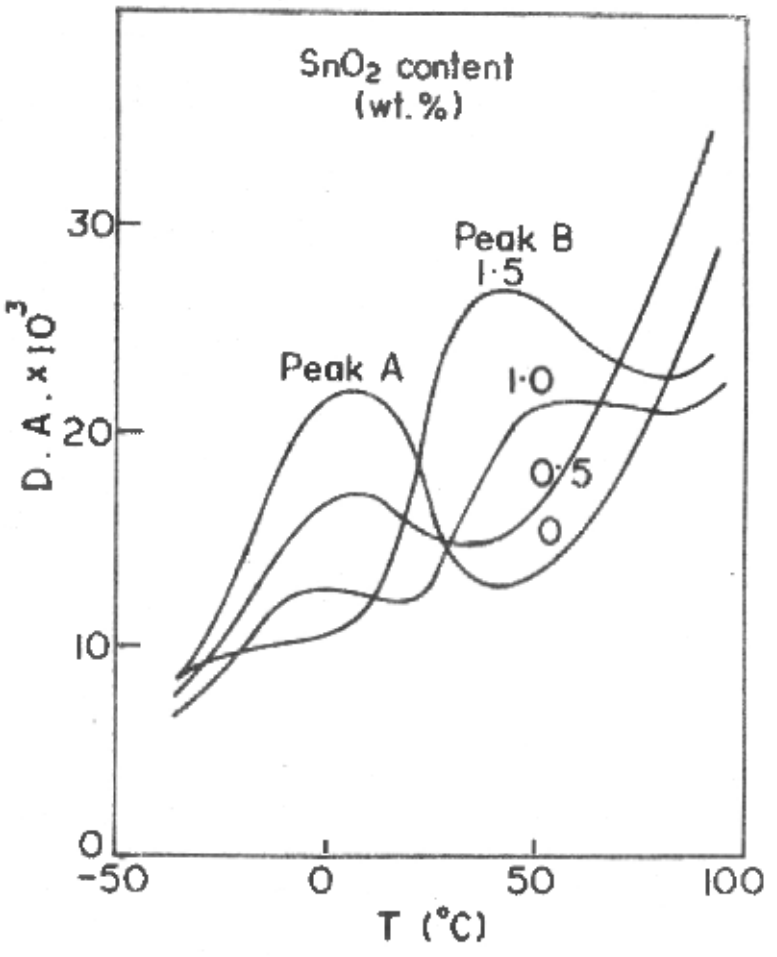

Fig. 4·4·2 Temperature dependecies of disaccomodation of $(Fe_2O_3)_{0.56}$ $(MnO)_{0.39}$ $(ZnO)_{0.05}$ containing various amounts of SnO_2 (Sintered in N_2 containing 0·6 % O_2) [ref. 20]

temperature depends upon the position and height of peak A and peak B. They have discussed that the peak height and the peak temperature are sensitively influenced by the basic composition, the additive components and the sintering conditions. They have observed a constant decrease in DA with increasing SnO_2 additions at $0^{\circ}C$ as is observed in the present case at $25^{\circ}C$ (room temperature). A better explanation of the deviation in results could only be put forward after the processing details of their ferrites are known.

For technical applications it is the D.F ($= DA/\mu_i$), which is an important parameter and is found to decrease significantly with SnO_2 additions.

4.4.5. D.C. Bulk Resistivity and its Temperature Variation SiO_2 and GeO_2

Both SiO_2 and GeO_2 alter the microstructure of the ferrite significantly. The effect of microstructure on the resistivity has already been explained in chapter I. Since solubility of both SiO_2 and GeO_2 is limited, the changes in the resistivity may be attributed to the corresponding changes in the microstructure.

The minimum in the resistivity in both the cases corresponds to a content which gives discontinuous grain structure with largest grain size. Large grain size means less concentration of grain boundaries which are the regions of high resistivity. This accounts for the increase in the conductivity with the grain size.

It has been said that beyond .08 mol% SiO_2 (and 1.28 mol% GeO_2), the grain boundaries start getting richer and richer with the second phase. This formation of a high resistivity layer at the grain boundaries results in the increase in the resistivity beyond these points.

SnO_2

In Mn-Zn-Fe^{II} ferrites the conductivity is proportional to the ferrous ion content. As earlier stated, the substitution of Sn^{4+} ions in the lattice should result in the increased number of ferrous ions. The Sn^{4+} ion also has the property of localizing a Fe^{2+} ion. Therefore the number of ferrous ions contributing to the conductivity decreases whereas all the ferrous ions present contribute to the anisotropy. This explains simultaneously the increase in the resistivity and shift of SMP towards the lower temperature side with SnO_2 additions. Similar effects have been observed with the addition of titanium also.[21-24] Hanke and Zenger[24] studied the resistivity of Mn-Zn ferrites doped with SnO_2 and TiO_2. They observed that the ρ increased very slowly with SnO_2 additions up to about 2.8 mol% while for the same amounts of TiO_2 additions the ρ increased by about 40 fold. They attributed their results to the fact that Ti ions form Ti^{4+} - Fe^{2+} pairs whereas Sn^{4+} ions might be forming pairs with other valencies other than Fe^{2+}.

Knowles[16] has inferred that the pair Sn^{4+} - Fe^{2+} is more weakly bound than the pair Ti^{4+} - Fe^{2+} because of the bigger size of tin ion, therefore at higher temperatures these pairs tend to disassociate and this probably accounts for the faster decrease in the resistivity with temperature for SnO_2 doped ferrites approaching the basic value of the resistivity (Fig. 3.3.12(b)). In the ferrite doped with 1.28 mol% SnO_2, the value of the resistivity tends to fall even below the basic value at temperatures around 145°C indicating higher ferrous content in this ferrite as compared to the basic ferrite. This is also learnt from the μ_i-T curves.

silica impurity lowers the sintering temperature i.e. the ferrite with higher content of silica sinters faster than the pure ferrite. This has also been observed by Giles and Westendorp.[6] They have shown that for the same sintering product higher densities are achieved in silica doped ferrites as against in the undoped one.

Density is found to be decreasing beyond a content of 0.16 mol% SiO_2. This corresponds to the region where the grain structure tends to get back to somewhat normal. The grain growth in this region is restricted as compared to that in intermediate levels. This accounts for lower densities obtained in this region.

It may be noticed that at SiO_2 contents of 0.64 and 1.28 mol%, even though the density values are higher than that of the basic, the M_s falls below the basic value. This may be because the non-magnetic second phase around the grains and inclusions etc. do not contribute to magnetisation.

Similar explanation should hold for GeO_2 additions. The change in M_s at higher concentration of SiO_2 is more than the change in M_s for higher concentration of GeO_2. This may be due to a smaller non-magnetic second phase in the case of GeO_2.

4.4.2. <u>The Initial Permeability</u>

<u>SiO_2 and GeO_2</u>

Referring to Fig.4.3.2, the increase in μ_i up to an addition of .04 mol% SiO_2 and .64 mol% GeO_2 (region I) is mainly achieved through the increase in M_s (Fig.4.3.1). The sudden drop at .08 mol% SiO_2 and at 1.28 mol% GeO_s is due to occurance of discontinuous grain growth, giving giant grains with large number of intragranular pores.

The product $M_s.D_p$ is plotted against various additions of SiO_2 and GeO_2 in Fig.4.4.1. It is self-explanatory that up to 0.32 mol% SiO_2 and 1.92 mol% GeO_2 levels, the μ_i is determined by the product $(M_s.D_p)$. This is in agreement with earlier established results that in case of ferrites with intragranular porosity, the μ_i is determined by the pore to pore distance, D_p.[7] Beyond these points, the μ_i deteriorates even though the product $M_s.D_p$ does not. At these points (0.64, 1.28 mol% SiO_2, 3.82 mol% GeO_2), the corresponding microstructures suggest the presence of a layer of second phase around the grains and also some precipitates inside the grains (as seen in case of 1.28 mol% SiO_2). This non-magnetic layer around the grains is bound to introduce wall discontinuities across the grain boundaries, resulting in a loss of certain amount permeability.[8] The non-magnetic inclusions inside the grains would hinder the reversible movement of domain walls lowering the μ_i.[9] Since it was not possible to 'see' the inclusions and their size and distribution inside the grains, no quantitative description can be given to their effect.

SnO_2

Additions of SnO_2, on the other hand, have not been found to affect M_s and density significantly and since no change in the microstructure is observed, the μ_i is mainly determined by the anisotropy and its variation with temperature. This could be clearly seen from the μ_i-T curves.

Effect of Sintering Temperatures

Referring to Fig.4.3.3(a), at a sintering temperature of 1200°C, peak in the μ_i is obtained at .08 mol% SiO_2 (and at 1.28 mol% GeO_2). Further increase in the sintering temperature does not improve the μ_i appreciably beyond .08 mol% SiO_2 (and

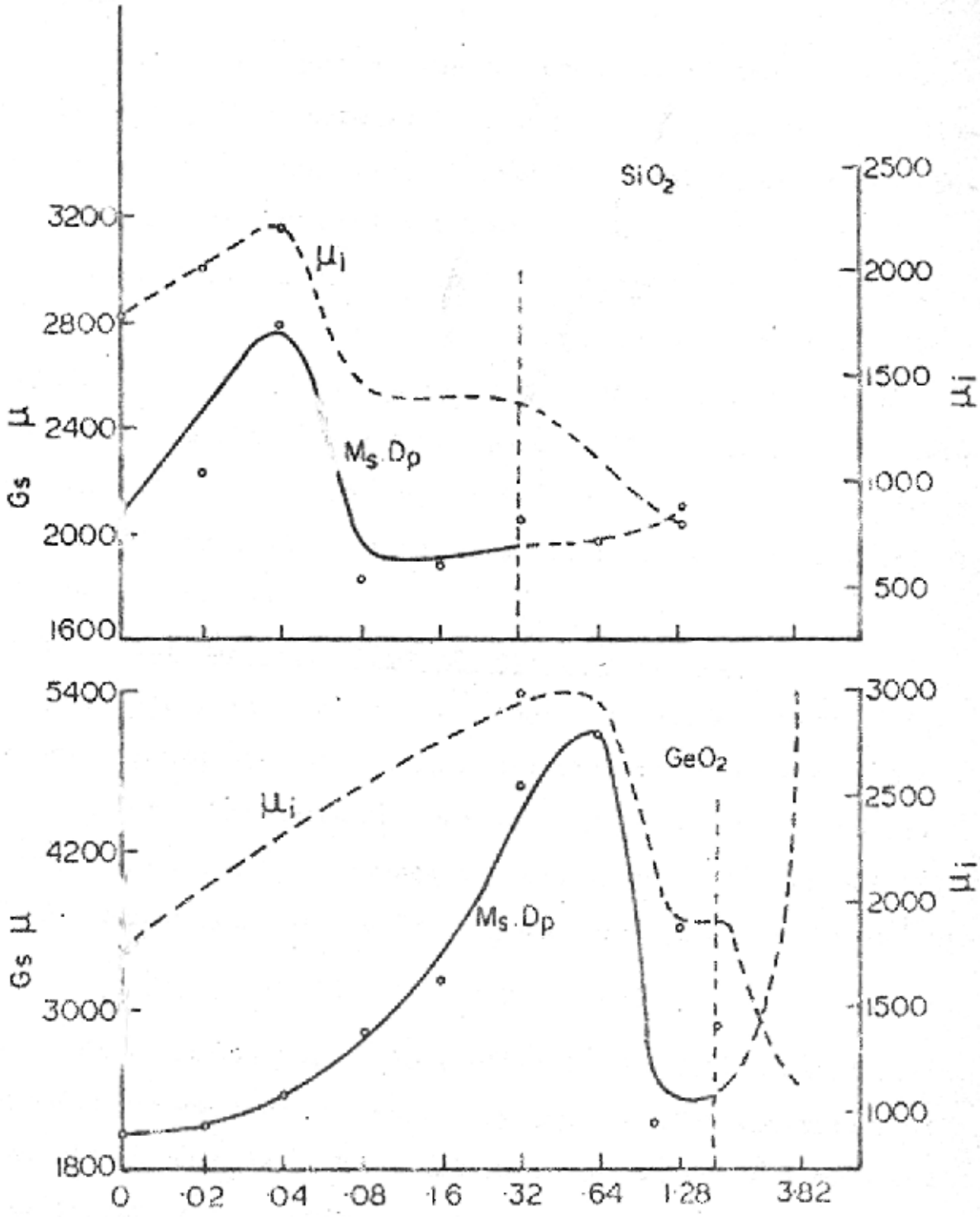
SiO2
μi
Ms. Dp
Gs μ
μi
3200
2800
2400
2000
1600
2500
2000
1500
1000
500
GeO2
μi
Ms. Dp
Gs μ
μi
5400
4200
3000
1800
3000
2500
2000
1500
1000
0
·02
·04
·08
·16
·32
·64
1·28
3·82

Fig. 4·4·1

1.28 mol% GeO_2). This is because at these levels of SiO_2 and GeO_2, cannibal grain growth takes place even at 1200°C leaving almost all the porosity in the grains stopping further densification.

Below these levels, the improvements in the μ_i occur mainly through the increase in the grain size and till the discontinuous grain growth sets in and the final value of the density that can be achieved has been reached.

Some fall in the μ_i at higher temperatures is expected due to the excessive zinc evaporation from the surface of the sample, specifically when sintering is done under nitrogen. This and the higher mobility of pore facilitating their coalescence are the reasons why oxygen sintered samples have a higher permeability than nitrogen sintered samples (see Figs.4.3.3.(b), 4.3.4(b) and 4.3.5)).

4.4.3. Temperature Variation of Initial Permeability

Previous investigations[10] show that the position of the secondary permeability maximum (SMP) depends primarily on the Fe^{2+} content. For manganese contents of $z = 0.52$ to 0.55, an empirical relationship between the calculated Fe^{2+} content (Y) and the temperature of the SMP, T_o has been given by Konig[11] as

$$T_o/T_c \simeq 0.88 - 2.9\ Y \quad \text{for } 0 < Y < 0.2 \qquad (4.5)$$

This relationship also applies if the Fe^{2+} content of the basic composition is changed by intralattice substitutions of different cations. The addition of monovalent and divalent metal oxides to the basic mixture before sintering causes a decrease in the Fe^{2+} content; the addition of trivalent and quadrivalent metal oxides causes an increase of the Fe^{2+} con-

tent.[12] This effect has been used to shift the SMP of iron-rich samples from low temperatures to a predetermined temperature. The idea was to change the anisotropy by means of relatively small amounts of substitutions, without much change in the Curie temperature and saturation magnetization.

$\underline{SiO_2}$

The secondary maximum peak (SMP) is not found to be shifting with silica additions. The SMP becomes more pronounced for .08 mol% SiO_2 where extreme discontinuous grain growth is observed. As has been said earlier, in case of grains having intragranular porosity the domain walls attach themselves to the pores within the crystallities as long as the pore diameter is equal to or larger than the thickness of the domain wall (as the blocking of domain walls at pores is determined by the ratio of pore size to wall thickness.[13]) In the temperature ranges of large anisotropy, the spacing of these pores determines the value of the initial permeability in the same way as the crystallite diameter does in the homogeneous (regular-grained) ferrites. In the range of K_1 zero crossing, the domain walls become very thick, the spacing of the pores with diameters equal to or larger than the domain wall thickness increases and the μ_i increases sharply.[14]

At higher levels of SiO_2 (0.64 and 1.28 mol%) the μ_i-T curves become quite flat and the SMP can not be located. Also the primary peaks are not sharp. Recently Franken[15] observed similar effects for TiO_2 additions in Mn-Zn ferrite. He has attributed the flattening of the μ_i-T curves to the heterogeneities caused by the Ti-concentration gradient across the grain boundaries which he observed using Auger analysis. In the present case also, the Si-rich second phase along the grain

boundaries would be giving rise to concentration (or compositional) gradients across the grain boundaries which has been varified in the present case.

The non-magnetic phase at the grain boundaries would also give rise to wall discontinuities. Globus and Duplex[8] have demonstrated that the degree of wall continuity strongly modifies the thermal spectra of initial permeability for a given composition in Ni-Zn ferrites. Their observations show that the two materials with same values of saturation magnetization, Curie temperature, saturation magnetostriction, porosity, and grain size but one sintered directly from constituent oxides and the other from the milled ferrite powder exhibited remarkably different temperature variation of initial permeability. The former one gave sharper temperature variation of μ_i with a much bigger primary peak whereas the later one gave a slow varying μ_i-T curve with a much shorter primary peak. They have attributed this effect to the fact that the wall continuity is more perfect in the former material than that in the later.

GeO_2

As concluded earlier inchapter II, the solubility of Ge^{4+} ions is more in Mn-Zn ferrite as compared to that of Si^{4+}. The effect of introducing quadrivalent Ge^{4+} ions would result in the increase in ferrous ion content. This would account for the slight shift in the SMP towards the lower temperature side.

At 1.28 mol% GeO_2, a well defined SMP is observed. Similar reasons could be attributed to this effect as those given for 0.08 mol% SiO_2, for, the grain structure is also very discontinuous here. At 3.82 mol% GeO_2, the occurance of flat μ_i-T curve could be interpreted in terms of the existence of Ge-

concentration gradients across the grain boundaries which would also affect the degree of wall continuity.

SnO_2

The substitution of Sn^{4+} ions in the intralattice positions would result in the increase in the Fe^{2+} ion content. This in turn should shift the SMP towards the lower temperature side which is exactly observed in the present case. Apart from this, the shape of the curve is also found to be changing, becoming more and more flat as the SnO_2 content increases. Similar effects have been observed in case of TiO_2 additions.[15]

In the presence of Fe^{2+} ions, Sn^{4+} is known to influence the anisotropy[16] in a similar way as Ti^{4+} does.[14] In fact, the behaviour of Sn^{4+} ions in affecting the properties of Mn-Zn ferrites is quite similar to that of Ti^{4+} ions with some difference which has been attributed to their ionic size difference[16] (Ti^{4+} = .60 Å, Sn^{4+} = .69 Å).

4.4.4. Disaccommodation

As mentioned in chapter I the after effect processes causing disaccommodation in Mn-Zn ferrites involve cation vacancies and ferrous ions. At room temperature, the disaccommodation is mainly caused by the migration of cations. The existence of Fe^{2+} facilitates the diffusionof cations. Cation migration causes an elevation of local potential. The cancellation of this local potential by electron charge displacement from Fe^{2+} to Fe^{3+} is one possible way Fe^{2+} facilitates diffusion. But the interaction between ionic distortion surrounding Fe^{2+} and that surrounding a cation vacancy should be considered as another mechanism. When electron hopping occurs, the change of the ionic distortion of Fe^{2+} would cause a change of the distortion

of a cation vacancy, thus facilitating the diffusion.[17]

It has been shown by a number of workers that the amplitude of this process is proportional to the product of the (small) concentration of ferrous ions and cation vacancies, which suggests that the effect is associated with Fe^{2+} - vacancy pairs.

According to Braginski,[18] there is another process causing disaccommodation, customarily referred to as 'process II' which is associated with the ordering of ferrous ion pairs through the agency of the diffusion of vacancies, which do not themselves contribute to the induced anisotropy. Thus, if the ferrous ion content per formula unit is Y, the amplitude of II is for small Y, proportional to Y^2.

The actual content of Fe^{2+} per formula unit of a typical Mn-Zn ferrite may be 'a', and if a substitution of bM^{4+} (M^{4+} : quadrivalent ion) is made, then since each M^{4+} ion localizes an Fe^{2+} ion, only (a-b) Fe^{2+} are free to participate in process II. The amplitude of II is then reduced by a factor of $(a/b)^2$.

Reported results indicate that all the three impurities SiO_2, GeO_2 and SnO_2 lower the $(DA)_{RT}$ (at room temperature) with reduction in DA being proportional to their respective solubility. Similar results have been reported in case of SiO_2 additions.[19] It has been observed that SiO_2 additions lower the DA at all temperatures in the range $-20^{\circ}C$ to $100^{\circ}C$.[20] The behaviour of GeO_2 as an additive on the disaccommodation of ferrites is expected to be more or less similar to that of SiO_2 as is observed in the present case. In case of SnO_2, however, the results seem to differ with those obtained by Matsubara and others[20] shown in Fig.4.4.2. It is observed from the figure that the DA at room

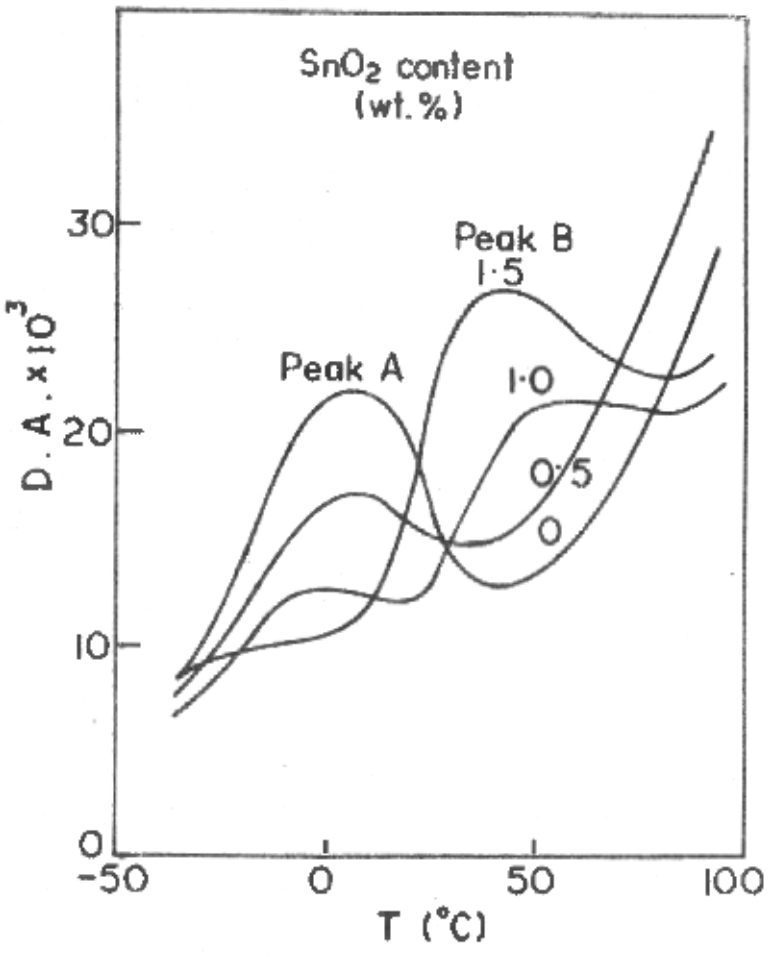

Fig. 4·4·2 Temperature dependecies of disaccomodation of $(Fe_2O_3)_{0.56}$ $(MnO)_{0.39}$ $(ZnO)_{0.05}$ containing various amounts of SnO_2 (Sintered in N_2 containing 0·6 % O_2) [ref. 20]

temperature depends upon the position and height of peak A and peak B. They have discussed that the peak height and the peak temperature are sensitively influenced by the basic composition, the additive components and the sintering conditions. They have observed a constant decrease in DA with increasing SnO_2 additions at $0^{\circ}C$ as is observed in the present case at $25^{\circ}C$ (room temperature). A better explanation of the deviation in results could only be put forward after the processing details of their ferrites are known.

For technical applications it is the D.F ($= DA/\mu_i$), which is an important parameter and is found to decrease significantly with SnO_2 additions.

4.4.5. D.C. Bulk Resistivity and its Temperature Variation SiO_2 and GeO_2

Both SiO_2 and GeO_2 alter the microstructure of the ferrite significantly. The effect of microstructure on the resistivity has already been explained in chapter I. Since solubility of both SiO_2 and GeO_2 is limited, the changes in the resistivity may be attributed to the corresponding changes in the microstructure.

The minimum in the resistivity in both the cases corresponds to a content which gives discontinuous grain structure with largest grain size. Large grain size means less concentration of grain boundaries which are the regions of high resistivity. This accounts for the increase in the conductivity with the grain size.

It has been said that beyond .08 mol% SiO_2 (and 1.28 mol% GeO_2), the grain boundaries start getting richer and richer with the second phase. This formation of a high resistivity layer at the grain boundaries results in the increase in the resistivity beyond these points.

SnO_2

In Mn-Zn-Fe^{II} ferrites the conductivity is proportional to the ferrous ion content. As earlier stated, the substitution of Sn^{4+} ions in the lattice should result in the increased number of ferrous ions. The Sn^{4+} ion also has the property of localizing a Fe^{2+} ion. Therefore the number of ferrous ions contributing to the conductivity decreases whereas all the ferrous ions present contribute to the anisotropy. This explains simultaneously the increase in the resistivity and shift of SMP towards the lower temperature side with SnO_2 additions. Similar effects have been observed with the addition of titanium also.[21-24] Hanke and Zenger[24] studied the resistivity of Mn-Zn ferrites doped with SnO_2 and TiO_2. They observed that the ρ increased very slowly with SnO_2 additions up to about 2.8 mol% while for the same amounts of TiO_2 additions the ρ increased by about 40 fold. They attributed their results to the fact that Ti ions form Ti^{4+} - Fe^{2+} pairs whereas Sn^{4+} ions might be forming pairs with other valencies other than Fe^{2+}.

Knowles[16] has inferred that the pair Sn^{4+} - Fe^{2+} is more weakly bound than the pair Ti^{4+} - Fe^{2+} because of the bigger size of tin ion, therefore at higher temperatures these pairs tend to disassociate and this probably accounts for the faster decrease in the resistivity with temperature for SnO_2 doped ferrites approaching the basic value of the resistivity (Fig. 3.3.12(b)). In the ferrite doped with 1.28 mol% SnO_2, the value of the resistivity tends to fall even below the basic value at temperatures around 145°C indicating higher ferrous content in this ferrite as compared to the basic ferrite. This is also learnt from the μ_i-T curves.

REFERENCES

1. B.L. Worsnop and H.T. Flint, 'Advanced Practical Physics', Asia Publishing House, p.481.
2. ASTM Designation C20-70, Part-B (1971), p.6.
3. E.C. Snelling, Soft Ferrites, Ilifee Books Ltd., London (1969).
4. L.G. van Uitert, J. Chem. Phys., Vol.23, pp.1883-1887, Oct. 1955.
5. J. Smit and H.P.J. Wijn, Ferrites, Philips Technical Library.
6. A.D. Giles and F.F. Westendorp, Journal de Physique, Colloque C1, Supplement au n° 4, Tome 38, April, 1977, p.C1-317.
7. G.C. Jain et al., J. Mater. Sci., 11, (1976), p.1335-1338.
8. A. Globus and P. Duplex, Phys. Stat. Sol. 31, 765 (1969).
9. H.G. Brion and E. Nemback, Phys. Stat. Sol(a), 599 (1974).
10. K. Ohta, J. Phys. Soc. Japan, 18(5), (1963), p.685.
11. U. Konig, Appl. Phys., Vol.4, p.237, 1974.
12. U. Konig, IEEE Trans. on Magnetics, Vol. Mag-11, No.5, Sept. 1975, p.1306.
13. A. Broese van Groenou et al., Review Paper, Mater. Sci. Eng., 3 (1968-69), 317-392.
14. E. Roess, Ferrites : Proc. Internat. July, 1970, Japan, p.203.
15. P.E.C. Franken, Intermag. Conf. May, 1978.
16. J.E. Knowles, Philips. Res. Repts., 29, (1974), p.93.
17. A. Broese van Groenou and R.F. Pearson, J. Chem. Solids, 28, 1027 (1967).

18. Braginski, Phys. Stat. Sol. 11, 603-616, 1965.

19. T. Hiraga, Ferrites : Proc. Internat. Conf. July, 1970, Japan, p.179.

20. T. Matsubara et al., Ferrites : Proc. Internat. Conf., July 1970, Japan, p.214.

21. T.G.W. Stijutjes, J. Klerk, C.J.M. Rooymans, A. Broese van Groenou, R.F. Pearson, J.E. Knowles and P. Rankin, Ferrites : Proc. Internat. Conf. July 1970, Japan, p.191.

22. T.G.W. Stijntjes, A. Broese van Groenou, R.F. Pearson, J.E. Knowles and P. Rankin, Ferrites : Proc. Internat. Conf. July 1970, Japan, p.194.

23. J.E. Knowles and P. Rankin, Journal de Physique, Colloque C1, Supplement au n° 2-3, Tome 32, Fevrier - Mars 1971, p.C1-845.

24. I. Hanke and M. Zenger, J. Magn. and Magn. Materials (Netherlands), Vol.4, No.1-4, 120-8 (1977).

CHAPTER - V

EFFECT OF SiO_2, GeO_2 AND SnO_2 ADDITIONS ON THE CORE LOSSES OF THE Mn-Zn FERRITE

5.1. INTRODUCTION

Among the high flux density applications of ferrites are cores for television line output transformers, inverter power transformers and switched mode power supplies (SMPS) transformers etc., in which the material requirements are similar but apply over different frequency ranges.[1]

At frequencies below about 0.5 MHz Mn-Zn ferrites are suitable. The major requirements are low core losses at high flux densities and a high value of saturation flux density. Typical values of the later at room temperature are in the region of 5 wb/m^2 (5000 gauss). If reasonable freedom from waveform distortion is to be obtained, the peak operating flux density must be less than about 2.5 wb/m^2. Thus the core losses are usually quoted in terms of power loss per unit volume at 2.0 wb/m^2 (2000 gauss) and at typical operating frequencies, e.g. 10 tc 16 KHz. Generally the loss is proportional to frequency up to about 100 KHz.

Core losses at a peak flux density of 2000 gauss and up to a frequency of 15.75 KHz of the ferrite under investigation with various amounts of the three additives - SiO_2, GeO_2 and SnO_2 have been studied. In order to understand the origin of core losses in these ferrites, D.C. hysteresis loops (to determine H_c) and A.C. hysteresis loops under the same operating conditions have also been studied.

5.2. EXPERIMENTAL METHODS

5.2.1. Core Losses

An incremental inductance bridge type 1633-A with an inductance measuring assembly type 1630-AV (General Radio Co., USA) was used for this purpose.

Insulated primary and secondary windings of equal number of turns (30 turns each) were wound on toroidal cores of average dimensions : OD=14mm, ID=9mm, h=2mm. The primary was subjected to a calculated A.C. voltage V given by[2]

$$V = \frac{\omega \hat{B} A_e N}{\sqrt{2}} 10^{-8} \text{ volts} \qquad (5.1)$$

where

$\hat{B}$ = peak flux density

A_e = effective cross-sectional area

$$= \frac{h(\ln(OD/ID))^2}{(2/ID - 2/OD)} \text{ cm}^2$$

N = number of turns in the primary

$\omega = 2\pi f$

f = frequency

Since the number of turns were same on the primary and the secondary, the voltage was measured at the secondary by VTVM. The primary was also connected to the bridge to measure L (inductance) and R (series loss resistance).

Total core losses are then given by

$$P_T = VI \cos\phi = V \cdot \frac{V}{Z} \cdot \frac{R}{Z} = \frac{V^2 R}{Z^2} \text{ Watts} \qquad (5.2)$$

$$Z = \sqrt{R^2 + (\omega L)^2}$$

Core losses per unit volume (P_T/core volume) were then computed.

This instrument could provide measurements only at discrete frequencies : 0.4 KHz, 1.0 KHz, 10 KHz and 15.75 KHz.

The losses in the winding were found to be less than 2.0%. The accuracy of the measurement was estimated to be within ± 5%.

5.2.2. Hysteresis Loops

Under the same conditions of flux density and frequency at which the core losses were measured, AC hysteresis loops for each sample were viewed and photographed using a Hungarian make Ferro-Tester (Type TR-9801/A/ORION, FOHGYEM).

Only qualitative measurements were done in order to see changes in the loop shape and loop area with additions of different impurities.

D.C. loops were plotted to measure H_c using the ballistic galvanometer method.[3] The main aim of these measurements was to estimate the hysteresis loss contribution to the core losses qualitatively.

5.3. EXPERIMENTAL RESULTS

5.3.1. Effect of SiO_2 on the Core Losses and Hysteresis Loops

(i) Core Losses for Different Frequencies

Figure 5.3.1 gives core losses in mW/cm^3 for different silica additions ('Standard' firing) at four different frequencies (B = 2000 gauss). At 15.75 KHz, the losses first decrease up to a content of .04 mol%, where the μ_i shows an increase (region I in Fig.4.3.1). At.08 mol% SiO_2, there is a sharp peak coinciding with the dip in μ_i. After this peak the losses again fall up to 0.32 mol% SiO_2 beyond which they rise further (region III).

It may be noticed that the peak in losses at .08 mol% SiO_2 becomes more and more predominant as the frequency rises. It can be clearly seen from Fig.5.3.2 where the core losses/

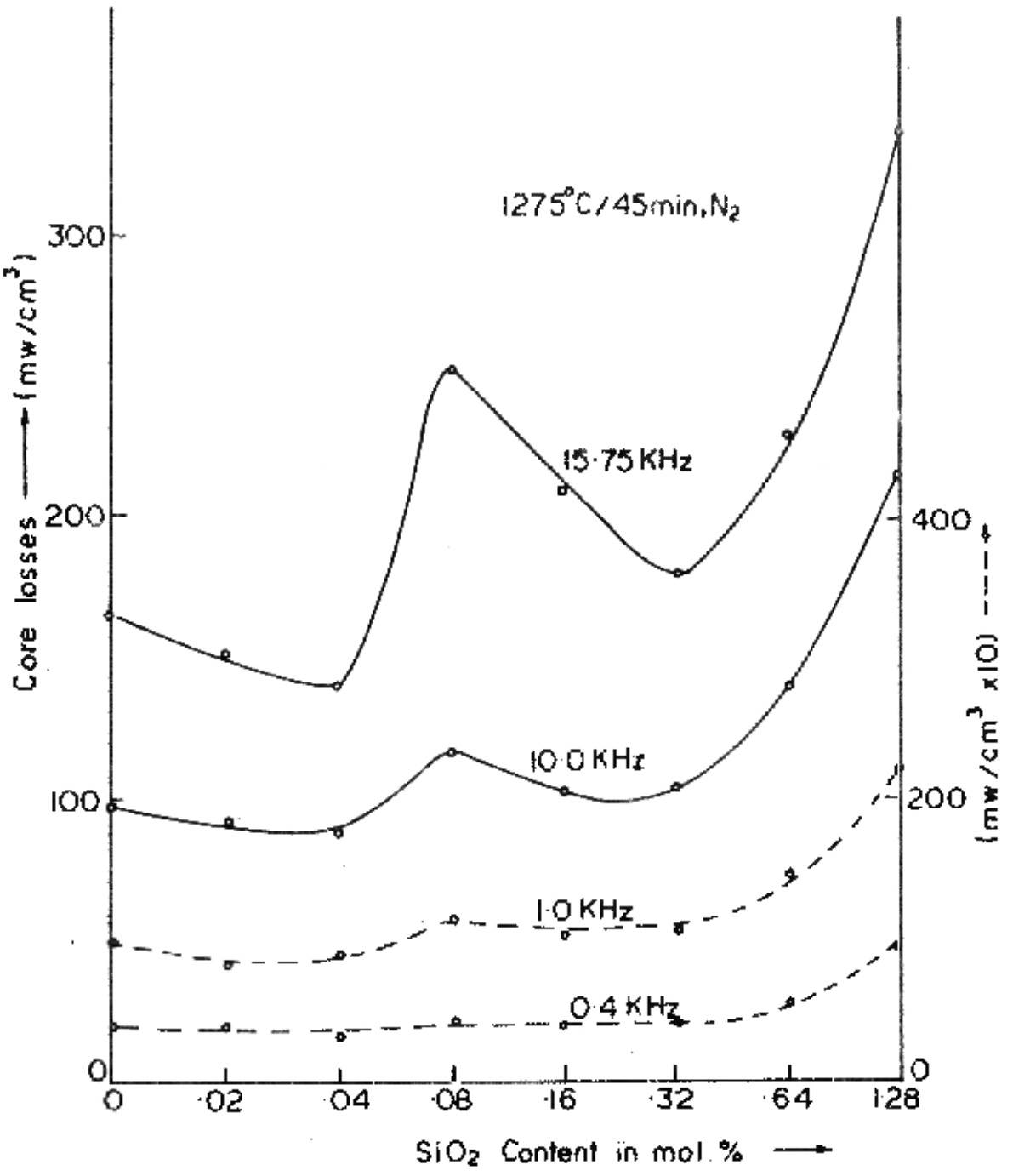

Fig. 5·3·1 Core losses versus SiO_2 content for different frequencies.

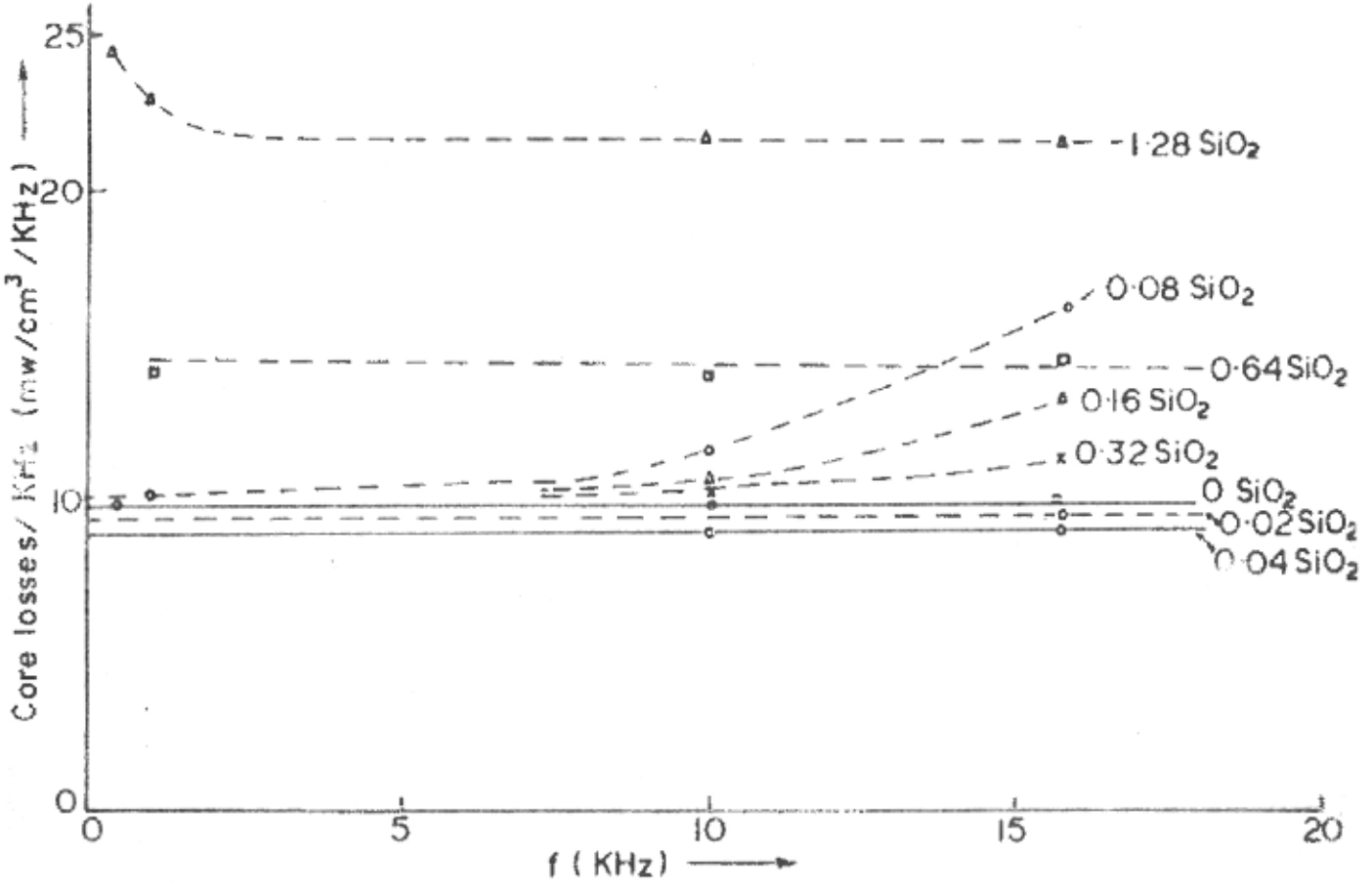

Fig. 5·3·2 Core losses/KHz versus frequency for various SiO_2 contents.

frequency are plotted against frequency. The basic composition and the first two levels of silica show horizontal lines showing that the core losses are directly proportional to the frequency. For .08 mol% SiO_2 the curve shows a positive slope showing significant increase of losses with frequency. This slope reduces as one goes higher with SiO_2 content. At .64 and 1.28 mol% SiO_2, again horizontal lines are obtained i.e. the core losses/KHz are essentially independent of frequency.

(ii) Core Losses for Different Sinterings

Core losses for samples fired at different sintering temperatures ranging from 1200°C to 1350°C are plotted against the silica content in Fig.5.3.3. At lower sintering temperatures (1200°C and 1225°C) the losses decrease with silica content reaching a minimum and then increase at the two highest silica levels. At further higher sintering temperatures (1250°C and 1275°C), the losses decrease to much lower values for individual SiO_2 contents but a significant peak in losses is observed at a content of .08 mol% SiO_2 before rising further at the highest contents. At 1350°C losses are found to be constantly increasing with SiO_2 content. It may be noticed that losses are always high at the highest silica level of 1.28 mol%, and the dip in the losses moves more and more towards the lower silica levels as the sintering temperature is increased.

(iii) A.C. Hysteresis Loops

Figure 5.3.4 gives hysteresis curves at a peak flux density of 2000 gauss and at frequencies of 1.00 and 15.75 KHz for various silica additions. At 1.00 KHz there is not much change in the loop shape even up to a content .32 mol%.

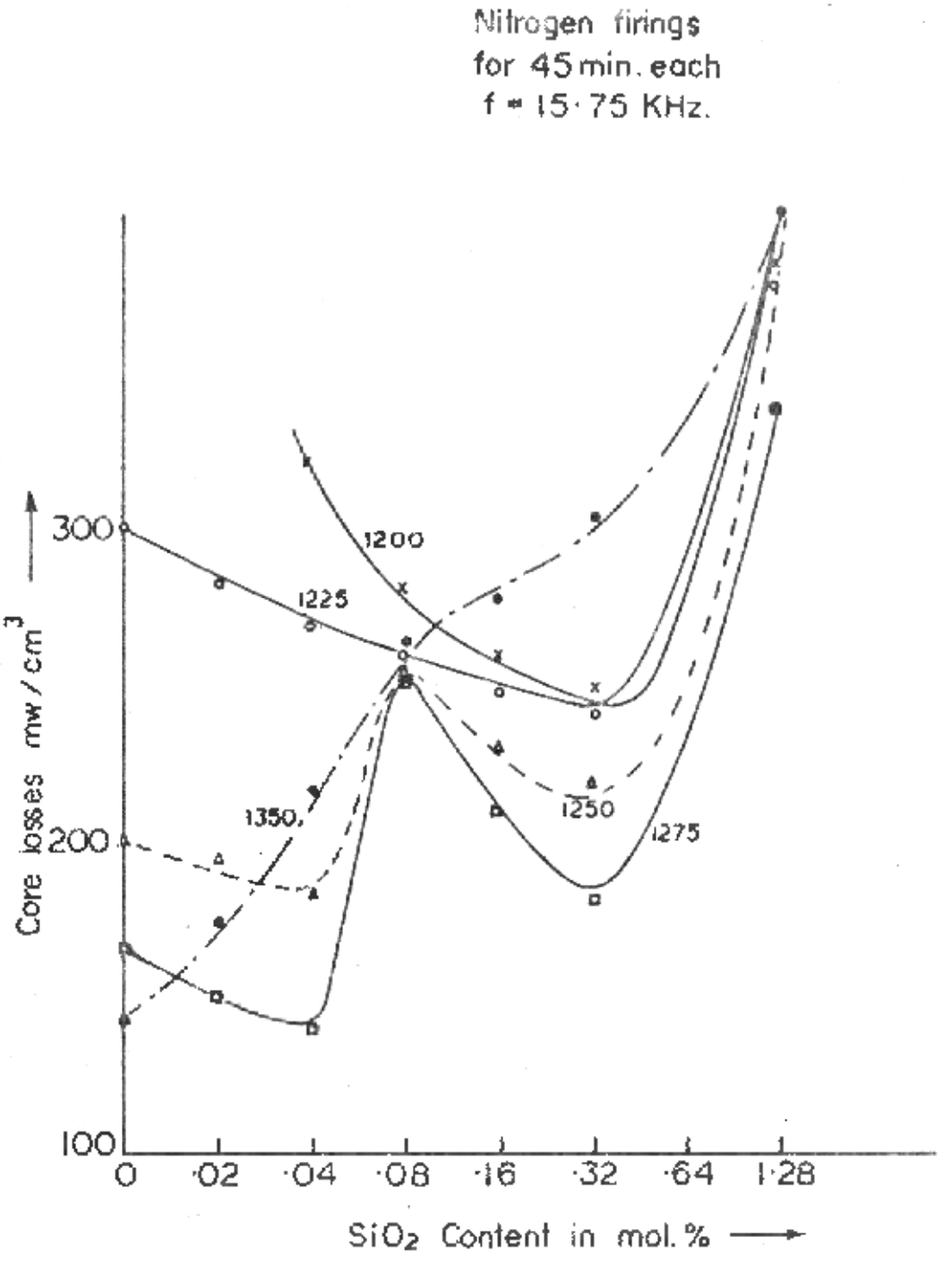

Fig. 5·3·3 Core losses versus SiO_2 content for various sintering temperatures.

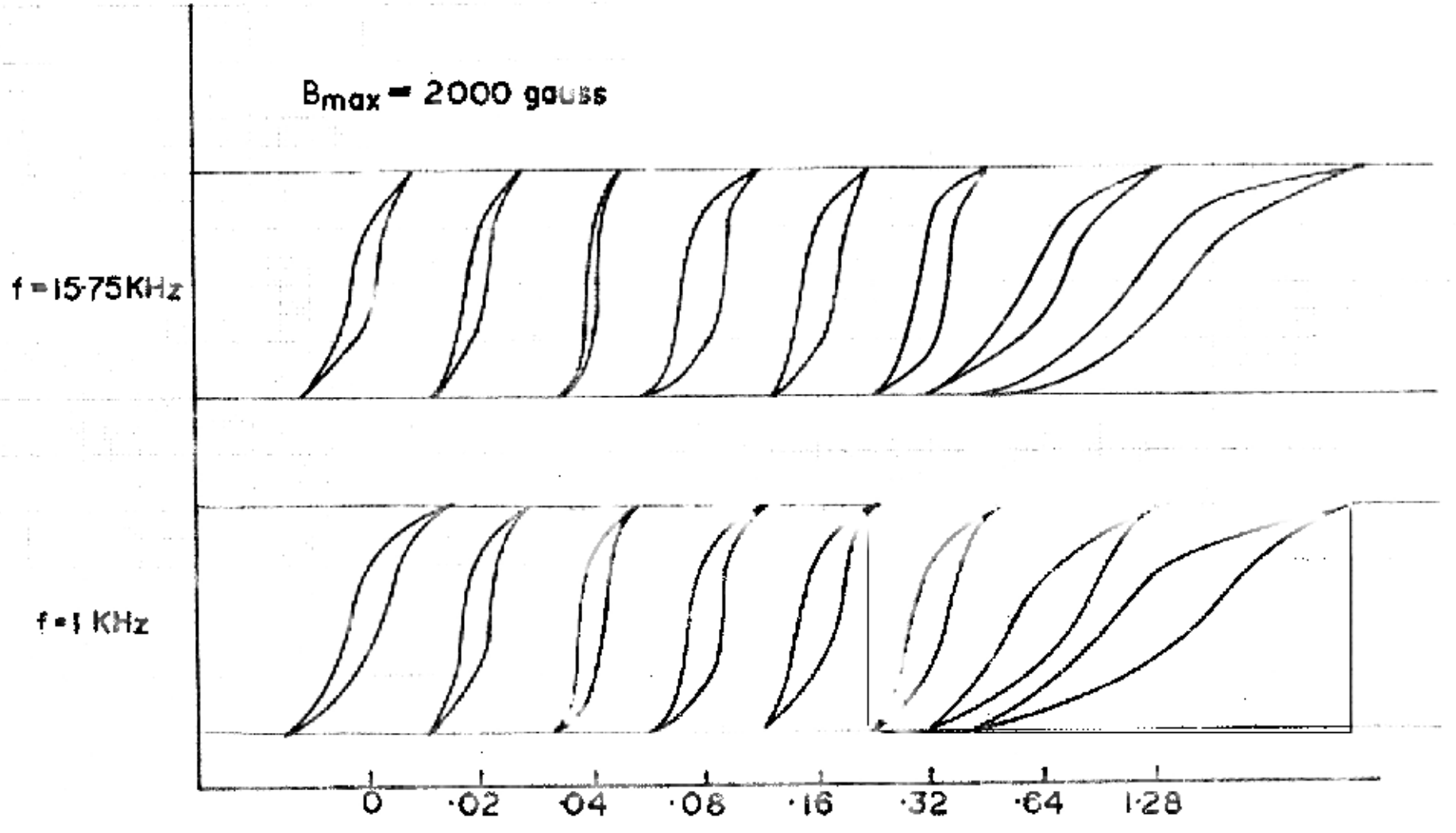

Fig. 5·3·4 A.C. Hysteresis loops for various SiO_2 contents.

At higher contents, the loop is found to be tilting more and more. H_c is also higher in these levels. At 15.75 KHz, the loop first shrinks up to a content of .04 mol% and at .08 mol%, the loop becomes fat with high coercive force. Slanting loops are found at the contents of .64 and 1.28 mol%. The loop areas are plotted in Fig.5.3.5. It may be noticed that from .08 mol% SiO_2 to .32 mol% SiO_2, the loop area shows increase with frequency. There is one to one correlation between the loop area versus SiO_2 content curve and core losses versus SiO_2 content curve (Fig.5.3.1).

(iv) D.C. Loops : Coercive Force

The M-H loops for various additions of silica are shown in Fig.5.3.6. It is observed that up to a content of 0.16 mol%, the loop shape is not changing significantly. Beyond 0.16 mol% SiO_2 the loop tilts with higher saturation field strength.

The variation in H_c is plotted in Fig.5.3.7. Initially it increases at a content of 0.08 mol% slightly and then increases sharply at the two highest levels SiO_2.

5.3.2. Effect of GeO_2 on the Core Losses and Hysteresis Loop

(i) Core Losses for Different Frequencies

Almost similar results are obtained for GeO_2 additions (Fig.5.3.8). At 15.75 KHz the core losses decrease with GeO_2 content to a minimum at .64 mol% GeO_2. At 1.28 mol% GeO_2 there is a peak similar to the one observed at .08 mol% SiO_2 content. It can also be seen that this peak becomes more and more predominant as the frequency rises (Fig.5.3.9). At highest GeO_2 contents losses increase again.

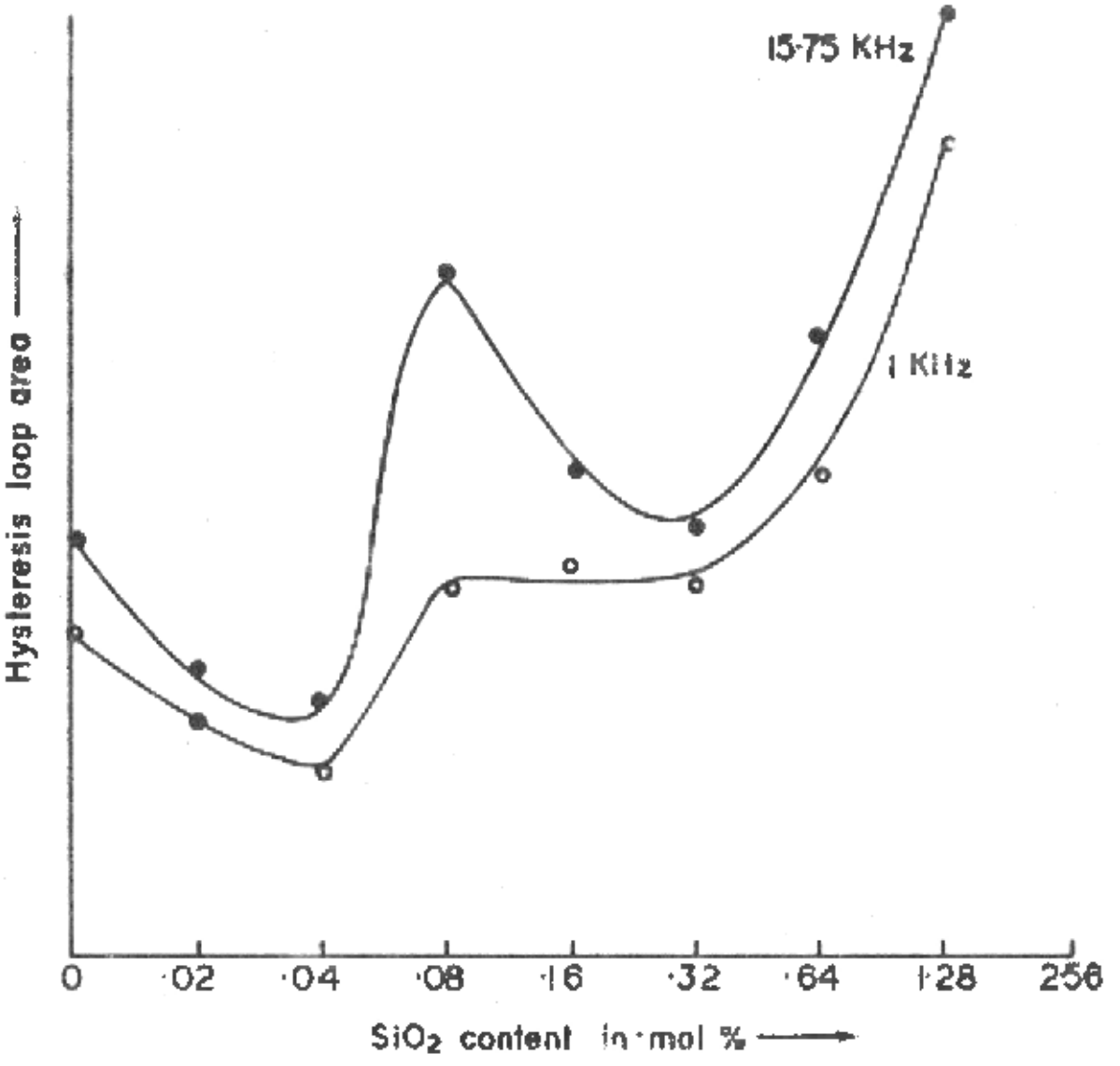

Fig.5·3·5 Hysteresis loop area versus SiO_2 content.

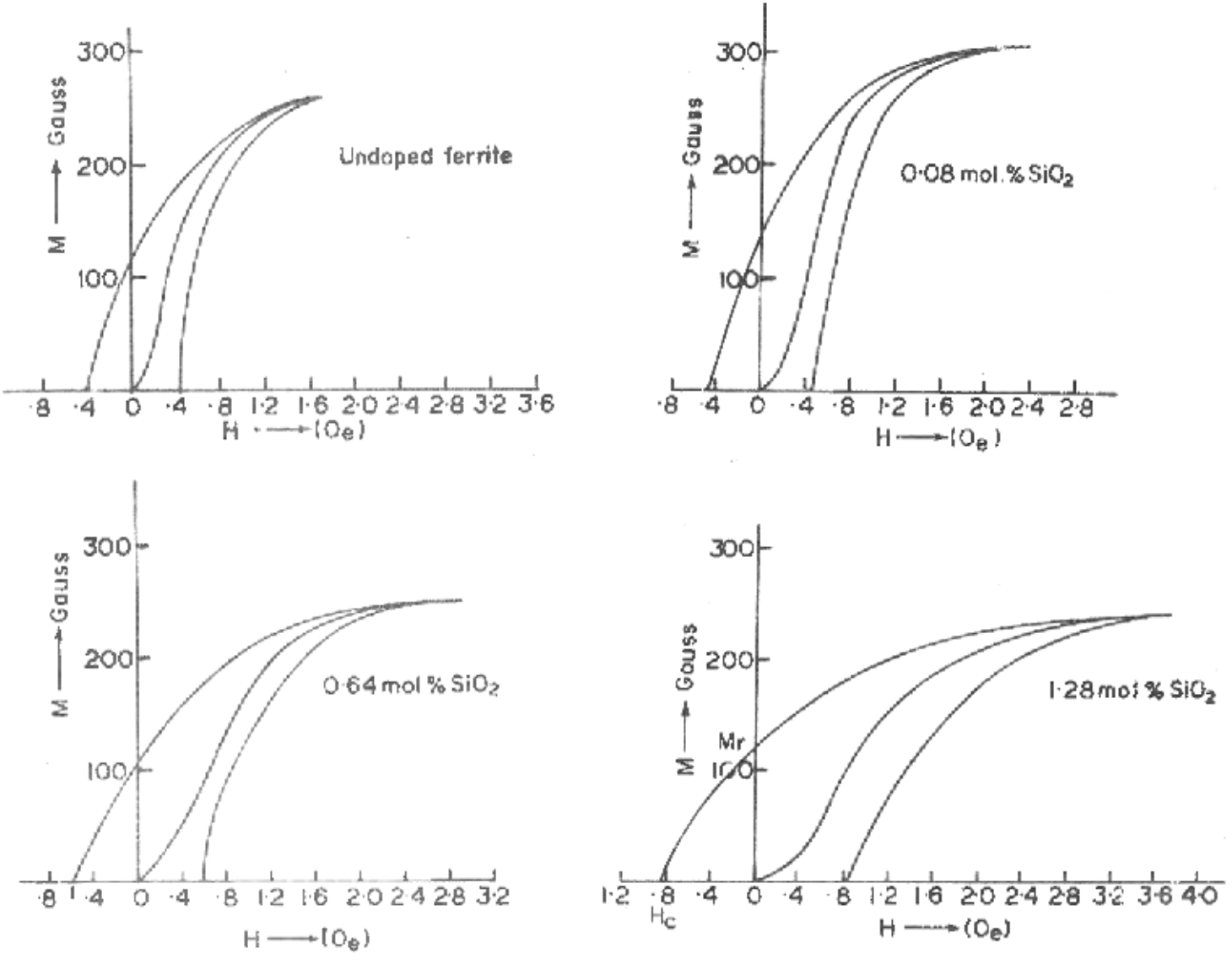

Fig.5·3·6 M–H curves (D.C.) for various SiO_2 contents.

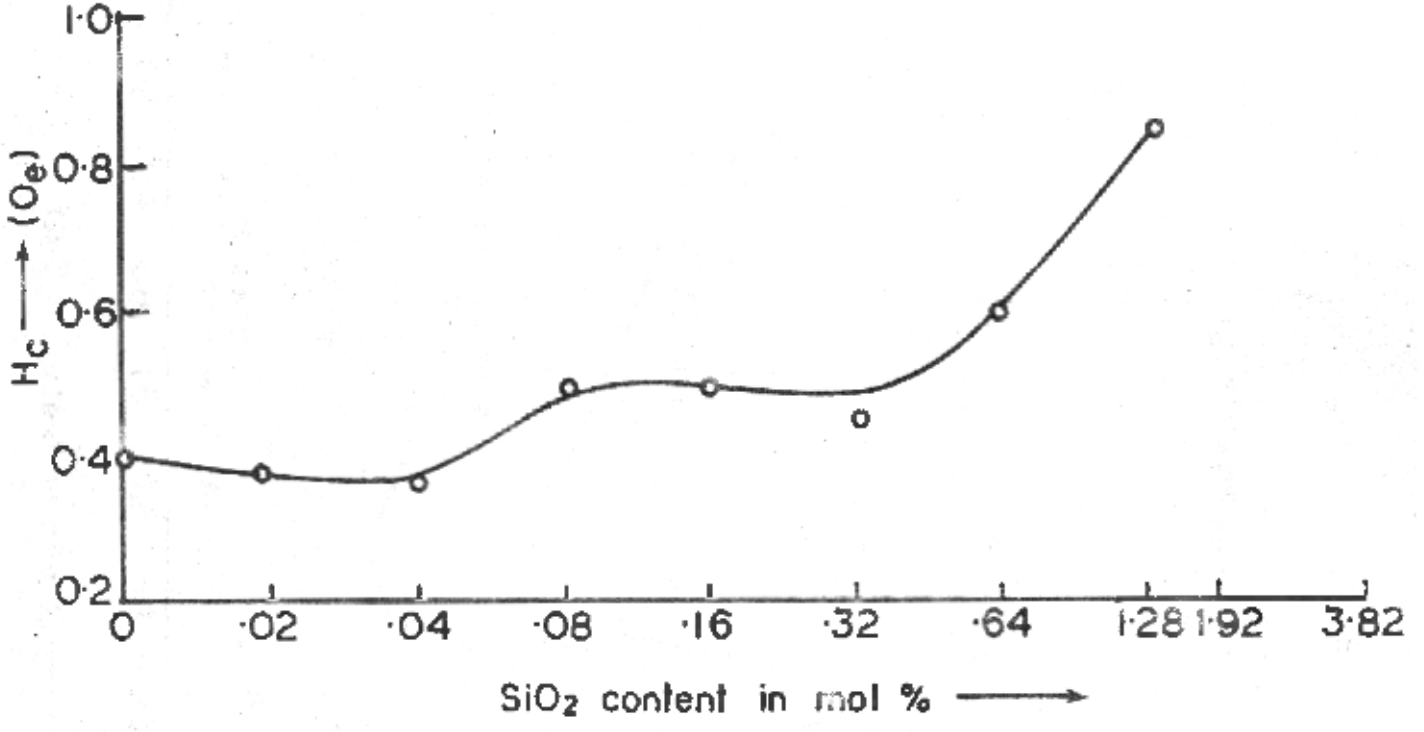

Fig. 5·3·7 H_c versus SiO_2 content.

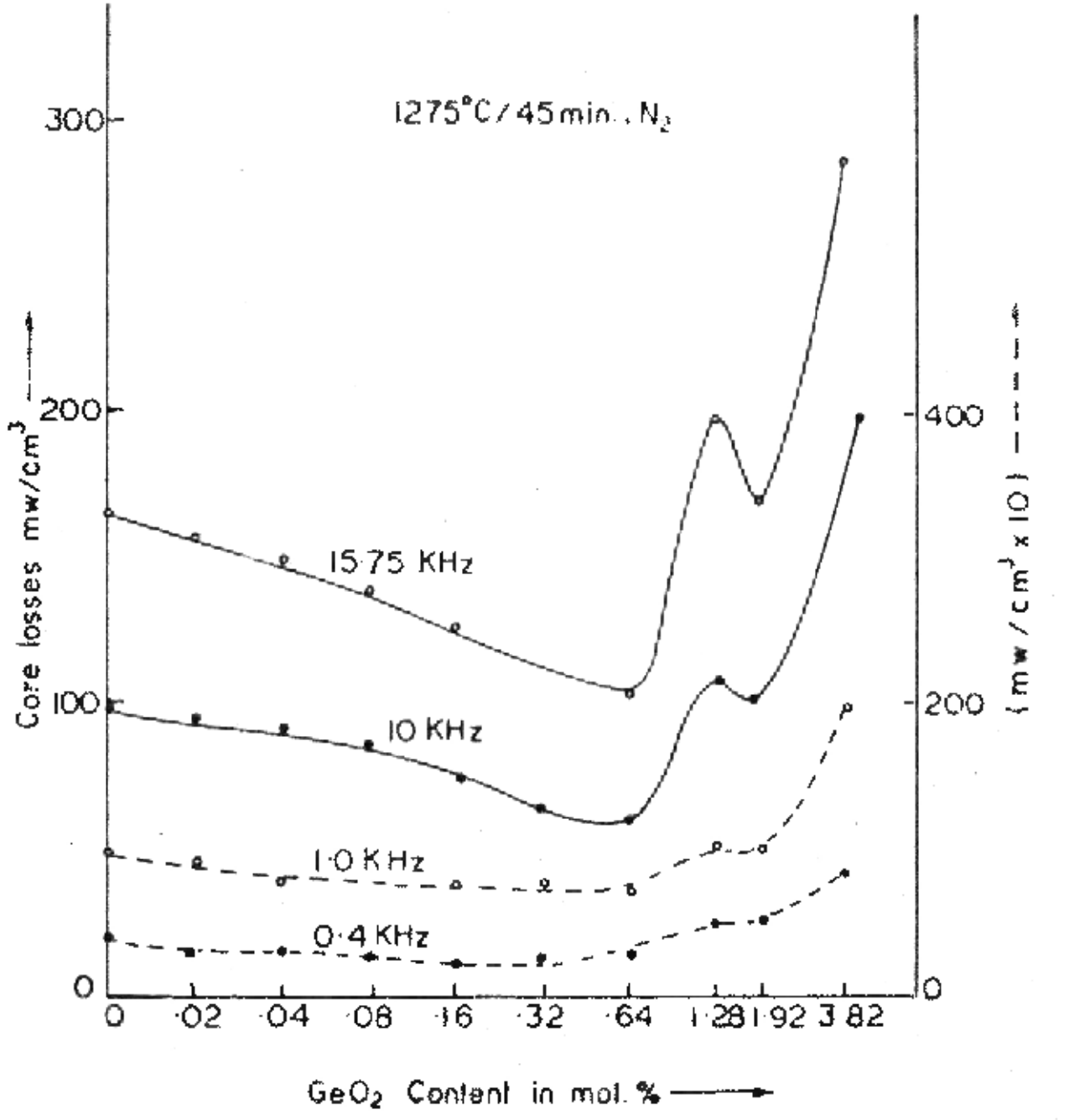

Fig. 5·3·8 Core losses versus GeO_2 content for different frequencies

(ii) Core Losses for Different Sinterings

Figure 5.3.10 shows core loss for different GeO_2 contents fired at various sintering temperatures. Losses are high at lower sintering temperatures e.g. at 1200°C, however, these losses decrease with GeO_2 content showing a dip at 1.92 mol% GeO_2 beyond which they rise again. At 1275°C the losses decrease considerably for all GeO_2 levels. The curve now shows a dip at .64 mol% and a peak at 1.28 mol%. The dip in losses moves more and more towards the lower GeO_2 side as the sintering temperature rises. At 3.82 mol%, losses are always high.

(iii) A.C. Hysteresis Loops

The hysteresis loops obtained for different GeO_2 additions at a peak flux density of 2000 gauss and at frequencies 1.00 KHz and 15.75 KHz are shown in Fig.5.3.11. At 15.75 KHz, the loop shrinks (i.e. H_c decreases) as the GeO_2 increases and at 1.28 mol% GeO_2 corresponding to the peak in core losses, a fat loop is obtained (high H_c). The loop is found to be sloping at the highest level of 3.82 mol% GeO_2. The loop areas are plotted in Fig.5.3.12 showing a variation similar to the one seen for core losses against GeO_2 content.

(iv) D.C. Loops : Coercive Force

Figure 5.3.13 shows M-H curves for different content of GeO_2. Almost similar effects have been observed as those observed in case of SiO_2 additions.

H_c decreases up to a content of 0.64 mol% GeO_2. At a content of 1.28 mol%, H_c increases. At 3.82 mol% GeO_2, the H_c is found to be very high (0.78 Oe). Figure 5.3.14 gives H_c versus GeO_2 additions.

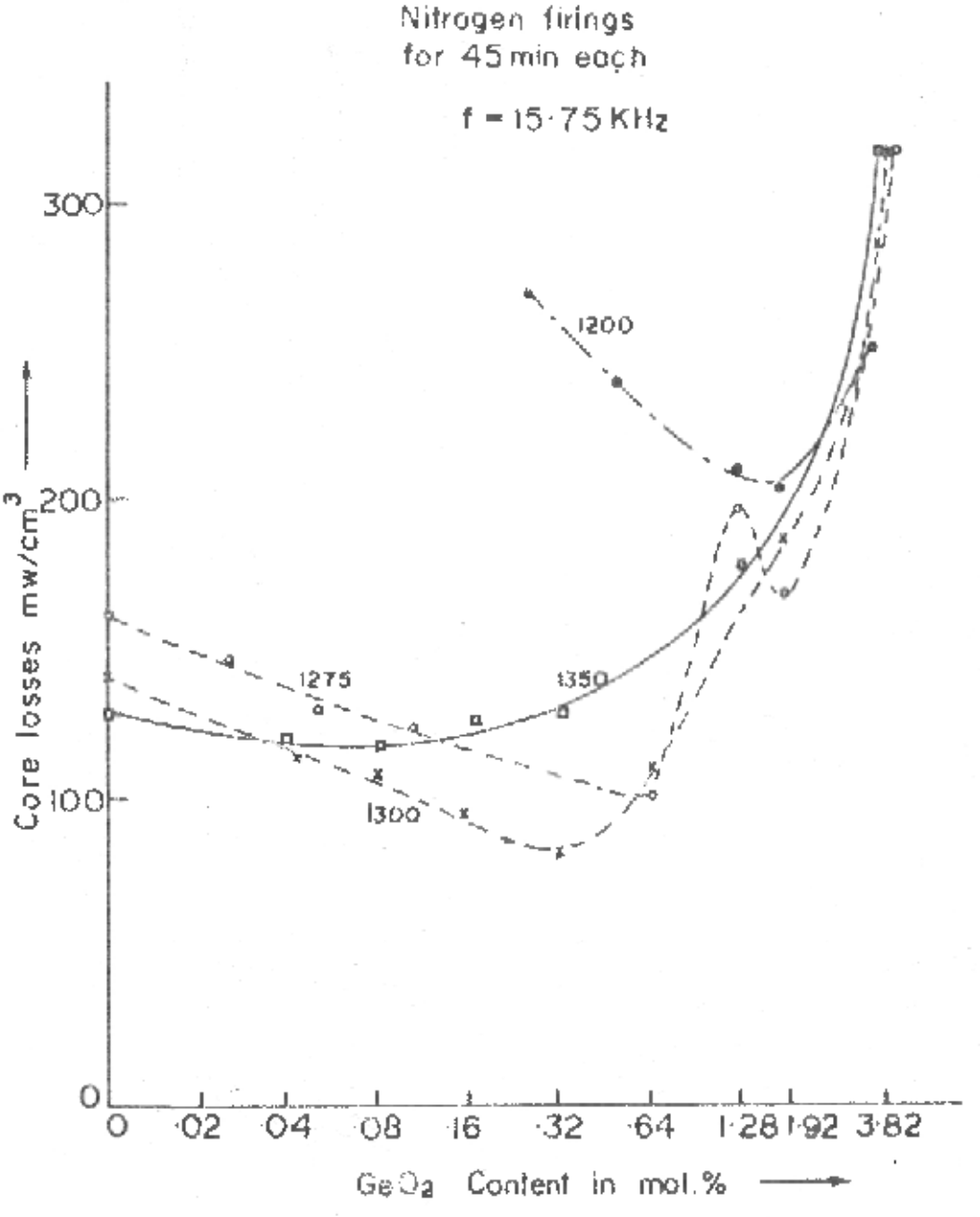

Fig. 5·3·10 Core losses versus GeO_2 content for various sintering temperatures.

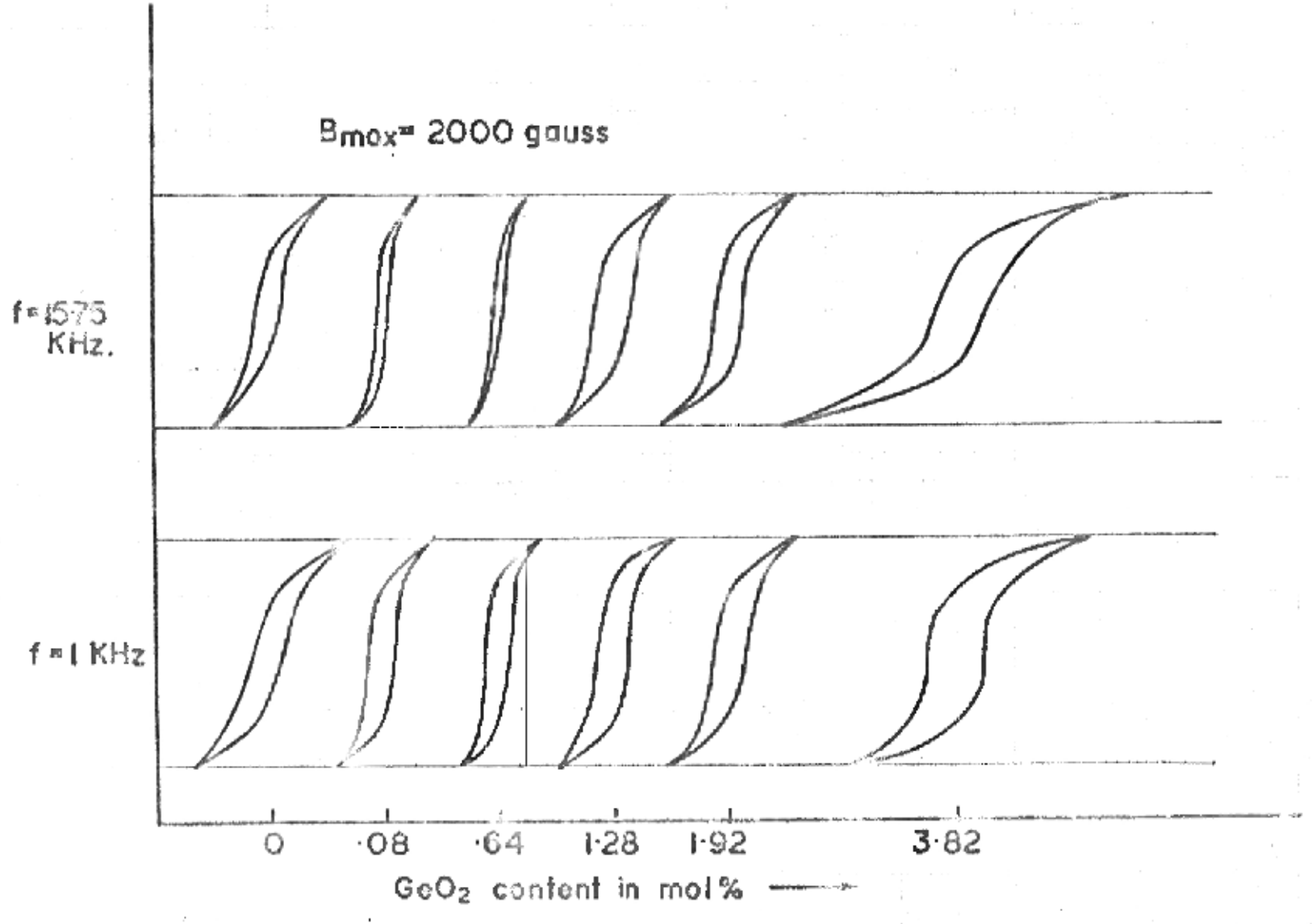

Fig. 5·3·11 A.C. Hysteresis loops for various GeO_2 contents.

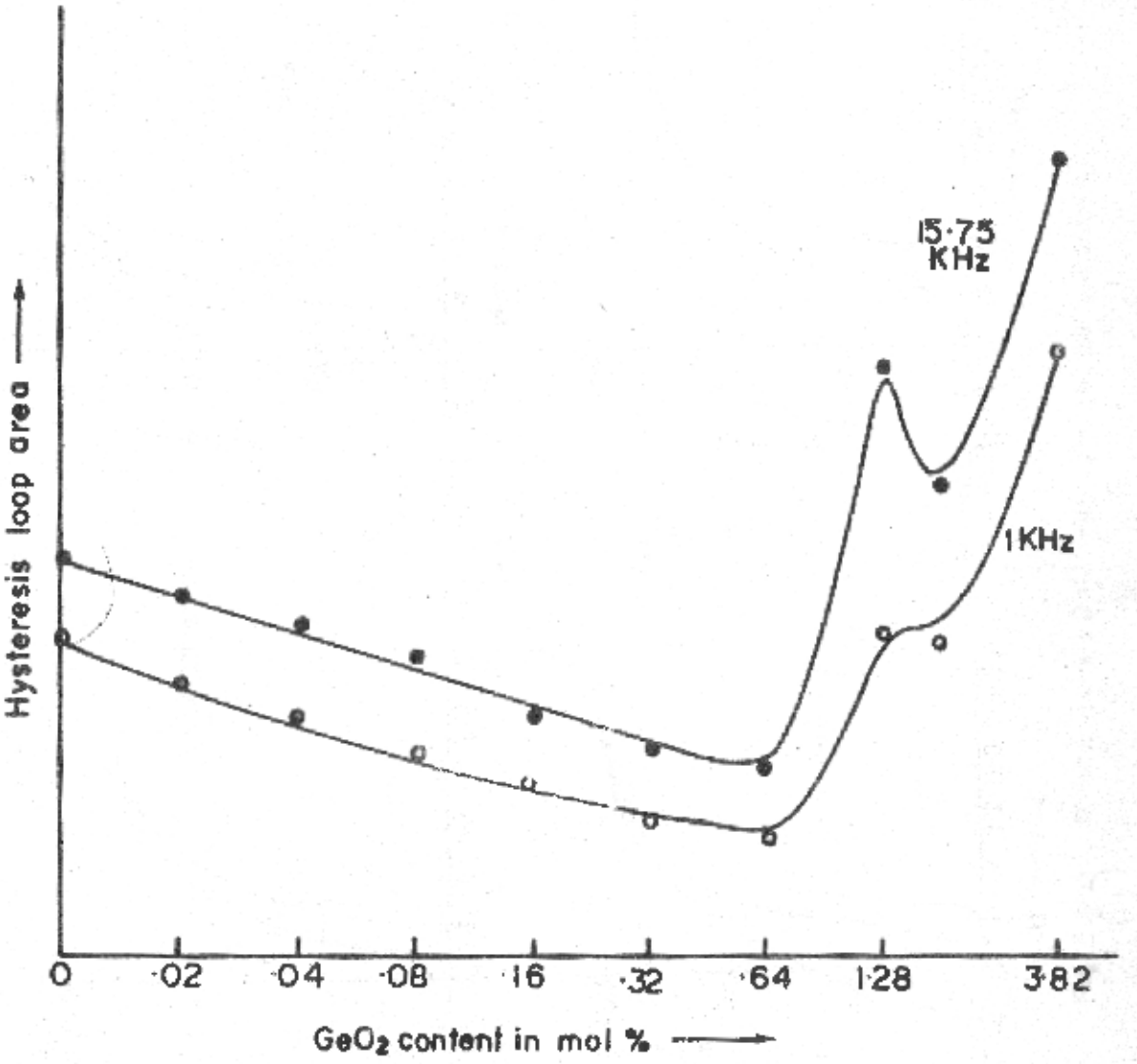

Fig. 5·3·12 Hysteresis loop area versus GeO_2 content.

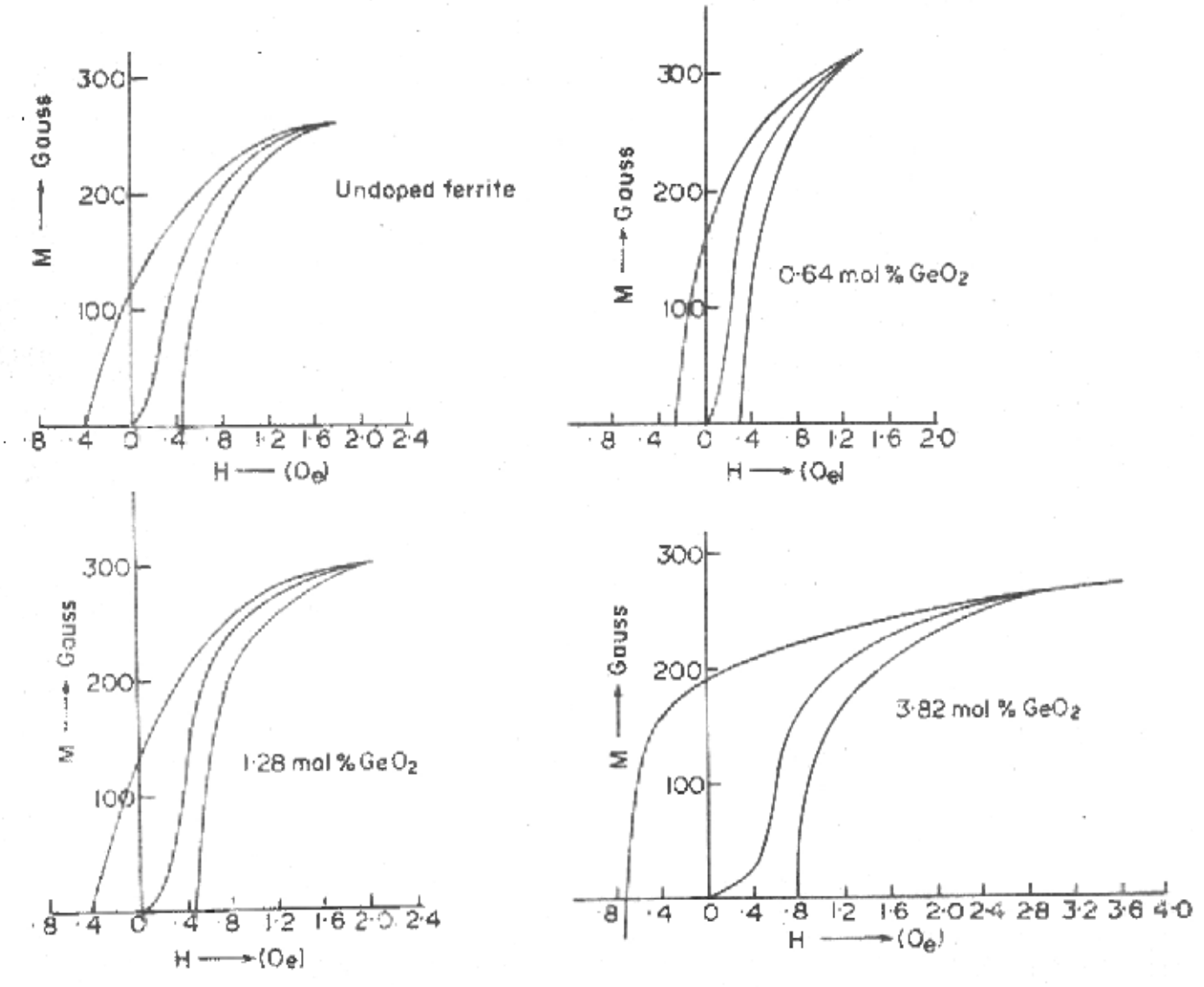

Fig. 5·3·13 M–H curves (D.C.) for various GeO_2 contents.

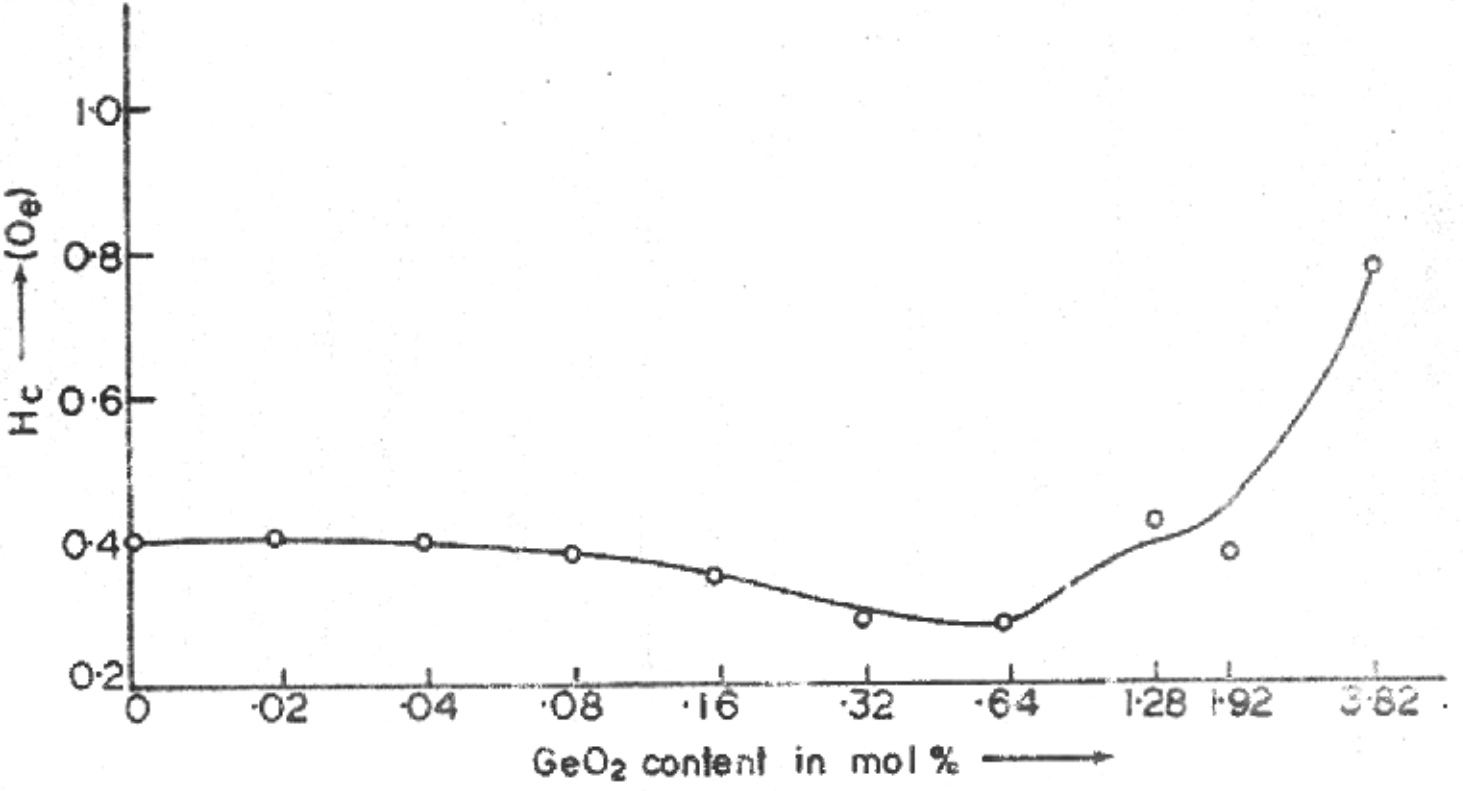

Fig. 5·3·14 H_c versus GeO_2 content.

5.3.3. Effect of SnO_2 on the Core Losses and Hysteresis Loop

Unlike SiO_2 and GeO_2, SnO_2 is not found to affect the core losses significantly. Core losses at 10 KHz and 15.75 KHz are shown in Fig.5.3.15 and the hysteresis loops are shown in Fig.5.3.16. The loops are also not showing any significant variation in shape or area.

For the sake of comparison, core losses for an oxygen firing for all the three impurity levels are shown in Fig. 5.3.17. It is observed that the additions of GeO_2 and SnO_2 yield much lower core losses as compared to those obtained with silica additions.

On the whole the experimental results reveal the foll owing main features

1) There is one to one correlation between the core losses versus impurity content curve and the loop area(under the same conditions) versus impurity content curve.
2) At lower SiO_2 and GeO_2 content the core losses decrease.
3) At .08 mol% SiO_2 and 1.28 mol% GeO_2 the core losses/KHz (loop area) show an increase with frequency. These very samples also exhibit coarse grain structure with giant grains and large intragranular porosity.
4) At high SiO_2 and GeO_2 contents (1.28 mol% and 3.82 mol% respectively) the losses are found to be high.

5.4. DISCUSSIONS

5.4.1. Core Losses in Mn-Zn Ferrites

The core losses in ferrites have been defined in section 1.8 of chapter I. It has been discussed that the various losses contributing to core losses are hysteresis losses, eddy current losses and residual losses.

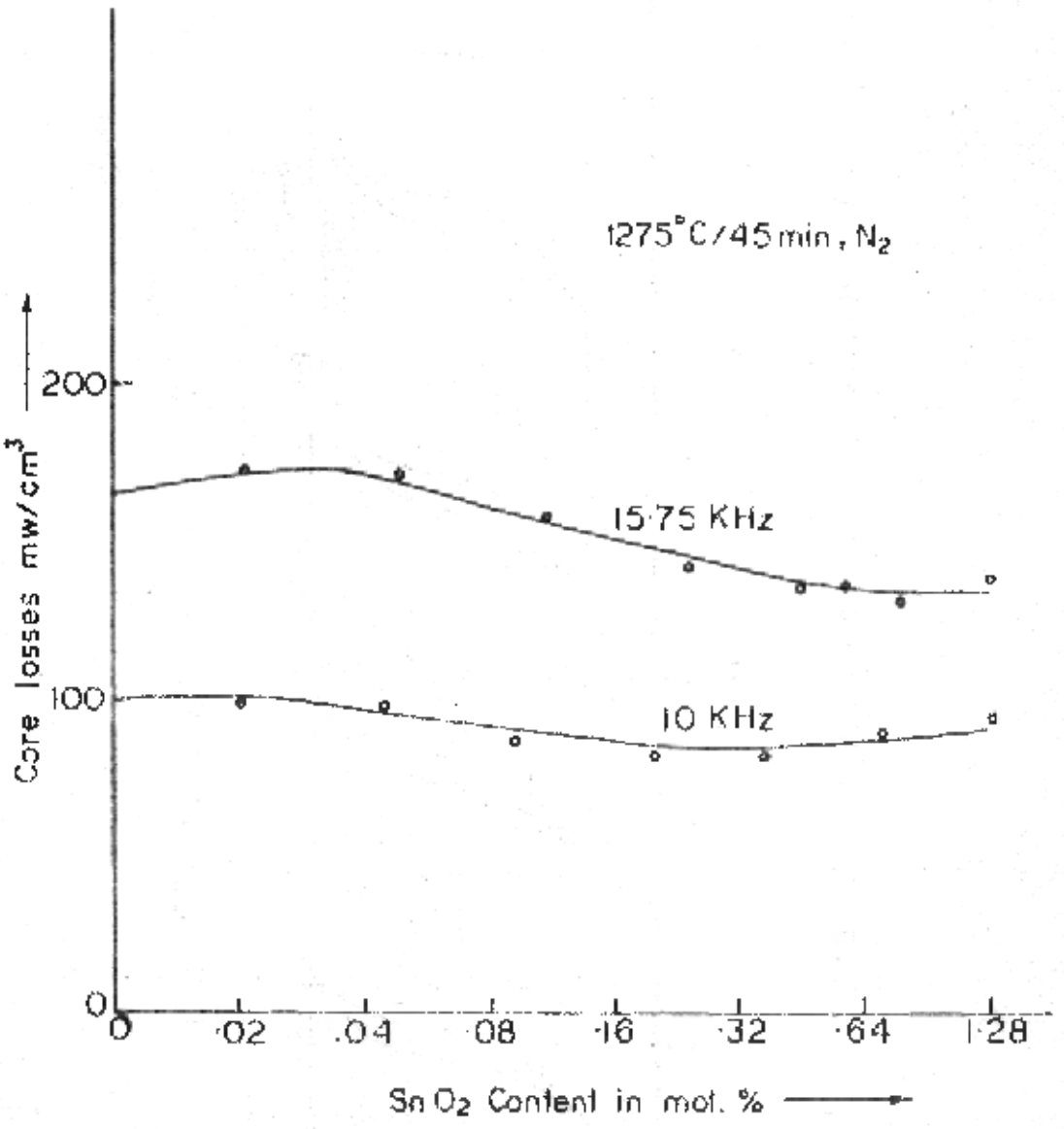

Fig. 5·3·15 Core losses versus SnO_2 content.

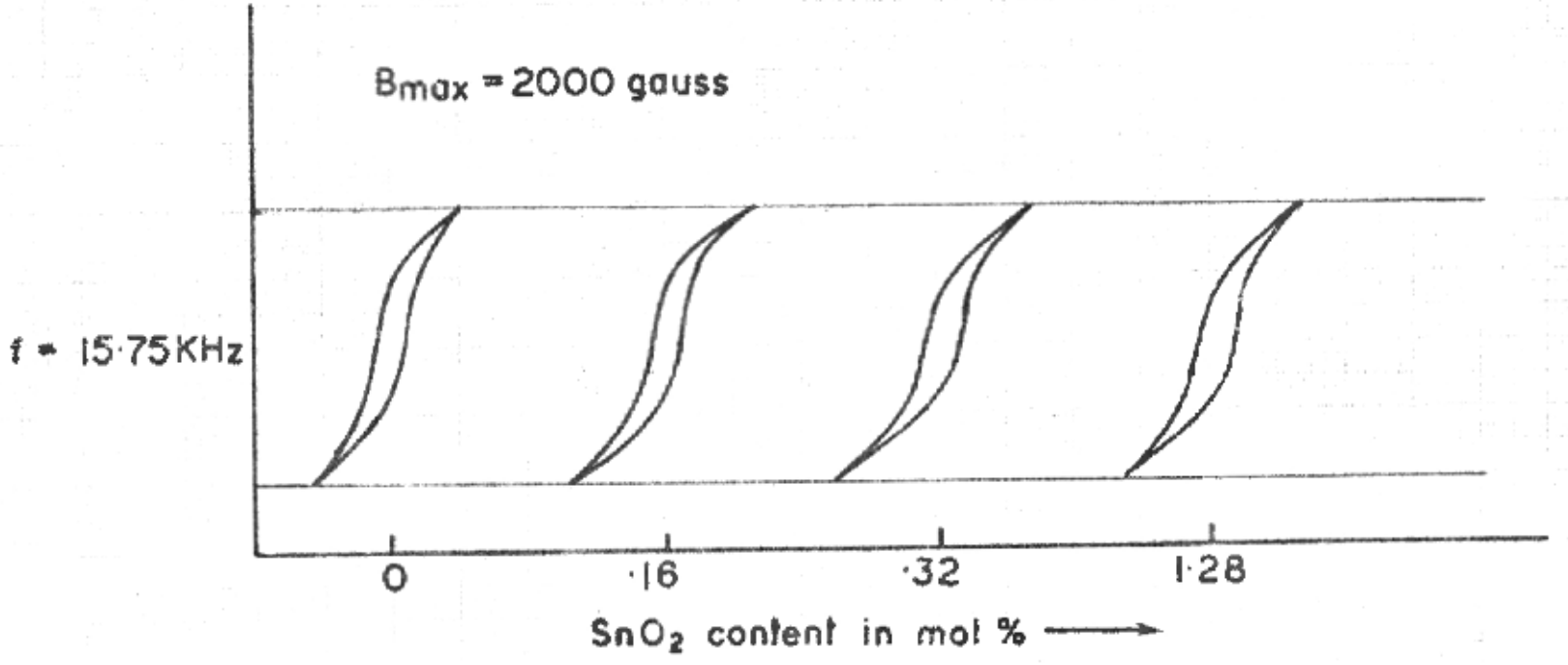

Fig. 5·3·16 A.C. Hysteresis loops for various SnO_2 contents.

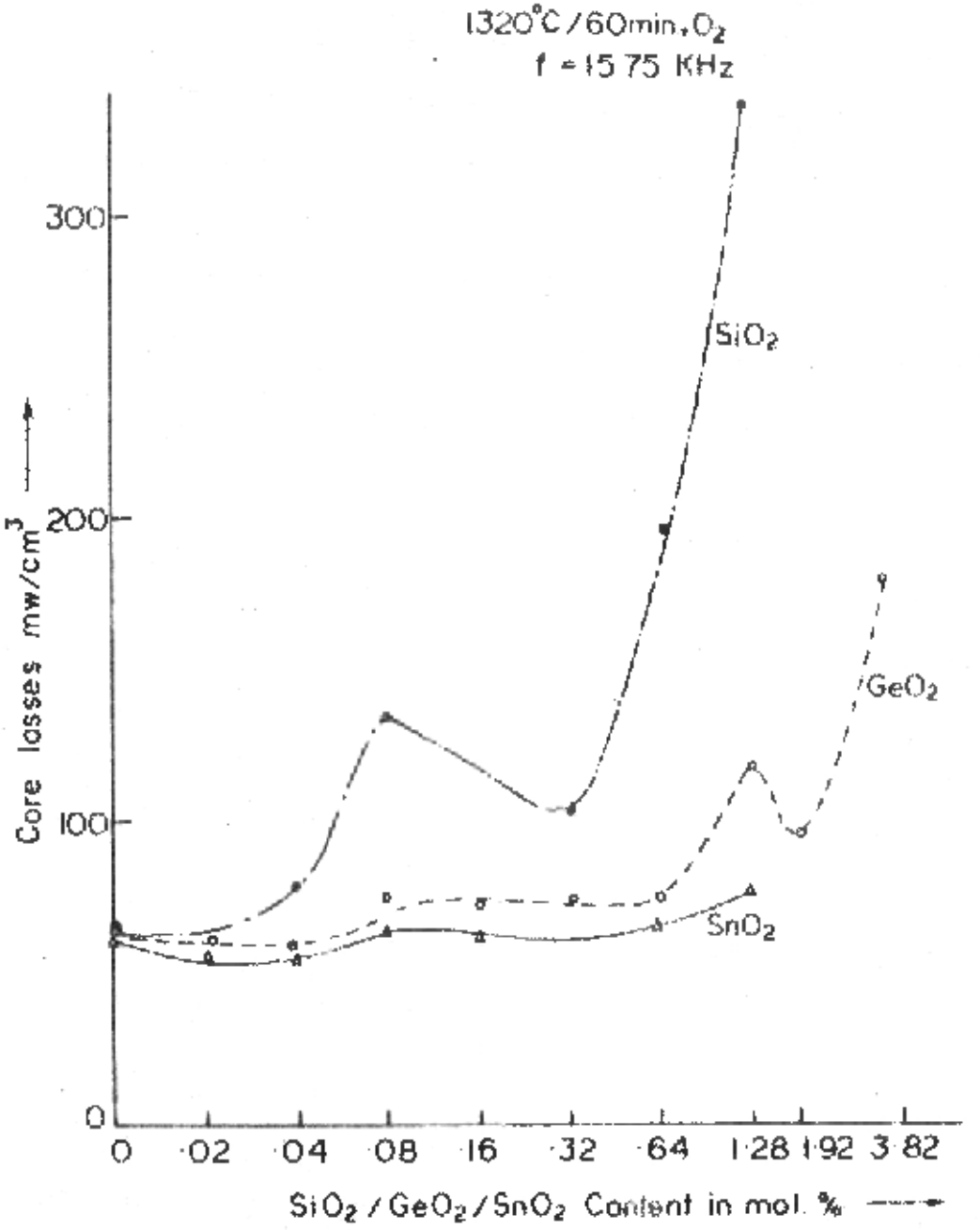

Fig. 5 3·17. Core losses for various contents of SiO_2, GeO_2 and SnO_2.

The eddy current losses are assumed to be negligible in ferrites because of low ferrite conductivity which is many order of magnitude below that of metals, especially in cores of moderate to small dimensions.[4] In high-μ_i ferrites it is apparent that the conductivity increases with the permeability and that eddy current effects begin to play an important role at frequencies as low as several KHz even in cores with dimensions of a few millimeters.[5]

For the present case at $\hat{B}$ = 2000 gauss, f = 15.75 KHz, a rough estimate of the upper limit of eddy current power loss per unit volume, P_e, could be made by[2] (ref. Eqn.1.32).

$$P_e = \frac{(\pi \hat{B} f d)^2}{\rho} \times 10^{-16} \text{ watts cm}^{-3} \qquad (5.3)$$

for d = 15 mm

ρ = 10-100 Ω cm

$P_e \sim$ 3 mW/cm^3

which is about 3% of the total core losses.

These eddy current losses become considerable at higher frequencies and at higher temperature range $\sim 100^{\circ}$C, which is the actual temperature range under which the cores are operated. The temperature dependence of these losses is given by

$$\left(\tan \frac{\delta}{\mu_i}\right)_e \propto \frac{1}{\rho} \qquad (5.4)$$

and

$$\rho = \rho_0 \exp\left(-\frac{E_\rho}{kT}\right) \qquad (5.5)$$

In the present case even at higher temperature range $\sim 100^{\circ}$C for ferrites operated at 15.75 KHz or lower, the eddy current losses contribute negligibly.

The residual losses are also negligible as compared to the hysteresis losses at high flux densities and low frequencies

since they show a peak close to the respective resonance frequencies of the various processes that contribute to these losses e.g. the domain wall resonance and some relaxation processes. At low frequencies it is only the tail of these resonances that contribute. Another reason to neglect the residual losses is that in Mn-Zn ferrites, the residual loss factor is found to be minimum near the secondary maximum where the anisotropy is near zero. This may be due to the fact that when $K_1 \sim 0$, domain walls become thick ($\delta \sim \sqrt{\frac{A}{K_1}}$) and magnetization change is not due to domain wall motion, but due to spin rotation which is an inherently less lossy process.

Jordan[2] proposed that the series loss resistance due to a magnetic core at low flux densities could be expressed in terms of the three losses as follows

$$\frac{R_s}{\mu_i f L_s} = \frac{h}{\mu_i} \frac{NI}{l} \frac{1}{800} + \frac{F}{\mu_i} \frac{f}{(800)^2} + \frac{t}{\mu_i} \frac{1}{(800)} \qquad (5.6)$$

where h = hysteresis loss coefficient in Ω/H at a frequency of 800 Hz for a field strength corresponding to NI/l = 1 ampere turn/cm. F = eddy current loss coefficient and t = residual loss coefficient, both in Ω/H at a frequency of 800 Hz.

It can be seen from Eqn.5.6 that at low flux densities, the losses are mostly eddy current and residual losses. At high frequencies, eddy current losses are predominant and at high flux densities hysteresis losses are predominant. The core losses measured therefore are mainly the hysteresis losses determined by the hysteresis loop area. For the subsequent discussion on the core losses the terms core losses and the hysteresis losses would be considered synonymous.

5.4.2. Decrease in Hysteresis Losses at Low Impurity Contents

Small additions of SiO_2 and GeO_2 are not expected to

affect K_1 as also observed from the μ_i-T curves. The microstructure, on the other hand, shows a significant change. Both SiO_2 and GeO_2 additions tend to increase the grain size and give rise to discontinuous grain structure.

The hysteresis losses and coercive force are strongly dependent on the microstructural features i.e. the grain size, pore size and pore distribution as has been discussed in chapter I. The effect of pore to pore distance, D_p, on H_c has been studied[6] and it has been reported that

$$H_c \propto D_p^{-0.5} \qquad (5.7)$$

in Mn-Zn ferrites.

In the present case also the variation in H_c at low impurity contents has been found to fit in this relationship. Figure 5.4.1 shows the product $H_c.D_p^{0.5}$ plotted against SiO_2 and GeO_2 contents. Up to a SiO_2 content of .32 mol% and GeO_2 content of 1.92 mol%, the product $H_c.D_p^{0.5}$ remains almost constant.

It is therefore evident that the decrease in hysteresis losses at low impurity contents (up to 0.04 mol% SiO_2 and 0.64 mol% GeO_2) is mainly through the increase in the average pore to pore distance.

5.4.3. Increase in Hysteresis Losses with Frequency at Intermediate Impurity Contents

It has been observed that samples exhibiting coarsely grained microstructure formed by growth of giant crystallities with intragranular porosity (.08 mol% SiO_2, 1.28 mol% GeO_2) show rise in hysteresis losses with frequency.

As earlier emphasized, the intracrystalline pores hinder the reversible movements of the domain walls due to the large stray fields at these pores. This causes the loss in the

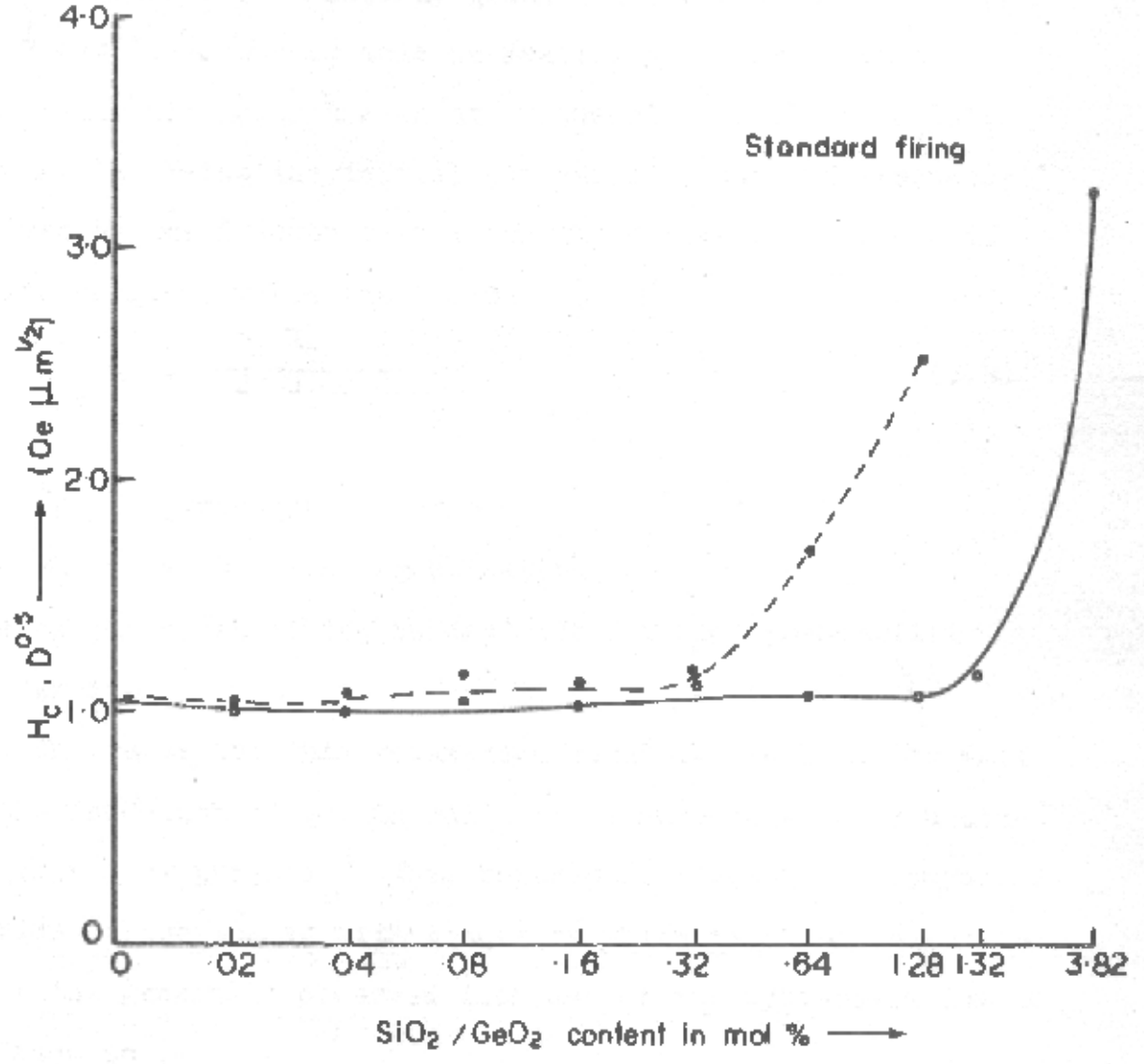

Fig. 5·4·1 It is evident from the figure that up to 0·32 mol % SiO_2 and 1·92 mol % GeO_2, $H_c \propto D_p^{-0.5}$.

initial permeability. At higher field strengths, closure domains are formed at these pores enabling the domain walls to become detached from the pores. The amplitude permeability may then reach levels exceeding the initial permeability as can be seen from Fig.5.4.2 which shows dispersion of permeability at high field strengths for a coarsely-grained Mn-Zn ferrite (observed by E. Roess[4]). However, this permeability is subjected to a strong relaxation effect even at frequencies of 10 to 50 KHz, which are far below the initial permeability cut-off frequency[7,8] f_{c_o} given by the frequency at which the permeability drops to half its original value (at f = 0)

$$f_{c_c} = \frac{1}{3} \frac{\gamma M_s}{2\pi \mu_i \mu_c} \qquad (5.8)$$

where

γ = gyromagnetic ratio

M_s = saturation magnetization

and is of the order of few hundred KHz for high permeability Mn-Zn ferrites.[5]

The cause for this relaxation might be found in the fact that the formation of domain walls at closure domains is a comparatively slow process.[9] This relaxation effect is accompanied by a rise of the losses with frequency which might be responsible for the generally observed increase of the hysteresis losses with frequency.

In Fig.5.4.3, the dispersion in the permeability at the flux density of 2000 gauss has been plotted for (a) basic ferrite with regular grained structure (b) ferrite with .08 mol% SiO_2 with extreme discontinuous grain structure (c) ferrite with 1.28 mol% GeO_2 with somewhat similar structure as that for (b). Unfortunately the instrument could not provide measure-

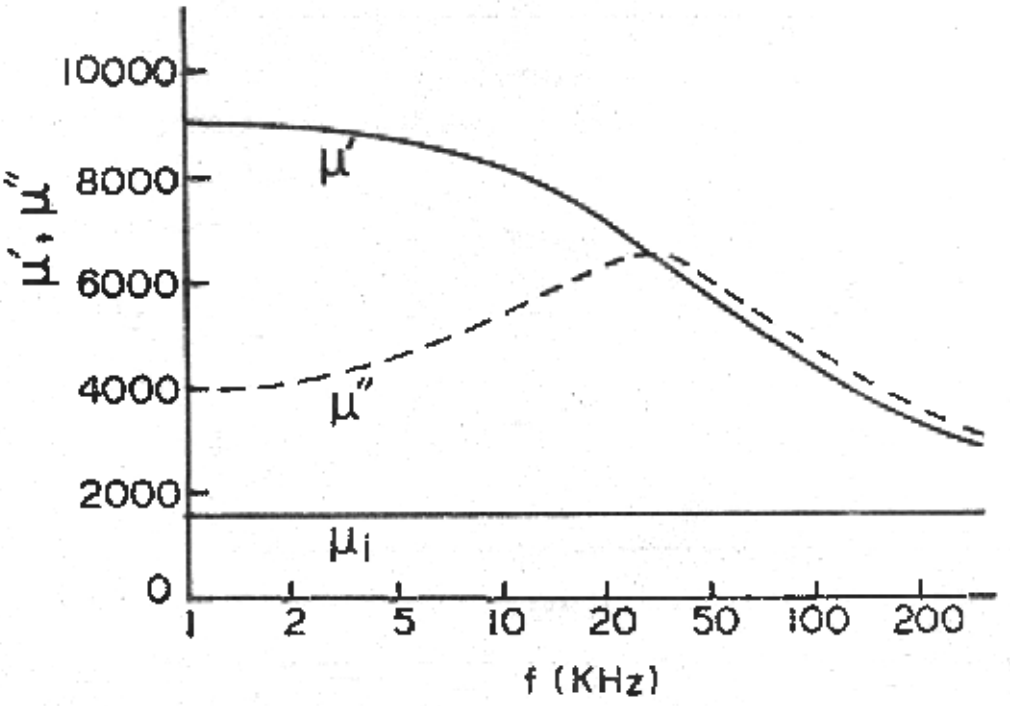

Fig. 5·4·2 Relaxation of the complex permeability at high field strengths. $\hat{H}$ = 200 mA/cm; μ_i = 1500. (After Roess[4] 1970)

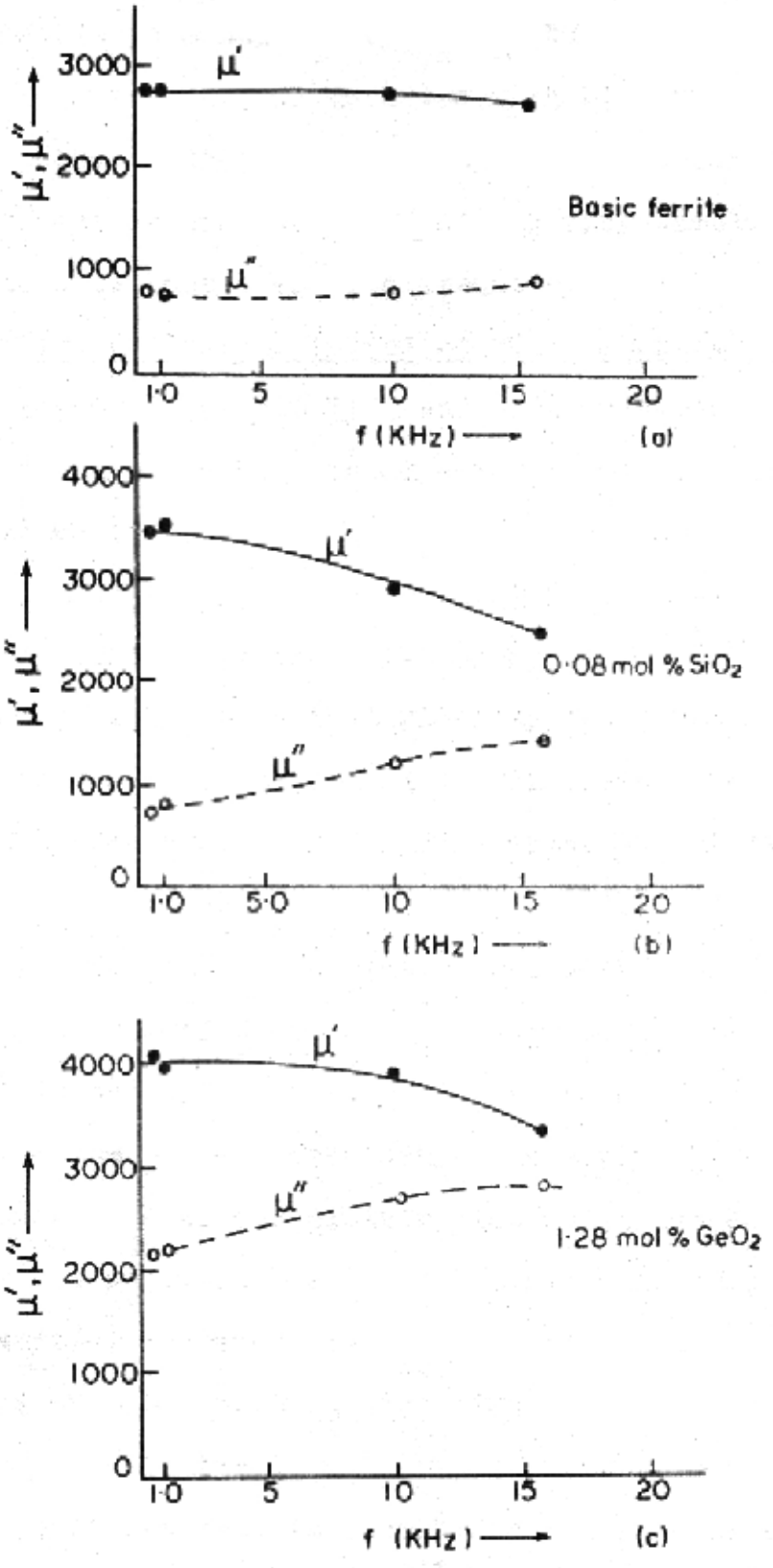

Fig. 5·4·3 μ' and μ'' for the Mn–Zn ferrite (a) Undoped ferrite, (b) Doped with 0·08 mol % SiO_2 and (c) Doped with 1·28 mol % GeO_2.

ments beyond 15.75 KHz and the mean relaxation frequency of the irreversible permeability could not be located. But in general, it can be seen that the ferrites with big grains enclosing the porosity show a tendency of going over to relaxation in the permeability around 20 KHz and these very samples show increase in hysteresis loop area with frequency.

5.4.4. High Hysteresis Losses at High Impurity Contents

Beyond 0.64 mol% SiO_2 and 1.92 mol% GeO_2 the losses are always found to be high accompanied by sloping B-H loops and high values of H_c.

It can also be seen from Fig.5.4.1 that H_c at these levels shows deviation from the relation $H_c \propto D_p^{-0.5}$. In other words, H_c is much higher than that given by the pore to pore distance. This effect may be attributed to the presence of inclusions which are also responsible for lowering μ_i at these concentration of SiO_2 and GeO_2.

The effect of nonmagnetic inclusions on H_c has been studied by a number of workers[10-12] (see sec.1.5.2). These inclusions interact with domain walls and reduce their mobility.

In the present case since the impurity inclusions and their average size and distribution could not be observed within the facilities available, a quantitative description of H_c is not possible. However, it is understood that higher concentrations of SiO_2 and GeO_2 give rise to high H_c and therefore high hysteresis losses.

These nonmagnetic inclusions can also affect the hysteresis losses indirectly. Giles[13] has argued that these inclusions are expected to have a different coefficient of thermal expansion than the ferrite, therefore local stresses may be set up in the

ferrite during cooling.[14] This may result in an increase of the total anisotropy K. According to Globus,[15] the irreversible processes are determined by K instead of K_1 and therefore an increase in K would result in an increase of hysteresis loop area.

It has been observed that at high concentrations of SiO_2 and GeO_2 a second phase appears at the grain boundaries. This nonmagnetic phase may be disturbing wall continuities across the grains giving rise to demagnetizing effects. The effect of wall discontinuities on μ_i has already been discussed in chapter IV. It is assumed that the overall effect of wall discontinuities would be equivalent to having an air gap in the magnetic path. M. Guyot[16] has shown that on introduction of an air gap, the B-H loop slopes, such that the area of the loop (and H_c) for the same m_r ($= M_r/M_s$) remains the same. In the present case, this effect could not be separated out since the sloping loops at high impurity concentrations are also accompained by higher coercive force (due to inclusions) than that of the pure ferrite, the contribution of which can not be estimated quantitatively for the reasons mentioned earlier.

5.4.5. Effect of SnO_2 Additions

SnO_2 additions up to a level of 1.28 mol%, are not found to affect core losses and hysteresis loops significantly for the simple reason that the microstructure remains unaltered.

REFERANCES

1. E.C. Snelling, Proc. Brit. Ceram. Soc., No.2, Dec. 1964, p.151.
2. E.C. Snelling, Soft Ferrites : Properties and Applications, London ILIFFE Books Ltd. 1969, Chap.II.
3. B.L. Worsnop and H.T. Fliut, 'Advanced Practical Physics', Asia Publishing House, p.481.
4. E. Roess, Ferrites : Proc. Internat. Conf., July 1970, Japan, p.187.
5. E. Roess, Ferrites : Proc.Internat. Conf., July 1970, Japan, p.203.
6. G.C. Jain et al., J. Mater. Sci., 11, 1335 (1976).
7. O. Buck and E. Roess, Phys. Stat. Sol. 32, 659 (1969).
8. E. Roess, Z. Angew. Phys. 30, 124 (1970).
9. J.F. Dillon and H.E. Earl, J. Appl. Phys., 30, 202 (1958).
10. H.G. Brion and E. Nembach, Phys. Stat. Sol(a), 26, 599 (1974).
11. H.G. Brion, C.K. Chow and E. Nembach, Int. J. Magnetism, 1973, Vol.5, pp.109-110.
12. L.J. Dijkstra and C. Wert, Phys. Rev., 79, 979 (1950).
13. A.D. Giles and F.F. Westendorp, Colloque C1 Supplement au n° 4, Tome 38, Auril 1977, p.C1-317, ICF-2, Journal de Physique.
14. R.E. Carter, J. Am. Ceram. Soc., 41, 545-550, 1958.
15. A. Globus, "Magnetization Mechanism and Specific Polycrystalline Properties in Soft Magnetic Materials", Invited Talk, Soft Magnetic Materials 2, Cardiff Conf., 1975.
16. M. Guyot, Thesis, Universite de Paris XI, 1975.

Conclusions

The major conclusions drawn from the present study can be summarised as follows:

1. Dopants SiO_2 and GeO_2 have a limited solubility in the Mn-Zn ferrite. These dopants exist as second phase additives in the ferrite forming a liquid like phase at the grain boundaries during sintering.
2. SnO_2 has been found to have a solid solubility with the ferrite even up to a level of 5.70 mol%, the highest level studied.
3. Both SiO_2 and GeO_2 have been found to lower the sintering temperature of the ferrite, i.e. the grain growth sets up at much lower temperatures in the ferrites containing SiO_2 or GeO_2 as against in the undoped one. They have also been found to promote coarse grain growth.

   At lower SiO_2 and GeO_2 concentrations, advantage is gained in the grain size and density due to their high sinterability.

   At intermediate concentrations of SiO_2 and GeO_2, complete discontinuous grain structure appears showing the occurance of giant grains with enclosed

porosity. This effect arises from the fact that at these levels the impurities are present as dispersed phase.

At still higher SiO_2 and GeO_2 contents, somewhat regular grain structure reappears though with higher intragranular porosity as compared to the undoped ferrite. This is because here the second phase is present as a liquid film around the grains during sintering suppressing the abnormal growth.

4. SnO_2 additions are not found to affect the microstructure of the Mn-Zn ferrite even up to a level of 5.70 mol%.

5. At lower SiO_2 and GeO_2 concentrations (up to 0.04 mol% SiO_2 and 0.64 mol% GeO_s) an improvement in the magnetic properties (μ_i and core losses) is obtained. This benefit is obtained due to the increase in the grain size and density. This fact indicates that there could be a possibility of using comparatively impure raw materials (for example SiO_2 which is a naturally present impurity) for ferrite fabrication.

6. At an intermediate concentration of 0.08 mol% SiO_2 and 1.28 mol% GeO_2, a drastic deterioration in the magnetic properties takes place. This is due to the occurance of cannibal grain growth. This concentration of impurity in the ferrite should be avoided for better magnetic properties as the core losses in this impurity range are strongly dependent upon frequency and the ferrite is extremely lossy for operations at high flux densities such as in E.H.T. cores.

7. Above this concentration, the core losses tend to decrease because the cannibal grain growth gets somewhat suppressed.

8. At still higher concentrations of SiO_2 and GeO_2, both μ_i and the core losses are always found to be poor.

9. SnO_2 additions, do not affect the magnetic properties appreciably. An advantage of this additive is found in its capacity to lower the disaccommodation factor and the temperature factor. In the μ_i-T curves, the secondary permeability maximum (SMP) is found to be shifting towards the lower temperature side on SnO_2 additions. This effect could be used to shift the SMP to a predetermined temperature. This could be achieved by doping relatively small amounts of this additive without much change in other properties like the saturation magnetization, Curie temperature and the losses.

10. In the case of SiO_2 and GeO_2, the changes in the resistivity with the amount of impurity doped are in agreement with the corresponding changes in the microstructure.

In the case of SnO_2, the resistivity is found to increase slowly with SnO_2 additions.

Variations in the resistivity with temperature for the three impurities indicate that the predominant conduction mechanism is the electron hopping from Fe^{3+} to Fe^{2+} and that the Sn^{4+} - Fe^{2+} pair formations dissociate at higher temperatures.

*****